

https://dspace.org/

The synthesis and evaluation of BIS-1,2,3- triazolylidene (carbazolide) gold complexes as anticancer agents

Van der Westhuizen, Danielle

2021

https://hdl.handle.net/10539/32435

Van der Westhuizen, Danielle (2021) The synthesis and evaluation of bis-1,2,3-triazolylidene (carbazolide) gold complexes as anti-cancer agents, University of the Witwatersrand, Johannesburg, <http://hdl.handle.net/10539/32435>

Downloaded from a DSpace repository. https://dspace.org/

THE SYNTHESIS AND EVALUATION OF BIS-1,2,3-TRIAZOLYLIDENE(CARBAZOLIDE) GOLD COMPLEXES AS ANTICANCER AGENTS

by

Danielle van der Westhuizen

A thesis submitted to the

Faculty of Science

University of the Witwatersrand

Johannesburg

in fulfilment of the requirements for the degree of

DOCTOR OF PHILOSOPHY

Under the supervision of

Prof D.I. Bezuidenhout (Oulu)

Prof O. Q. Munro (Wits)

February 2021

Declaration

I, Danielle van der Westhuizen, declare that this thesis, which I hereby submit for the degree of Doctor of Philosophy at the University of the Witwatersrand is my own work and have not been previously submitted for any degree or examination at this or any other University.

The syntheses and characterization of resulting compounds were carried out by me in the laboratory of Prof D.I. Bezuidenhout at the University of the Witwatersrand**.**

The collection and refinement of single-crystal X-ray diffraction data were performed by Dr M.A. Fernandes and Prof O.Q. Munro at the University of the Witwatersrand

All in vitro procedures were carried out by me under the assistance of D.F. Joubert in collaboration with Dr A. Stander at the University of Pretoria. Ethical clearance number: 46/2020 (UP).

All bioinorganic experiments were carried out by me under the assistance of Dr C. Slabber (except for the linear dichroism, which was carried out by Dr C. Slabber herself) in the laboratory of Prof O.Q. Munro at the University of the Witwatersrand**.**

The computational studies were performed by Dr C.J. van der Westhuizen using the Centre of High-Performance Computing (CHPC). The molecular docking was completed and interpreted by Prof O.Q. Munro at the University of the Witwatersrand.

I gratefully acknowledge the National Research Foundation (NRF) for financial support in the form of a bursary. Opinions expressed and conclusions arrived at, are those of the author and are not necessarily to be attributed to the NRF.

Results obtained from this study has been submitted for publication entitled “Cytotoxic bis(1,2,3-triazol-5-ylidene)carbazolide gold(I/III) complexes target DNA by partial intercalation” to *Chem – A Eur J*, manuscript ID: chem.202005389

Signature: 

Date: 10 February 2021

Abstract

Gold pincer complexes were evaluated for their potential as suitable anticancer agents. The use of a multidentate pincer ligand composed of an anionic carbazolide backbone and two flanking 1,2,3-triazol-5-ylidenes (trz) was proposed for the effective (redox) stabilization of the gold(III) complex under physiological conditions. A series of precursor triazolium salts of the form $[H_3CNC]2BF_4$ where H_3CNC = 3,6-diR-1,8-bis(N1-Ar, N3-ethyl-1,2,3-triazolium)-9*H*-carbazole (R = H or *tert*-butyl and Ar = phenyl or 2,6-diisopropylphenyl) was synthesized. Subsequent metalation with gold(I) via the free-carbene route of all N3-alkylated salts yielded unidentifiable products, possibly due to competing decomposition pathways. Successful metalation of the N1-phenyl, N3-ethyl triazolium salts via the transmetalation route resulted in the isolation of bi- and tetranuclear gold(I) and silver(I) complexes, respectively. These complexes exhibited varying degrees of stability and solubility and were therefore deemed unfit for biological screening against human cancer cell lines. The use of sterically demanding diarylated wingtip trz substituents did allow for the isolation of gold(I) and gold(III) CNC pincer complexes. The diarylated precursor salt, $[H_3CNC]Cl.PF_6$ (where H_3CNC = 1,8-bis(N1,N3-bis(2,6-diisopropylphenyl)-1,2,3-triazolium)-9*H*-carbazole) and corresponding gold(III) chloride complex, $[CNCAu^{III}Cl]Cl$ exhibited the highest cytotoxicity against a breast cancer cell line with calculated IC_{50} values of 0.4 (± 0.1) μM and 2.3 (± 0.8) μM, respectively. The gold(III) complex, $[CNCAu^{III}Cl]Cl$ showed improved selectivity towards the cancer cell line compared to the diarylated precursor triazolium salt, $[H_3CNC]Cl.PF_6$ with a therapeutic index of 3.8. The interaction of $[CNCAu^{III}Cl]Cl$ with biological macromolecules was investigated. DNA binding studies revealed that $[CNCAu^{III}Cl]Cl$ interacts modestly with DNA in a complete or partial intercalative manner with a calculated binding constant of $3.7 \times 10^4\ M^{-1}$. Interaction of ctDNA with $[CNCAu^{III}Cl]Cl$ leads to an increase of ∼3 °C in the melting temperature of ctDNA and ctDNA induces a negative linear dichroism spectrum of $[CNCAu^{III}Cl]Cl$. Furthermore, $[CNCAu^{III}Cl]Cl$ increases the viscosity of ctDNA in a dose-responsive manner. Molecular docking experiments suggest that $[CNCAu^{III}Cl]Cl$ has the potential to target DNA three-way junctions (ΔG_{score} = −11.89 kcal mol^{-1}) selectively over double-stranded DNA (ΔG_{score} = −7.93 kcal mol^{-1}). $[CNCAu^{III}Cl]Cl$ is inert towards proteins and in the presence of excess glutathione, $[CNCAu^{III}Cl]Cl$ does not reductively demetalate which implies that the cytotoxicity of the complex is due to the intact complex.

Acknowledgements

First and foremost, I would like to express my deepest gratitude to my supervisor, Prof Daniela Bezuidenhout. I met you in my final undergraduate year as a mentorship student and since then you moulded me into the scientist I am today. You never settle for anything but the best and provided the financial, emotional, and technical support to achieve just that. I am very fortunate to have you as a mentor.

I want to say thank you to my office partner and lab mate, Kabelo. You and I started walking this postgraduate journey together, thinking "How hard can this really be? People do this all the time." We were terribly wrong. Thank you for always being a helping hand and lending your ear, no matter the tribulations.

I thank Prof Orde Munro for teaching me that a picture is worth a thousand words and imparting a great deal of knowledge on to me in a short amount of time. I also want to thank the post-docs and the other postgraduate students from Prof Munro's lab for their hospitality and helpfulness.

I wish to thank the support staff of the School of Chemistry at the University of the Witwatersrand for ensuring a well-run department.

I am grateful to my parents. You were determined to provide my sisters and me with much more than you had growing up and ensured that we appreciate the value of a tertiary education. Although, you probably did not think I would take it this far (to a PhD) – I want to say thank you that you supported me whole-heartedly all the way.

Last, but not least. I want to thank Dr Johan van der Westhuizen, my husband. I got to know you during our chemistry honours degree at the University of Pretoria and I cannot imagine how different my path would have been if I have not had you as a partner-in-crime. Thank you for your unfailing support and superior levelheadedness. I am very lucky to have a confidant like you in my subject field (chemistry) and in life.

Table of Contents

Declaration II

Abstract III

Acknowledgements IV

List of Compounds XIV

Abbreviations XVI

Chapter 1 : Introduction 1

1.1 Introduction to cancer 1

1.2 DNA as a cancer drug target 10

1.3 Antiproliferative metallodrugs in clinical use today 14

1.4 Anticancer potential of gold complexes 16

1.5 Carbenes as suitable C-donor ligands 31

1.6 Research rationale and aim. 36

Chapter 2 : Synthesis of 1-aryl-3-alkyl-1,2,3-triazol-5-ylidene metal complexes 38

2.1 Introduction 38

2.2 Aim 41

2.3 Results and discussion 43

2.4 Conclusion 69

2.5 Experimental 72

Chapter 3 : Synthesis of N1,N3-diaryl-1,2,3-triazol-5-ylidene metal complexes and their evaluation as cytotoxic agents. 96

3.1 Introduction 96

3.2 Aim 98

3.3 Results and Discussion 99

3.4 Conclusion 113

3.5 Experimental 113

Chapter 4 : Interaction of the 1,3-diarylated-CNC-gold(III) complex with biological macromolecules. 126

4.1 Introduction 126

4.2 Aim 132

4.3 Results and Discussion 133

4.4 Conclusion 158

4.5 Experimental 159

Chapter 5 : Conclusion 166

5.1 Rationale of study hypothesis 166

5.2 Summary of study 167

5.3 Evaluation of study impact 168

5.4 Future perspectives 169

General Methodology and Instrumentation 171

References 173

List of Figures

Figure 1.1. Phases of the cell cycle. 2

Figure 1.2. A simplified representation of the MAPK cell signalling pathway. 4

Figure 1.3. A basic illustration of a signalling pathway initiated by DNA damage. 5

Figure 1.4. A basic representation of the intrinsic or mitochondrial apoptotic signalling pathway. 7

Figure 1.5. The double-helical structure of the most common conformer of DNA, B-form DNA, with distinguished major and minor grooves. 11

Figure 1.6. Various forms of DNA interactions by clinically relevant anticancer drugs. 12

Figure 1.7. Metal-based chemotherapeutic agents. 15

Figure 1.8. The thiol-disulfide exchange in the Trx system 19

Figure 1.9. Gold(I) complexes reported by the group of Berners-Price with phosphine (**1**–**3**) and NHC ligands (**4**) that have shown promising anticancer potential as DLCs. 21

Figure 1.10. Selected gold(I) complexes with promising anticancer potential. 23

Figure 1.11. Early examples of gold(III) complexes evaluated for their antitumour activity. . 25

Figure 1.12. Representative examples of multidentate gold(III) complexes with anticancer potential. 27

Figure 1.13. Representative examples of cytotoxic CNC pincer gold(III) complexes. 30

Figure 1.14. Representative free carbene structures of 1,2,3-triazol-4-ylidene, imidazole-4-ylidene and imidazole-2-ylidene. 31

Figure 1.15. 1,2,3-triazol-5-ylidene metal complexes investigated as potential anticancer agents. 35

Figure 1.16. The gold(I) complex of the CNC carbazole-based ligand (**33**) reported by Kleinhans et al. and the pyrrole-based multidentate gold(III) complex (**34**) reported by Munro et al. . 36

Figure 1.17. The proposed changes (black) to the original CNC ligand (in grey) to obtain a biologically relevant ligand scaffold with enough electronic stabilization to prevent the reduction of Au^{III} to Au^{I} under physiological conditions. 37

Figure 2.1. The ^{1}H NMR spectra of (a) 3,6-*tert*-butyl-9*H*-carbazole, (b) 1,8-dibromo-3,6-*tert*-butyl-9*H*-carbazole and (c) 1,8-dibromo-9*H*-carbazole in $CDCl_3$. 47

Figure 2.2. ^{1}H NMR spectrum of $\mathbf{K^{H}}$ in $(CD_3)_2SO$ 53

Figure 2.3. ^{1}H NMR spectrum of $\mathbf{L^{H}}$ in $(CD_3)_2SO$ 55

Figure 2.4. The ^{1}H NMR spectrum of $\mathbf{L^{tBu}}$-***N*-AgCl-Au^{I}** in $CDCl_3$ 59

Figure 2.5. (a) Molecular structure $\mathbf{L^{tBu}}$-***N*-AgCl-Au^{I}**, showing 50% probability ellipsoids and partial atom-numbering scheme. 60

Figure 2.6. (a) Molecular structure of $\mathbf{L^{tBu}}$-Au^{I}** showing 50% probability ellipsoids and partial atom-numbering scheme. 61

Figure 2.7. The ^{1}H NMR spectrum of $\mathbf{L^{tBu}}$-Ag^{I}** in $CDCl_3$. 64

Figure 2.8. (a) Molecular structure of $\mathbf{L^{tBu}\text{-}Ag^{I}}$ showing 50% probability ellipsoids and partial atom-numbering scheme. 65

Figure 2.9. The first two examples of isolated N3-alkylated silver(I) triazolylidenes. 66

Figure 2.10. (a) Molecular structure of the $\mathbf{L^{H}\text{-}Ag^{I}}$ showing 50% probability ellipsoids and partial atom-numbering scheme. 69

Figure 2.11. ^{1}H NMR spectrum of $\mathbf{K^{H}}$ in $(CD_3)_2SO$. 73

Figure 2.12. The ^{13}C {^{1}H} NMR spectrum of K^{H} in $(CD_3)_2SO$. 74

Figure 2.13. ^{1}H NMR spectrum of $\mathbf{K^{tBu}}$ in $CDCl_3$. 75

Figure 2.14. The ^{13}C {^{1}H} NMR spectrum of $\mathbf{K^{tBu}}$ in $CDCl_3$. 76

Figure 2.15. ^{1}H NMR spectrum of $\mathbf{K^{tBu}_{dipp}}$ in $CDCl_3$. 77

Figure 2.16. The ^{13}C {^{1}H} NMR spectrum of $\mathbf{K^{tBu}_{dipp}}$ in $CDCl_3$. 78

Figure 2.17. ^{1}H NMR spectrum of $\mathbf{K^{H}_{dipp}}$ in $CDCl_3$. 79

Figure 2.18. The ^{13}C {^{1}H} NMR spectrum of $\mathbf{K^{H}_{dipp}}$ in $CDCl_3$ 80

Figure 2.19. ^{1}H NMR spectrum of $\mathbf{L^{H}}$ in $(CD_3)_2SO$. 82

Figure 2.20. The ^{13}C {^{1}H} NMR spectrum of $\mathbf{L^{H}}$ in $(CD_3)_2SO$. 83

Figure 2.21. ^{1}H NMR spectrum of $\mathbf{L^{tBu}}$ in $CDCl_3$ 83

Figure 2.22. The ^{13}C {^{1}H} NMR spectrum of $\mathbf{L^{tBu}}$ in $CDCl_3$. 84

Figure 2.23. ^{1}H NMR spectrum of $\mathbf{L^{tBu}_{dipp}}$ in $CDCl_3$ 84

Figure 2.24. The ^{13}C {^{1}H} NMR spectrum of $\mathbf{L^{tBu}_{dipp}}$ in $CDCl_3$. 85

Figure 2.25. ^{1}H NMR spectrum of $\mathbf{L^{tBu}\text{-}Ag^{I}}$ in $CDCl_3$ (*grease) 87

Figure 2.26. The ^{13}C {^{1}H} NMR spectrum of $\mathbf{L^{tBu}\text{-}Ag^{I}}$ in $CDCl_3$ (*grease). 87

Figure 2.27. ^{1}H NMR spectrum of $\mathbf{L^{tBu}\text{-}\textit{N}\text{-}AgCl\text{-}Au^{I}}$ in $CDCl_3$ 89

Figure 2.28. The ^{13}C {^{1}H} NMR spectrum of $\mathbf{L^{tBu}\text{-}\textit{N}\text{-}AgCl\text{-}Au^{I}}$ in $CDCl_3$. 90

Figure 2.29. ^{1}H NMR spectrum of $\mathbf{L^{H}\text{-}Ag^{I}}$ in $CDCl_3$ 92

Figure 2.30. The ^{13}C {^{1}H} NMR spectrum of $\mathbf{L^{H}\text{-}Ag^{I}}$ in $CDCl_3$. 92

Figure 2.31. Molecular structures of the triazoles $\mathbf{K^{tBu}}$, $\mathbf{K^{H}_{dipp}}$ and the triazolium salt, $\mathbf{L^{H}}$, showing 50% probability ellipsoids and partial atom-numbering scheme. 93

Figure 3.1. The ^{1}H NMR spectrum of $\mathbf{R^{H}}$ in CD_3CN 101

Figure 3.2. The ^{1}H NMR spectrum of $\mathbf{R^{H}\text{-}Au^{I}}$ in CD_2Cl_2. The carbene resonance of the ^{13}C NMR spectrum is included as an inset. 103

Figure 3.3. Molecular structure of $\mathbf{R^{H}\text{-}Au^{I}}$, viewed from the (a) front and the (b) side showing 50% probability ellipsoids and partial atom-numbering scheme. 104

Figure 3.4. Molecular structure of $\mathbf{R^{H}\text{-}Au^{III}}$, viewed from the (a) front and the (b) side, and $\mathbf{R^{tBu}\text{-}Au^{III}}$ viewed from the (c) front and the (d) side, showing 50% probability ellipsoids and partial atom-numbering scheme. 106

Figure 3.5. The percentage cell viability (determined by CVS assay) of MDA-MB-231 cells treated against the CNC gold(I/III) pincer complexes and their corresponding precursor ligand salts at 5 μM and 50 μM after 48 h of drug exposure compared to the control (0.1% DMSO). Data represent the average ± standard error from mean for 6 replicates of one experiment. 108

Figure 3.6. The ^{1}H NMR spectra of **R^{H}-Au^{III}** in $(CD_3)_2SO$ at 0 hr (green), 48 h (red) and 2 months (blue). 109

Figure 3.7. Dose-response curve of (a) **R^{H}-Au^{III}** and (b) **R^{H}** against MDA-MB-231 cells (red) and EA.hy926 (blue) cells. 112

Figure 3.8. The ^{1}H NMR spectrum of **R^{H}** in CD_3CN 115

Figure 3.9. The ^{13}C {^{1}H} NMR spectrum of **R^{H}** in CD_3CN 115

Figure 3.10. The ^{1}H NMR spectrum of **R^{H}-Au^{I}** in CD_2Cl_2. 117

Figure 3.11. The ^{13}C {^{1}H} NMR spectrum of **R^{H}-Au^{I}** in CD_2Cl_2. 118

Figure 3.12. The ^{1}H NMR spectrum of **R^{H}-Au^{III}** in $(CD_3)_2SO$. 120

Figure 3.13. The ^{13}C {^{1}H} NMR spectrum of **R^{H}-Au^{III}** in $(CD_3)_2SO$. 120

Figure 3.14. The ^{1}H NMR spectrum of **R^{tBu}-Au^{III}** in $(CD_3)_2SO$. 122

Figure 3.15. The ^{13}C {^{1}H} NMR spectrum of **R^{tBu}-Au^{III}** in $(CD_3)_2SO$ 122

Figure 4.1. The crystal structures of cisplatin covalently bound to two N7-atoms of two adjacent guanine residues of duplex DNA (**A**, PDB 1AIO) and a gold(I) biscarbene complex, **12**, interacting with telomeric G-quadruplex DNA in a non-covalent manner (**B**, PDB 5CCW). .127

Figure 4.2. Crystal structures of gold-protein adducts. 128

Figure 4.3. The chemical structures of DNA-binding compounds: ethidium bromide, methyl green, Hoechst 33258 and TriplatinNC. 130

Figure 4.4. The different topological forms of plasmid DNA used in EMSA. 132

Figure 4.5. (a) The UV-vis absorption spectrum of **R^{H}-Au^{III}** in DMSO 134

Figure 4.6. EMSA of **R^{H}-Au^{III}** with pUC57 plasmid DNA (2.5 ng/well, 1× TAE buffer (10% DMSO) that have SC, NOC and Lin DNA. 136

Figure 4.7. (a) The UV-vis absorption spectra of **R^{H}-Au^{III}** in 1× PBS and 10% DMSO before (30.8 μM, blue spectrum) and after sequential additions of ctDNA (final [ctDNA] = 87.7 μM bp, green spectrum). 138

Figure 4.8. Selected examples of metal complexes with known DNA binding motifs proposed by extensive DNA-binding studies. 140

Figure 4.9. The change in the relative viscosity of ctDNA in the presence of **R^{H}-Au^{III}** (red circles), EB (green squares) and HS (blue triangles) as a function of increasing molar ratios of compound to ctDNA (in base pairs) at 37 °C in 1× PBS (10% DMSO). 142

Figure 4.10. The thermal denaturation curves of 75 μM bp ctDNA measured as the change in the absorbance at 260 nm as a function of time in the presence of 35 μM **R^{H}-Au^{III}** or 35 μM EB at 37 °C in 1× PBS (10% DMSO) 144

Figure 4.11. (a) A schematic illustration of a Couette cell 146

Figure 4.12. (a) The ∆LD spectrum of EB with ctDNA 148

Figure 4.13. The ∆LD spectrum of **R^H-Au^{III}** with 10 μM ctDNA 149

Figure 4.14. The space-filled DFT-optimized structure of **R^H-Au^{III}** 151

Figure 4.15. The lowest-energy docking pose of **R^H-Au^{III}** within the central 5'-AT-3' step of the 5'-D(CGGAAAATTACCG)-3' DNA sequence. 152

Figure 4.16. The docking pose of **R^H-Au^{III}** with a palindromic hexameric three-way junction with the sequence 5'-d(CGTACG)-3'. 153

Figure 4.17. (a) The UV-vis absorption spectra of HSA in 1× PBS and 10% DMSO before (12.5 μM, blue spectrum) and after sequential additions of **R^H-Au^{III}** (final [**R^H-Au^{III}**] = 6.5 μM, green spectrum). (b) The UV-vis absorption spectra of HEWL in 1× PBS and 10% DMSO before (30.7 μM, red spectrum) and after sequential additions of **R^H-Au^{III}** (final [**R^H-Au^{III}**] = 17.0 μM, blue spectrum). 155

Figure 4.18. (a) The ^{1}H NMR spectra of **R^H-Au^{III}** in the presence of excess GSH.....156

Figure 4.19. The UV-vis absorption spectra of **R^H-Au^{III}** in DMSO and GSH over 10 h at a molar ratio of 1:7 representing [**R^H-Au^{III}**]:[GSH]. 157

Figure 4.20. A representative ESI-MS of **R^H-Au^{III}** with HEWL at a molar ratio of 10:1 (HEWL: **R^H-Au^{III}**) after 28 days in solution (1× PBS, 10% DMSO). 164

Figure 4.21. The ^{1}H NMR spectrum of **R^H-Au^{III}** in $(CD_3)_2SO$ before the addition of GSH (bottom, blue) and after 5 days in the presence of 8 mM GSH (top, red). 165

List of Schemes

Scheme 1.1. The first imidazole-4-ylidene metal complex reported by Crabtree and co-workers. 32

Scheme 1.2. The first reported 1,2,3-triazolylidene metal complex by Albrecht and co-workers. 33

Scheme 1.3. (a) The isolation of the first free imidazol-2-ylidene. (b) The isolation of the first aNHC and (c) The isolation of the first 1,2,3-triazol-5-ylidene. 34

Scheme 2.1. (a) Huisgen's [3+2] cycloaddition of a generic 1,3-dipole and dipolarophile to generate a 5-membered heterocycle product. (b) The [3+2] cycloaddition of azides and terminal alkynes also described by Huisgen, where the azide acts as the 1,3-dipole reactant and the alkyne as the dipolarophile. (c) The copper(I)-catalysed cycloaddition of azides and terminal alkynes (CuAAC) where only the 1,4-regioisomer is formed. 39

Scheme 2.2. The most popular metalation routes for the complexation of 1,2,3-triazolylidenes. 40

Scheme 2.3. (a) The first report of the isolation of 1,2,3-triazol-5-ylidene which when heated undergoes N3-alkyl group transfer. (b) The attempted isolation of a 1,3-dialkylated-1,2,3-triazolium salt by deprotonation resulted in debenzylation of the triazole ring instead of the expected free carbene. 41

Scheme 2.4. The complete proposed retrosynthetic pathway for the synthesis of the gold(III) CNC pincer complex, **L^{H}-CNC-Au^{III}** from 9*H*-carbazole. 42

Scheme 2.5. The synthetic route to 1,8-dibromo-9*H*-carbazole from 9*H*-carbazole by protecting the most reactive positions of the 9*H*-carbazole (i.e. 3 and 6) with nitro groups. 44

Scheme 2.6. The synthetic route of 1,8-dibromo-9*H*-carbazole from 9*H*-carbazole 46

Scheme 2.7. The synthesis of 1,8-bis((trimethylsilyl)ethynyl)-9*H*-carbazole and the subsequent deprotection to 1,8-diethynyl-9*H*-carbazole. 48

Scheme 2.8. The proposed mechanism for the copper co-catalysed Sonagashira coupling. .49

Scheme 2.9. The mechanism of the CuAAC reaction elucidated by Bertrand and co-workers by isolating key intermediates in the cycle using CAAC ligands. 51

Scheme 2.10. The synthesis of the 1,4-disubstituted-1,2,3-triazoles, **K^{H}** and **K^{tBu}** from aniline and their respective dialkynes. 52

Scheme 2.11. N3-alkylation of triazoles, **K^{H}** and **K^{tBu}** to their respective triazolium salts, **L^{H}** and **L^{tBu}** with triethyloxonium tetrafluoroborate. 54

Scheme 2.12. (a) The previously reported synthesis (concerted free carbene route) of the analogous N1,N3-diarylated **R^{tBu}-Au^{I}** complex on which (b) the metalation of the ligand salts, **L^{H}** and **L^{tBu}** to their expected respective pincer gold(I) complexes are based. 56

Scheme 2.13. The attempted metalation of an N3-alkylated- 1,2,3-triazolylidene with ruthenium that resulted in complete decomposition. 57

Scheme 2.14. The metalation of the ligand salt, **L^{tBu}** to the expected pincer gold(I) complex, **L^{tBu}-CNC-Au^{I}**, using the transmetalation route. 58

Scheme 2.16. The synthesis of the bis-triazolylidene complexes, $\mathbf{L^{tBu}}$-***N***-**AgCl-Au^{I}** and **$\mathbf{L^{tBu}}$-Au^{I}** via the transmetalation route from the triazolium salt, **$\mathbf{L^{tBu}}$**. 62

Scheme 2.17. (a) The synthesis of a possible pincer silver(I) triazolylidene complex, **$\mathbf{L^{tBu}}$-CNC-Ag^{I}** 63

Scheme 2.18. The silver(I) complex isolated from the reaction of **$\mathbf{L^{tBu}}$** and silver(I) oxide with potassium chloride, instead of the desired **$\mathbf{L^{tBu}}$-CNC-Ag^{I}** complex. 64

Scheme 2.19. The synthesis of **$\mathbf{L^{H}}$-Ag^{I}** from the direct metalation of **$\mathbf{L^{H}}$** with silver(I) oxide and potassium chloride.....67

Scheme 2.20. The attempted synthesis of the pincer gold(I) complex, **$\mathbf{L^{tBu}_{dipp}}$-Au^{I}** by substituting the N1-wingtips of the triazole ring with bulky 2,6-diisopropylphenyl groups. The metalation of **$\mathbf{L^{tBu}_{dipp}}$** was unsuccessful regardless of the metalation route employed.....71

Scheme 3.1. The various synthetic routes available for 1,2,3-triazolium salts. 96

Scheme 3.2. The synthesis of the new triazolium salt, **$\mathbf{R^{H}}$** and the corresponding gold(I) (**$\mathbf{R^{H}}$-Au^{I}**) and gold(III) (**$\mathbf{R^{H}}$-Au^{III}**) complexes 99

Scheme 3.3. (a) The synthesis of **$\mathbf{R^{H}}$** and **$\mathbf{R^{tBu}}$** from their respective carbazole-based dialkynes with 1,3-diisopropylphenyltriaz-1-ene and (b) the in situ generation of the 1,3-diaza-2-azoniaallene salt from 1,3-diisopropylphenyltriaz-1-ene. 100

Scheme 3.4. The synthesis of the pincer CNC gold(I) complexes, **$\mathbf{R^{H}}$-Au^{I}** and **$\mathbf{R^{tBu}}$-Au^{I}** via the concerted free-carbene route previously reported for **$\mathbf{R^{tBu}}$-Au^{I}**. 102

Scheme 3.5. The oxidation of the pincer CNC gold(I) complexes **$\mathbf{R^{H}}$-Au^{I}** and **$\mathbf{R^{tBu}}$-Au^{I}** to their corresponding gold(III) chlorido complexes, **$\mathbf{R^{H}}$-Au^{III}** and **$\mathbf{R^{tBu}}$-Au^{III}**, respectively. 104

List of Tables

Table 1.1. The cytotoxicity (IC_{50}) of the gold(I) complexes 5–12 against cancer- and normal (healthy) cells. 24

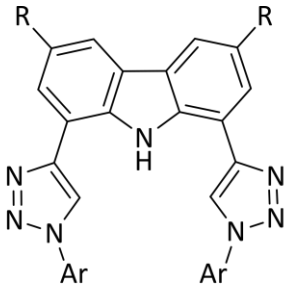
Table 1.2. The cytotoxicity (IC_{50}, μM) of the gold(III) complexes **13**–**18** and **23** with human ovarian carcinoma cell line A2780 and the cisplatin-resistant equivalent cell line, A2780-R. 26

Table 1.3. The cytotoxicity data (IC_{50}, μM) for gold(III) complexes **19**–**22** and **24**–**28** against various cancer- and healthy cell lines. Where applicable, the therapeutic index (T.I.) is indicated. 29

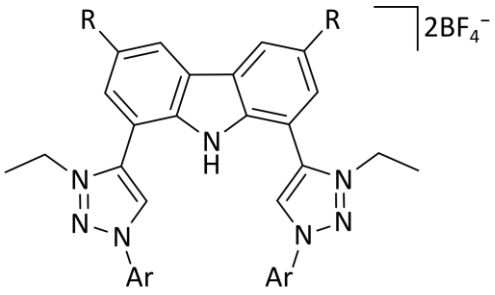
Table 3.1. The IC_{50} (± SEM) values in μM of $\mathbf{R^H}$-$\mathbf{Au^{III}}$ and $\mathbf{R^H}$ against MDA-MB-231 and EA.hy926 cells 110

Table 4.1. Experimental UV-vis absorption maxima and DFT-calculated absorbance data with major contributions to key transitions of $\mathbf{R^H}$-$\mathbf{Au^{III}}$ in DMSO. 135

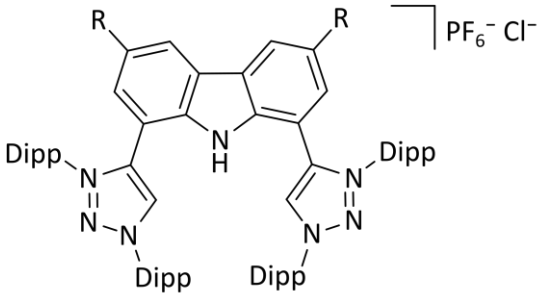
List of Compounds



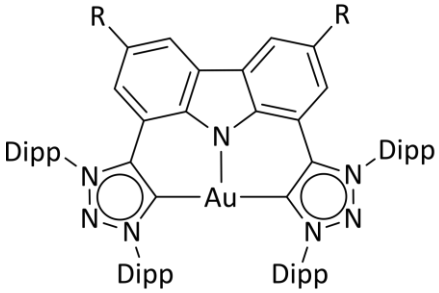
K^{H}: R = H, Ar = Ph
K^{tBu}: R = ^{t}Bu, Ar = Ph
K$^{H}_{dipp}$: R = H, Ar = Dipp
K$^{tBu}_{dipp}$: R = ^{t}Bu, Ar = Dipp



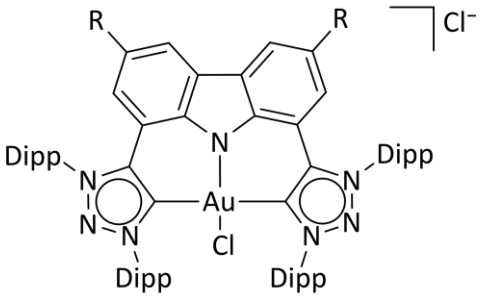
L^{H}: R = H, Ar = Ph
L^{tBu}: R = ^{t}Bu, Ar = Ph
L$^{tBu}_{dipp}$: R = ^{t}Bu, Ar = Dipp



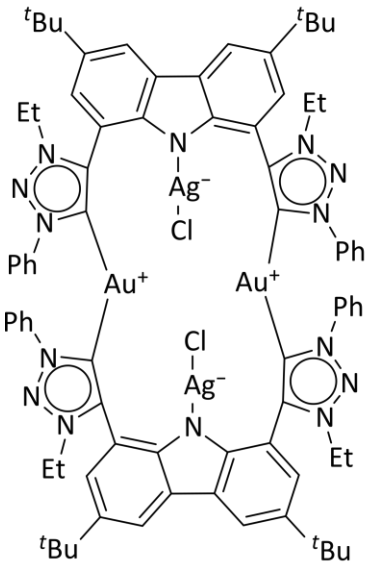
R^{H}: R = H
R^{tBu}: R = ^{t}Bu



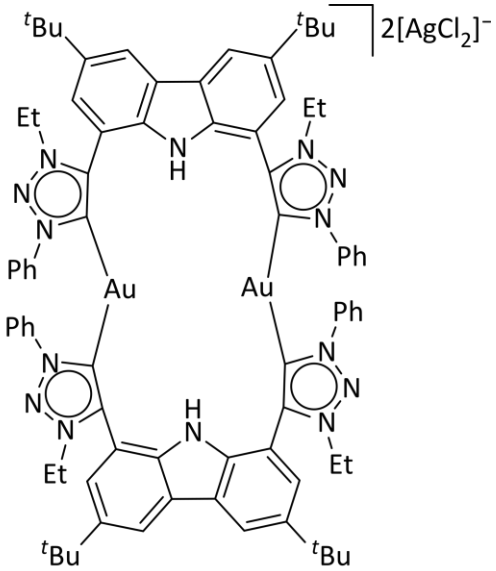
R^{H}-Au^{I}: R = H
R^{tBu}-Au^{I}: R = ^{t}Bu



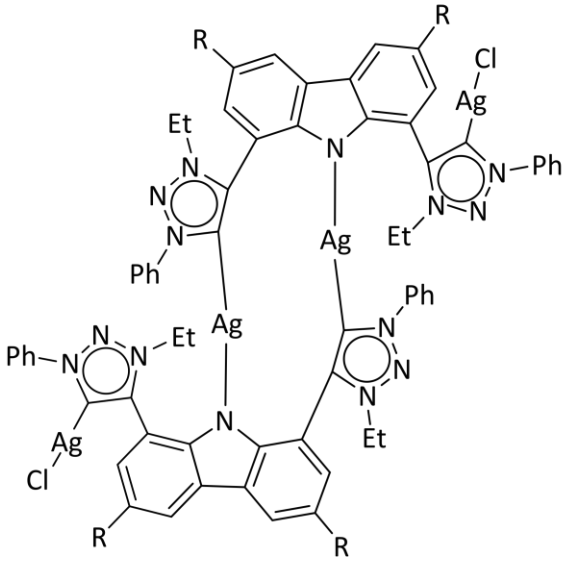
R^{H}-Au^{III}: R = H
R^{tBu}-Au^{III}: R = ^{t}Bu



L^{tBu}-*N*-AgCl-Au^{I}



L^{tBu}-Au^{I}



L^{H}-Ag^{I}: R = H

L^{tBu}-Ag^{I}: R = ^{t}Bu

Abbreviations

A	adenine
aNHC	abnormal N-heterocyclic carbene
Asn	asparagine
ATP	adenosine triphosphate
bp	base pairs
BSA	bovine serum albumin
C	cytosine
CD	circular dichroism
CDK	cyclin-dependant kinases
ctDNA	calf thymus DNA
CuAAC	copper(I)-catalysed 1,3-cycloaddition of terminal alkynes and azides
CVS	crystal violet staining
Cys	cysteine
DCM	dichloromethane
DFT	density-functional theory
Dipp	2,6-diisopropylphenyl
DLC	delocalized lipophilic cations
DMSO	dimethylsulfoxide
DNA	deoxyribonucleic acid
dppz	-dipyrido[3,2-a:2′,3′-c]phenazine
EB	ethidium bromide
EMSA	electrophoretic mobility shift assays
ER	endoplasmic reticulum
ESI-MS	electrospray ionization mass spectrometry
G	guanine
GR	glutathione reductase
GSH	glutathione (reduced)
HEWL	hen egg-white lysozyme
HIC	high-income countries
His	histidine
HMGB	high-motility group box proteins
HS	Hoechst 33258
HSA	human serum albumin
Hsp60	heat shock protein 60
IC_{50}	half maximal inhibitory concentration
IMM	inner mitochondrial membrane
K_b	binding constant
K_i	inhibitory coefficient
LD	linear dichroism
Lin	linear
LMIC	low- to middle-income countries
Lys	lysine
MIC	mesoionic carbene
MOMP	mitochondrial outer membrane permeabilization

MTT	3-(4,5-dimethylthiazol-2-yl)-2,5-diphenyl-2H-tetrazolium bromide
NER	nucleotide excision repair
NHC	N-heterocyclic carbene
NMR	nuclear magnetic resonance
NOC	nicked-open circular
OMM	outer mitochondrial membrane
PBS	(1x) 8 mM NaH_2PO_4, 2 mM KH_2PO_4, 0.14 M NaCl, 10 mM KCl
PCM	polarizable continuum model
PDB	protein data bank
phen	1,10-phenanthroline
PT	permeability transitions
ROS	reactive oxygen species
SC	supercoiled
SC XRD	single crystal X-ray diffraction
T	thymine
TAE	(1x) 40 mM Tris-acetate, 1 mM EDTA
TD-DFT	time-dependent density-functional theory
terpy	terpyridine
THF	tetrahydrofuran
tht	tetrahydrothiophene
T_m	temperature at which half the DNA double helix denatures
Topo	topoisomerase
Trp	tryptophan
Trx	thioredoxin
TrxR	thioredoxin reductase
trz	1,2,3-triazol-5-ylidene
ΔG_{score}	*Glide* scoring function
$\Delta\psi_m$	mitochondrial membrane potential

Chapter 1: Introduction

Cancer is predicted to affect more than 20 million people per year by 2030 in all countries, irrespective of their income levels. The incidence rates for high-income countries (HIC) are the highest for all cancers, especially for lung-, colorectal-, breast- and prostate cancer. Remarkably, the incidence of lung cancers, albeit high, has peaked and is starting to plateau as awareness rise and stricter smoking laws are enforced in most HIC. In the low- to middle-income countries (LMIC), the mortality rates have increased, and there is a high prevalence of infection-related cancers such as stomach-, liver- and cervical cancer. As more LMIC transition to HIC due to economic transformation, it is predicted that exposure to lifestyle factors such as smoking, obesity, inactivity and changes in reproductive patterns will increase the prevalence of cancers associated with reproductive, hormonal, and dietary factors. Indeed, a steep rise in the numbers of breast-, prostate-, colorectal- and lung cancers are already reported for middle-income countries.[1,2]

1.1 Introduction to cancer

1.1.1 Cancer is associated with irregularities in cellular proliferation

The proliferation of healthy cells is controlled by their response to extracellular signals that influence the internal circuitry of the cell i.e., the cell cycle. For the duration of the cycle (Figure 1.1), the cell grows (G_1 and G_2-phase), replicates DNA (S-phase) and divide into two genetically identical daughter cells (M-phase). Cells can withdraw from this cycle to enter a non-dividing state (G_0) as a response to intra- or extracellular signals to either temporarily halt proliferation, to differentiate and mature or undergo cell death. The progression from one stage to the next within the cell cycle is heavily regulated by a cascade of protein kinases (cyclin-dependent kinases, CDKs) and a checkpoint control system.[3] The regulation of the cell cycle is crucial to ensure the homeostasis of cell number and maintenance of normal tissue function.

Protein kinases (such as CDKs) are enzymes that activate or inactivate other proteins and play significant roles in signal transduction pathways within cells. In the case of CDKs, these kinases themselves are only activated by proteins named cyclins (hence the term “cyclin-dependent kinase”). Cyclins are present at different concentrations at different phases of the cell cycle

and therefore orchestrate the events of the cell cycle depending on the type, activity and concentration of specific CDK-cyclin complexes within the cell.[3,4]

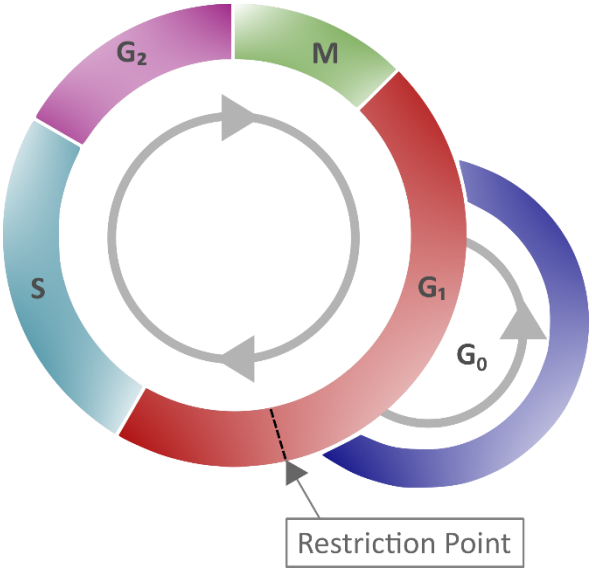


Figure 1.1. Phases of the cell cycle. The cell cycle describes the life of a cell from where it is initially formed from a dividing parent cell until the cell itself divides into two daughter cells. The cycle is divided into sequential phases namely G_1 (first gap), S (synthesis), G_2 (second gap), and M (mitotic). During the G_1 and G_2 phases, the cell grows and carries out functions such as forming new organelles and protein synthesis. Between these two phases, the cell undergoes DNA replication (S-phase) to prepare for cell division and cytokinesis (M-phase). If too few growth factors are available when the cell reaches the restriction point, the cell enter a quiescent stage, G_0.[3,5]

The checkpoint control system evaluates if critical events such as replication of DNA or chromosome segregation occurred correctly and signals the cell cycle machinery to either stop or proceed with the cycle. Critical checkpoints are found in the G_1, G_2 and M phase, but the G_1 checkpoint (the restriction point, Figure 1.1) is considered the most important as cells that proceed past this checkpoint usually transit through the S, G_2 and M phase.[3] The cell responds to extracellular signals only in the G_1 phase, after which the progression to division is autonomous. Cells that receive a stop signal at the restriction point, withdraw from the cycle and transition to G_0.[6]

The lack of cell cycle regulation can result in limitless replicative potential and is therefore associated with the development of cancer.[4] Indeed, cancer cells can proceed through the restriction point independent of extracellular signals (both growth and antigrowth signals) and remain in the cycle to avoid terminal differentiation or cell death.[6] However, the

progression from healthy cells to cancerous cells is a multistep process and is associated with many more acquired capabilities that are common to most types of cancer cells. Cancer cells are able to evade the immune system, generate neovascular support by the process of angiogenesis and can invade tissues and metastasize. In recent years, more studies suggest that cancer cells can also reprogram cellular energy metabolism to sustain uncontrolled proliferation.[7,8]

1.1.2 Cancer, a result of genomic instability

Cancer cells can achieve these hallmarks because of changes in their genomes. More specifically, the success of the cancer cell relies on multiple mutations in the genes of which the products of these genes are key players in maintaining the genomic stability in healthy cells.[7,8] Mutations in two types of genes have been identified in the pathogenesis of cancer, namely oncogenes and tumour suppressor genes.

Proto-oncogenes, which are the non-mutated form of oncogenes, code for proteins that function in signal transduction pathways that stimulate cell growth and division. Mutations in proto-oncogenes (e.g. the *ras* gene that codes for the Ras protein) usually leads to increased activity. The products of tumour suppressor genes, on the other hand, play key roles in signalling pathways that result in inhibited cell division. Mutations in tumour suppressor genes (e.g. the TP53 gene that codes for the p53 protein) leads to a loss in function. Both scenarios can result in increased cellular proliferation and destabilize the genome.[3–5,7,8]

For instance, in about 40% of human melanomas and 25% of human tumours, the MAPK (mitogen-activated protein kinase) signalling pathway is deregulated due to mutated proteins that play key roles in the pathway. The MAPK pathway is a signal transduction pathway that stimulates cellular proliferation and consist of a cascade of proteins, which are products of proto-oncogenes (Figure 1.2). Ras proteins initiate the cascade by relaying signals that are received from an extracellular growth factor. In some cancers, mutated Ras can initiate the signalling cascade without the extracellular growth factor. Moreover, this activation can affect downstream transcription factors, which regulate a repertoire of cellular functions such as DNA replication, cell cycle progression, apoptosis, differentiation and proliferation.[9–11] Cancer cells can potentially acquire multiple hallmark capabilities such as sustained

proliferative signalling, evasion of apoptosis, angiogenesis, modified metabolism and invasion by the mutations of these oncogenic genes.[8,9]

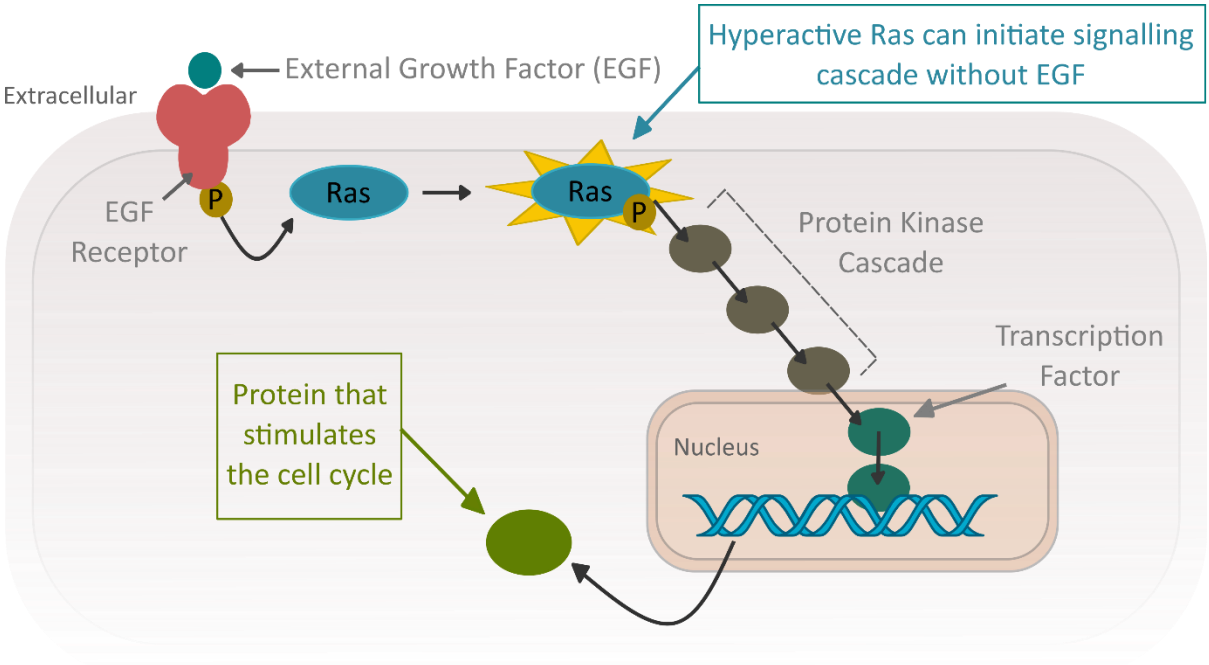


Figure 1.2. A simplified representation of the MAPK cell signalling pathway. This pathway is triggered by the binding of external growth factor (EGF) to the EGF receptor on the membrane of the cell. Ras is activated by the receptor and initiates the signaling cascade involving a series of protein kinases. The last kinase activates a transcription factor that allows the synthesis of a protein that stimulates the cell cycle. Excessive cell replication can occur as a result of a mutated Ras protein, as the pathway can be initiated without the binding of EGF.[3,9,11]

Furthermore, mutations in tumour suppressor genes (e.g. TP53) and the subsequent inactivation of their products (e.g. p53 protein) enable cancer cells to be insensitive to antigrowth signals, evade differentiation and avoid death. Tumour suppressors control cellular proliferation and inhibit tumour development. In more than half of human cancers, TP53 is mutated and leads to a loss of function in p53; an important transcription factor that prevents, as a response to damaged DNA, mutated DNA from being replicated by activating several genes (Figure 1.3). An example of one such gene is *p21*, whose product can halt the cell cycle by binding to CDKs to allow time for DNA repair to take place. Moreover, p53 activates DNA repair genes. However, when the damage to DNA is irreparable, p53 initiates apoptosis by activating pro-apoptotic genes that induce cell death. Cells with damaged DNA or intracellular operating circuits have increased frequency of mutations and loss of genomic stability.[5,7,8]

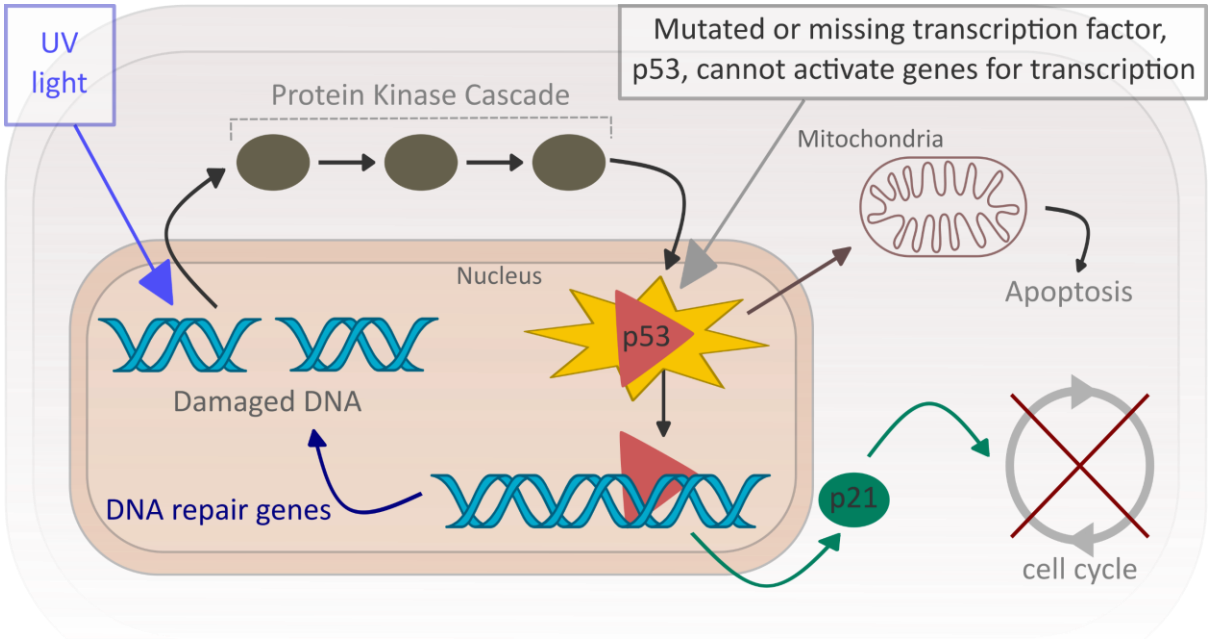


Figure 1.3. A basic illustration of a signalling pathway initiated by DNA damage. The transcription factor, p53 is activated and promotes either the transcription of genes directly involved in DNA repair, the transcription of p21 that can halt the cell cycle to prevent damaged DNA from being copied or induce apoptosis if the DNA is damaged beyond repair. If p53 is missing or defective due to a mutation in TP53, the response system fails to prevent the cell cycle from copying faulty genetic material and fails to induce apoptosis.[3,5,7,8]

1.1.3 Cell death, chemotherapeutics' defense against cancer

The ability of cancer cells to develop into a mass of cells is not only attributed to a rise of uncontrolled proliferation, but also to the reduced rate at which these cells are dying. Although cancer cells successfully evade cell death,[7] they are not fully resistant. The physiological mission of cytotoxic anticancer drugs is to kill cells directly, thereby decreasing the tumour mass, irrespective of the intended cellular target.[12]

Apoptosis is a highly conserved mechanism of cell death that regulates the number of cells in the body. There are two general cell signalling pathways that induce apoptosis, namely the extrinsic and intrinsic pathway. The extrinsic pathway is initiated by extracellular death receptors and has a significant role in immune system functions. The intrinsic pathway, which is also known as the mitochondrial pathway, is of interest as this pathway is initiated intracellularly as a response to DNA damage, anticancer therapy, depleted growth factors and oxidative stress.[13,14]

These diverse apoptotic signals all converge on the mitochondria and stimulate changes in the mitochondria that results in mitochondrial outer membrane permeabilization (MOMP); an event that induces apoptosis by either the release of pro-apoptotic proteins such as cytochrome c from the mitochondria or leads to the loss of vital mitochondrial functions (e.g. respiration). MOMP involves the opening of permeability transitions (PT) pores located on the inner mitochondrial membrane (IMM) and is accompanied by a sudden increase in IMM permeability allowing ions and water to enter the matrix, leading to a loss in mitochondrial transmembrane potential and swelling of the matrix. The outer mitochondrial membrane ruptures as a result and releases pro-apoptotic proteins into the cytoplasm of the cell. The respiratory chain and production of ATP ceases in response to MOMP as vital proteins leak out of the mitochondria, also leading to cell death.[14–16]

The release of the pro-apoptotic protein, cytochrome c, initiates a signalling cascade of the major protein group involved in apoptosis i.e. caspases (Figure 1.4). Cytochrome c binds to Apaf-1 (apoptosis protease-activating factor-1) facilitating the binding of procaspase-9, forming an apoptosome. Pro-caspase-9 is activated to caspase-9, which subsequently activates caspase-3, an effector caspase. Effector caspases initiate apoptosis by activating proteins that are responsible for the cellular changes associated with apoptosis and are characterized by cell membrane blebbing, cell shrinkage, chromatin condensation and DNA fragmentation. Thereafter, the contents are packaged into apoptotic bodies and ingested by neighbouring- or immune cells through phagocytosis.[5,13,14,16]

The Bcl-2 protein family are considered the regulators of apoptosis but more specifically, they mediate and control the events leading to MOMP. The Bcl-2 protein family consists of a group of proteins that all have at least one of the four relatively conserved Bcl-2 homology (BH) domains (illustrated in Figure 1.4 as an inset). Members of this protein family are either initiators (pro-apoptotic) or inhibitors (anti-apoptotic) of apoptosis. The pro-apoptotic members are further divided into BH3-only (e.g., Noxa, Puma) and multi-domain members (e.g., Bax, Bak), the latter sequestered or neutralized by anti-apoptotic members (e.g., Bcl-2, Bcl-X_L). The relative ratio of anti- and proapoptotic members function as a rheostatic control over cell death.[5,14–16]

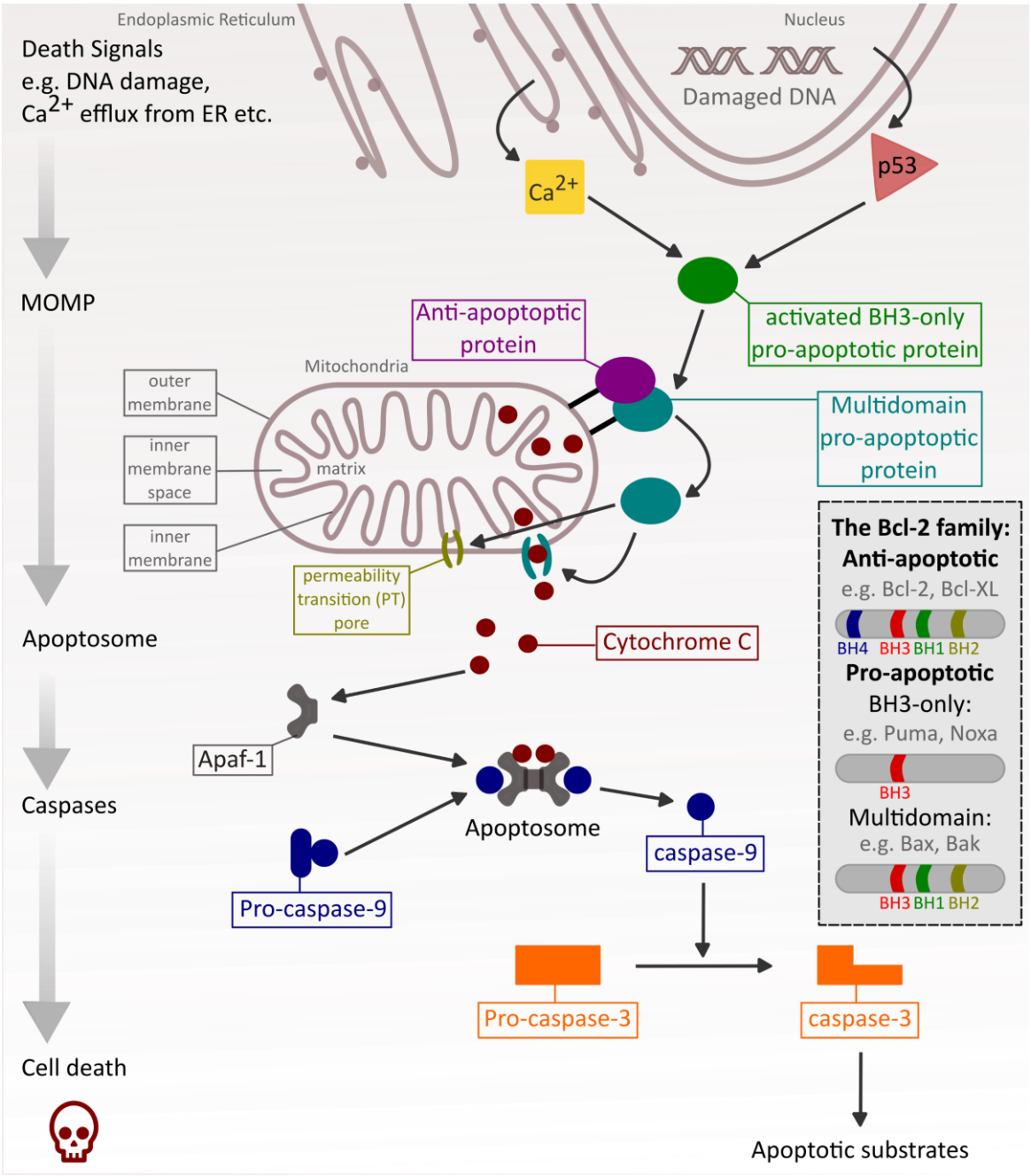


Figure 1.4. A basic representation of the intrinsic or mitochondrial apoptotic signalling pathway. Internal signals from the cell converge on the mitochondria, resulting in MOMP mediated by pro-apoptotic proteins of the Bcl-2 family. MOMP results in the release of cytochrome c, which binds to Apaf-1 to form an apoptosome with pro-caspase-9, which is subsequently activated to caspase 9. The effector caspase, pro-caspase-3, is activated by caspase-9 and activates proteins that execute apoptosis. The inset illustrates how the members of the Bcl-2 family are group based on their functions (i.e. anti- and pro-apoptotic) and number of BH domains.[5,14,16]

Apoptosis is triggered once BH3-only proteins (i.e. Noxa and Puma) receive a death signal (for e.g. in response to DNA damage) from p53. The activation of the BH3 only proteins leads to

the activation of downstream multi-domain proapoptotic proteins. BH3-only proteins can release multi-domain pro-apoptotic proteins such as Bax and Bak from anti-apoptotic proteins (e.g. Bcl-2) to allow the transition of the unbound Bax and Bak to permeabilize the OMM for the release of cytochrome c by either forming pores in the OMM themselves or opening the PT pores to induce MOMP (Figure 1.4). The anti-apoptotic proteins such as Bcl-2 maintain the mitochondrial membrane status to prevent the release of cytochrome c, balance the interactions between the members of the Bcl-2 family and counterbalance the damage done to the mitochondria, nucleus and endoplasmic reticulum (ER) by reactive oxygen species (ROS).[14,15]

Stress to the ER can also initiate apoptosis. The main function of the ER involves protein processing and sorting. The ER also plays a key role in the homeostasis of calcium, as it is the major store of intracellular calcium.[5] When the ER experiences stress due to the exposure of chemical toxins, oxidative stress etc., proteins are misfolded and the ER initiates repair mechanisms to either remedy or degrade the faulty proteins. When the response fails to resolve the problem, the ER releases calcium into the cytoplasm. The mitochondria respond by releasing a small amount of cytochrome c where it interacts with ER receptors. The ER releases more calcium, resulting in a mass release of cytochrome c from the mitochondria, thereby initiating stress-induced apoptosis.[14]

Cancer cells have various mechanisms to avoid apoptosis. In B-cell lymphoma, the anti-apoptotic protein, Bcl-2 is overexpressed thereby tipping the scales in favour of survival. The loss of p53 is one of the most successful ways cancer cells avoid cell death as p53 initiates the apoptotic caspase cascade not only in response to DNA damage but also in abnormal conditions such as hypoxia and overexpression of oncogenes (e.g. Bcl-2).[7,13]

Other mechanisms of cell death include necrosis and autophagy. Cell death by necrosis is often associated with cells that suffer excessive damage. Necrotic conditions are favoured when normal physiological function (e.g., ion transport, pH balance and cellular respiration) is inhibited due to either pathological events (e.g., microbial, or viral infection) or injury. Necrosis is characterized by the release of cellular contents into surrounding tissues due to the swelling of the cytoplasm and the breakdown of the cell membrane, thereby eliciting an inflammatory response by the immune system.[14,16]

Cell death can also occur through autophagy, an intracellular lysosome-mediated catabolic mechanism. Autophagy essentially recovers nutrients such as amino acids during periods of nutrient scarcity by degrading proteins within the cell and digesting damaged or dysfunctional cellular components to ensure cytoplasmic homeostasis. At first glance, autophagy promotes cell survival, but cell death can occur due to extensive vacuolization of the cytoplasm and therefore participate in the destruction of cells.[14,16,17]

Alas, the relationship between cancer and cell death is not as straightforward as predicted. In recent years, a mounting body of evidence has revealed that cell death can promote tumourigenesis. For instance, cancer cells can initiate autophagy under the same stressful conditions (starvation, oxidative stress etc.,) as healthy cells, to the extent where this state becomes protective and reversable, especially when exposed to anticancer treatment. In the event of necrotic death, pro-inflammatory signals are elicited, alerting immune inflammatory cells to the site of damage. Bioactive molecules such as growth factors, survival factors and enzymes that promote angiogenesis, invasion and metastasis are supplied to the tumour microenvironment as a response. In early tumour development, the sacrificial death of a pre-malignant cell possibly allows the development of more aggressive- and apoptosis-resistant cancer cells.[8,12]

Taking the new evidence into account, it remains true that cancer cells avoid death, and that cell death is still the intended outcome of anticancer therapy. However, considering the tumour environment, drugs that elicit inflammatory responses and unnecessary tissue damage are seemingly best avoided. Drugs that are highly effective at killing all tumour cells are ideal as death induced by chemotherapeutic drugs impose a selective pressure on cancer cells. The chance of treatment-resistant cancer arises as a result of feeble anticancer agents.[12]

Cancer is the result of defects in cellular regulatory mechanisms, and the examples discussed above do not do the complexity around the disease any justice. The list of possible faults in the internal circuitry and potential checkpoint fails is non-exhaustive. The advances made in elucidating the molecular biology of cancer allow for the development of target-specific treatments. Unfortunately, these targets match those operating in healthy cells, and achieving selective therapy remains elusive. Also, as one tumourigenic mechanism is blocked by a drug, another arises resulting in the prevalence of drug resistance. Ideally,

chemotherapeutic agents should have a multi-faceted approach to successfully induce cell death, a demise cancer cells dutifully avoid.

1.2 DNA as a cancer drug target

The chemotherapeutic effects of mustard gas, ironically discovered during the First World War, is attributed to its ability to alkylate DNA. The use of mustard gas and nitrogen mustard, an easier to manage alternative in clinical trials, is one of the first examples of DNA targeted chemotherapy.[18,19] The appropriateness of DNA as an anticancer drug target is validated by the predominant role it plays in cellular division, the transmission of genetic material and control of cellular processes and how closely these functions relate to the development of cancer.[20]

1.2.1 The structure of DNA

DNA is a polynucleotide, where each nucleotide consists of a deoxyribose sugar, a phosphate group and an aromatic nitrogenous base, of which there are four types: adenine (A), guanine (G), thymine (T) and cytosine (C). The individual nucleotide residues are joined by a phosphodiester bond between the sugar of one nucleotide and the phosphate group of another, forming one DNA strand. The direction of the DNA strand depends on the direction of the phosphodiester bond i.e., a 3’ – 5’ phosphodiester bond is between carbon-3 of the sugar of one nucleotide and carbon-5 of the sugar of the succeeding nucleotide. The structure of duplex DNA takes on the form of a double helix, whereby two DNA strands are aligned antiparallel (5’–3’ and 3’–5’) and are held together by hydrogen bonds between complementary base pairs (A–T, G–C), as illustrated in Figure 1.5. The base pairs (bp) are stacked in the centre of the helix and the sugar-phosphate backbone frame the outside of the helix.[21]

The helical structure of B-DNA, the most common conformer of DNA, is presented in Figure 1.5. The helix is right-handed and is defined by a helix pitch of 35.7 Å and 10.5 bp per turn. Since each helical turn is 360°, each base is rotated 34.3° from the subsequent base. A-form DNA deviates from these parameters because of sugar puckering that results in a smaller helix pitch (28.15 Å), 11 base pairs per turn and a significant base tilt of 20 ° from the helical axis. Another variant, Z-DNA, is a left-handed helix with a zig-zag backbone.[20,21] Of the conformations, the helical structure of B-DNA offers the best distinction between the major

and the minor grooves. These grooves vary quite significantly due to the exposure of different functional groups as potential binding sites for proteins, chemicals and drugs.[20–22]

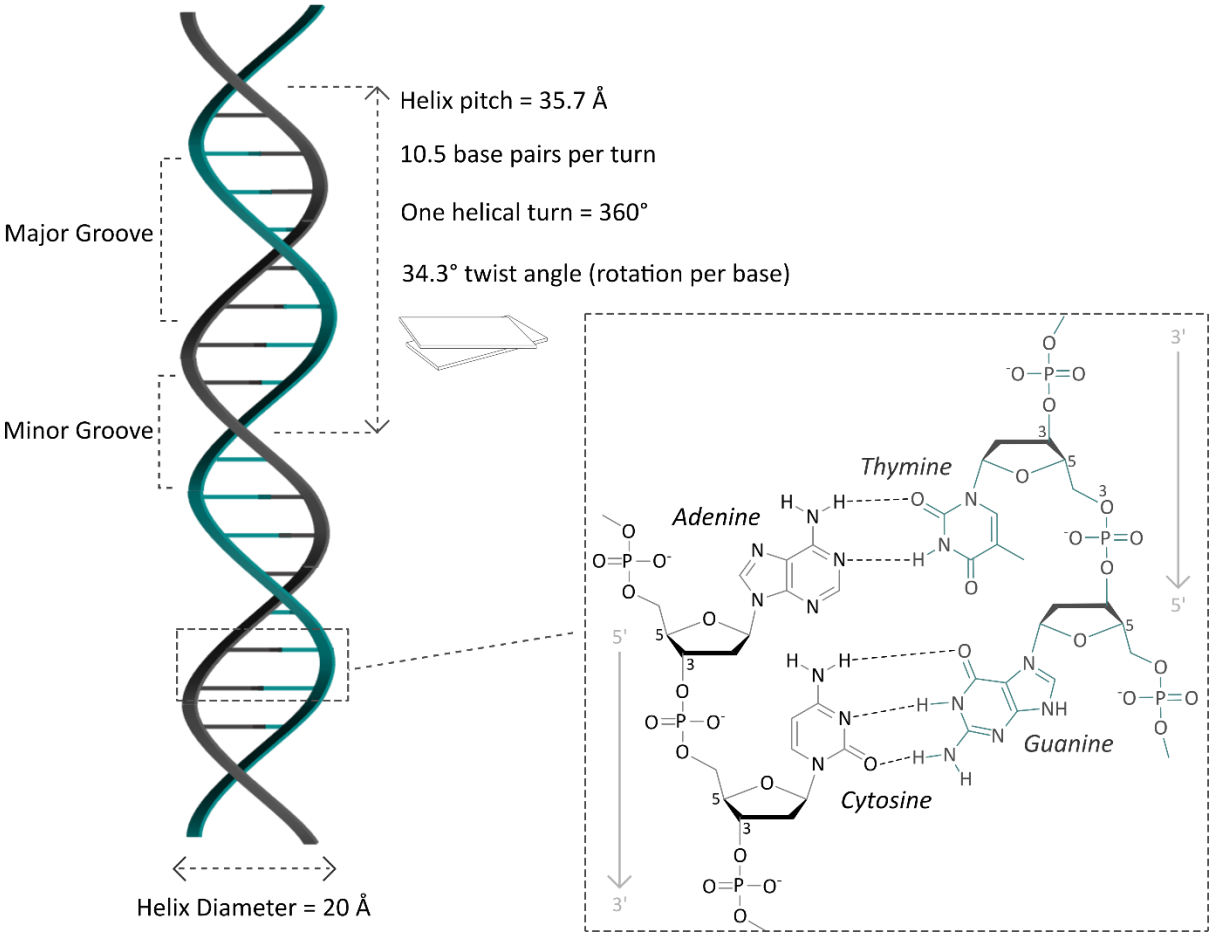


Figure 1.5. The double-helical structure of the most common conformer of DNA, B-form DNA, with distinguished major and minor grooves. The structural parameters (helical pitch of 35.7 Å, 10.5 residues per turn, 34.3 ° twist angle between residues and a diameter of 20 Å associated with B-DNA are shown. The inset shows the chemical structure of the residues and their complementary interactions. The direction of the strands is also indicated.[21]

1.2.2 Interactions of DNA with clinically approved anticancer drugs

Alkylating agents such as nitrogen mustard are among the most effective anticancer drugs due to their ability to crosslink DNA strands. Two nucleotide residues on the same strand (intrastrand) or opposite strands (interstrand) can be covalently connected by dialkylating agents (Figure 1.6). In the case of nitrogen mustard, interstrand crosslinks are formed, subsequently preventing the separation of DNA strands during critical cellular processes such as replication and transcription of proteins. Therefore, nitrogen mustard and its derivatives are most effective against highly proliferating cancers such as leukaemias and lymphomas.

Unfortunately, though, high proliferating healthy tissues are also targeted and result in side effects such as nausea, vomiting, hair loss and decreased production of blood cells during treatment.[18,19,23]

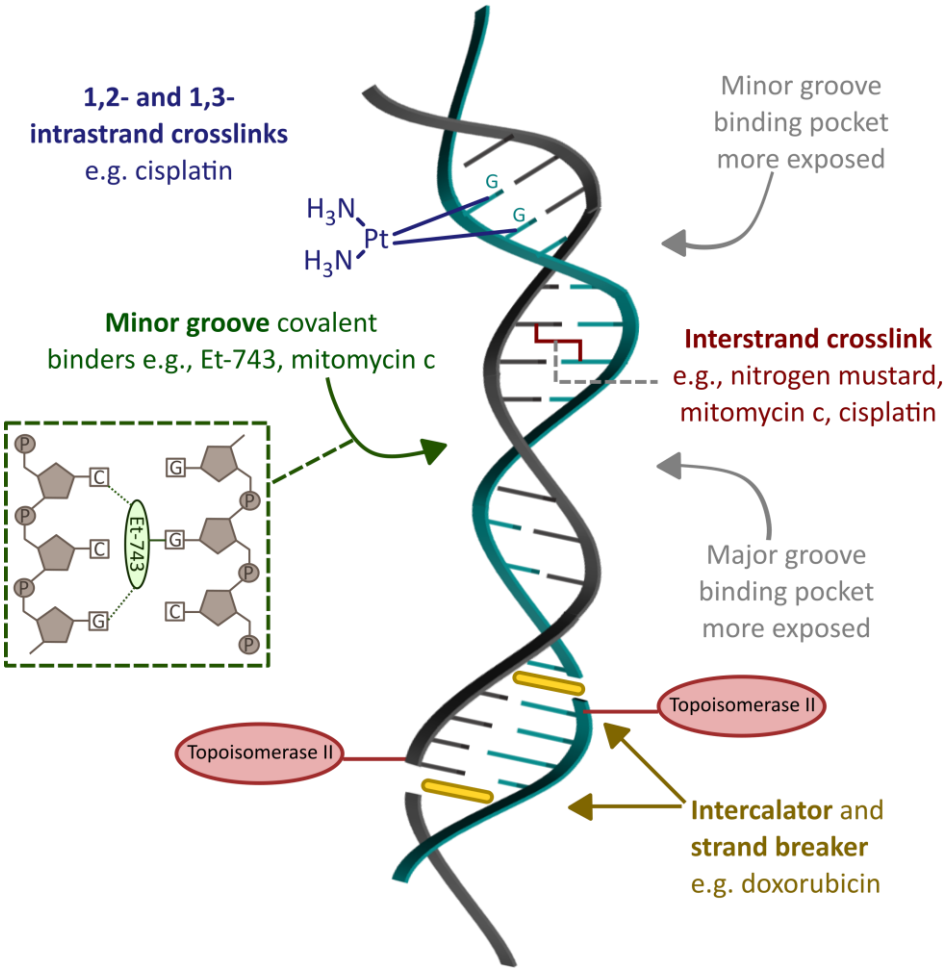


Figure 1.6. Various forms of DNA interactions by clinically relevant anticancer drugs. Cisplatin forms 1,2- and 1,3-intrastrand linkages (forming covalent bonds with the N7 of guanine residues), bending the DNA towards the major groove, opening the minor groove for potential protein binding. Cisplatin can also form interstrand links like nitrogen mustard and the antibiotic, mitomycin C. Trabectedin (Et-743) is a sequence-specific (one of the known sequences are shown in the inset) covalent minor groove binder and distorts the DNA helix in exposing the major groove binding pocket. Lastly, doxorubicin is a DNA intercalator and breaks DNA strands where Topoisomerase II is bound.[19,24,25] Not all known interactions of each drug are shown.

Other clinically approved drugs i.e., cisplatin, mitomycin C and the naturally occurring, Et-743 also covalently bind to, and from cross-linked DNA but elicit markedly different cellular responses and therefore have distinctive chemotherapeutic mechanisms and selectivity (Figure 1.6). Often, drugs that bind to DNA influence the interaction of proteins with DNA, as

DNA is the framework on to which proteins, responsible for replication, transcription, packaging, recombination, repair, etc. bind.[19]

Cisplatin preferentially binds to the N7 of two guanine residues on the same strand, forming 1,2- or 1,3 intrastrand cross-linked DNA (the inactive *trans*-isomer of cisplatin cannot form these intrastrand links). These crosslinks significantly bend the DNA towards the major groove and a minor groove binding pocket is exposed to which several proteins can bind (e.g., high-motility group box proteins (HMGB), repair proteins, transcription factors and other damage recognition proteins). Trapped proteins are prevented from carrying out their intended functions or mask the distortion of DNA from the nucleotide excision repair (NER) mechanism: a process that repairs DNA lesions caused by environmental or chemical damage by recognizing, removing and resynthesizing the damaged region. The details regarding the progression from initial damage to cell death remain to some extent unclear but several DNA-damage transduction signal pathways (e.g., AKT-, c-ABL-, MAPK-, p53 pathways, etc.) are thought to be influenced in response to cisplatin-induced damage.[19,24,26–33]

While cisplatin bends the DNA towards the minor groove, the naturally occurring Et-743 anticancer drug covalently binds to the minor groove of DNA and unveils the major groove pocket for protein binding. Thus, a whole host of different proteins are targeted including key players in transcription-coupled NER (the repair of genes that are coded into proteins).[25] Et-743 and mitomycin C,[34,35] also a minor groove binder, has far greater DNA binding selectivity than normal DNA alkylators, due to their sequence specificity (see inset of Figure 1.6).[19]

Influencing DNA-protein complexes are not limited to covalent binders. Doxorubicin, a non-specific DNA intercalator, which is unexpectedly selective towards cancer cells, induces DNA strand breaks where the enzyme topoisomerase II (Topo II) is bound to DNA. Topoisomerases are responsible for maintaining the correct DNA structure during critical cellular functions such as replication and transcription by introducing temporary single-(topo I) or double-stranded (topo II) breaks.[36] Cancer cells might be more susceptible to doxorubicin due to the elevated levels of topoisomerases found in most cancer cells.[19]

Although not clinically relevant yet, drugs that target DNA secondary structures such as G-quadruplexes are also being investigated. G-quadruplexes form readily under physiological conditions and consist of intermittent runs of guanine residues. These quadruplex structures mainly form in the promoter (DNA sequences to which the enzyme RNA polymerase bind to

initiate protein synthesis) and telomeric regions of the DNA sequence. Telomeres protect the ends of chromosomes during DNA replication and shorten progressively during each cell division until cell death ensues. Cancer cells have highly expressed telomerase activity, the enzyme responsible for the maintenance of telomeres and is another mechanism of acquired immortality. G-quadruplex interacting drugs can either result in the inhibition of telomerase by blocking the binding of the enzyme or prevent the formation of G-quadruplexes (i.e. telomeres and promoters) altogether.[5,7,8,19,37]

The structural diversity of DNA allows for a variety of interactions as potential drug-binding sites. Some interactions prove more toxic to healthy cells, where other interactions take advantage of elevated protein levels found in cancer cells, but drugs that target DNA are some of the most successful anticancer drugs and have proved to be clinically appropriate.

Metal complexes, due to their own high tolerance for structural and electronic modification, can exploit various DNA binding sites with great success.[20,22,37,38] Moreover, metal complexes offer the possibility of interacting with a diverse range of molecular targets, not limited to DNA which can allow the development of a drug with a multi-faceted approach. Investigations into the anticancer potential of metal complexes were initiated after the discovery of cisplatin's anticancer properties.

1.3 Antiproliferative metallodrugs in clinical use today

The antiproliferative properties of cisplatin (*cis*-diamminedichloroplatinum(II), Figure 1.7) was discovered serendipitously when the cell division of *Escherichia coli* was halted during an experiment that involved platinum mesh electrodes. The electrolysis products responsible for the inhibition were found to be, what is now known as, cisplatin and the platinum(IV) analogue. Further in vivo tests and clinical studies revealed cisplatin to be a potent anticancer agent and gained approval in 1978.[39–42] Since then, many other platinum(II) complexes were evaluated for their potential as anticancer agents, but only two more, carboplatin and oxaliplatin (Figure 1.7) have reached international approval.[43]

The success of cisplatin lead to widespread investigations into the antitumour properties of other transition metal complexes,[44–50] especially since platinum-based agents lack true specificity and have been found to target healthy, highly proliferating cells. This lack of selectivity results in toxic side effects and therefore limits the administered dose to sub-lethal

for tumours which ultimately leads to drug resistance.[31,43,51,52] Indeed, other metallodrugs (Figure 1.7) have entered clinical trials as anticancer therapeutics[44] and include ruthenium complexes (NAMI-A,[53] KP1019,[53] KP1339),[54,55] and gold(I) complexes (auranofin and myocrisin).[56]

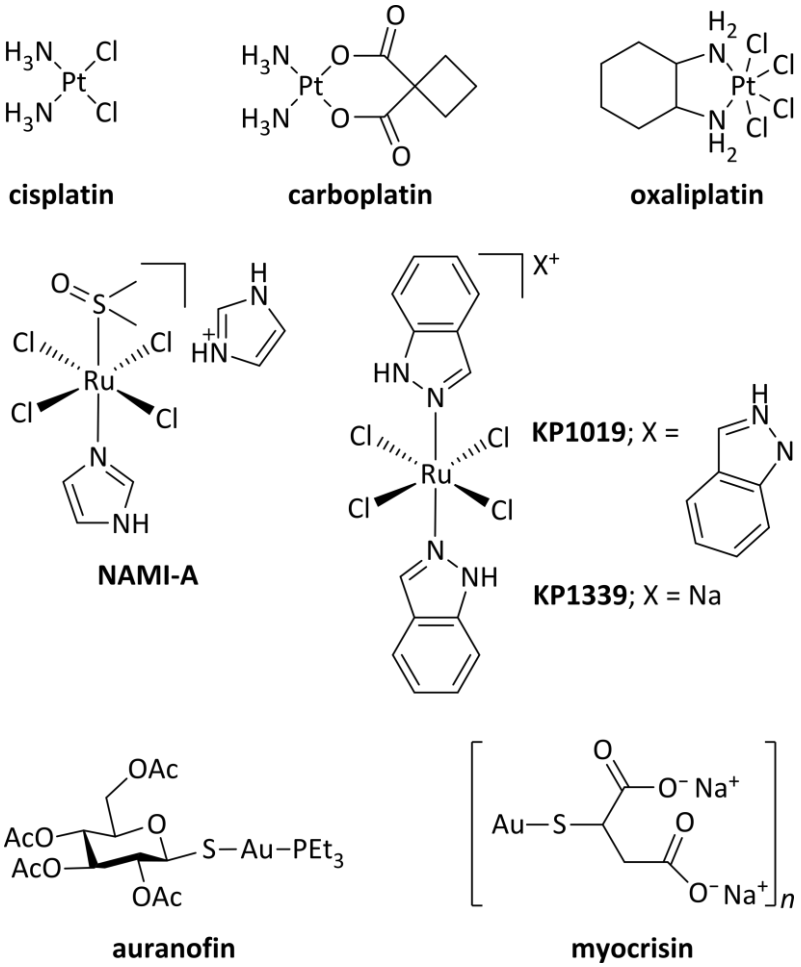


Figure 1.7. Metal-based chemotherapeutic agents.

The molecular target for the ruthenium complexes, NAMI-A and KP1019/KP1339 was originally thought to be DNA and even though cell-free experiments corroborate the possibility of covalent interactions, the distortion in DNA structure is not as pronounced as with cisplatin. Further cellular uptake studies conclude that NAMI-A does not enter cells but rather interacts in the extracellular matrix or on the cell membrane. This finding can explain the high antimetastatic effects and the low cytotoxicity of NAMI-A. In contrast, KP1019 does enter cells and presumably binds to cytosolic proteins, generates ROS and induce ER stress. The cytotoxicity of these ruthenium drugs is generally low but their enhanced selectivity towards cancer cells warrants their use clinically.[55]

The gold(I) complexes, auranofin and myocrisin (Figure 1.7), both antiarthritic drugs, are currently undergoing clinical trials as anticancer drugs.[56] Auranofin (tetraacetyl-β-D-thioglucose gold(I) triethylphosphine), a gold(I) phosphane thiolate, is a potent inhibitor of the enzyme thioredoxin reductase, increases cellular ROS and induces the mitochondrial apoptotic pathway.[57–59] Myocrisin, an aurothiomalate complex, specifically binds to a cysteine residue in the binding pocket of protein kinase C iota (PKCí), thereby preventing the downstream protein, par-6, to bind to the kinase. The PKCí-par 6 complex is a signalling intermediate within a cellular pathway that stimulates tumour growth and invasion.[60,61]

The attributes of metal complexes, such as their wide range of coordination numbers, geometries and variable redox states are attractive for the strategies used in the unpredictable field of drug discovery and design. Metals have been used since ancient times for medicinal purposes for a wide range of ailments e.g., zinc for wounds, copper to sterilize water and mercurous chloride as a diuretic. However, the first rational use of medicinal metal compounds was the treatment of tuberculosis with $K[Au(CN)_2]$. Different metals tend to target diverse biological molecules and even more interestingly, the same metal in a different oxidation state can bind to different drug targets.[62–66] For instance, gold(I) compounds interact preferentially with sulfur and phosphine ligands and therefore can bind to, and subsequently inactivate proteins. Gold(III) complexes favour nitrogen and oxygen donors and gold(III) salts were used previously to stain nucleic acids for electron microscopy imaging.[67] Moreover, the redox chemistry and associated change in coordination number of gold complexes can be an advantage as the reduction of the square-planar gold(III) to the linear coordinated Au^{I} is associated with the release of ligands, whereby these ligands can have medicinal properties themselves.[68] Metal complexes, specifically gold complexes, are therefore a fascinating group of compounds to explore further for their anticancer potential.

1.4 Anticancer potential of gold complexes

1.4.1 Historic use of medicinal gold

The earliest known application of medicinal gold was in China dating back to perhaps as far as 2500 BC in pursuit of longevity; arguably so, as gold itself is resistant to corrosion and rust. In early times, gold powder was rubbed on open wounds and said to remove the toxins

associated with smallpox and skin ulcers as well as mercury from the body. Heated gold relieved toothache and golden amulets were worn to repel evil spirits.[69]

The medicinal use of gold was limited to topical ailments as there was no way to dissolve gold. In medieval times, potable gold (i.e., drinkable gold) emerged as elixirs of life to restore youth. These elixirs contained very low concentrations of dissolved gold as one of the many recipes for potable gold stated: "to quench a heated gold plate in wines four to five times." Undeniably, scepticism arose around the medicinal properties of gold as some potable gold recipes cured ailments (in these recipes aqua regia was used to generate the soluble salt, $AuCl_3$) and others did not (e.g. heated gold in wine).[69,70]

In the 17th century, several preparations for medicinal gold were known. One of the preparations required the distillation of dissolved gold and aqua regia, resulting in the soluble $AuCl_3$ salt. A second preparation, the fulminate of gold, was made by adding ammonia to aqua regia and gold. Not unexpectedly, gold chloride was deemed too corrosive and gold fulminate too dangerous (explosive) for any medicinal use. In the 19th century, after the use of medicinal gold had declined dramatically, a French physician used a less caustic mixture of gold- and sodium chloride, so-called "a muriate of gold and soda," to treat syphilis. Although the reproducibility of his findings was ambiguous, by the mid-19th century, this double chloride of gold was prescribed as a secondary drug, only when the primary would fail, to treat morphine addiction, nephritis, anaemia, premature senility, neurasthenia, lupus and alcoholism.[70]

In 1890, Robert Koch found that gold cyanide, $K[Au(CN)_2]$ was bacteriostatic against tubercle bacillus, a strain of bacteria now known as *Mycobacterium tuberculosis* and the causative agent of tuberculosis. During the clinical trials, however, gold cyanide proved ineffective in treating tuberculosis and had serious toxic side effects. Gold(I) thiols, such as sodium aurothiosulfate (myocrisin, Figure 1.7) were much less toxic and were administered to tuberculosis patients during 1925–1935 (known as the Gold Decade) but the usage declined as reports on toxicity increased along with very little evidence of treatment efficacy. Later on, these gold thiolates were investigated against rheumatoid arthritis after the idea that tubercle bacillus caused rheumatoid arthritis.[70–72]

Today, after years of debate and results obtained from a very large, well-controlled, double-blind trial concluded that gold compounds have a beneficial effect on rheumatoid arthritis and injectable gold(I) thiolates are included in a class of disease-modifying antirheumatic

drugs (DMARDs).[58,59,72] These drugs do have their drawbacks, as they are slow acting and accumulate in the kidneys, giving rise to nephrotoxicity.[71] In the 1970s, an orally administered gold(I) phosphine drug, auranofin (Figure 1.7)[73,74] was introduced and though only mild side-effects were reported, was less effective than the injectable gold drugs in treating rheumatoid arthritis.[37,38] However, auranofin is still used clinically today for psoriatic arthritis and juvenile rheumatoid arthritis.[41]

1.4.2 Antitumour activity of gold(I) compounds and major biological targets

The use of gold(I) compounds as potential anticancer agents was sparked by the in vitro cytotoxicity of auranofin against HeLa (human cervical epithelioid carcinoma) cells[75] and further studies that revealed auranofin's similar or in some cases superior, cytotoxicity compared to cisplatin.[76–78] The in vivo activity of auranofin, however was found to be limited to leukaemia P388 mouse models only.[79–81] Once injected, auranofin undergoes rapid ligand exchange and binds covalently to the cysteine residue (Cys-34) of human serum albumin, the most abundant blood protein,[82] an event which subsequently decreases the concentration of the active gold species and the rate of cellular uptake.[83] Despite the limited in vivo activity, auranofin is a potent inhibitor of mitochondrial thioredoxin reductase and has identified this enzyme as a promising new drug target for other potential chemotherapeutic gold(I) complexes.[57,84]

Thioredoxin reductases (TrxR) are a class of enzymes that catalyse the reduction of thioredoxins (Trx), proteins which themselves are responsible for maintaining other cellular proteins in their reduced state. TrxR, Trx and the redox co-enzyme, NADP(H) collectively form the Trx system, a ubiquitous system that is crucial in maintaining intracellular redox conditions (Figure 1.8). Reduced Trx are responsible for the reduction of cellular proteins that play critical roles in cell division, transcription of genes, apoptosis and proteins that protect the cell against ROS species. Specifically, Trx reduces proteins such as ribonuclease reductase, a critical enzyme in DNA synthesis, and thioredoxin peroxidase that catalyses the reduction of hydrogen peroxide into water.[85–87]

The Au^{I} atom of auranofin binds covalently to the selenium-containing (Sec; selenocysteine) residue in the active site of TrxR with impressive selectivity as auranofin binds to the mechanically and structurally similar but selenium-free enzyme, glutathione reductase (GR)

at a 1000-fold higher concentration.[57,88] The binding prevents the substrate, Trx, from binding and being reduced by TrxR. The mitochondrial PT pores sense the imbalance of thiol proteins, opens and induces MOMP, which ultimately leads to cell death due to the release of cytochrome c. MOMP is also induced by the accumulation of H_2O_2, as auranofin prevents the removal of hydrogen peroxide, due to the inhibition of TrxR. Furthermore, MOMP leads to the leaking of important respiratory chain components into the cytosol, inevitably causing the respiration chain to uncouple and the production of ATP to cease. Indeed, a decrease in basal oxygen consumption and ATP output of cells has been observed in auranofin-treated cells.[15,57,89]

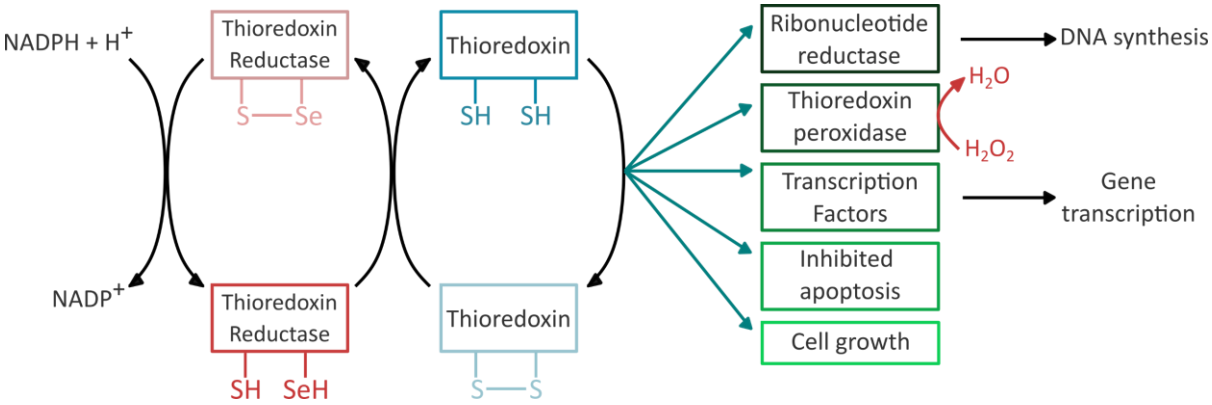


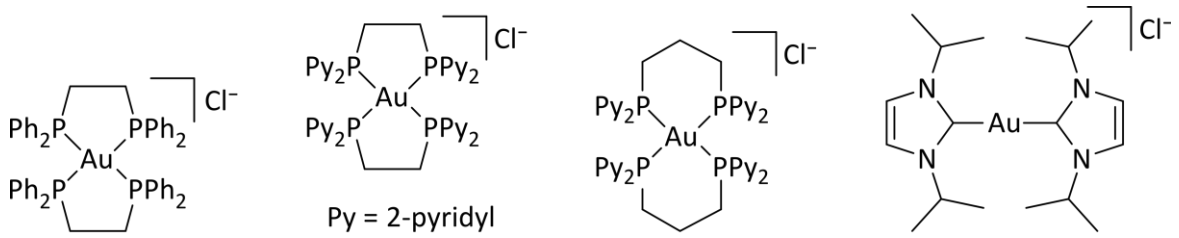
Figure 1.8. The thiol-disulfide exchange in the Trx system is presented in where the co-enzyme NADPH is oxidized to $NADP^+$ to reduce $TrxR_{ox}$(-S-Se-) to $TrxR_{red}$(-SH, -SeH), for use in the reduction of Trx_{ox}(-S-S-) to Trx_{red}(-SH, -SH). The latter is then available to reduce substrate proteins or carry out required cellular functions such as the following: Trx reduces ribonucleotide reductase, an enzyme that reduces the ribose- to deoxyribose sugar, a component of DNA nucleotides required for DNA synthesis. Trx also reduces other proteins such as thioredoxin peroxidases which is responsible for converting toxic H_2O_2 to water and transcription factors that regulate gene expression. In addition, Trx functions as a cell growth factor and can inhibit apoptosis.[57,85,86]

The mitochondria are a suitable drug target for chemotherapeutics as this organelle is a crucial regulator of cell death, an endpoint most cancer cells are resistant to. These resistant pathways, due to either defective pro-apoptotic or overexpressed anti-apoptotic members, are potentially avoided with drugs that induce MOMP directly.[90,91] The challenge however, is to target the mitochondria of cancer cells selectively. The selective inhibition of mitochondrial TrxR is one such strategy by taking advantage of the fact that cancer cells have elevated levels of these proteins to protect themselves from the high levels of ROS generated due to increased proliferation and respiration. When these proteins are inhibited, cancer cells are

much more vulnerable to these elevated intracellular ROS levels than healthy cells.[85,87] Unfortunately, most known TrxR inhibitors cannot distinguish between mitochondrial TrxR and the cytosolic TrxR. MOMP is only associated with the effective inhibition of mitochondrial TrxR.[57,89]

Another approach to targeting the mitochondria of cancer cells is the development of a diverse group of compounds called delocalized lipophilic cations (DLCs). These compounds are characterized by elevated partition coefficient values to easily pass lipid membranes and a delocalized positive charge, which allows these DLCs to be driven towards negatively charged species. In fact, the mitochondria of cancer cells have elevated mitochondrial membrane potential ($\Delta\psi_m$) due to an increased rate of ATP production. Hyperpolarized mitochondria are linked to more aggressive and treatment-resistant cancers. DLCs selectively accumulate in the mitochondria of cancer cells due to the difference in $\Delta\psi_m$ between healthy and cancer cells.[57,89]

The DLCs reported by the group of Berners-Price such as the tetrahedral gold(I) phosphine complex, **3** (Figure 1.9)[92,93] and the cationic bis-N-heterocyclic (NHC) carbene gold(I) complex, **4** (Figure 1.9)[94,95] showed high selectivity towards breast cancer cell lines. These findings were not just due to chance but a result of carefully considered lipophilic characteristics that are required for the selective accumulation of DLCs in cancer cells.[96,97] The parent compound of **3**, the tetrahedral gold(I) phosphine complex, **1** (Figure 1.9) was developed as an attempt to decrease the known tendency of linear two-coordinate gold(I) complexes to rapidly undergo ligand exchange reactions under physiological conditions. They are very reactive towards thiol proteins in blood serum, limiting their in vivo cytotoxicity, such as the case with auranofin.[80,98] Complex **1** is stable against GSH (reduced glutathione), a thiol-containing tripeptide used as a model protein to assess the reactivity of gold(I) complexes towards either blood thiol proteins such albumin or the potential of inhibiting a thiol-containing protein target such as TrxR. Although complex **1** exhibited excellent in vitro and in vivo activity,[99] **1** was found to be very toxic during preclinical trials, likely due to the high lipophilicity of the complex as non-selective accumulation in the mitochondria leads to severe mitochondrial dysfunction. Moreover, the extreme stability of **1** towards GSH suggests that TrxR would be an unlikely intracellular target.[57,58]



1 **2** **3** **4**

Figure 1.9. Gold(I) complexes reported by the group of Berners-Price with phosphine (**1**–**3**) and NHC ligands (**4**) that have shown promising anticancer potential as DLCs.[93,94,99,100]

The first-generation tetrahedral phosphine complexes (complexes of type **2**, Figure 1.9) were developed to assess the influence of the lipophilic/hydrophilic ratio on in vitro and in vivo anticancer activity. By substituting the phenyl substituents with more hydrophilic 2-, 3- or 4-pyridyl ligands, a whole range of complexes was assessed with varying degrees of lipophilic and hydrophilic character. The complexes with higher lipophilic character were more cytotoxic but also less selective. The more hydrophilic complexes were much less cytotoxic, due to low cellular uptake, high rates of excretion and low protein binding affinity. From these results, the complex with intermediate lipophilicity, **2** (Figure 1.9) was the best performing complex, in both in vitro and in vivo studies.[57,58,100]

The hydrophilic/lipophilic balance were further fine-tuned for the second-generation complexes, where the ethyl linker of **2** was replaced with a propyl bridge (**3**, Figure 1.9). By increasing the chelate ring size, ligand exchange reactions with thiol/selenol proteins are more favourable. Complex **3** therefore possesses the lipophilic properties resembling those of the first-generation complex **2** but potentially has auranofin's protein inhibiting properties due to the possibility of ligand exchange.[58] Complex **3** is highly selective towards breast cancer cells and mechanistic studies reveal that complex **3** selectively accumulates in the mitochondria and inhibits TxrR.[93]

From the same research group, the cationic biscarbene gold(I) complexes of type **4** (Figure 1.9) were also reported to be selective towards breast cancer cells as well.[95] NHCs are a very attractive class of ligands mostly due to their facile synthesis of a wide range of metal complexes from their respective imidazolium salts. The NHCs possess high functional group tolerability and allow easier access to fine-tune the required properties than the conventional phosphine ligands. Furthermore, NHCs are relatively non-toxic ligands and stabilize Au^{I} under physiological conditions by being inherently strong σ-donors.[84,101–109] Gold(I) biscarbene

complexes of type **4** also accumulate in the mitochondria and trigger mitochondrial swelling.[94] Kinetic studies on these complexes reveal that the substitution of the NHC ligands is faster for selenium-containing residues (Sec) than for thiols (Cys) thereby offering an explanation of the high selective inhibition of TrxR over GR. Bulkier groups (e.g. ^{i}Pr in complex **4**) induce a slower reactivity towards the protein likely due to the added steric protection preventing the substitution with Cys/Sec residues.[95]

Combining the properties of both phosphines and NHCs, the group of Che reported on the anticancer properties of a dinuclear gold(I) complex with bridging disphosphines and bisNHCs (**5**, Figure 1.10). The complex displayed sufficient stability against serum proteins but also had enough reactivity towards thiol proteins to be a potent TrxR inhibitor (0.038 μM, entry 1, Table 1.1). This complex is the first reported gold(I) complex to inhibit cancer stem cell activity and inhibit angiogenesis in vivo.[68,83]

The benzimidazole complexes (**6** – **8**, Figure 1.10) reported by Ott et al., although not very selective in terms of cytotoxicity, contributed valuable information in terms of anticancer properties for this class of NHCs. For instance, the cationic complexes (**7** and **8**, Figure 1.10) were more cytotoxic than the neutral complex (**6**, Figure 1.10), had higher cellular uptake and increased accumulation in the mitochondria. However, the neutral complex, due to the more labile *trans* chloride ligand, was the best and most selective inhibitor of TrxR (24-fold over GR) in this series.[110–112]

Other ligands complexed to Au^{I} such as thiourea (**9**, Figure 1.10) and alkynes (**10**, Figure 1.10) have also been reported as highly potent TrxR inhibitors. In fact, complex **9** is the most potent complex ever reported with a K_i (inhibitory coefficient) value between 18 and 36 pM (entry 6, Table 1.1).[113] Auranofin has a K_i value of 4 nM (entry 15, Table 1.1).[88] The cytotoxicity, however of both cisplatin (entry 10, Table 1.1) and auranofin (entry 14, Table 1.1) against HeLa cells surpass that of **9**. Alkyne complexes like complex **10** are also potent TrxR inhibitors (entry 7, Table 1.1) with very promising anticancer potential.[114]

To enhance the cytotoxicity of gold(I) complexes, some gold(I) NHC complexes are synthesized with biologically relevant substituents, such as the DNA intercalator, naphthalimide, (**11**, Figure 1.10) for a multi-faceted anticancer approach. Complex **11** is both a TxrR inhibitor and a DNA intercalator.[115]

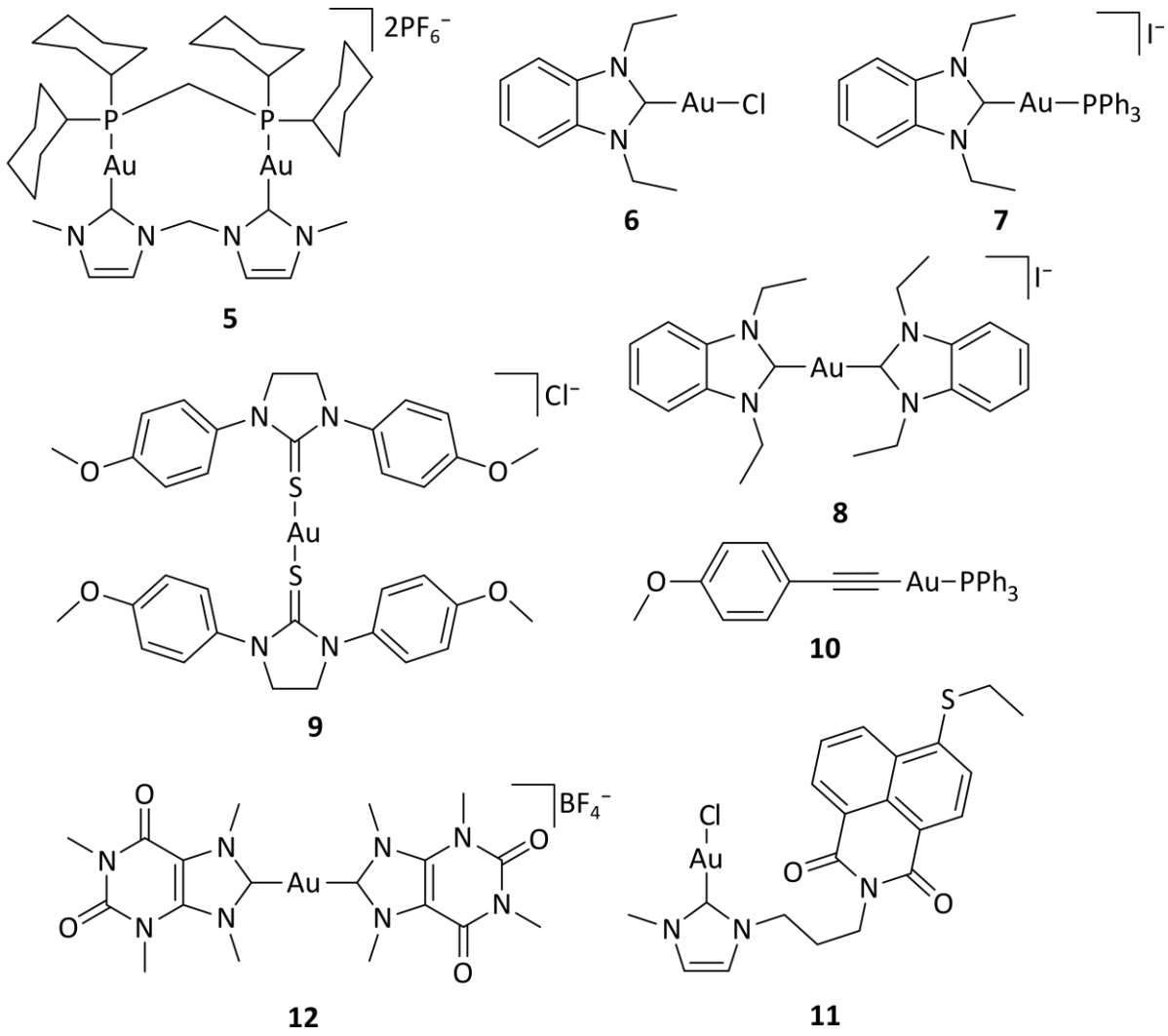


Figure 1.10. Selected gold(I) complexes with promising anticancer potential.[112–117]

Taking advantage of the imidazole ring of caffeine, Casini et al. developed a series of bis-carbene complexes of type **12** (Figure 1.10). Even though the cytotoxicity of **12** against A2780 cancer cells (entry 9, Table 1.1) was higher than both cisplatin's (entry 11, Table 1.1) and auranofin's (entry 15, Table 1.1) cytotoxicity, the selectivity of **12** towards healthy cells was much higher. Moreover, complex **12** selectively interacts with DNA G-quadruplex structures, over the DNA duplex structure.[117]

Many more gold(I) complexes have been reported that show very promising in vitro and in vivo cytotoxicity bearing a variety of different ligands. The most probable molecular target for gold(I) complexes seems to be proteins with cysteine (-thiol) and selenocysteine (-selenium) residues and can elicit mitochondrial changes that lead to cell death. Gold(I) complexes do undergo ligand exchange and careful consideration of ligands can dictate the reactivity of gold(I) species with thiol proteins which can subsequently lead to either their selective

targeting of cellular proteins or inactivation by serum proteins.[118–124] The other biologically relevant oxidation state of gold, namely gold(III), has recently re-emerged as a class of compounds with potent cytotoxicity against cancer cells.[125–129]

Table 1.1. The cytotoxicity (IC_{50}) of the gold(I) complexes 5–12 against cancer- and normal (healthy) cells. For comparison, the IC_{50} values of cisplatin and auranofin are also shown. Where applicable, the inhibition of the enzyme, thioredoxin reductase (TrxR) is also reported.

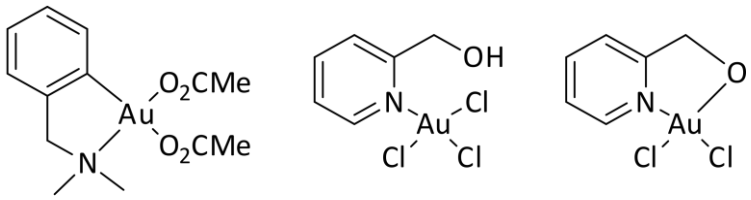
Entry	Complex	IC_{50}[a] (μM) against cancer cells (cell lines, incubation time)	IC_{50}[a] (μM) against healthy cells (cell lines, incubation time)	IC_{50}[a] (μM) of isolated TrxR
1	**5**[116]	1.8 ± 0.6 (HeLa, 72 h)[b]		0.04 (TxrR1, rat)
2		2.5 ± 0.4 (MCF-7, 72 h)[b]		
3	**6**[112]	4.6 ± 0.03 (MCF-7, 96 h)[c]	10.3 ± 1.1 (HEK293, 72 h)[c]	0.36 ± 0.04 (TxrR, rat)
4	**7**[112]	0.9 ± 0.4 (MCF-7, 96 h)[c]	0.4 ± 0.2 (HEK293, 72 h)[c]	0.7 ± 0.02 (TxrR, rat)
5	**8**[112]	0.8 ± 0.1 (MCF-7, 96 h)[c]	3.1 ± 0.5 (HEK293, 72 h)[c]	4.9 ± 1.2 (TxrR, rat)
6	**9**[113]	14.6 ± 0.7 (HeLa, 72 h)[b]		K_i = 18 – 36 pM (TxrR, rat)
7	**10**[114]	1.0 ± 0.2 (MCF-7, 96 h)[c]		0.05 ± 0.03 (rat, TxrR)
8	**11**[115]	2.1 ± 0.5 (MCF-7, 96 h)[c]		0.40 ± 0.13 (rat, TxrR
9	**12**[117]	16.2 ± 2.1 (A2780, 72 h)[b]	> 100 (HEK293T, 72 h)[b]	
10	**Cisplatin**	4.7 ± 0.3 (HeLa, 72 h)[b,113]	11.0 ± 2.9 (HEK293T, 72 h)[b,117]	
11		5.2 ± 1.9 (A2780, 72 h)[b,117]		
12		33.7 ± 7.8 (MCF-7, 72 h)[b,116]		
13		7.8 ± 0.8 (MDA-MB-231, 72 h)[c,130]		
14	**Auranofin**	1.8 ± 0.1 (HeLa, 72 h)[b,131]	1.7 ± 0.3 (HEK293T, 72 h)[b,132]	0.020 (TxrR, human)[88]
15		1.2 ± 0.5 (A2780, 72 h)[b,132]		K_i = 4 nM [88]
16		0.98 ± 0.32 (MCF-7, 72 h)[b,133]		0.009 ± 0.000 (TxrR, rat)[110]

Cell viability data were reported as [a] the half maximal inhibitory concentration (μM) required to inhibit the growth of 50% of cells in the culture or 50% of the enzyme activity (IC_{50} values) and were determined by either the [b] MTT assay (MTT = 3-(4,5-dimethylthiazol-2-yl)-2,5-diphenyltetrazolium bromide) or the [c] crystal violet assay.

1.4.3 Antitumour activity of gold(III) compounds and their biological targets

Gold(III) complexes were among the first complexes investigated as alternatives to platinum drugs and arguably so, as gold(III) and platinum(II) are both isoelectronic (d^8), square planar complexes[121,134,135] with a high affinity towards DNA nucleotides.[67,136] However, the kinetic lability, light sensitivity and the tendency for Au^{III} to reduce to Au^{I} or Au^{0} under physiological conditions hampered investigations considerably until some gold(III) complexes, years later, were reported with improved stability and antitumour activity.[124,137]

Of the most noteworthy were the complexes reported by Buckley et al. where **13** (Figure 1.11) was stable against reduction in the presence of GSH and underwent hydrolysis in water to form the [Au(damp)(H_2O)$_2$] (damp = 2-[dimethylamino)methyl]phenyl) complex, similar to cisplatin's reactivity in biological medium. Both the in vitro (entry 1, Table 1.2) and in vivo cytotoxicity showed promising but modest results compared to cisplatin.[138–141] At the same time, the monodentate (**14**, Figure 1.11) and the bidentate (**15**, Figure 1.11) pyridine based gold(III) complexes were reported by Messori et al., but these complexes underwent rapid ligand exchange in water. Despite showing promising in vitro cytotoxicity, especially against cisplatin resistant cell lines (entry 2 and 3, Table 1.2), these complexes were deemed too unstable for medicinal purposes and weren't pursued any further.[142]



13 **14** **15**

Figure 1.11. Early examples of gold(III) complexes evaluated for their antitumour activity.[138,142]

Polydentate N-donor ligands considerably improved the stability of gold(III) complexes in solution and soon numerous complexes bearing these ligands were reported. However, reduction to Au^{I} in the presence of ascorbic acid or GSH occurs more readily with N-donor functionalities followed by the release of coordinated ligands.[68,83,126] For instance, the cytotoxicity of complexes **16** and **17** (Figure 1.12), although very promising (entries 4 and 5, Table 1.2), was close to the cytotoxicity reported for the gold-free phenanthroline (phen) and terpyridine (terpy) ligands, respectively.[143] It is suggested that complex **18** (Figure 1.12) also

undergoes reduction to Au^{I} intracellularly, associates with and causes oxidative damage to proteins and DNA.[127,128]

Table 1.2. The cytotoxicity (IC_{50}, μM) of the gold(III) complexes **13**–**18** and **23** with human ovarian carcinoma cell line A2780 and the cisplatin-resistant equivalent cell line, A2780-R. For comparison, the IC_{50} (μM) values of cisplatin that were measured under the same conditions are shown in brackets.

Entry	Complex	Cytotoxicity (IC_{50} in μM)[a,b] against A2780	Cytotoxicity (IC_{50} in μM)[a,b] against A2780R
1	**13**[140]	3.5, 96 h *(1.2)*	35, 96 h *(10)*
2	**14**[142]	10.0 *(5.3)*	21.0 *(57.0)*
3	**15**[142]	8.4 *(5.3)*	13.8 *(57.0)*
4	**16**[143]	3.8 ± 1.1, 72 h *(1.2 ± 0.43)*	3.5 ± 0.9, 72 h *(14.2 ± 2.72)*
5	**17**[143]	0.1, 72 h *(1.2 ± 0.43)*	0.4, 72 r *(14.2 ± 2.72)*
6	**18**[144]	1.8 ± 0.2, 72 h *(2.1 ± 0.1)*	4.8 ± 0.5, 72 h *(24.4 ± 0.1)*
7	**23**[128,145]	3.3 ± 1.4, 72 h	8.2 ± 1.5, 72 h

Cell viability data were reported as [a] the half maximal inhibitory concentration (μM) required to inhibit the growth of 50% of cells in the culture (IC_{50} values) during [b] indicated time of drug exposure and were determined by the sulforhodamine assay.

The group of Che made use of the reactivity of N-donor functionalized gold(III) complexes by designing a range of complexes, exemplified by complexes **19** and **20** (Figure 1.12), that act dually as fluorescent thiol probes and exhibit cytotoxicity. These complexes bear the highly emissive 2,6-bis(imidazole-2-yl)pyridine (**19**) and 2,6-bis(benzimidazole-2-yl)pyridine (**20**) ligands to act as thiol fluorescent probes when the Au^{III} is reduced to Au^{I} by thiol proteins. The released Au^{I} is stabilized by the NHC ligand, inhibits TrxR and is cytotoxic to cancer cells.[131]

The water soluble corrole-based gold(III) complex, **21** (Figure 1.12) effectively protects the Au^{III} from reduction and demetalation. Complex **21** exhibited much greater cytotoxicity (entry 3, Table 1.3) compared to the gallium analogue and out-performed cisplatin on most of the cell lines. The activity is likely attributed to the low binding affinity of **21** towards HSA.[146] Gold(III) porphyrin complexes of type **22** (Figure 1.12) are characterized with very high redox stability and as such are stable against reduction by GSH. These complexes are reportedly very successful cytotoxic agents as **22** is significantly more potent in vitro than cisplatin (entry 4, Table 1.3) especially in cisplatin- and multidrug resistant cell lines and is able to inhibit the self-renewal ability of cancer stem-like cells. The molecular target of **22** remains somewhat elusive but extensive mechanistic studies suggest that **22** reduces the mitochondrial membrane potential and targets the mitochondrial chaperone Hsp60 (heat shock protein 60), a protein that is involved in the transport and folding of mitochondrial proteins.[68,83,147]

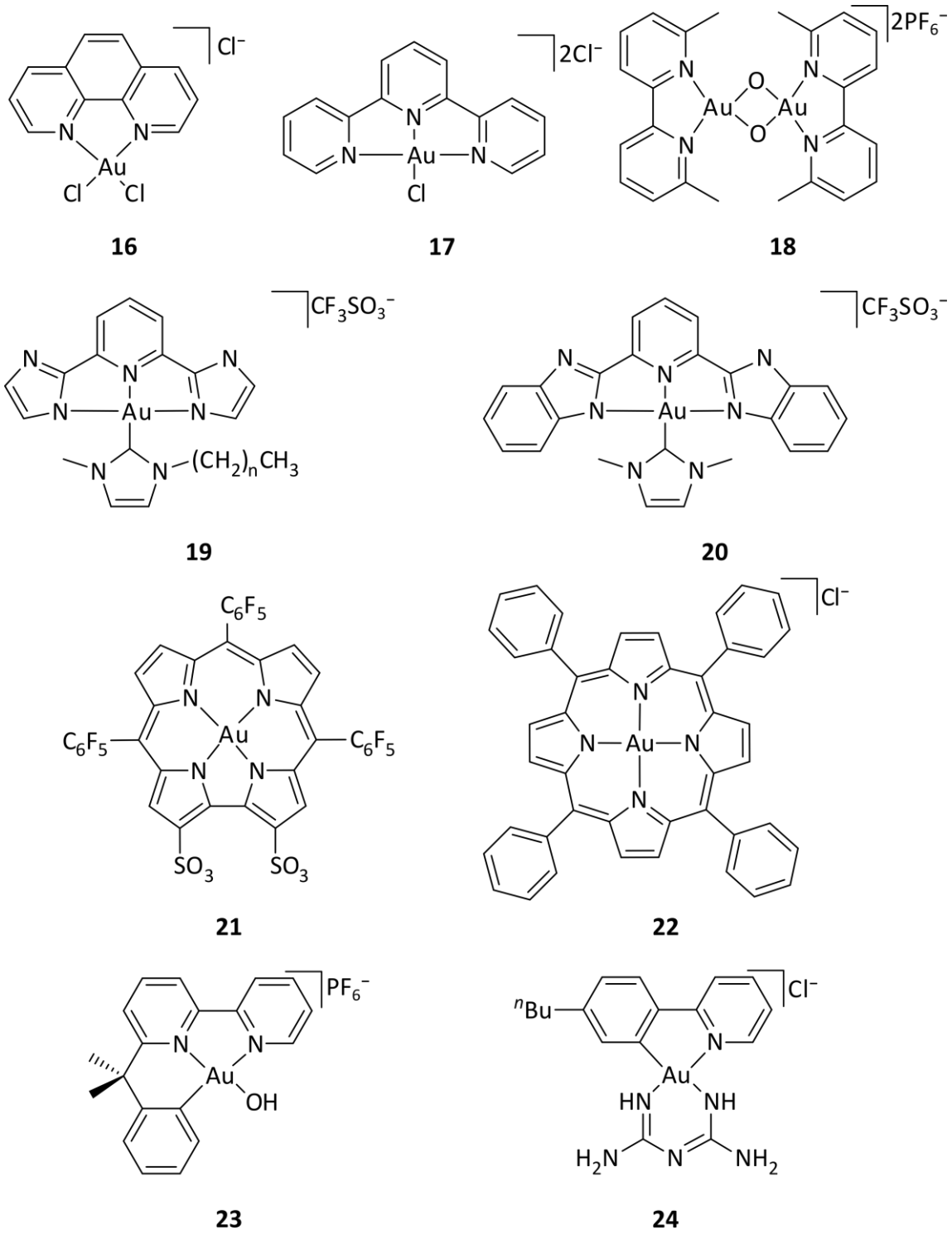


Figure 1.12. Representative examples of multidentate gold(III) complexes with anticancer potential.[128,131,144–149]

The complexes reported by Buckley et al. in the 1990's (e.g. **13**, Figure 1.11) are stable against reducing agents such as ascorbic acid and GSH, whereas the similarly structured pyridine-based complexes (**14** and **15**, Figure 1.11) were not stable even in aqueous solution. These organogold complexes from Buckley led the development of multidentate ligand scaffolds

and revealed that at least one C-deprotonated (C^-) ligand coordinated to the metal is enough to stabilize the Au^{III} against reduction.[68,83,126] Representative examples of tridentate (CNN)- (**23**) and bidentate (CN) organogold(III) complexes (**24**) are shown in Figure 1.12.

Compared to cisplatin and the other reported (NN)-, (NNC)- and (NC) bipyramidal-based gold(III) complexes in the series reported by Messori et al., **23** was among the most potent (entry 7, Table 1.2). Interaction with nucleic acids were found to be weak, but **23** does inhibit TrxR2 (0.28 μM) and interacts strongly with other proteins such as lysozyme and cytochrome c.[145] Proteomic studies were conducted to identify the effect of **23** on protein expression in whole cells and found that only a few proteins had modified expressions. Of those modified proteins, most of them were involved in the stress response of the cell and proteins associated with the glucose metabolism were downregulated, identifying the mitochondria as key target in the cytotoxicity of this complex.[126]

Complex **24** is a stable, water soluble complex that is able to form gold(III)-GSH adducts and induce ER stress. The in vitro cytotoxicity of **24** was evaluated against several cancer cell lines and although not as potent as the porphyrin complex **22**, slightly better selectivity towards the normal lung cell line (CCD-19Lu) was found (entries 4 and 5, Table 1.3).[149]

In pursuit of suitable gold(III) DNA-metallointercalators (to potentially mimic the mode of action of $[Pt(terpy)L]^+$), Che and co-workers synthesized structurally varied CNC gold(III) complexes based on 2,6-diphenylpyridine (**25**–**27**, Figure 1.13). Not only would the dianionic $[CNC]^{2-}$ ligand scaffold provide sufficient stabilization for the Au^{III} but it also lends itself to diverse structural modifications. Although these modifications included varying the scaffold using 2,4,6-triphenylpyridine and 2,6-dinaphthylpyridine, it was the variation of the ancillary ligand, L in $[Au(CNC)L]^+$, that had the biggest impact on activity (complexes **25a**–**25d** in Figure 1.13 and entries 6–9, Table 1.3). The mechanism of action is also influenced by the variation of L, for instance, the N-imidazole complex, **25c**, intercalates double-stranded DNA and arrests the cell cycle in S-phase, the phase in which DNA replication takes place. Therefore, it is suggested that **25c** induces apoptosis by inhibiting DNA replication. Conversely, the triphenylphosphine complex (**25b**) interacts only weakly with DNA.[83,150,151]

The cytotoxicity of both **25b** and **25c** were drastically improved by modifying the mononuclear **25b** to a dinuclear gold(III), **26** (Figure 1.13) by utilizing a bridging bis(diphenylphosphino)propane (μ-dppp) ligand[152] and substituting the N-imidazole ligand of

25c with NHCs resulting in complex **27a** and **27b** (Figure 1.13).[153] Complex **26** showed impressive cytotoxicity in the submicromolar range against a range of cancer cell lines (entry 10, Table 1.3) with a 37-fold selectivity towards healthy cells. Complex **26** is a potent TrxR inhibitor (2.7 nM, rat TxrR1) and induces ER stress.[152]

Table 1.3. The cytotoxicity data (IC_{50}, μM) for gold(III) complexes **19**–**22** and **24**–**28** against various cancer- and healthy cell lines. Where applicable, the therapeutic index (T.I.) is indicated. For comparison, the IC_{50} (uM) of cisplatin, measured under identical experimental conditions, are shown in brackets.[83,150,151]

Entry	Complex	IC_{50}[a] (μM) against cancer cells (Cell lines, time[b])	IC_{50}[a] (μM) against healthy cells (cell lines, time[b])	T.I.[f]
1	**19**[131]	1.4 ± 0.2 (HeLa, 72 h)[c], *(1.8 ± 0.1)*[e]		
2	**20**[131]	14.4 ± 2.2 (HeLa, 72 h)[c], *(1.8 ± 0.1)*[e]		
3	**21**[146]	19.7 (MDA-MB-231, 72 h), *(44.8)*		
4	**22**[147]	0.3 ± 0.02 (HeLa, 48 h)[c], *(11.2 ± 0.96)*	0.9 (CCD-19Lu, 48 h)[c]	3.3
5	**24**[149]	7.7 ± 0.1 (HeLa, 72 h)[c], *(5.2 ± 0.1)*	32.8 ± 2.6 (CCD-19Lu, 72 h)[c], *(36.2 ± 0.4)*	4.1
6	**25a**[150]	3.4 ± 0.6 (HeLa, 72 h)[c], *(11 ± 1.0)*		
7	**25b**[152]	7.2 ± 0.6 (HeLa, 72 h)[c]	18 ± 0.6 (CCD-19Lu, 72 h)[c]	3
8	**25c**[150]	8.0 ± 0.5 (HeLa, 72 h)[c] , *(11 ± 1.0)*		
9	**25d**[150]	8.2 ± 0.5 (HeLa, 72h)[c], *(11 ± 1.0)*		
10	**26**[152]	0.04 ± 0.006 (HeLa, 72 h)[c], *(11 ± 1.0)*	1.6 ± 0.1 (CCD-19Lu, 72 h)[c]	37
11	**27a**[152]	0.08 ± 0.007 (HeLa, 72 h)[c], *(11 ± 1.0)*	1.9 ± 0.1 (CCD-19Lu, 72 h)[c]	23
12	**27b**[153]	0.2 ± 0.05 (NCI-H460, 72 h)[c] *(3.5 ± 1.0)*	25 ± 3.8 (CCD-19Lu, 72 h)[c]	147
13	**28**[154]	0.3 ± 0.15 (HL60, 72 h)[d], *(3.70± 0.25)*	1.4 ± 0.4 (MRC-5, 72 h)[d], *(10.7 ± 3.0)*	5

Cell viability data were reported as [a] the half maximal inhibitory concentration (μM) required to inhibit the growth of 50% of cells in the culture (IC_{50} values) during [b] indicated time of drug exposure and were determined by either the [c] the MTT assay (MTT = 3-(4,5-dimethylthiazol-2-yl)-2,5-diphenyltetrazolium bromide), or the [d] MTS assay (MTS = 5-(3-carboxymethoxyphenyl)-2-(4,5-dimethylthiazolyl)-3-(4-sulfophenyl) tetrazolium. [e] IC^{50} of auranofin measured under the same conditions. [f] ratio of IC_{50} of healthy cells to cancer cells.

Complex **27a** is 100-fold more active against Hela cancer cells (entry 11, Table 1.3) compared with **25c** (entry 8, Table 1.3). The dimethylated NHC gold(III) complex, **27b**, showed remarkable selectivity towards normal fibroblast cells (entry 12, Table 1.3) compared to the non-small cell lung cancer cells (NCI-H460, entry 12, Table 1.3). Complex **27b** is able to intercalate into DNA and subsequently prevent topoisomerase-I mediated relaxation of

supercoiled DNA.[68,83,153] Moreover, multiple targets for gold(III) CNC NHC complexes of type **27** were identified by Che and co-workers, when they designed a clickable photoaffinity probe,[155] that indicated multiple proteins binding to these complexes such as hsp60, vimentin, nucleoside disphosphatase kinase A, nucleophosmin, nuclease-sensitive element binding protein and peroxiredoxin 1, proteins that all have been identified as potential anticancer targets.[83,126,151]

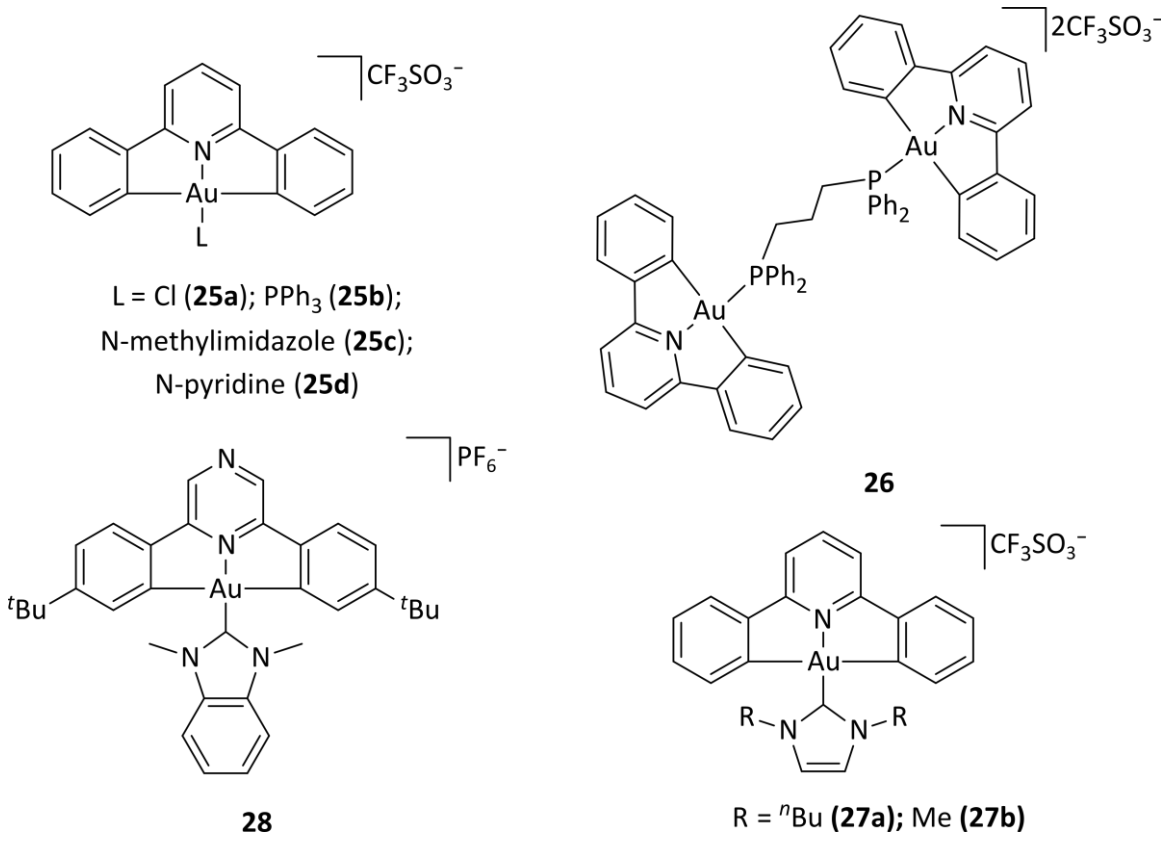


Figure 1.13. Representative examples of cytotoxic CNC pincer gold(III) complexes.[150,152,154]

The pyrazine-based CNC complex, **28**, also showed high in vitro cytotoxicity with a 4.5-fold selectivity toward the healthy fetal lung fibroblasts cells (MRC-5) (entry 13, Table 1.3). DNA binding studies reveal that complex **28** is capable of stabilizing G-quadruplex structures of DNA. Surprisingly, the caffeine analogue of **28** was 10 times less cytotoxic and this was attributed to lower cellular uptake. The cellular uptake studies suggest that the more polar caffeine-based ligand possibly hinders the cellular uptake of the complex, which potentially occurs through passive diffusion.[154]

Since the discovery that Au^{III} can be stabilized for use in biological media and protected against reduction under physiological conditions by the careful consideration of appropriate ligand scaffolds, many more examples have been reported and mechanistically explored for

their antitumour potential. In particular, porphyrin and CNC pincer stabilized gold(III) complexes show exceptional promise, although selectivity towards cancer over healthy cells remains a challenge, calling for future solutions. Using non-toxic ligands such as NHCs improves the selectivity; however too few gold(III) complexes, including gold(III)-NHC complexes, have been evaluated against healthy cell lines to arrive at firm conclusions. NHCs, however, are strong σ-donors and have shown to effectively stabilize both Au^{I} and Au^{III} under physiological conditions.[125–129]

1.5 Carbenes as suitable C-donor ligands

NHCs, especially imidazole-2-ylidenes, have enjoyed considerable attention over the past few decades, predominantly as highly successful ancillary ligands to transition metals in catalytic processes.[156–160] The popularity is warranted as they are easy to synthesize, exceptionally stable and open to both structural and electronic modulation. Also, the metal-carbene bond is strong, underpinning the traction of these robust NHC complexes in chemical biology as promising anticancer and antimicrobial agents.[161–166]

1,2,3-Triazolylidenes (trz, Figure 1.14) are mesoionic carbenes (MICs), also known and often synonymously referred to as abnormal N-heterocyclic carbenes (aNHCs).[167–170] Originally, the term 'abnormal' referred to imidazol-4-ylidenes (Figure 1.14), since coordination of the metal occurs at the C4 (or C5) position[171] of the heterocycle instead of at the 'normal' C2 position of imidazolium salts, the precursors to imidazol-2-ylidenes ('normal' NHCs; Figure 1.14). Currently, however, the term 'abnormal NHC' refers to any NHCs (including pyridylidenes, pyrazolylidenes) where no resonance structure can be drawn without the inclusion of both formal positive- and negative charges and is therefore tantamount to the IUPAC definition of MICs.[172–174]

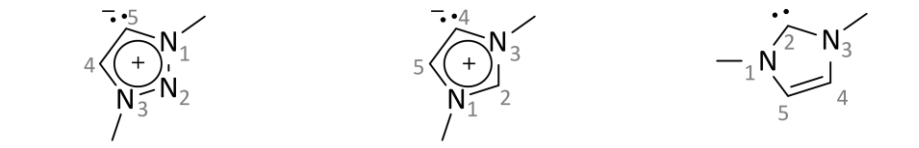
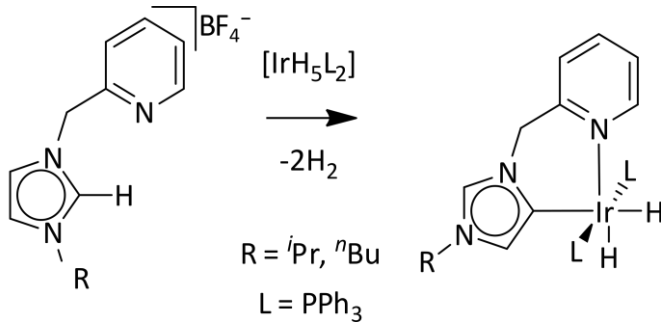


Figure 1.14. Representative free carbene structures of 1,2,3-triazol-4-ylidene, imidazole-4-ylidene and imidazole-2-ylidene.

The group of Crabtree were the first to report on an abnormally bound metal complex.[171,175] The pyridine-appended imidazolium salt was reacted with an iridium polyhydride and metalation occurred at C4 instead of the expected C2 position (Scheme 1.1). This outcome was surprising since DFT calculations predicted a C4-bound metal complex (to platinum) to be thermodynamically unfavoured, by 23.3 kcal mol^{-1}, compared to the C2-isomer. In terms of C-H activation and stability, the C2-H is much more acidic (predicted nine pK_a units lower) than the C4-H, and the free imidazol-2-ylidene is more stable than the imidazole-4-ylidene (by 20 kcal mol^{-1}).[170,176,177]

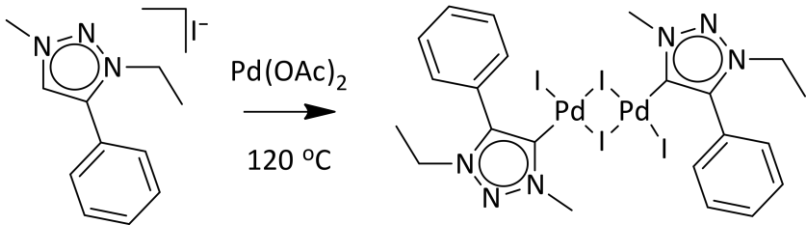


Scheme 1.1. The first imidazole-4-ylidene metal complex reported by Crabtree and co-workers.[171]

Since then, multiple literature reports followed to understand the formation of aNHCs and to determine the conditions required to ensure selectivity towards the C4-isomer.[170,172] Computationally, the metalation on C4 is proposed to occur via C4-H oxidative addition, whereas C2-metalation via C2-H heterolytic bond cleavage is predicted. Experimentally, large non-coordinating counterions (PF_6^-, BF_4^-) which promote oxidative addition, have yielded the C4-isomer. The wingtip substituents on the nitrogens of the imidazolium salt also seem to influence the outcome of the products, whereby large aromatic wingtip groups favour C4-metalation by enforcing steric hindrance at the C2 position. Additives such as the base, Cs_2CO_3, exclusively forms the C2-metallated product. In the absence of the base, C4 metalation occurs. Unfortunately, even though all these experimental conditions yield the C4-isomer, it cannot be exclusively assumed until full characterisation has been done.

Primarily though, metalation on the C2 will occur if the C2-position is unprotected. Selective formation of the aNHC can be achieved by protecting the C2 position with aryl and alkyl substituents. Not all protecting groups are effective since C2-alkylated imidazolium salts can undergo C–C bond activation promoted by some metal precursors and yield the C2-metalated product. In 2008, Albrecht and co-workers circumvented this completely by replacing the C2

with nitrogen and thereby reporting on the first trz metal complexes of palladium (Scheme 1.2), silver, ruthenium, iridium and rhodium.[178] The precursor 1,2,3-triazolium salts are easy to synthesize with a wide variety of substituents available for the required modification of the salt. More importantly, only the C5 position is available for metalation, ensuring selective product formation.



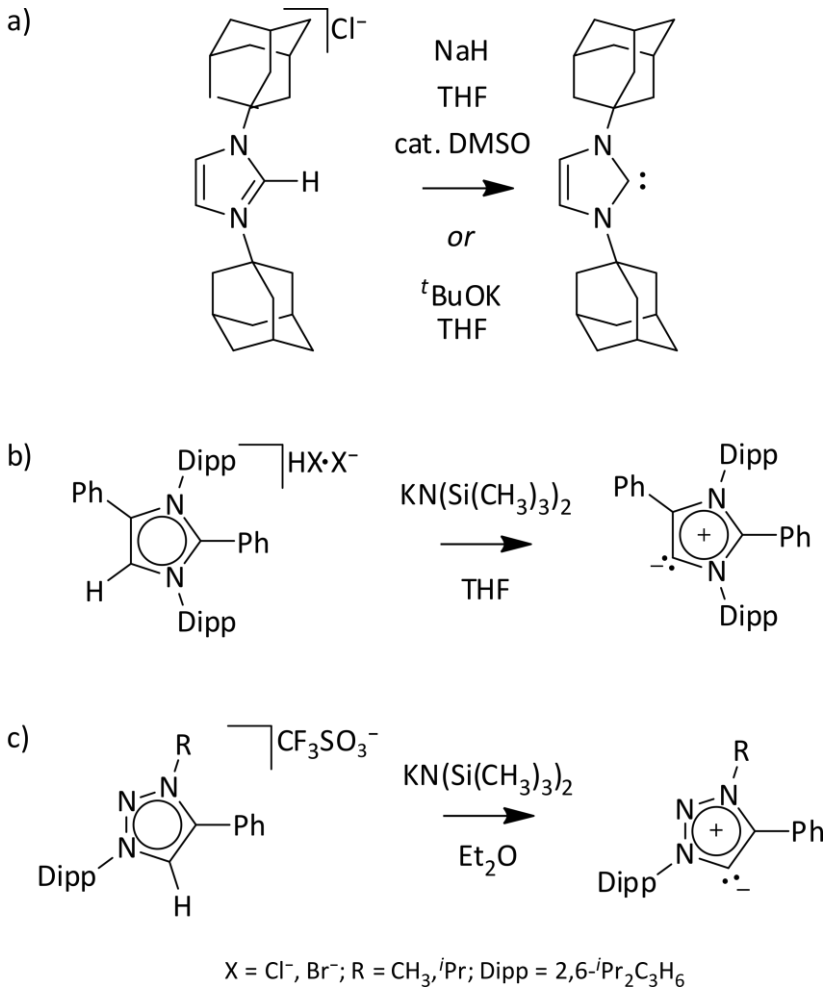
Scheme 1.2. The first reported 1,2,3-triazolylidene metal complex by Albrecht and co-workers.[178]

Imidazol-2-ylidenes (Scheme 1.3a), along with imidazol-4-ylidenes (Scheme 1.3b) and trz (Scheme 1.3c) are stable carbenes as proven by their ability to be isolated as free carbenes. The imidazol-2-ylidene was famously isolated by Arduengo et al., in 1999 by using bulky adamantyl wingtip groups, [179] almost two decades after Wanzlick and co-workers reported that imidazolium salts can be deprotonated by potassium *tert*-butoxide but not isolated.[180,181] Only after this has research into NHCs and their applications been explored. Subsequently, the free aNHCs, an imidazol-4-ylidene and an trz, were isolated by the group of Bertrand et al.[182,183]

The stability of the carbenes is dependent on a number of factors; among them are the number and proximity of the heteroatoms in the heterocycle respective to the carbene. Imidazol-2-ylidenes are singlet carbenes stabilized by adjacent nitrogen atoms, which are σ-withdrawing, π-donating substituents. The σ-withdrawing affect inductively stabilizes the lone pair of the carbene as the singlet state is favoured. The electron deficiency of the carbene is reduced by the mesomeric π-donation experienced. The aromaticity present in imidazol-2-ylidenes, which is absent in the precursor salts, is also a contributing factor to the stability as well as the substituents on the nitrogens (wingtips).[184–187]

NHCs and MICs are largely σ-donors with some π-character. Less heteroatom stabilized carbenes tend to be more σ-donating as the removal of one σ-withdrawing nitrogen adjacent to the carbene increases the basicity of the coordinated carbene.[167,168,172,173] Imidazol-4-ylidenes are more donating than imidazol-2-ylidenes, making them very valuable in catalytic

processes especially where oxidative addition is the rate limiting step. Although only flanked with one nitrogen, the additional nitrogen in the heterocycle of trz decreases the donor properties such that it is less donating than imidazol-4-ylidenes but still more donating than imidazol-2-ylidenes.[185,186] Recently, 1,2,4-substituted 1,2,3-triazolylidenes ('normal'/non-mesoionic) have been reported. Further studies reveal that there is no substantial difference in donating properties between the normal and abnormal 1,2,3-triazolylidenes, indicating that the donor properties of trz are not related to the mesoionic (or absence thereof) nature of these carbenes. [173,188–190]



X = Cl^-, Br^-; R = CH_3, ^{i}Pr; Dipp = 2,6-$^i Pr_2C_3H_6$

Scheme 1.3. (a) The isolation of the first free imidazol-2-ylidene. (b) The isolation of the first aNHC and (c) The isolation of the first 1,2,3-triazol-5-ylidene.[179,182,183]

Briefly, trz are more donating than NHCs and more stable than aNHCs. Further fine-tuning of the required properties can easily be obtained from the careful consideration of wingtip- and C4-substituents which are accessible from the high functional group tolerant CuAAC reaction employed for the synthesis of the precursors. Since the first report, trz complexes have been

successfully incorporated as suitable pre-catalysts for a number of organic transformations and explored for their photophysical properties[191–194] In the biological field, however, the use of trz remains scarcely explored.

The group of Kilpin and Dyson was the first to report on ruthenium(II) and osmium(II) trz complexes as potential anticancer compounds (**29**, Figure 1.15).[195] The N3-substituents of both sets of metal complexes were varied from short chain and long chain alkyl chains, aromatic and sugar functional groups. All the complexes showed in vitro cytotoxicity against A2780 and A2780R cells (<50 μM), with a high degree of selectivity towards normal human embryonic kidney (HEK) cells (> 435 μM), especially observed for the ruthenium ethyl-substituted complex. Throughout the study, no metal dissociation under physiological conditions occurred.

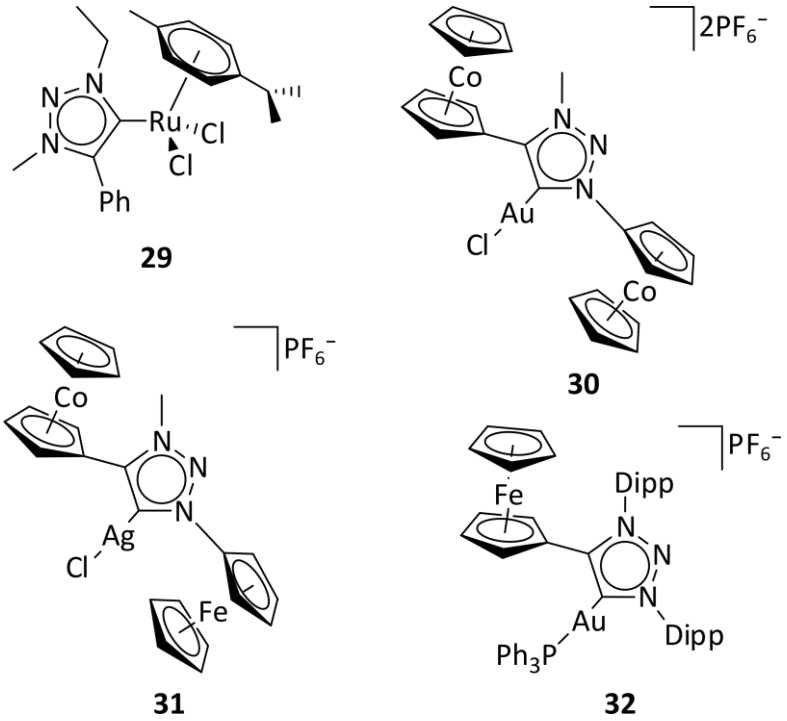


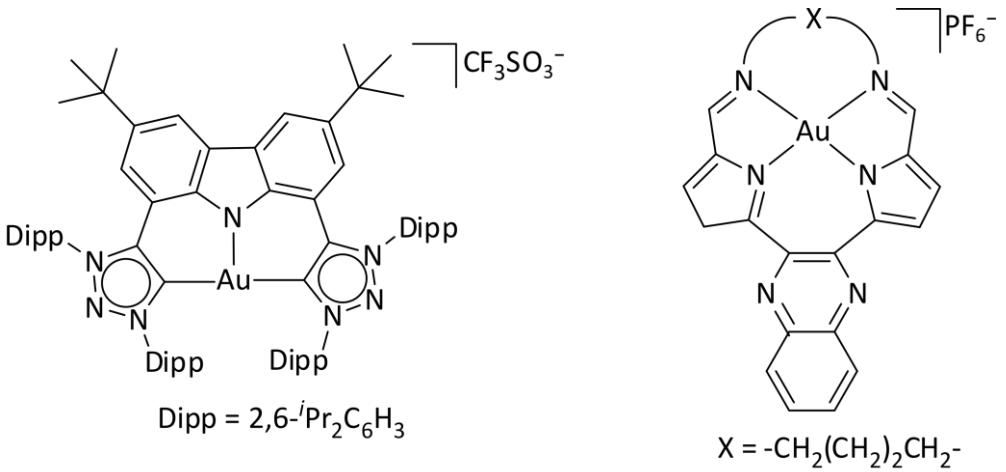
Figure 1.15. 1,2,3-triazol-5-ylidene metal complexes investigated as potential anticancer agents.[195–197]

The same selectivity was not achieved by the heterobimetallic complexes of **30**–**32** (Figure 1.15). Complexes **30** and **31**[196] showed moderate activity (27–50 μM) against breast and colon cancer cell lines. Unfortunately, though, these complexes were slightly more potent against the non-tumourigenic cell line (9–35 μM). The cationic gold(I) complex, **32**, reported by Bezuidenhout et al., showed antiproliferative activity against lung cancer in the sub micromolar range (0.2–0.9 μM) with improved selectivity against healthy cells (5 μM).[197]

Although a relatively new introduction into the organometallic field, the number and applications of trz metal complexes have progressed substantially since the first report.[173] They have proven to be very adaptable towards the intended application due to the ease of substituent variations and high functional group tolerability. These two factors alone indicate their potential in medicinal applications as facile ligand modification (e.g., changing functional groups to alter lipophilicity, etc.) to synthesize a number of potential anticancer agents lead to earlier deductions of the functional groups required to optimize selective cytotoxicity.

1.6 Research rationale and aim.

Recently, a monoanionic CNC pincer ligand, based on a carbazole backbone with two flanking trz was synthesized in our laboratories and has shown to successfully stabilize reactive late transition metal centres such as Ni^{II} and Cu^{II}.[118] The gold analogues are robust complexes (**33**, Figure 1.16), whereby the Au^{III} is fairly unreactive towards reduction to Au^{I} in the presence of a strong base.[198] Moreover, this ligand scaffold has lent itself to rhodium(I) complexation for the selective homodimerization and hydrothiolation of alkynes[199] and ruthenium(II) as catalyst in the transfer hydrogenation of ketones.[200] Recently, the photophysical properties of the silver(I), gold(I) and gold(III) complexes have been explored.[201]



33 **34**

Figure 1.16. The gold(I) complex of the CNC carbazole-based ligand (**33**) reported by Kleinhans et al. and the pyrrole-based multidentate gold(III) complex (**34**) reported by Munro et al.[198,202]

In 2014, Munro et al.,[202] reported the effective inhibition of Topo I with the use of the planar cationic pyrrole based gold(III) macrocycles (**34**, Figure 1.16) and have successfully proven that these complexes' mode of action involve the highly specific catalytic inhibition of Topo I. Complex **34** intercalates DNA directly at the sequence targeted by the enzyme and therefore

hinders the binding of Topo I to DNA. Molecular simulations demonstrated the pivotal role of the Au^{III} in both the intercalation to DNA and enzyme inhibition. The in vitro cytotoxicity of **34** was investigated against 60 human cancer cells and the average IC_{50} value obtained was 16 ± 7 μM, where the most sensitive cancer cell line was the non-small lung cancer of which an IC_{50} of 280 nM was obtained. Complex **34** proceeded to in vivo hollow-fibre studies but unfortunately did not show the desired cytotoxicity to warrant further investigation.

It is suggested that for this research project, the behaviour of the carbazole-based CNC ligand is further explored for its physiological potential. The carbazole scaffold is planar and rigid. By substituting the *tert*-butyl groups on the 3- and 6-positions with hydrogens might allow DNA intercalation to occur as a potential mode of action for a likely anticancer agent with a similar mode of action to **34**. Further, the 2,6-diisopropylphenyl (Dipp) wingtips on the trz can be substituted for less bulky alkylated substituents (Figure 1.17). Even with the structural modifications, the flanking trz and the anionic N-donor of the carbazole should offer sufficient stabilization of the Au^{III} under physiological conditions.

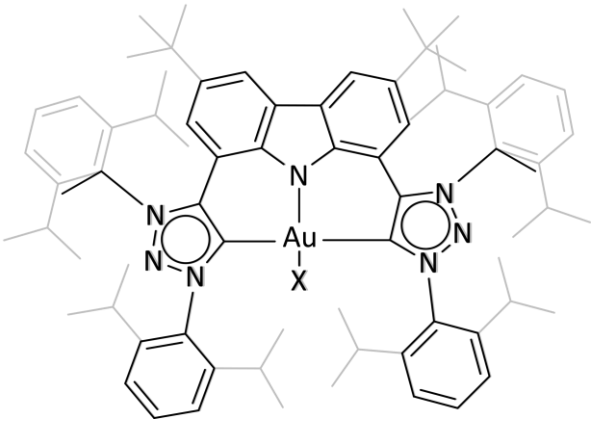


Figure 1.17. The proposed changes (black) to the original CNC ligand (in grey) to obtain a biologically relevant ligand scaffold with enough electronic stabilization to prevent the reduction of Au^{III} to Au^{I} under physiological conditions.

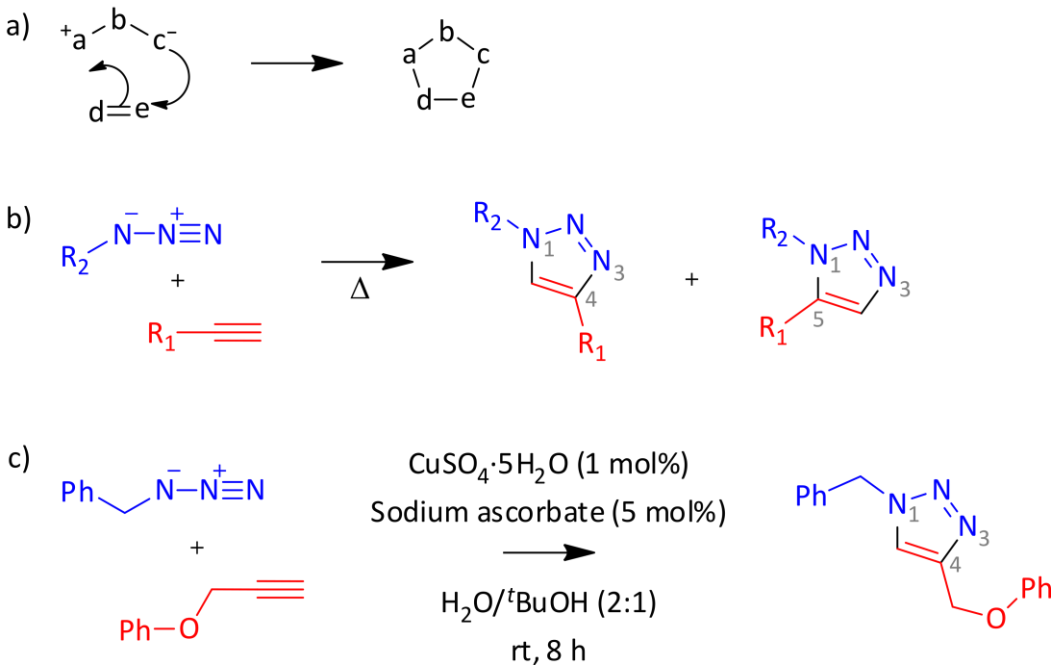
The synthesis and characterization of the lead complex, the CNC pincer gold(III) complex analogous to **33** is described whereafter the cytotoxicity is evaluated against both breast cancer cells and normal, healthy cells. Further information regarding DNA and protein binding ability and stability is performed in attempt to elucidate the mode of action of the target gold(III) complex.

Chapter 2: Synthesis of 1-aryl-3-alkyl-1,2,3-triazol-5-ylidene metal complexes

2.1 Introduction

Mesoionic carbenes, specifically 1,2,3-triazol-5-ylidenes (trz) are an appealing group of ligands to use in medicinal chemistry because their precursors, 1,2,3-triazole rings, are readily synthesized using click chemistry.[173,203] The term "click chemistry" was coined in 2001 by Sharpless et al.,[204] where they describe a group of organic processes (e.g., hetero-Diels-Alder cycloaddition and ring-opening nucleophilic substitution reactions etc.) that comply to a set of criteria that allow for the fast development of a wide range of compounds with valuable properties for use in the medicinal field. The requirements for an organic process to be classified as 'click' are among the following: the reaction must be modular, produce high yields with simple product isolation, have a wide substrate scope with minimal by-products and are preferably indifferent to solvents, oxygen and water. These features are likely achieved due to the high thermodynamic driving force in the formation of the carbon-heteroatom links in these organic reactions.

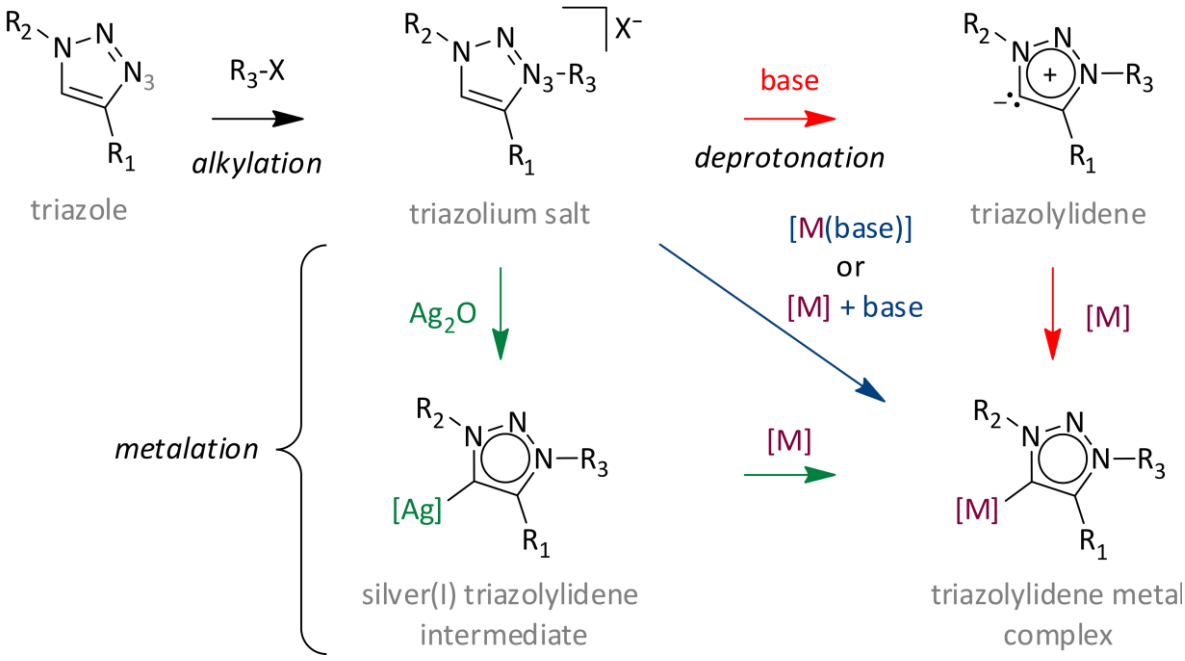
Huisgen's 1,3-dipolar [3+2] cycloaddition of terminal alkynes and azides (Scheme 2.1a,b)[205,206] generates 1,2,3-triazoles and are deemed the "cream of the crop" of click chemistry as this reaction is a pure fusion process (the sum of the reactant's formulae equals that of the product) and have little dependence on solvent. The reaction is highly modular and unites a 1,3-dipole (the azide) and a dipolarophile (the alkyne) to produce a high number of diverse 5-membered-1,2,3-triazoles. The azide reactant is considered the only 1,3-dipole devoid of side reactions.[204] Originally however, the reaction was not regioselective as both the 1,4- and 1,5-disubstituted triazoles were formed. Independently, the groups of Sharpless[207] and Meldal[208] developed the copper(I)-catalysed 1,3-cycloaddition of terminal alkynes and azides (CuAAC) in which only the 1,4-regioisomer is formed (Scheme 2.1c). Since then, many more reports on the CuAAC reaction followed whereby reaction conditions e.g., type of copper catalysts, solvent etc., were varied to suit a particular functional group or application and all these conditions maintain high yields and selectivity towards the 1,4-regioisomer.[209–215] The 1,5-regioisomer can be selectively obtained by using either a ruthenium(II) catalyst[216] or catalytic amount of certain bases.[217,218]



Scheme 2.1. (a) Huisgen's [3+2] cycloaddition of a generic 1,3-dipole and dipolarophile to generate a 5-membered heterocycle product. (b) The [3+2] cycloaddition of azides and terminal alkynes also described by Huisgen, where the azide acts as the 1,3-dipole reactant and the alkyne as the dipolarophile. (c) The copper(I)-catalysed cycloaddition of azides and terminal alkynes (CuAAC) where only the 1,4-regioisomer is formed.[205–207]

The 1,4-disubstituted-1,2,3-triazoles are chemo-selectively alkylated at the N3 position with suitable electrophiles such as alkyl halides or triflates (unless other more nucleophilic donor groups are present elsewhere on the triazole), to produce the cationic 1,3,4-trisubstituted-1,2,3-triazolium salts (Scheme 2.2).[173,219]

There are multiple routes for metalation of these triazolium precursor salts and the most widely used method involves the deprotonation of the triazolium C5-H with a base. More often than not, the base is bound to the metal in the metal precursor e.g. in Ag_2O (green route, Scheme 2.2) and $Pd(OAc)_2$ (blue route, Scheme 2.2). External bases such as metal bis(trimethylsilyl) amides e.g. $K[N(SiMe_3)_2]$ are used to deprotonate the triazolium salt and isolate the free trz (if stable enough, to store as a "bottleable" ligand for complexation) followed by metalation with a suitable metal precursor (red route, Scheme 2.2). The free carbene displaces one or more ligands in the coordination sphere of the metal precursor. The use of a bulky base such as $K[N(SiMe_3)_2]$ presumably prevents the insertion of the free carbene into the N-H bond of the conjugate acid, $HN(SiMe_3)_2$.[220]

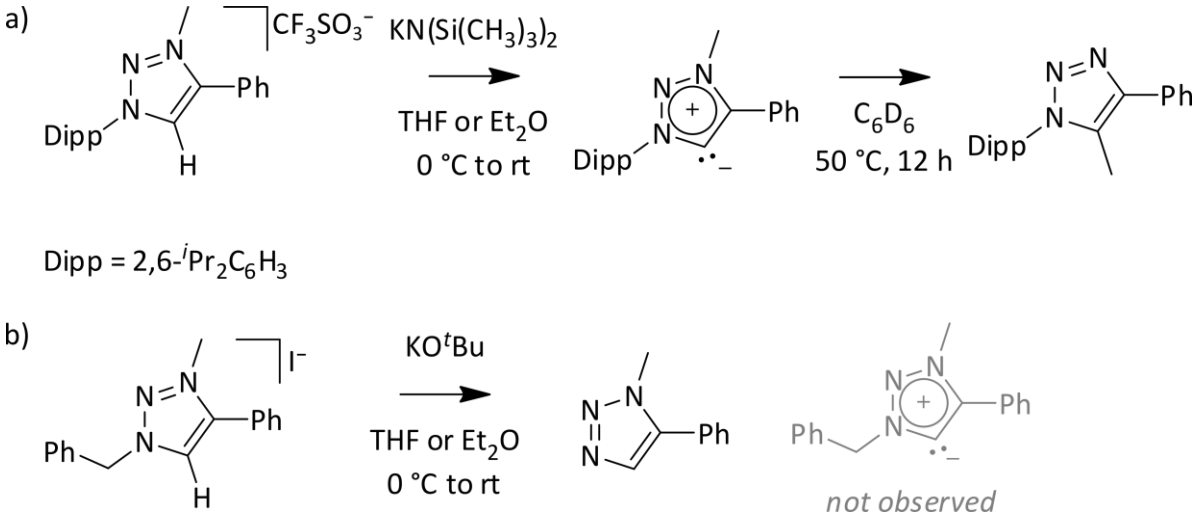


Scheme 2.2. The most popular metalation routes for the complexation of 1,2,3-triazolylidenes. The triazole, obtained from the CuAAC reaction, is alkylated on the N3-position to produce the 1,3-disubstituted-1,2-3-triazolium salt. Thereafter, various metalation methods can be employed for the complexation of the triazolium salts. Three of the most used metalation routes are shown. Transmetalation from the silver(I) 1,2,3-triazol-5-ylidene is depicted with the green arrows and the free carbene route is described by the red arrows. The blue arrow represents the concerted free-carbene route, whereby the free carbene is generated in situ in the presence of the metal precursor or represents the direct metalation of the triazolium salt with a metal precursor bound to a basic ligand.[173]

The stability of the 1,2,3-triazolium salt under deprotonation conditions and the stability of the isolated free carbene play an important role when considering the metalation route to follow for complexation.

As mentioned earlier, free trz can be isolated from their corresponding triazolium salts by using a strong non-nucleophilic base. Although the free carbene (Scheme 2.3a) is stable at room temperature, at higher temperatures intramolecular rearrangement of the N3-alkyl group occurs. Substituting the N3-methyl with a less electrophilic and more sterically hindered isopropyl group delays this rearrangement, and N3-aryl substituents suppress this process completely.[183] The presence of at least one aryl substituent significantly increases the stability of the free trz as the attempted isolation of the free carbene of 1,3-dialkylated-1,2,3-triazolium salt (Scheme 2.3b) resulted in debenzylation instead.[221] To prevent side reactions

such as N3-dealkylation, the in situ generation of the free carbene with a base in the presence of the metal precursor (i.e., concerted, one-pot) also yield successful results (Scheme 2.2, blue route).

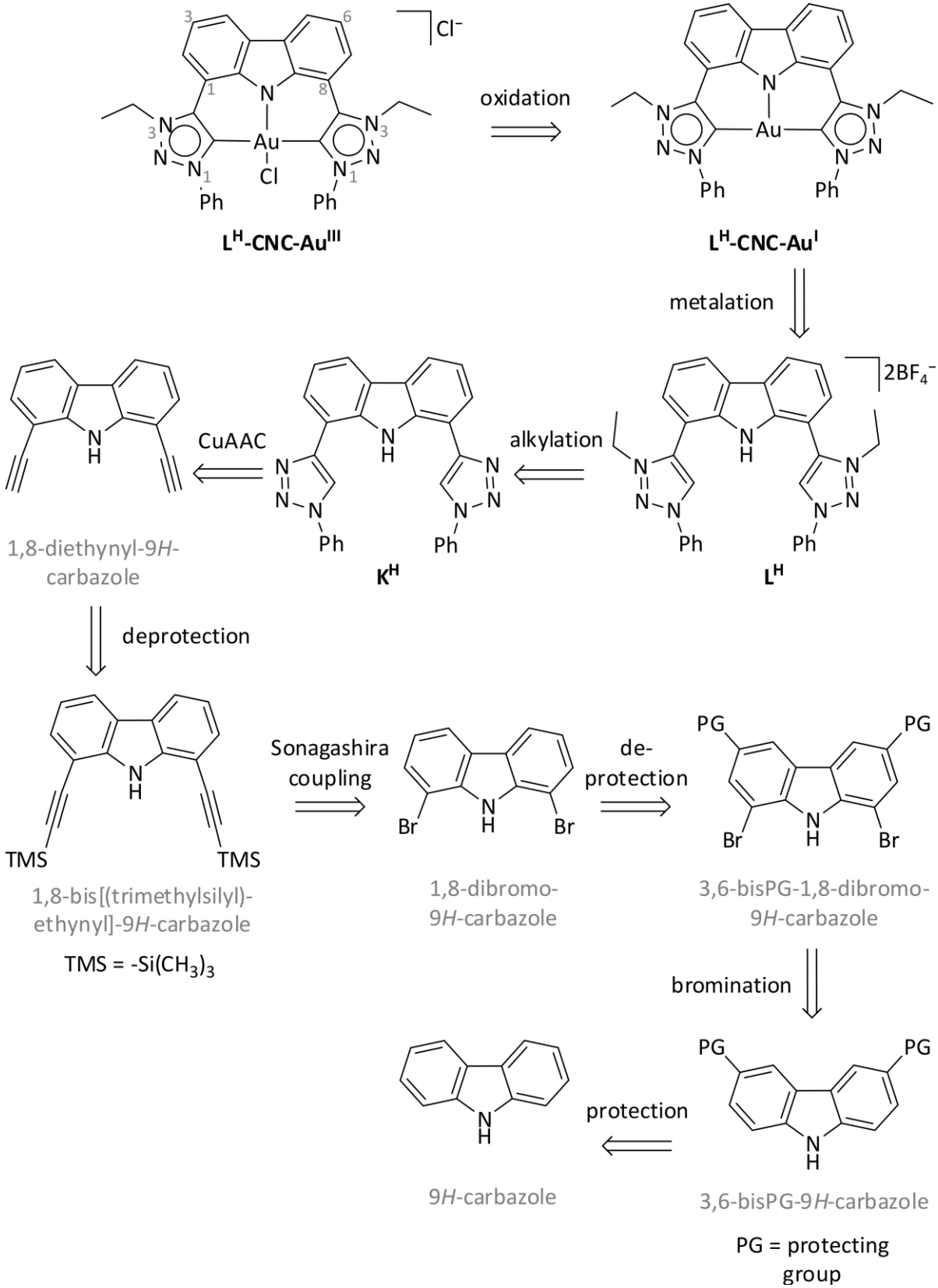


Scheme 2.3. (a) The first report of the isolation of 1,2,3-triazol-5-ylidene which when heated undergoes N3-alkyl group transfer. (b) The attempted isolation of a 1,3-dialkylated-1,2,3-triazolium salt by deprotonation resulted in debenzylation of the triazole ring instead of the expected free carbene.[183,221]

The formation of the free trz is avoided in metalation reactions where the precursors Ag_2O and $Pd(OAc)_2$ are used and are suitable for 1,3-dialkylated-1,2,3-triazolium salts. The transmetalation of the silver(I) complex to a wide variety of other metal complexes, is the most widely employed metalation route (green route, Scheme 2.2). The carbene bond in silver(I) complexes is labile and the carbene transfers readily to other metal species present in the reaction.[220,222] The silver(I) trz intermediate is rarely isolated and transmetalation reactions are successful even when the preferred metal precursor and the Ag_2O is reacted under "one-pot" conditions with the triazolium salt.[173,194]

2.2 Aim

In this chapter, the development of a synthetic route towards the cationic gold(III) CNC pincer complex **L^H-CNC-Au^{III}** as the target compound for the eventual assessment of potential antiproliferative properties, is described. The proposed retrosynthetic pathway employing 9*H*-carbazole as the starting material is outlined in Scheme 2.4.



Scheme 2.4. The complete proposed retrosynthetic pathway for the synthesis of the gold(III) CNC pincer complex, **L^{H}-CNC-Au^{III}** from 9*H*-carbazole.

Specifically, **L^H-CNC-Au^{III}** is a square planar gold(III)-chloride complex enclosed ('pinced') by an anionic 1,8-functionalized carbazolide scaffold with two flanking trz to provide sufficient redox stability. The N1- and N3-positions of the trz (the so-called wingtip functionalities) are occupied by the simplest aromatic group, i.e. a phenyl on N1, for additional stabilization, and the non-sterically demanding ethyl group on N3 for reduced sterical hindrance to facilitate potential DNA intercalation. The 3- and 6-positions of the carbazole are left unsubstituted for this same reason.

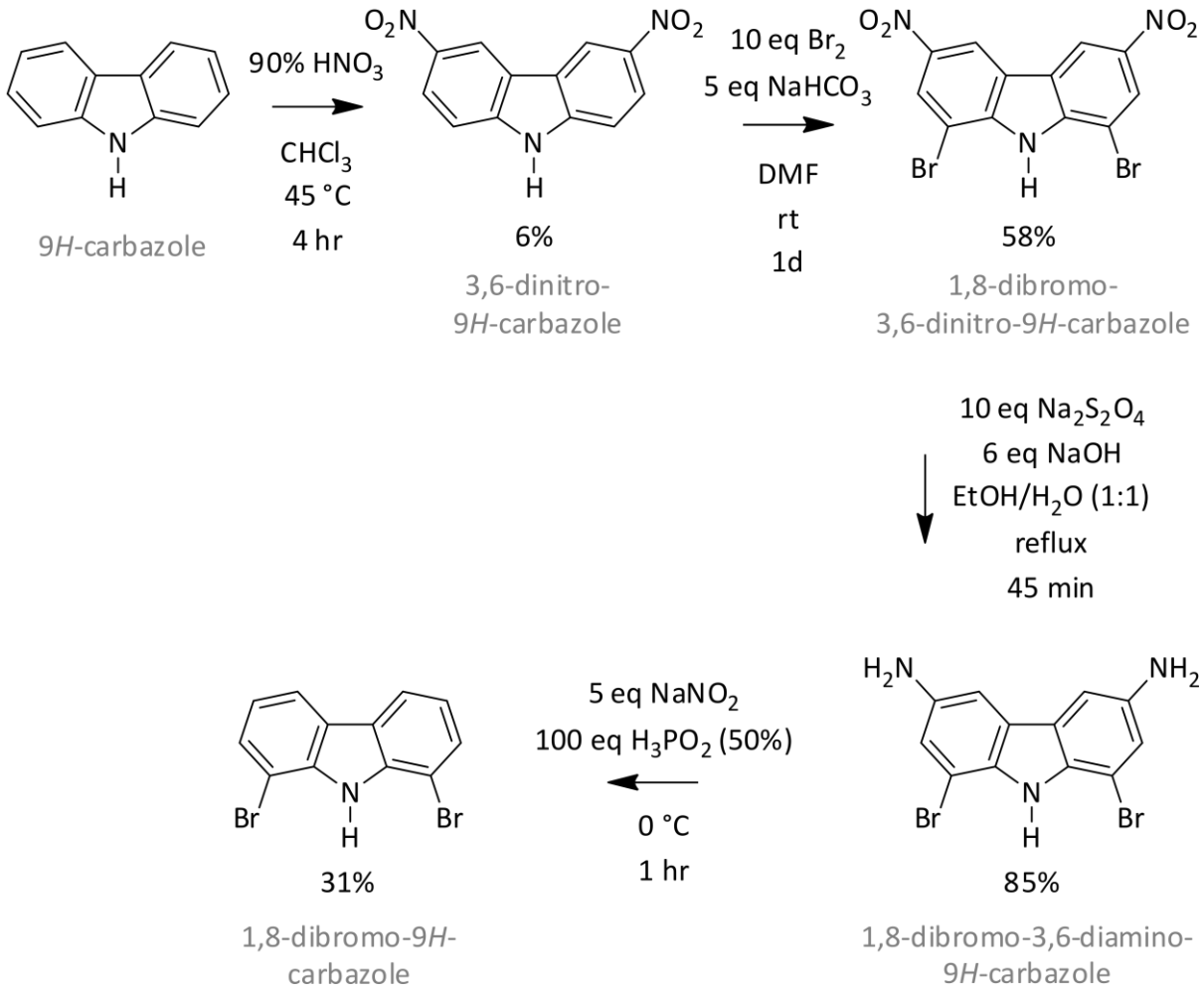
The CNC organic ligand scaffold is synthetically assembled starting from the commercially available 9*H*-carbazole precursor. The 3- and 6-positions of the carbazole are the most reactive and to functionalize the 1- and 8-positions, the 3- and 6-positions must be protected. Thereafter a sequence of synthetic modifications allows the synthesis of the terminal alkyne i.e. the 1,8-diethynyl-9*H*-carbazole to use as precursor with phenyl azide in the CuAAC reaction to produce the 1,4-disubstituted-1,2,3-triazole, **K^H**. Alkylation on both N3-positions of the triazole affords the triazolium salt, **L^H**, as precursor for metalation with gold(I) followed by oxidation to gold(III).

Owing to the use of protecting groups for positions 3 and 6 on the carbazole, the synthesis of the 3,6-protected-1,8-functionalized carbazolide ligand scaffold is also reported, to compare DNA binding ability between a sterically hindered and unhindered carbazolide gold(III) complex.

2.3 Results and discussion

2.3.1 Synthesis of 1,8-dibromo-9*H*-carbazole

The most widely known method for protecting the 3- and 6-positions of the carbazole for the eventual functionalization of the 1-and 8-positions is the use of a nitronium protecting group (Scheme 2.5).[223] The first step involves the nitration of 9*H*-carbazole with nitric acid in chloroform at 45 °C for 4 hours following a known literature procedure.[224] The reaction produced a yellow suspension which was quenched with water and the reaction mixture was filtered. The crude solid was dissolved in KOH (10 g in 250 mL H_2O/EtOH (1:1)) to a red solution and filtered again. The filtrate was acidified with concentrated HCl which produced a yellow precipitate that once filtered and dried afforded the purified product as a dark yellow solid at a very low yield of 6%.



Scheme 2.5. The synthetic route to 1,8-dibromo-9*H*-carbazole from 9*H*-carbazole by protecting the most reactive positions of the 9*H*-carbazole (i.e. 3 and 6) with nitro groups.

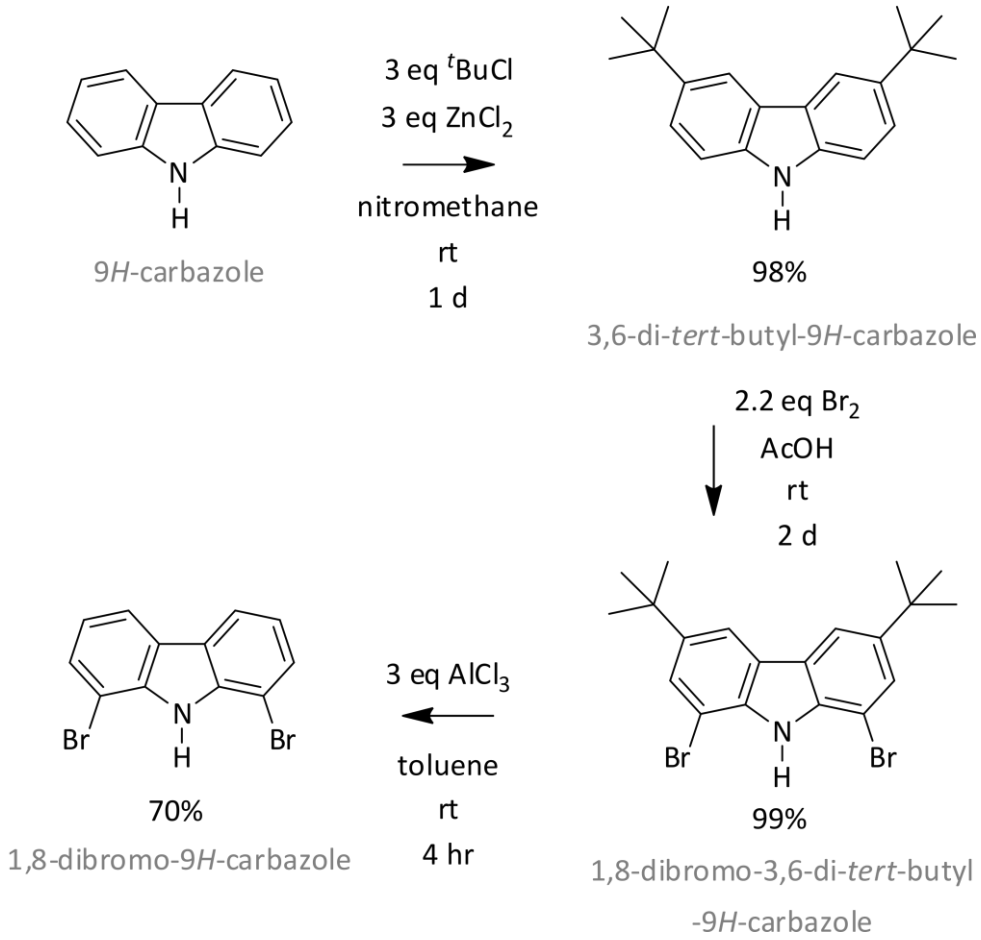
The following step is the bromination of 2,6-dinitro-9*H*-carbazole to 1,8-dibromo-3,6-dinitro-9*H*-carbazole (Scheme 2.5). Initially, the reaction was done according to a known literature report[223] whereby Br_2 is added to a suspension of 2,6-dinitro-9*H*-carbazole in sulfuric acid but this reaction produced several side-products. The bromination reaction whereby Br_2 is added to a solution of 3,6-dinitro-9*H*-carbazole in DMF in the presence of $NaHCO_3$ instead,[225] lead to the isolation of the product as a yellow solid in 58% yield.

To remove the nitro groups, they are reduced to amines followed by deamination via the in situ generated diazonium salt which undergoes substitution with protons sourced by H_3PO_2 (Scheme 2.5). Suzuki et al.[225] reported on the 'one-pot' reduction and deamination of 1,8-dibromo-3,6-dinitro-9*H*-carbazole to 1,8-dibromo-9*H*-carbazole but in our hands, this methodology did not succeed. However, if the 1,8-dibromo-3,6-diamino-9*H*-carbazole intermediate is isolated first, successful deamination to 1,8-dibromo-9*H*-carbazole could

proceed. The reduction of the nitro groups was executed by adding 1,8-dibromo-3,6-dinitro-9*H*-carbazole and sodium hydroxide to a degassed solution of H_2O and EtOH (1:1) under a nitrogen atmosphere. The reducing agent, sodium dithionite was added, and the reaction was refluxed for 45 min. The reaction mixture was cooled, and the product was extracted with ethyl acetate and dried over magnesium sulfate. The solvent was evaporated in vacuo resulting in a purple-grey solid obtained at 85% yield. Subsequently, the 1,8-dibromo-3,6-diamino-9*H*-carbazole was resuspended in a solution of H_2O/EtOH (1:2) and 50% of H_3PO_2 was added. The reaction mixture was cooled down to 0 °C and sodium nitrite was added. The reaction proceeded for 1 hour, after which the product was extracted with DCM, dried in vacuo and affording a brown solid as 1,8-dibromo-9*H*-carbazole in 31% yield.

The overall yield of the reaction route (5 steps) from 9*H*-carbazole to 1,8-dibromo-9*H*-carbazole using nitronium as a protecting group is 0.9%. In literature though, higher yields of 15–18% were reported.[223] Since the 1,8-dibromo-9*H*-carbazole is a precursor which requires further synthetic modifications to the desired ligand scaffold, the recovery of only 360 mg of this key precursor from a large scale reaction (20 g starting material) was not sustainable. Another synthetic route was therefore considered. Brooker et al.[226] recently reported their use of *tert*-butyl groups as suitable protecting groups for positions 3 and 6 of 9*H*-carbazole. The removal of the *tert*-butyl groups involves the reverse Friedel-Craft alkylation described by Tashiro et al.,[227,228] in 1979. The reaction route is described in Scheme 2.6 and the overall yield for this reaction (4 steps) was 68%, obtaining 26.4 g of 1,8-dibromo-9*H*-carbazole from 20 g of 9*H*-carbazole.

The dialkylated carbazole, 3,6-*tert*-butyl-9*H*-carbazole was prepared according to the previously reported procedure by Hou[229] using $ZnCl_2$ as the catalyst during the Friedel-Crafts alkylation of 9*H*-carbazole with 2-methyl-2-propane in nitromethane at room temperature (Scheme 2.6). The green-white suspension was stirred overnight and then quenched with water. The product was extracted with DCM, dried over magnesium sulfate, and was isolated as a white crystalline solid, after the evaporation of the solvent, in excellent (98%) yield. Figure 2.1a shows the ^{1}H NMR spectrum of 3,6-*tert*-butyl-9*H*-carbazole in $CDCl_3$ with the distinctive singlet at δ_H 1.46 ppm accounting for 18 new CH_3-protons from the *tert*-butyl group. The alkylation with the well-known $AlCl_3$ catalyst produce much lower yields (50 – 70%) with longer reaction times.[230]



Scheme 2.6. The synthetic route of 1,8-dibromo-9*H*-carbazole from 9*H*-carbazole using *tert*-butyl groups to protect the 3-and 6-positions for the functionalization of positions 1 and 8 of 9*H*-carbazole.

The subsequent bromination of 3,6-*tert*-butyl-9*H*-carbazole was done by adding bromine dropwise to a suspension of 3,6-*tert*-butyl-9*H*-carbazole in glacial acetic acid in the dark (Scheme 2.6). The red-orange reaction mixture continued to stir over 2 days and was quenched with water and the formed precipitate, a light brown solid, was collected by filtration. The solid was dissolved in diethyl ether and washed with 1 M NaOH, followed by 1 M $NaHCO_3$, and dried over magnesium sulfate. The solvent was evaporated resulting in a cream coloured solid as 1,8-dibromo-3,6-*tert*-butyl-9*H*-carbazole in near quantitative yield. The formation of 1,8-dibromo-3,6-*tert*-butyl-9*H*-carbazole was confirmed by ^{1}H NMR spectroscopy in $CDCl_3$ with the disappearance of two aromatic proton (1c, Figure 2.1b) resonance signals.

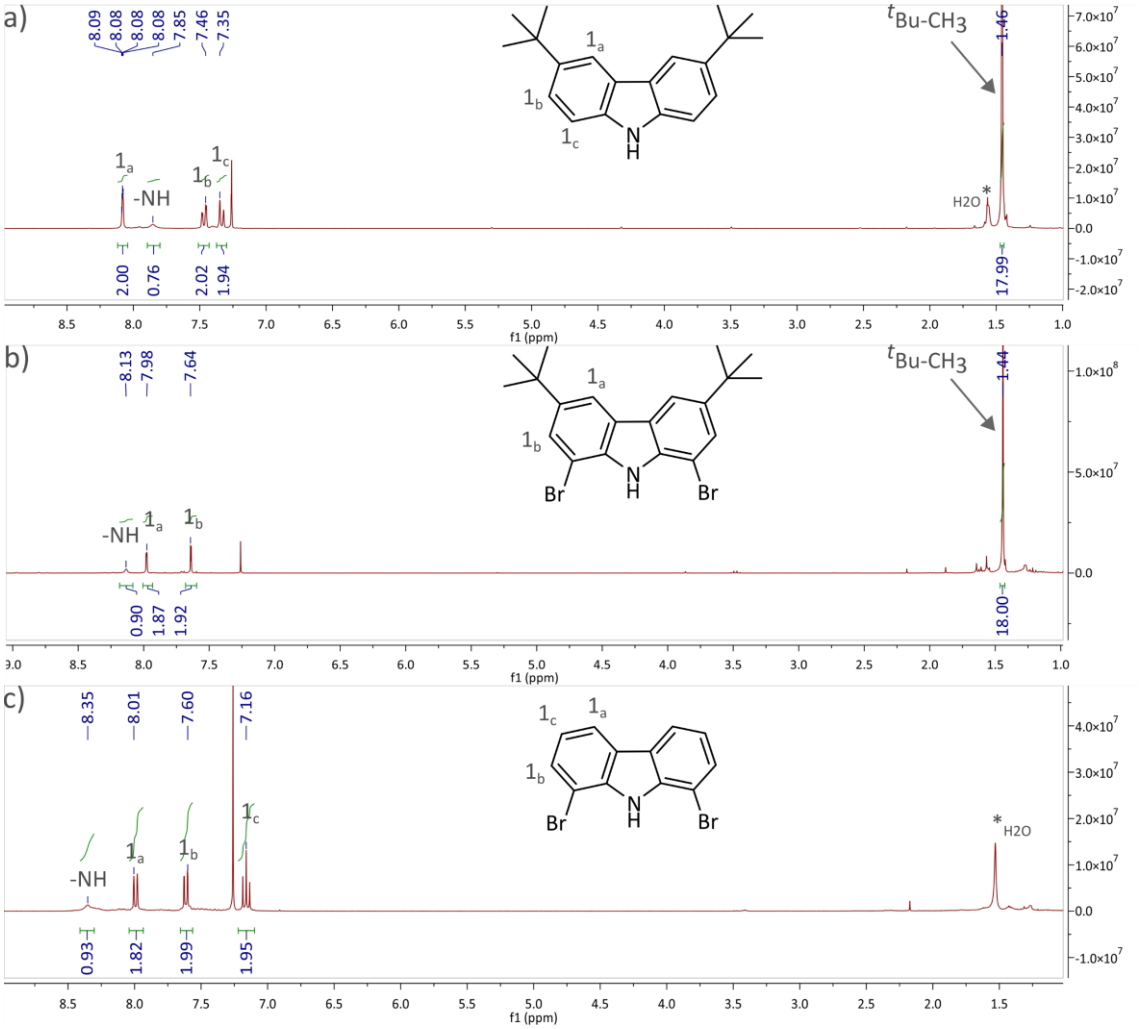


Figure 2.1. The ^{1}H NMR spectra of (a) 3,6-*tert*-butyl-9*H*-carbazole, (b) 1,8-dibromo-3,6-*tert*-butyl-9*H*-carbazole and (c) 1,8-dibromo-9*H*-carbazole in $CDCl_3$.

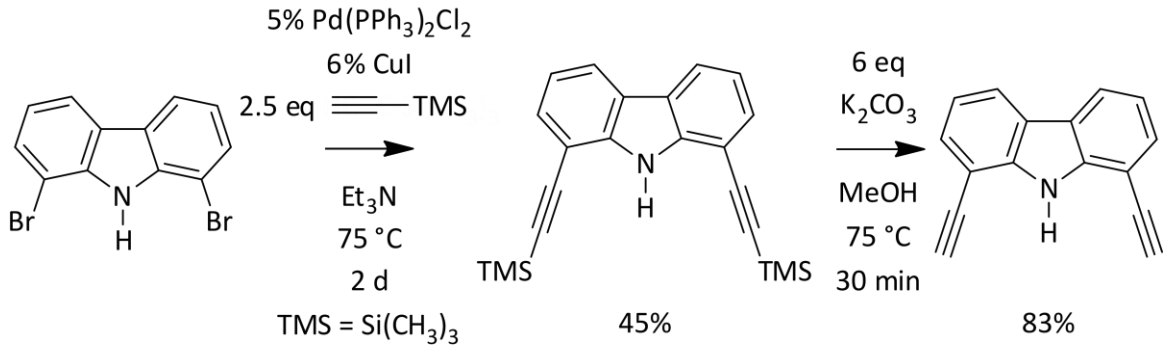
The removal of the *tert*-butyl groups to synthesize 1,8-dibromo-9*H*-carbazole followed (Scheme 2.6). The *tert*-butyl groups are removed in a 'reverse' Friedel-crafts alkylation type reaction whereby the *tert*-butyl groups of the dialkylated carbazole is transferred to the aromatic solvent, i.e. toluene, in the presence of $AlCl_3$.[231,232] The synthesis of 1,8-dibromo-9*H*-carbazole was done according to the previous literature report.[233] To a dried, purged Schlenk tube, 1,8-dibromo-3,6-*tert*-butyl-9*H*-carbazole was added and dissolved in anhydrous toluene. Small amounts of solid $AlCl_3$ were added periodically under a nitrogen atmosphere. After 1 hour, the reaction mixture turned dark green and remained that colour for 3 more hours. The reaction was slowly quenched with ice followed by water and DCM was added. The orange organic fraction was washed repeatedly with water and dried over magnesium sulfate. The product after evaporation is a sticky dark brown solid, which after stirring in pentane overnight, is collected via filtration as a cream coloured solid in 70% yield.

Interestingly, when the reaction was repeated with anhydrous $ZnCl_2$, the dealkylation of the *tert*-butyl did not occur and the starting material, 1,8-dibromo-3,6-*tert*-butyl-9*H*-carbazole was recovered. The ^1H NMR spectrum of 1,8-dibromo-9*H*-carbazole in $CDCl_3$ indicates the reappearance of two aromatic protons (1c at δ_H 7.16 ppm, Figure 2.1c) with the accompanied removal of the *tert*-butyl CH_3-groups.

Furthermore, the *tert*-butyl, when not removed, can be used as a sterically hindered analogue of the 3,6-unfunctionalized ligand scaffold to compare DNA binding affinity and antitumour potential.

2.3.2 Synthesis of 1,8-diethynyl-9*H*-carbazole

1,8-diethynyl-9*H*-carbazole is a suitable precursor for the CuAAC reaction to functionalize positions 1 and 8 of 9*H*-carbazole with 1,2,3-triazoles. The synthesis of the protected dialkyne i.e. 1,8-bis((trimethylsilyl)ethynyl)-9*H*-carbazole involves the C(sp^2)-C(sp) coupling reaction, better known as Sonagashira coupling, between an aryl-halide, 1,8-dibromo-9*H*-carbazole, and the terminal alkyne, ethynyltrimethylsilane (Scheme 2.7). The protected dialkyne is subsequently deprotected for use during the CuAAC reaction to produce 1,2,3-triazoles.

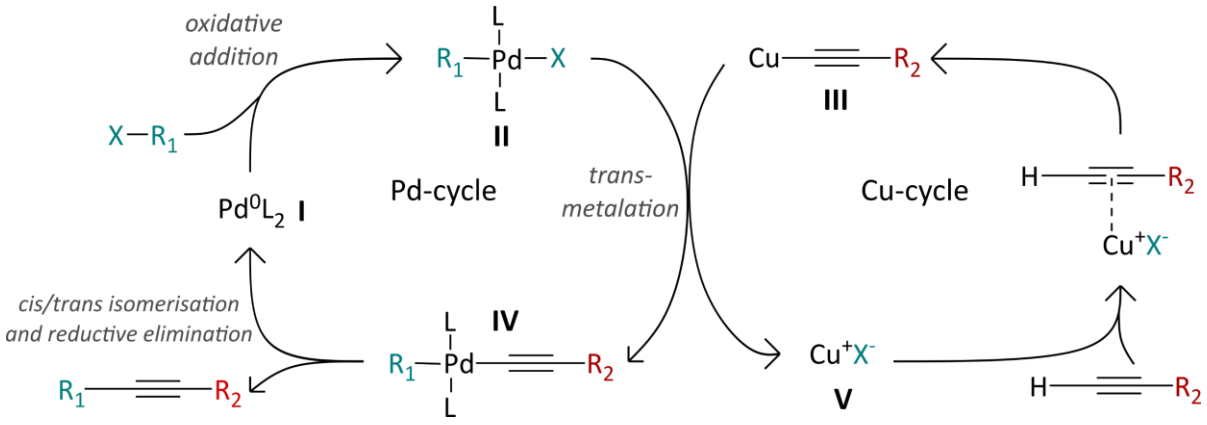


Scheme 2.7. The synthesis of 1,8-bis((trimethylsilyl)ethynyl)-9*H*-carbazole and the subsequent deprotection to 1,8-diethynyl-9*H*-carbazole.

The synthesis of 1,8-bis((trimethylsilyl)ethynyl-9*H*-carbazole was carried out according to a previous literature report[226] which involves the addition of the palladium(II)-phosphane catalyst and the copper(I) co-catalyst to a dried purged Schlenk flask, which was deoxygenated overnight in vacuo in the absence of light. 1,8-dibromo-9*H*-carbazole was added under an argon atmosphere, and the solid mixture was suspended in freshly distilled dried triethylamine. Ethynyltrimethylsilane was added dropwise and the reaction mixture was

degassed. The reaction continued for 2 days at 75 °C and the dark brown suspension was cooled down, diluted with DCM and filtered through celite. The crude product was purified by column chromatography on aluminium oxide and elution with diethyl ether affords 1,8-bis((trimethylsilyl)ethynyl-9*H*-carbazole as a yellow solid with 45% yield. This reaction was repeated with the 3,6-di-*tert*-butyl analogue to afford 3,6-di-*tert*-butyl-1,8-bis((trimethylsilyl)ethynyl-9*H*-carbazole as a pale yellow solid (elution with hexane instead of diethyl ether) obtained in higher yield (86%).

The mechanism of the Sonagashira coupling is still unknown but it is generally considered to proceed over two independent cycles namely the palladium cycle and the copper cycle and a schematic is shown in Scheme 2.8.



Scheme 2.8. The proposed mechanism for the copper co-catalysed Sonagashira coupling. During the palladium cycle, Pd^0L_2 undergoes oxidative addition with the aryl chloride (X-R_1) and forms **II**. A copper-acetylide intermediate (**III**) is formed during the copper cycle and undergoes transmetalation with species II to form **IV** and the copper-halide salt, **V**. The palladium intermediate, **IV**, undergoes *cis/trans* isomerisation followed by reductive elimination to produce the newly coupled product.[234]

During the palladium cycle, the palladium(II) catalyst is reduced to Pd^0 by the amine base (triethylamine) (**I**, Scheme 2.8) to undergo oxidative addition with the aryl halide. $Pd(PPh_3)_2Cl_2$ is used the most due to its stability and solubility. The formed palladium intermediate, (**II**, Scheme 2.8) then undergoes transmetalation with the Cu^I-acetylide intermediate (**III**, Scheme 2.8), which was formed during the copper cycle to generate a palladium species that has both the alkyne and the aryl-group bound (**IV**, Scheme 2.8) and a copper-halide species (**V**, Scheme 2.8). The final coupled alkyne arises from *cis/trans* isomerisation of the palladium intermediate followed by reductive elimination that regenerates the Pd^0-catalytic species.

The dimerization of alkynes can occur during the copper cycle on exposure to air or oxidative agents and therefore the reaction is conducted under an argon atmosphere.[234]

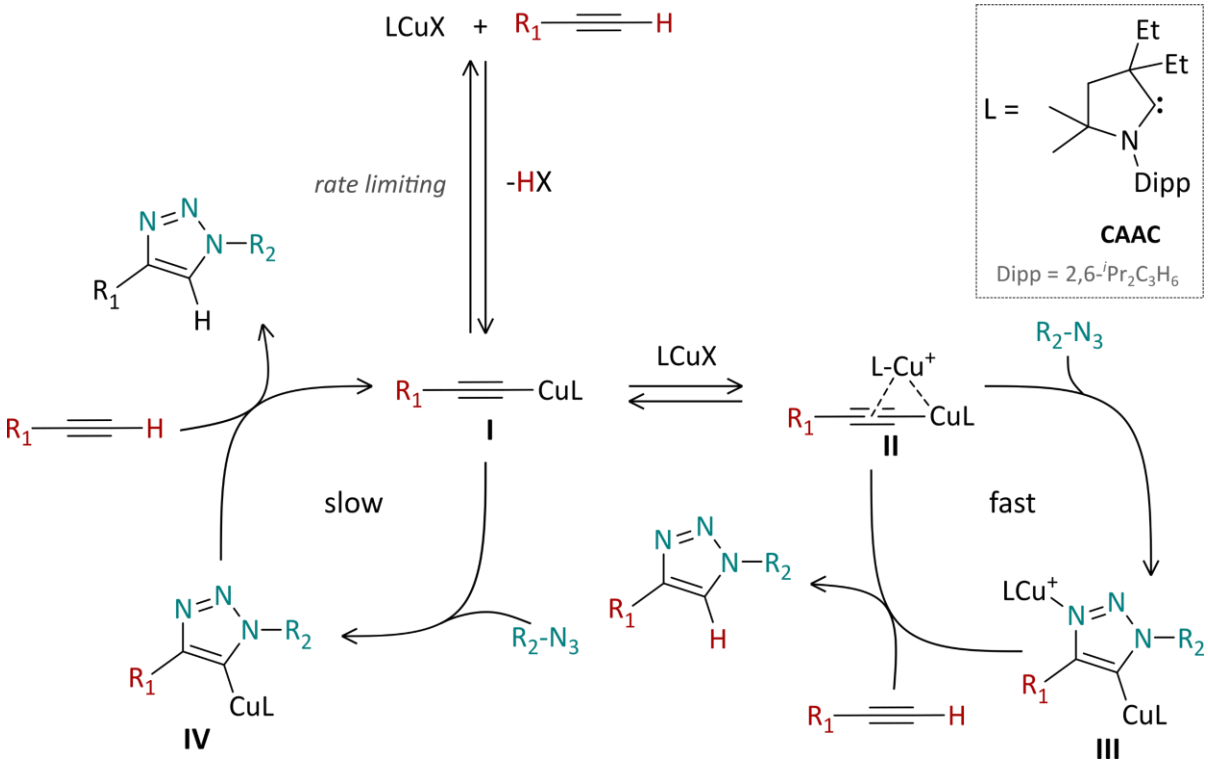
The TMS-protected alkyne is much more stable than the deprotected alkyne as the former can be stored at 0 °C indefinitely. For the subsequent CuAAC reaction, however, the deprotection of the dialkyne was necessary as the yields for CuAAC significantly decreased when the protected alkyne was used instead. The deprotection of the dialkyne was done according to the reported literature procedure for the synthesis of 1,8-diethynylcarbazole[226] using potassium carbonate and deoxygenated methanol[235] at 75 °C for 30 min to undergo desilylation via methanolysis.[236] After cooling down to room temperature, the reaction was quenched with water and the unprotected alkyne was extracted with DCM. After evaporation, 1,8-diethynylcarbazole was obtained as a light brown solid in high yield (83%). The same reaction conditions were repeated for the *tert*-butyl analogue and upon evaporation of DCM, 1,8-diethynyl-3,6-*tert*-butyl-9*H*-carbazole was collected as light-yellow foam that upon drying solidifies into a crystalline powder.

2.3.3 Synthesis of the triazoles, K^{H} and K^{tBu} and their corresponding triazolium salts, L^{H} and L^{tBu}.

As mentioned previously, the 1,4-disubstituted-1,2,3-triazoles are synthesized from the CuAAC reaction, originally reported independently by Sharpless[207] and Meldal.[208] In the original report of Sharpless, various azides and terminal alkynes were reacted with a Cu^{II} source specifically copper(II)sulfate pentahydrate and a reducing agent namely sodium ascorbate, in a water and alcohol solution. The Cu^{II} is reduced to the catalytically active Cu^{I} in situ and is favoured over the direct use of Cu^{I} salts, the latter being quite sensitive to reaction conditions and increased side-reactions. Since then, many more reports with varying reaction conditions and modifications have been published along with theoretical investigations into the possible mechanism for the CuAAC reaction.[237]

Originally, Sharpless proposed that the CuAAC mechanism proceeds via a stepwise mechanism as the concerted route were, according to DFT calculations, unfavoured. Further studies confirmed this finding and suggested the presence of polynuclear copper(I) species in the catalytic cycle.[237] Later on, Fokin et al., published a mechanistic study using isotopic enrichment studies of isolated σ-bound copper acetylide (of type **I** in Scheme 2.9) and

triazolide (of type **IV** in Scheme 2.9) intermediates and found that the mononuclear σ-bound copper acetylide was unreactive towards azides. An external copper source was necessary for the reaction to take place to presumably form a π-bound Cu^{I}-atom to the σ-bound copper acetylide (of type **II,** Scheme 2.9).[238]

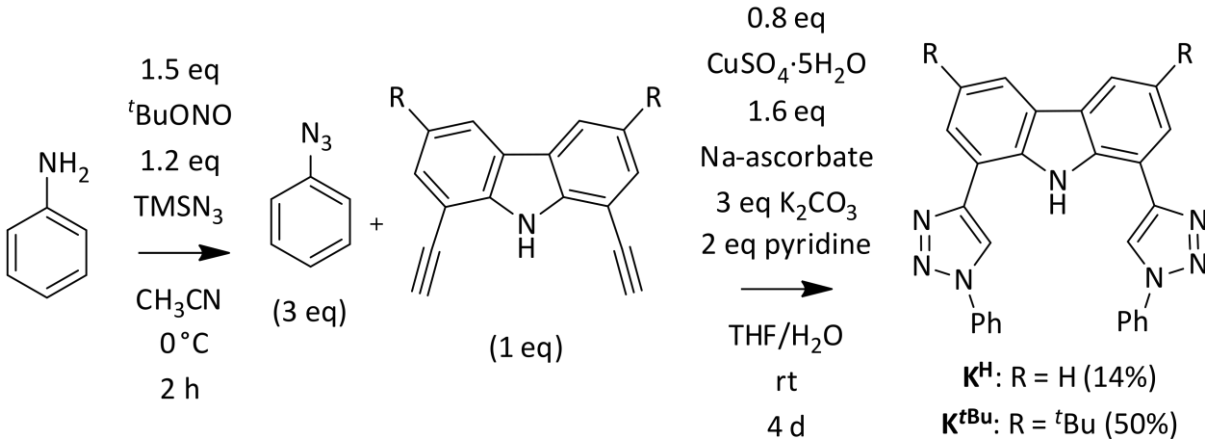


Scheme 2.9. The mechanism of the CuAAC reaction elucidated by Bertrand and co-workers by isolating key intermediates in the cycle using CAAC ligands. Using LCuX as a precursor catalyst, where L = CAAC; X = $CF_3SO_3^-$, the rate-limiting step of the catalytic cycle is the formation of σ-bound copper(I) acetylide complex (**I**). Hereafter, the formation of the dinuclear species, π,σ-bis(copper) acetylide (**II**) is possible. Both **I** and **II** are catalytically active and react with the azide, to form the copper triazolides, **IV** and **III** respectively, the latter occurring at higher rates. The alkyne serves as the proton source for the demetallation of **III** and **IV** to produce the 1,2,3-triazole products.[239]

Bertrand and co-workers used the strong σ-donating and π-accepting CAACs (cyclic (alkyl)(amino) carbenes) to isolate the catalytically active mononuclear (**I** and **IV**, Scheme 2.9) and dinuclear (**II** and **III**, Scheme 2.9) copper(I) complexes. Kinetic studies revealed that both the mono and dinuclear species were capable of transforming azides and alkynes into their corresponding triazoles, but that the rate of the reaction catalyzed by the dinuclear species was significantly higher. They also demonstrated that the addition of base greatly accelerates

the reaction as the rate-limiting step was found to be the formation of the σ-bound copper(I) acetylide (**I**, Scheme 2.9) when LCuX (where L = CAAC, X = OTf) was used as a precatalyst.[239]

The triazoles, $\mathbf{K^{H}}$ and $\mathbf{K^{tBu}}$ have not been reported and their syntheses were adapted from a previously reported procedure[240] that combined the methods of two prior reports from Moses et al.[241] and the group of Fletcher.[242] Moses et al. describes the safer and more convenient synthetic protocol for aryl azides and their subsequent transformation to triazoles without the need to isolate the azide. Fletcher et al. reported on the synthesis of 1,2,3-triazoles from pyridine-based TMS-protected dialkynes by adding potassium carbonate and ensuring that the solvent system used during the CuAAC is a combination of water and alcohol. They also found that the pyridine-free dialkyne did not yield the desired triazole unless pyridine was added. As mentioned earlier, the yields for the triazoles were significantly decreased when the protected alkynes were reacted in the CuAAC reaction.



Scheme 2.10. The synthesis of the 1,4-disubstituted-1,2,3-triazoles, $\mathbf{K^{H}}$ and $\mathbf{K^{tBu}}$ from aniline and their respective dialkynes.[240,241]

The triazoles $\mathbf{K^{H}}$ and $\mathbf{K^{tBu}}$ were synthesized directly from aniline (Scheme 2.10), whereby the phenyl-azide was generated in situ, with the dropwise addition of *tert*-butyl nitrite and azido trimethylsilane to aniline dissolved in acetonitrile at 0 °C. After two hours at room temperature, a solution of dialkyne in THF was added followed by the addition of two separate solutions of copper(II)sulfate pentahydrate and sodium ascorbate in water, such that the volumes of the solvents were of the ratio 1:1:2 for acetonitrile, THF and water. Following these additions, potassium carbonate and pyridine were added to the reaction mixture. Both dialkynes were insoluble in the acetonitrile/water solvent system of the CuAAC reaction and therefore THF was used to aid their dissolution. The reaction mixture for $\mathbf{K^{H}}$

turned brick red immediately after addition where the reaction mixture of **K^{tBu}** also turned red but with no visible precipitation. The reaction was continued for 4 days and was quenched with 1.0 M EDTA in NH_4OH (10% v/v).

After the reaction was quenched, the crude product of **K^{H}** was collected by filtration and the red solid was dissolved in DCM and washed with water. The solution was dried over magnesium sulfate and the solvent was evaporated leaving a red oil as crude product. The crude oil was subjected to column chromatography and the yellow fraction was eluted with DCM, collected, and evaporated to an oily solid. After overnight stirring in diethyl ether, a bright yellow solid was collected by filtration as **K^{H}** obtained in low yields (14%). The triazole is insoluble in most solvents and only partially soluble in $(CD_3)_2SO$ (the deuterated solvent employed for NMR spectroscopy). The lack of solubility presumably explains the low yield obtained although other side-reactions might be involved.[215,238] The purification of **K^{tBu}** followed the same route as **K^{H}** except that the quenched reaction mixture had no precipitate and the crude product was extracted from the quenched reaction mixture by DCM directly. **K^{tBu}** was obtained in much higher yield (50%) as a bright yellow solid and had a greater solubility profile in organic solvents compared to **K^{H}**.

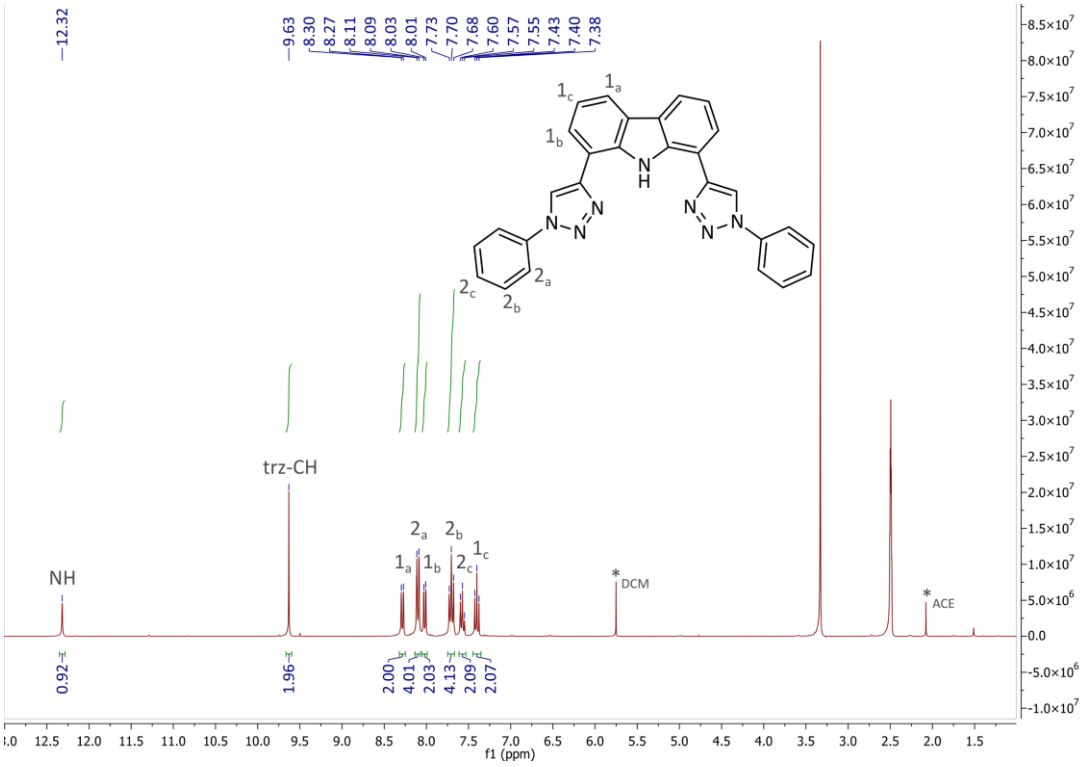
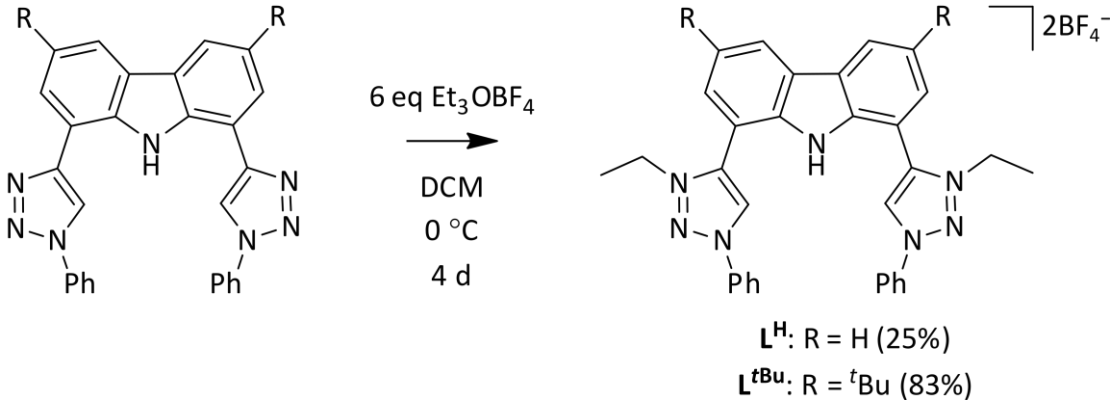


Figure 2.2. ^{1}H NMR spectrum of **K^{H}** in $(CD_3)_2SO$

Evidence of the formation of both triazoles, $\mathbf{K^{H}}$ and $\mathbf{K^{tBu}}$ is unambiguously provided by NMR spectroscopy and the ^{1}H NMR spectrum of $\mathbf{K^{H}}$ in $(CD_3)_2SO$ is shown in Figure 2.2. Several aromatic resonances are observed accounting for both the carbazole and the phenyl protons. For $\mathbf{K^{H}}$, the amine proton signal resonates the most downfield at 12.32 ppm followed by the C5 protons of the two triazole rings at δ_H 9.63 ppm. By comparison, the amine proton resonates more upfield at δ_H 11.89 ppm and the triazole protons at δ_H 8.48 ppm for $\mathbf{K^{tBu}}$, though the direct comparison is precluded as the ^{1}H NMR spectrum for $\mathbf{K^{tBu}}$ was measured in $CDCl_3$. The chemical signals observed for both triazoles are comparable to closely related triazoles reported.[226]

The triazoles $\mathbf{K^{H}}$ and $\mathbf{K^{tBu}}$ were subsequently alkylated with triethyloxonium tetrafluoroborate to produce their respective N3-alkylated-1,3,4-trisubstituted-1,2,3-triazolium salts, $\mathbf{L^{H}}$ and $\mathbf{L^{tBu}}$ (Scheme 2.11). Generally, a solution of triethyloxonium tetrafluoroborate in anhydrous DCM was added to a solution of triazole (**K**) in anhydrous DCM under an argon atmosphere at 0 °C. The reaction was left to reach room temperature overnight and the reaction continued to stir for 3 more days. Thereafter, the solvent was evaporated and the solid dissolved in the minimum amount of acetone. Diethyl ether was added until precipitation occurred. The solid was filtered and dried. Both salts $\mathbf{L^{H}}$ and $\mathbf{L^{tBu}}$ were obtained as white solids at significantly different yields of 25% and 83%, respectively. The low yield for $\mathbf{L^{H}}$ is a likely consequence of the poor solubility of $\mathbf{K^{H}}$ in DCM. The salt, $\mathbf{L^{H}}$, however, does exhibit greater solubility in organic solvents than the triazole, $\mathbf{K^{H}}$.



Scheme 2.11. N3-alkylation of triazoles, $\mathbf{K^{H}}$ and $\mathbf{K^{tBu}}$ to their respective triazolium salts, $\mathbf{L^{H}}$ and $\mathbf{L^{tBu}}$ with triethyloxonium tetrafluoroborate.

The ^{1}H NMR spectrum of $\mathbf{L^{H}}$ in $(CD_3)_2SO$ is shown in Figure 2.3. The appearance of two sets of alkyl peaks (3a and 3b, Figure 2.3) indicates the formation of the N3-alkylated triazolium salt.

Compared to the triazole **K^{H}**, the amine proton resonance shifted more upfield (δ_H 11.41 ppm) but the C5-triazolium proton resonance signal appeared more acidic and shifted more downfield (δ_H 10.04 ppm). Those same signals are both shifted more upfield in **L^{tBu}** (δ_H NH: 9.80 ppm; trz-CH: 9.45 ppm) compared to **L^{H}**.

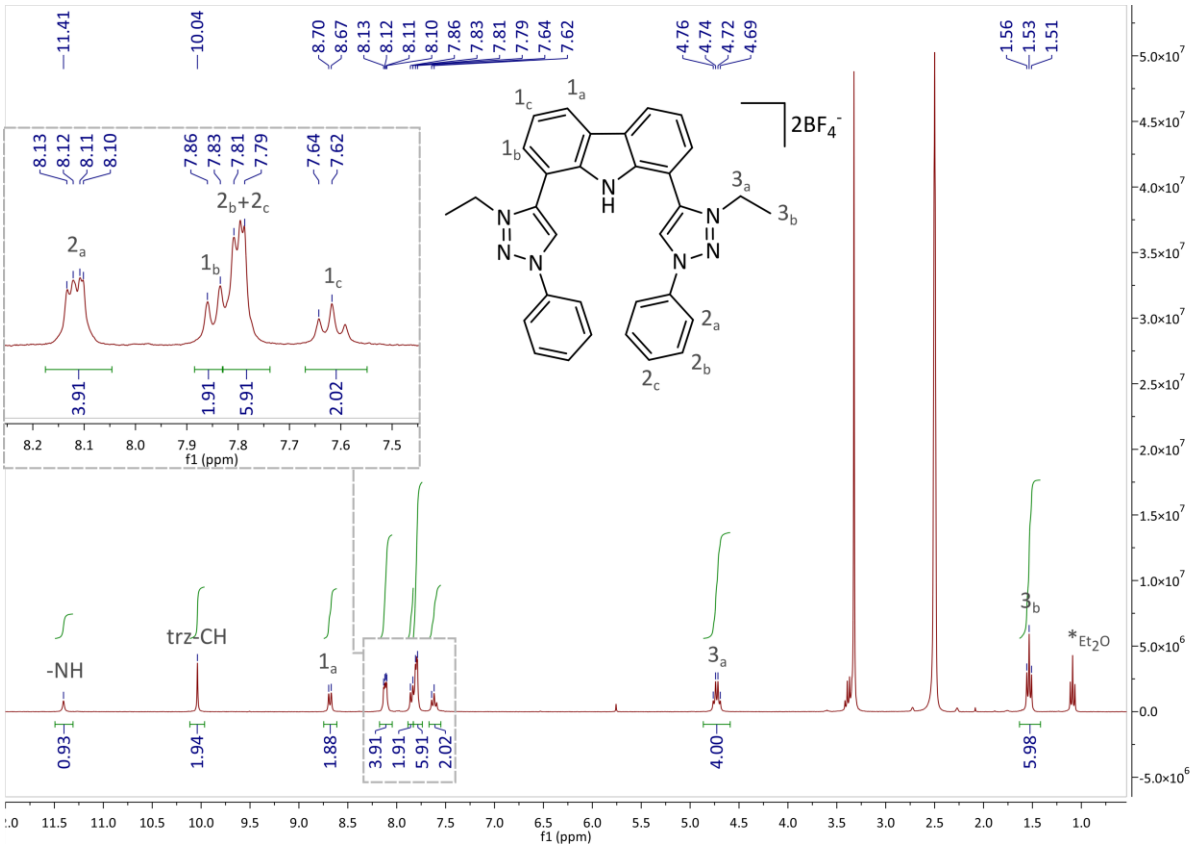


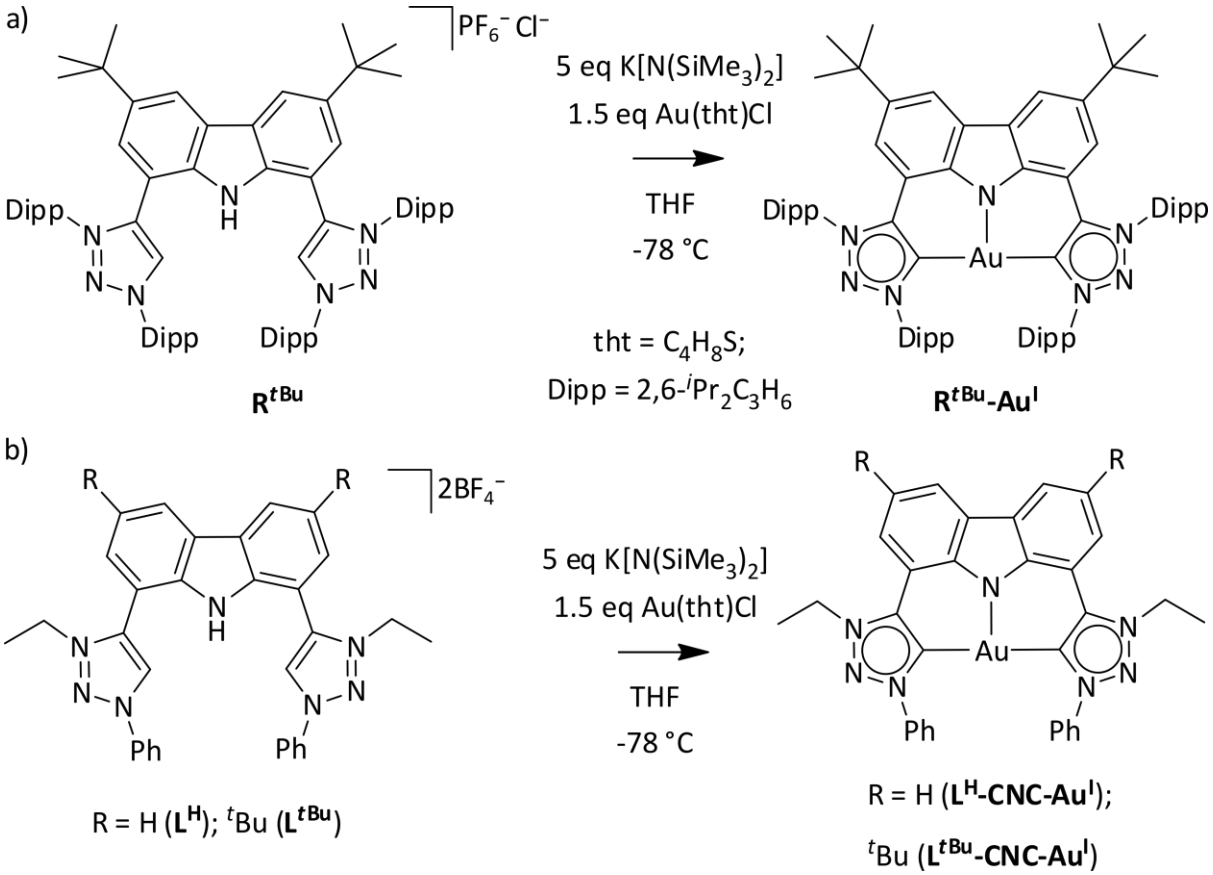
Figure 2.3. ^{1}H NMR spectrum of **L^{H}** in $(CD_3)_2SO$.

2.3.4 Metalation to gold(I) and silver(I)

2.3.4.1 Concerted free-carbene route towards gold(I) metalation

After the two triazolium salts **L^{H}** and **L^{tBu}** were obtained and purified, metalation towards the CNC pincer gold(I) complexes were pursued. Direct metalation of the precursor triazolium salts with a gold(III) metal precursor towards the desired pincer gold(III) complex is feasible but often results in the presence of a tetrachloroaurate(III) ($AuCl_4^-$) counterion..[243] For biological purposes, 'innocent' counterions such as BF_4^- and PF_6^- are preferred to ensure that if the complex should possess any cytotoxicity towards cancer cells, that the activity is due to the complexed metal and not the counterion. Therefore, to avoid the possibility of a metal-containing counterion, the oxidation of the gold(I) complex to gold(III) was proposed and thus metalation of the precursor salts initially involved a gold(I) metal precursor.

Initially, the metalation to Au^{I} was attempted by the in situ deprotonation of both ligand precursor salts $\mathbf{L^{H}}$ and $\mathbf{L^{tBu}}$ with 5 eq $K[N(SiMe_3)_2]$ in the presence of 1.5 eq Au(tht)Cl (tht = tetrahydrothiophene), following the synthetic protocol previously reported for the analogous N1,N3-diarylated ligand, $\mathbf{R^{tBu}\text{-}Au^{I}}$ (Scheme 2.12).[198]



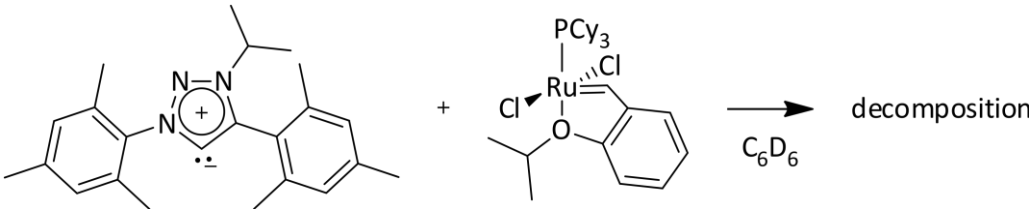
Scheme 2.12. (a) The previously reported synthesis (concerted free carbene route) of the analogous N1,N3-diarylated $\mathbf{R^{tBu}\text{-}Au^{I}}$ complex on which (b) the metalation of the ligand salts, $\mathbf{L^{H}}$ and $\mathbf{L^{tBu}}$ to their expected respective pincer gold(I) complexes are based.[198]

All the solids required for the reaction i.e., the salt, base, and the metal precursor were weighed off in a dried Schlenk reaction vessel inside a glovebox. The Schlenk tube was removed from the glovebox and cooled down to −78 °C under an argon atmosphere. Anhydrous THF was transferred to the reaction vessel via cannula in the dark, resulting in a red-orange solution. After two days, the reaction mixture was a red-brown suspension. The THF was evaporated in vacuo and the reaction residue was washed with hexane to remove tetrahydrothiophene dissociated from the metal precursor. Both extractions with hexane followed by toluene resulted in red-orange solutions which, when the solvent was

evaporated, yielded orange solids. The neutral gold(I) CNC complex is expected to be soluble in non-polar solvents such as toluene and diethyl ether and only marginally soluble in hexane. Unfortunately, in both cases ($\mathbf{L^{H}}$ and $\mathbf{L^{tBu}}$) the desired CNC pincer gold(I) complexes were not isolated. The reaction products obtained from both the hexane and toluene extractions were NMR silent. Further characterization was hampered as these solids quickly converted into oily solids which were insoluble in all solvents, and thus these reaction products could not be identified.

Modifications of the free-carbene metalation route were attempted where the base, $K[N(SiMe_3)_2]$ was replaced by a slightly weaker base, KO^tBu or the gold(III) metal precursor, $[^nBu_4N][AuCl_4]$ was used instead of Au(tht)Cl. Neither of these reactions yielded the desired gold complex and the same NMR silent fractions were obtained.

Bertrand and co-workers reported on the complete decomposition of the N3-alkylated triazolylidene when reacted with a ruthenium-based precursor, even though the free carbene was isolated (Scheme 2.13).[221] They were, however, able to successfully synthesize the ruthenium-triazolylidene complexes by using the more robust N1,N3-diarylated triazolylidenes. Their account along with the results obtained from the attempted metalation of $\mathbf{L^{H}}$ and $\mathbf{L^{tBu}}$ suggest that on rare occasions, the use of the free-carbene metalation route, whether concerted or not, does not always result in the intended metal complex for N3-alkylated triazolium salts.[221]

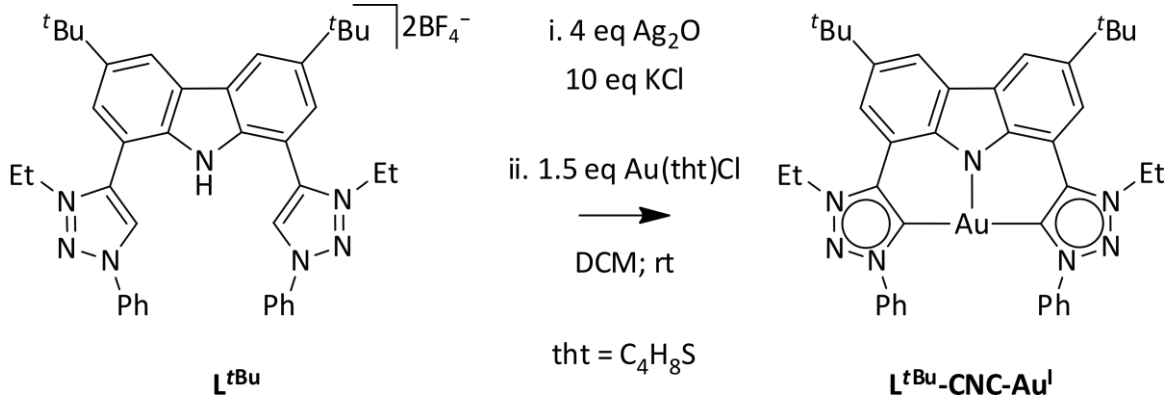


Scheme 2.13. The attempted metalation of an N3-alkylated- 1,2,3-triazolylidene with ruthenium that resulted in complete decomposition.[221]

2.3.4.2 Transmetalation route towards gold(I) complexation

Since the desired CNC gold(I) pincer complexes, $\mathbf{L^{H}/L^{tBu}}$**-CNC-Au^{I}** were not obtained by the concerted free-carbene route, the transmetalation route was considered next. Silver(I) trz complexes are structurally dynamic,[244] rarely isolated due to their instability and transmetalation is possible when the salt is reacted with Ag_2O and the preferred metal precursor under 'one-pot' conditions (Scheme 2.14).[173] For the reaction, the addition of a

halide source such as Cl^- is necessary to stabilize the reaction intermediates when the counterion of the triazolium salt is a weakly- or non-coordinating anion. The theoretical equivalents of Ag_2O needed in the reaction is based on the number of deprotonated acidic triazolium protons (C5-H) required by the ligand, as one equivalent Ag_2O deprotonates two equivalents of C5-H to form water.[220,245] However, based on previous experimental experience, 4 equivalents of Ag_2O to 1 equivalent of ligand is usually required for the successful formation of the silver(I) triazolylidene complex.[197]



Scheme 2.14. The metalation of the ligand salt, $\mathbf{L^{tBu}}$ to the expected pincer gold(I) complex, $\mathbf{L^{tBu}}$**-CNC-Au^{I}**, using the transmetalation route.

The transmetalation reaction was performed on $\mathbf{L^{tBu,}}$ to use as a predictive model for how $\mathbf{L^H}$ would react, since the synthesis of the triazole $\mathbf{K^{tBu}}$ and the subsequent alkylation to $\mathbf{L^{tBu}}$ are overall higher-yielding reactions than $\mathbf{K^H}$ and $\mathbf{L^H}$. The triazolium salt $\mathbf{L^{tBu}}$ along with 4 eq of Ag_2O and excess KCl were added together in a purged dried Schlenk flask. At room temperature, under a nitrogen atmosphere in the dark, anhydrous DCM was added to the reaction vessel. After one week of stirring at room temperature in the dark, the reaction was red-orange in colour. The DCM was filtered via cannula into a clean purged Schlenk tube and 1.5 equivalents of Au(tht)Cl were added. Immediately upon addition of the gold(I) precursor, a white precipitate formed, and the reaction was left to stir overnight. The reaction mixture was filtered, and the filtrate was evaporated in vacuo. After the solid was washed with hexane, a bright yellow solid was obtained.

Analysis of the ^{1}H NMR spectrum of the yellow solid in $CDCl_3$ confirmed the disappearance of the two acidic triazolium- (C5-H) and carbazole (N-H) protons indicative of complex formation. However, each set of resonance was doubled in the ^{1}H NMR spectrum (Figure 2.4) and two carbene carbon atom resonances (δ_C 157.08 and 157.06 ppm) were observed in the ^{13}C {^{1}H}

NMR spectrum at chemical shifts significantly upfield to the expected resonance of δ_C 176 ppm in C_6D_6 for the CNC gold(I) complex previously reported, **R^{tBu}-Au^{I}**.[198]

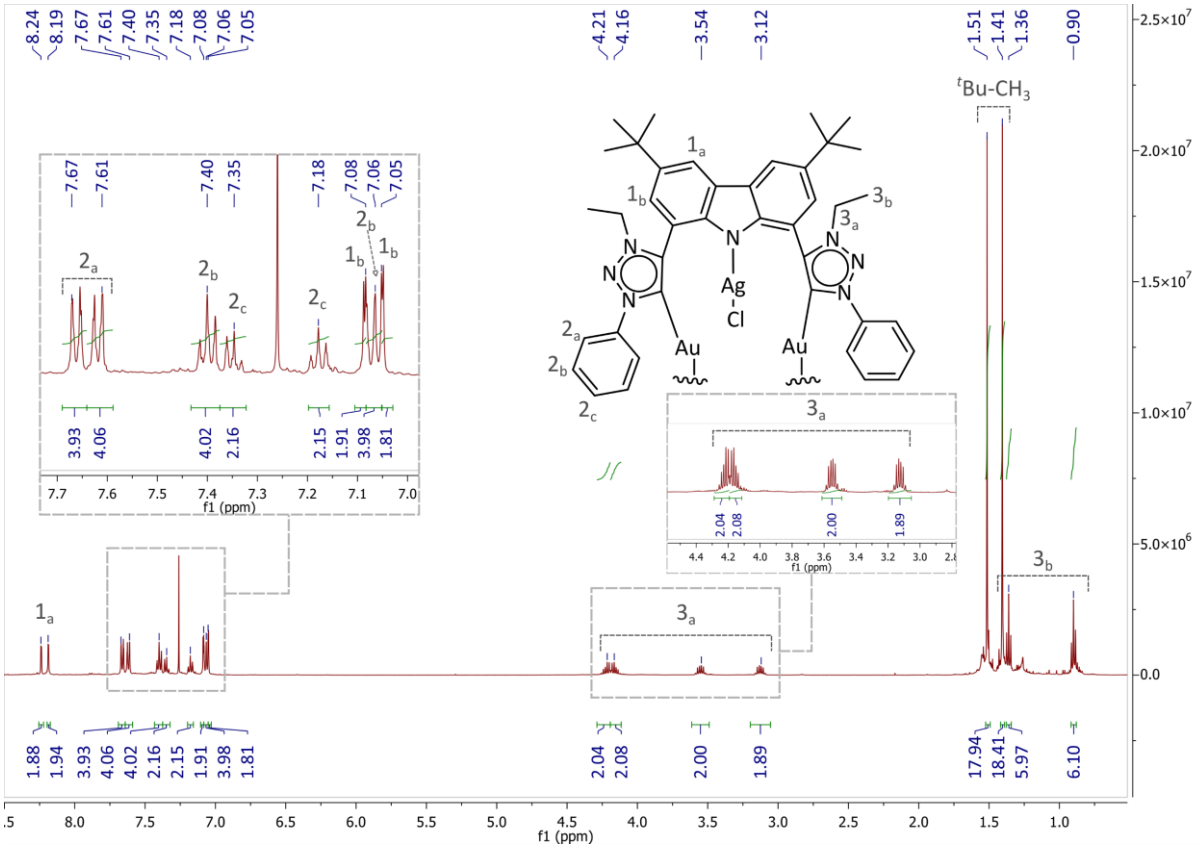


Figure 2.4. The ^{1}H NMR spectrum of **L^{tBu}-*N*-AgCl-Au^{I}** in $CDCl_3$.

It was thought that the yellow solid was a mixture of two complexes and crystals were grown from a concentrated DCM solution layered with pentane. Single crystal X-ray diffraction (SC XRD) studies revealed that the yellow solid was indeed one product, the zwitterionic gold(I) biscarbene complex with silver(I) chloride bound to the nitrogen of the carbazole (Figure 2.5). The crystal structure explained both the ^{1}H and ^{13}C {^{1}H} NMR spectra measured for this complex, **L^{tBu}-*N*-AgCl-Au^{I}**. The average Au–$C_{carbene}$ bond length of 1.965(9) Å is in the range of previously reported N3-alkylated gold(I) bistriazolylidenes with an expected linear $C_{carbene}$–Au–$C_{carbene}$ angle of 176.7(4)°.[246] The distance between the Ag and Au atom is 2.924(11) Å and is considered a short interaction since the sum of the covalent radii of Au and Ag is 2.89 Å. The interaction might explain the slight deviation in the linear geometry of the Au atom.[247]

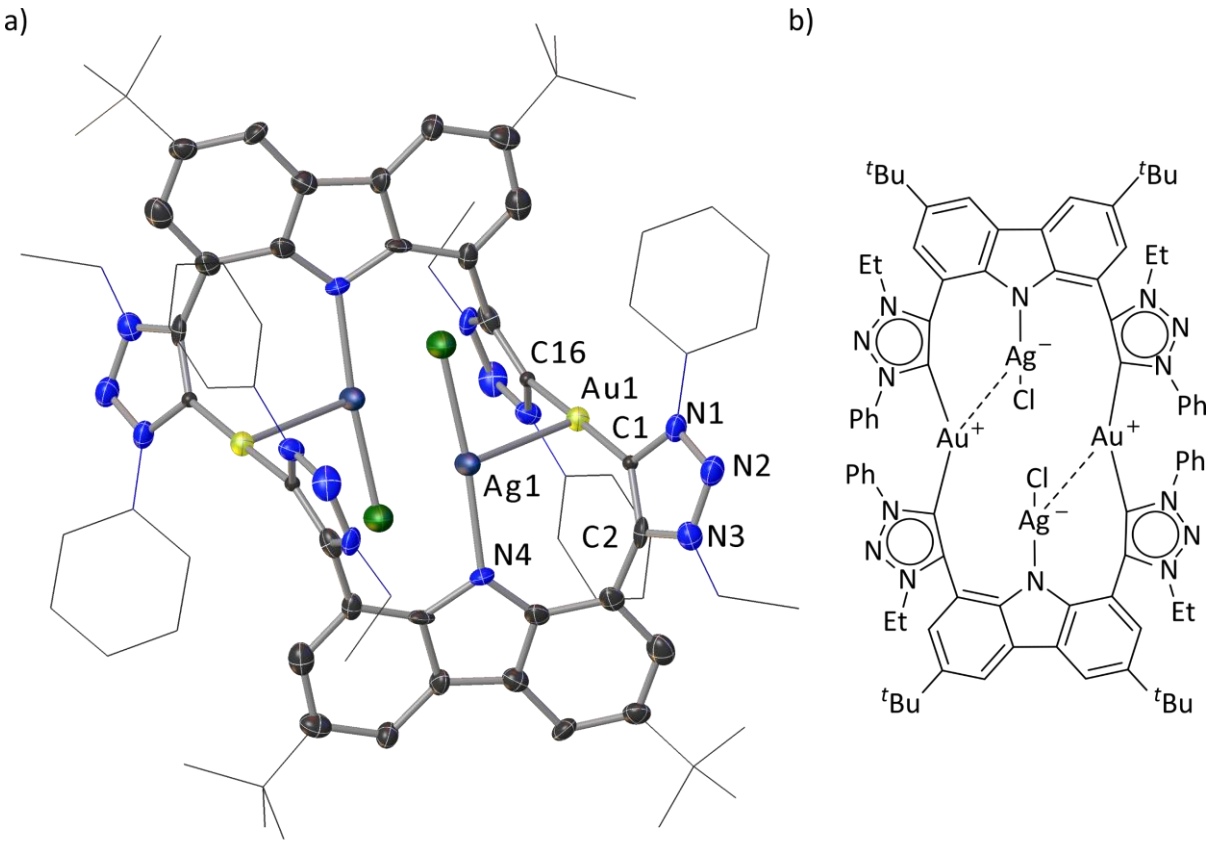


Figure 2.5. (a) Molecular structure **L^{tBu}-*N*-AgCl-Au^{I}**, showing 50% probability ellipsoids and partial atom-numbering scheme.Hydrogens are omitted and the wingtip functionalities are displayed as a wireframe for clarity. Selected bond lengths (Å) and angles (°): Ag1–Au1 2.924 (11), Au1–C1 1.965(9), Au1–C16 1.964(9), Ag1–N4 2.119(9), C1–C2 1.368(14), C2–N3 1.359(13), N2–N3 1.332(13), N1–N2 1.327(12), N1–C1 1.426(13), N1–C1–C2 99.0(9), C1–Au1–C16 176.7(4). (b) Illustrative representation of the molecular structure of **L^{tBu}-*N*-AgCl-Au^{I}**.

The difficulty encountered in assigning the carbene carbon atoms (vs triazole nitrogen atoms) during refinement for the structure shown in Figure 2.5, prompted the submission of another crystal of **L^{tBu}-*N*-AgCl-Au^{I}** for XRD analysis to collect improved data. The second crystal (Figure 2.6) showed the dicationic gold(I) biscarbene complex, but with protonated carbazoles and silver(I) dichloride counterion (**L^{tBu}-Au^{I}**). Attempts to record the NMR spectra of these crystals were futile as the $AgCl_2^-$ counterion drastically reduced the solubility of this complex in NMR solvents. Both mass spectrometry and microanalysis of C, H and N confirmed the eventual formation of **L^{tBu}-Au^{I}** in the solid state.

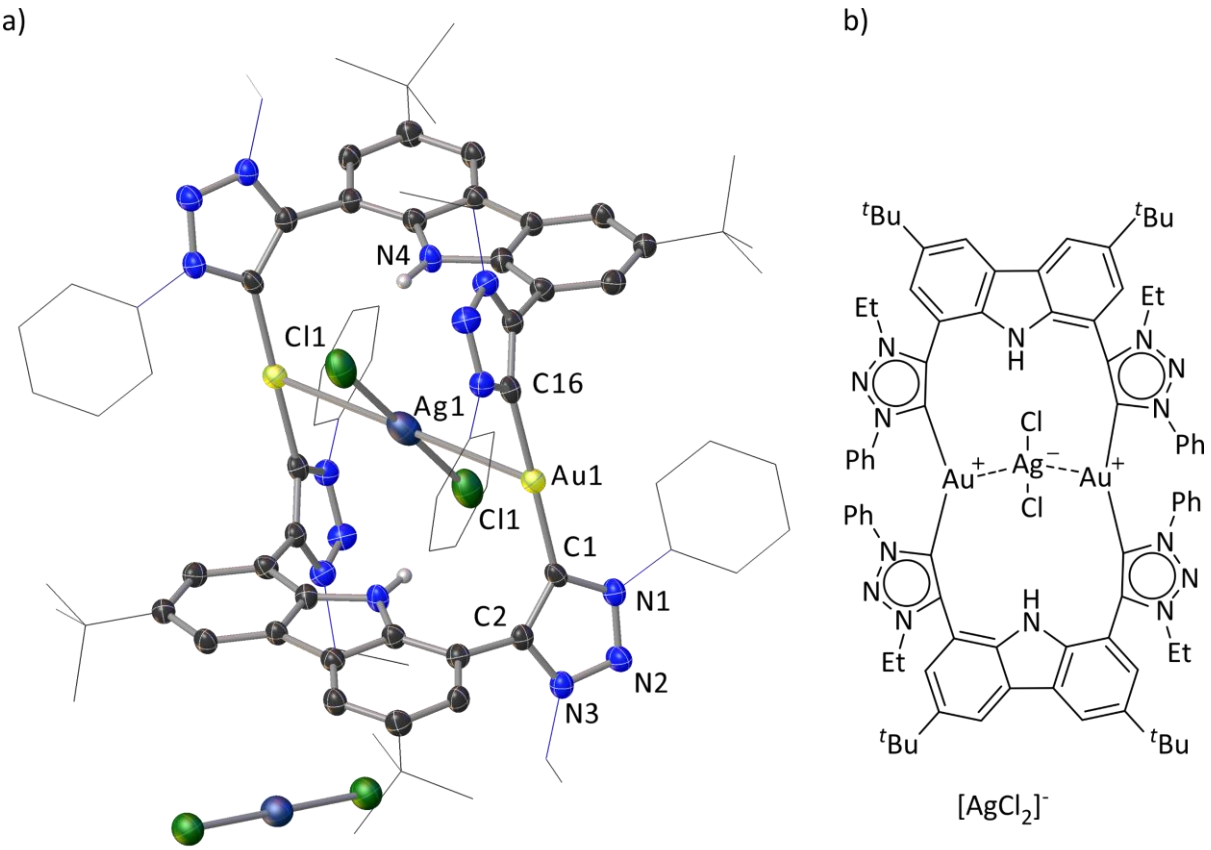
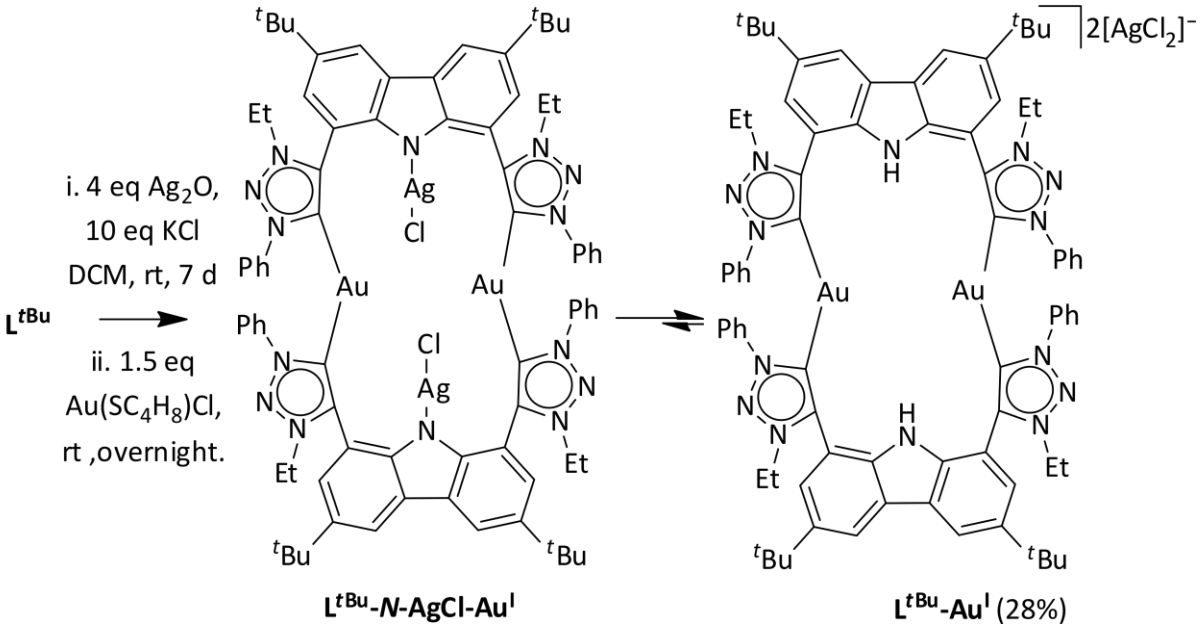


Figure 2.6. (a) Molecular structure of **L^{tBu}-Au^{I}** showing 50% probability ellipsoids and partial atom-numbering scheme. Hydrogens are omitted (except for N4-H) and the wingtip functionalities are displayed as wireframe for clarity. Selected bond lengths (Å) and angles (°): Ag1—Au1 3.2209(19), Au1–C1 2.024(4), Au1–C16 2.019(4), C1–C2 1.383(6), C2–N3 1.364(6), N2–N3 1.314 (5), N1–N2 1.336(5), N1–C1 1.369(5), N1–C1–C2 102.3(4); C1–Au1–C16 176.4(17). (b) Illustrative representation of the molecular structure of **L^{tBu}-Au^{I}**.

Compared to **L^{tBu}-*N*-AgCl-Au^{I}**, the average Au–$C_{carbene}$ bond lengths of **L^{tBu}-Au^{I}** slightly increased to 2.022(4) Å (compared to 1.965(9) Å) but are still in the range of reported gold(I) bistriazolylidenes.[246] Also, there is no significant deviation in the $C_{carbene}$–Au–$C_{carbene}$ bond angle of 176.4(17)° compared to the same bond angle reported for **L^{tBu}-*N*-AgCl-Au^{I}** (176.7(4)°). The average Ag–Au bond lengths between the Au atoms of the carbenes and the Ag atom of the silver(I) dichloride counterion has significantly increased to 3.2209(19) Å compared to the bond lengths of 2.924(11) Å in **L^{tBu}-*N*-AgCl-Au^{I}**. The solid-state structure of **L^{tBu}-Au^{I}** resembles that of a Z-configuration or a chair described by the carbazole-Au-carbazole framework, with the carbazole moieties aligned in the same plane but orientated in opposite directions. For the one $[AgCl_2]^-$ anion that interacts with the Au-atoms, the arrangement of

the Ag-Au-Ag atoms is such that they define a plane perpendicular to that of the carbazole rings.

This reaction was repeated to confirm the reproducibility of both **L^{tBu}-Au^{I}** and **L^{tBu}-*N*-AgCl-Au^{I}** (Scheme 2.15). From the repeat experiments it is seen that the NMR-characterized complex, **L^{tBu}-*N*-AgCl-Au^{I}** slowly converts to the insoluble **L^{tBu}-Au^{I}** complex without the need for solvent and that there is no true equilibrium between the two complexes. Instead, **L^{tBu}-*N*-AgCl-Au^{I}** possibly represents a stable intermediate during the carbene transfer from silver(I) to gold(I) and indicates that the $Ag^{I}—C_{carbene}$ bonds are more labile than the $Ag^{I}—N_{amido}$ bond. The presence of the metal-metal interaction between Ag and Au in **L^{tBu}-*N*-AgCl-Au^{I}** might aid in the stabilization of this intermediate and possibly facilitates the abstraction of the Ag^{I} ion from the carbazole nitrogen to form **L^{tBu}-Au^{I}**.

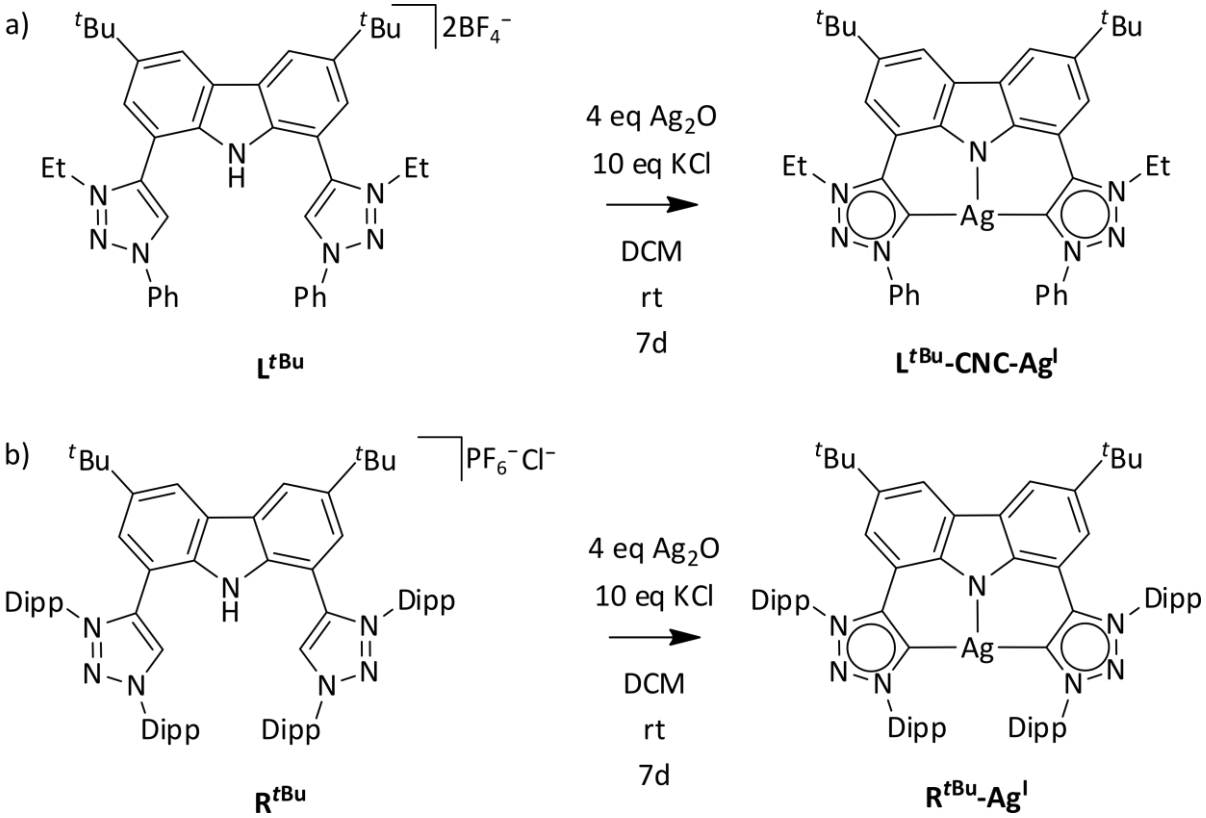


Scheme 2.15. The synthesis of the bis-triazolylidene complexes, **L^{tBu}-*N*-AgCl-Au^{I}** and **L^{tBu}-Au^{I}** via the transmetalation route from the triazolium salt, **L^{tBu}**.

2.3.4.3 Isolation of the silver(I) triazolylidene complexes

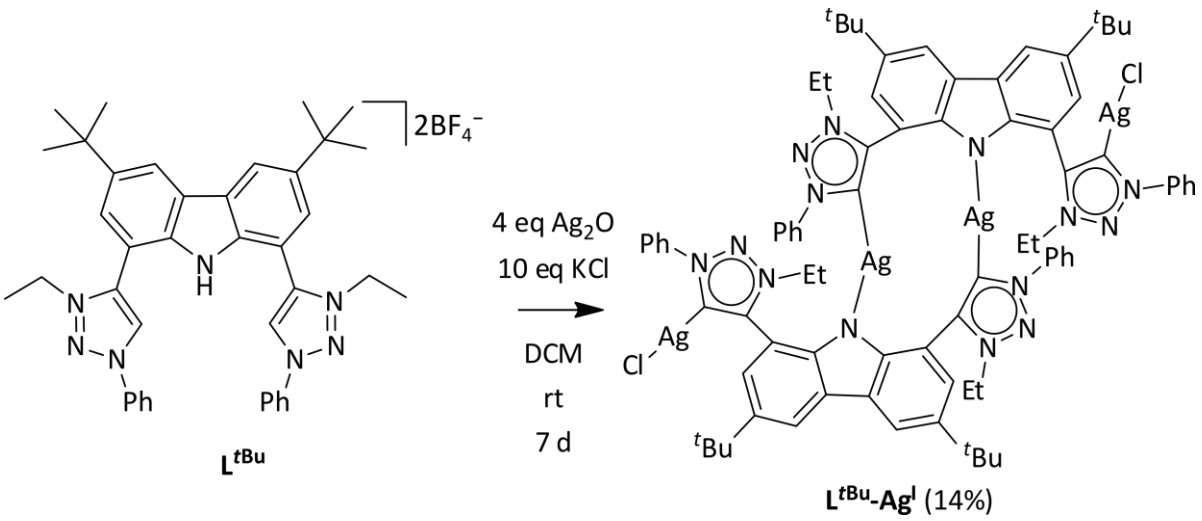
The bound *N*-AgCl in **L^{tBu}-*N*-AgCl-Au^{I}** might indicate the possibility of a pincer silver(I) complex (**L^{tBu}-CNC-Ag^{I}**, Scheme 2.16a) which under transmetalation conditions, forms the biscarbene gold(I) complex, **L^{tBu}-Au^{I}**. As this complex is a result of the transmetalation of a silver(I) complex, **L^{tBu}-Ag^{I}**, that was not isolated, the structure of the latter complex was of interest. To the best of our knowledge, only three examples of T-shaped silver(I) complexes are

known.[201,248,249] One such example is the silver(I) complex **R^{tBu}-Ag^{I}** based on the N1,N3-diarylated ligand analogue of **L^{tBu}** (Scheme 2.16b).



Scheme 2.16. (a) The synthesis of a possible pincer silver(I) triazolylidene complex, **L^{tBu}-CNC-Ag^{I}** from the direct metalation of **L^{tBu}** with silver(I) oxide and potassium chloride based on (b) the synthesis of the previously reported T-shaped silver(I) complex **R^{tBu}-Ag^{I}**.[201]

The triazolium salt **L^{tBu}**, was reacted directly with 4 eq of Ag_2O and 10 eq KCl in DCM at room temperature for 7 days. The reaction mixture was filtered, and the solvent evaporated in vacuo. The silver(I) complex was extracted with DCM and washed with hexane to obtain a yellow powder.



Scheme 2.17. The silver(I) complex isolated from the reaction of **L^{tBu}** and silver(I) oxide with potassium chloride, instead of the desired **L^{tBu}-CNC-Ag^{I}** complex.

From ^{1}H NMR analysis (Figure 2.7), complex formation was confirmed by the disappearance of both the triazolium (C5-H) and carbazole (N-H) proton resonances. The resonance signals are doubled, similar to **L^{tBu}-*N*-AgCl-Au^{I}** and suggest the formation of the biscarbene silver(I) complex analogous in structure to **L^{tBu}-*N*-AgCl-Au^{I}** instead of the desired silver(I) pincer complex (Scheme 2.17). The molecular structure of **L^{tBu}-*N*-AgCl-Au^{I}** is shown in Figure 2.8a.

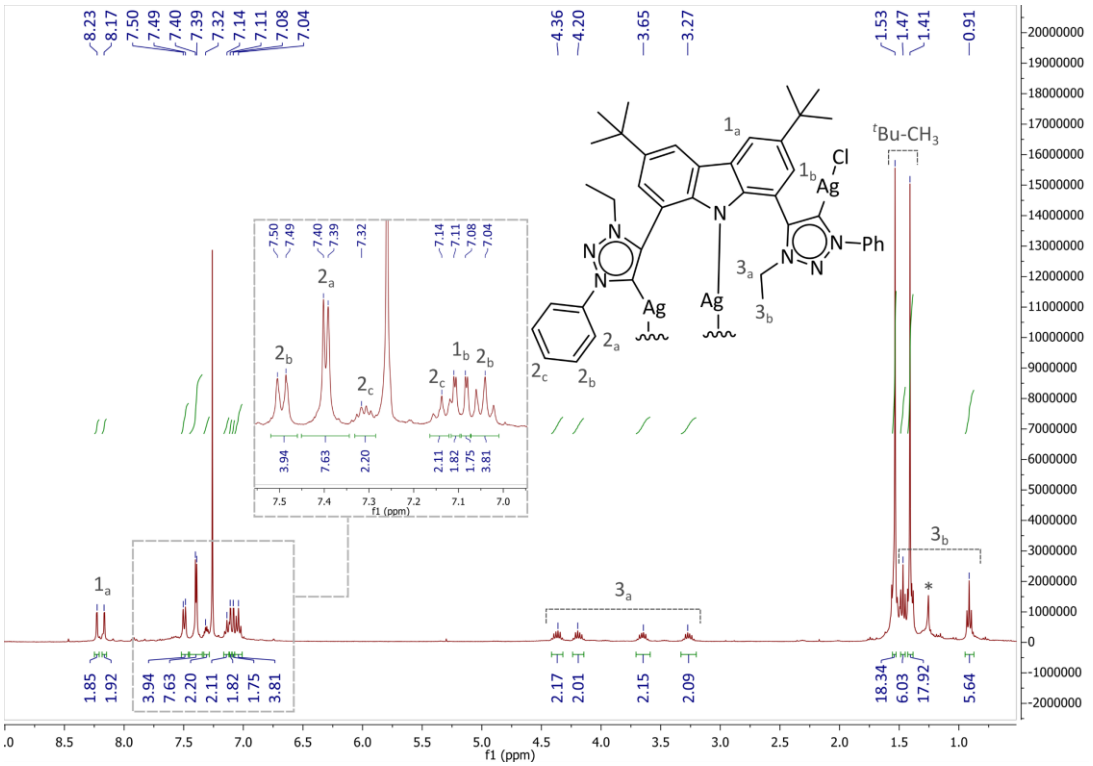


Figure 2.7. The ^{1}H NMR spectrum of **L^{tBu}-Ag^{I}** in $CDCl_3$.

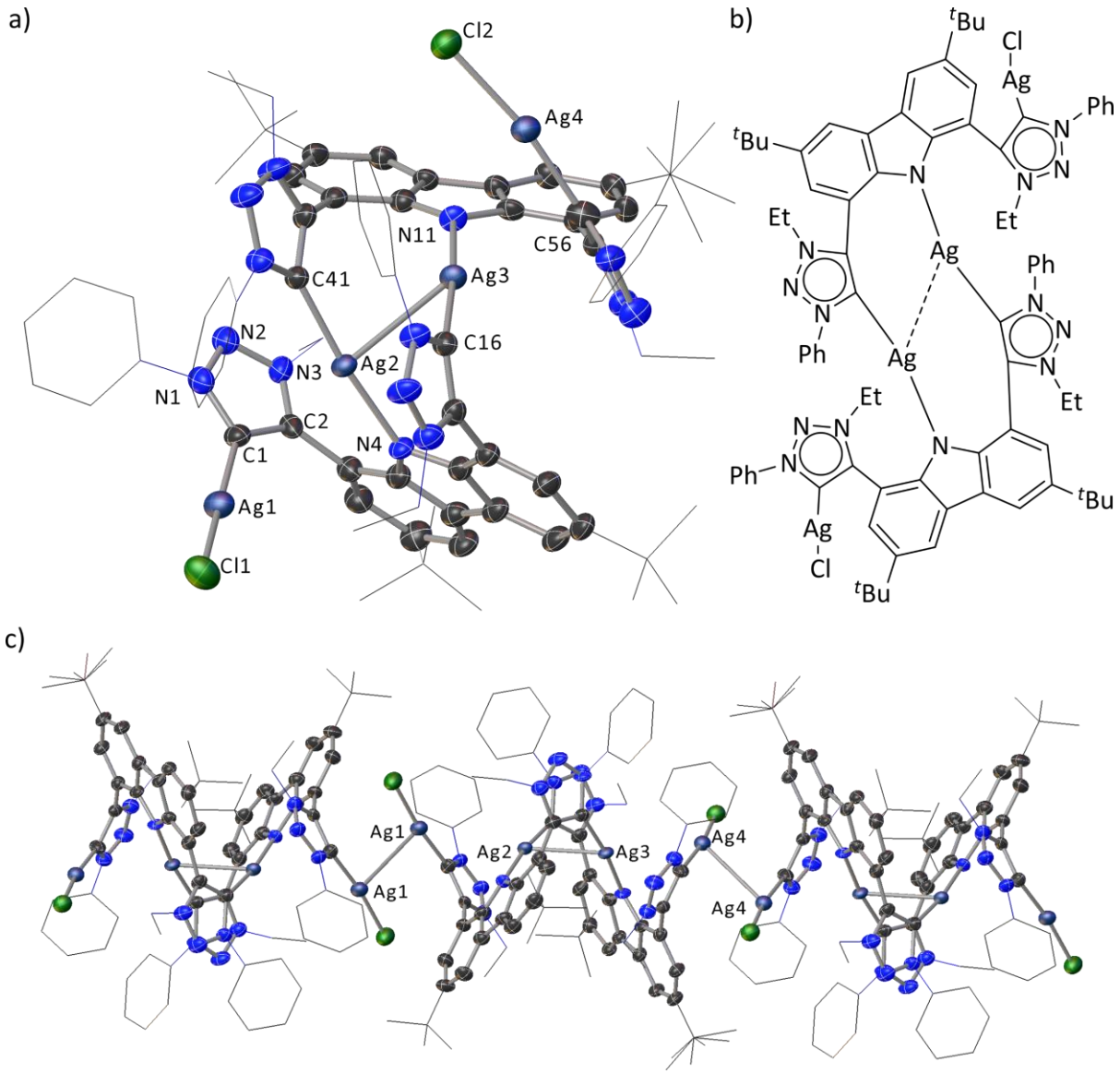
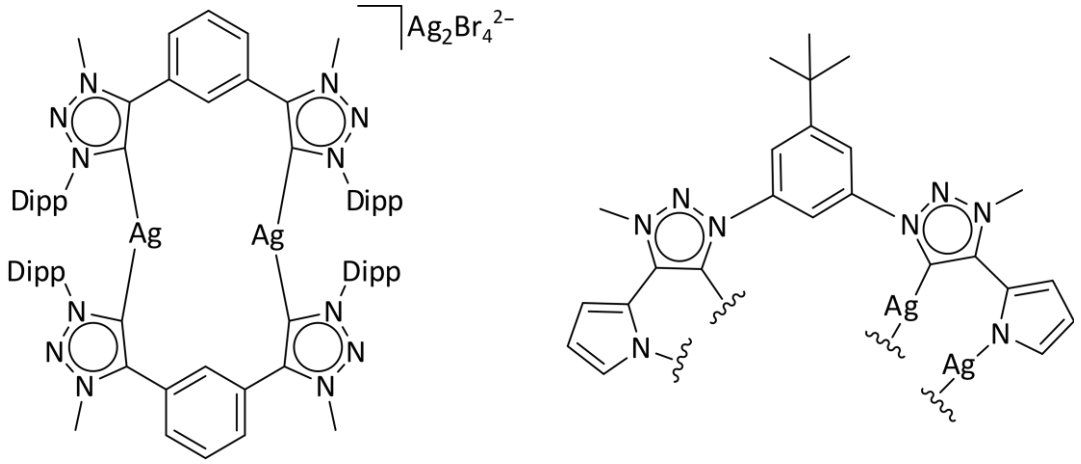


Figure 2.8. (a) Molecular structure of **L^{tBu}-Ag^{I}** showing 50% probability ellipsoids and partial atom-numbering scheme. Hydrogens are omitted and the wingtip functionalities are displayed as wireframe for clarity. Selected bond lengths (Å) and angles (°): Ag1–C1 2.065(7), Ag2–C41 2.061(6), Ag3–C16 2.072(6), Ag4–C56 2.104(8), Ag1–Cl1 2.328(2), Ag2–N4 2.099(5), Ag3–N11 2.100(5), Ag4–Cl2 2.359(19), Ag2–Ag3 2.9382(7), Ag1–Ag1' 3.2811 (12), Ag4–Ag4' 3.2489(11), C1–C2 1.423(9), C2–N3 1.337(9), N2–N3 1.312(8), N1–N2 1.326(8), N1–C1 1.368(9), N1–C1–C2 99.8(6); C1–Ag1–Cl1 173.1(2), N4–Ag2–C41 172.5(2), N11–Ag3–C16 172.3(2), C56–Ag4–Cl2 169.8(2). (b) Illustrative representation of the molecular structure of **L^{tBu}-Ag^{I}** . (c) The polymeric nature of **L^{tBu}-Ag^{I}** due to the metal-metal interactions between the Ag atoms of the triazolylidene Au^{I}-chlorido between neighbouring structures.

SC XRD analysis (Figure 2.8a) revealed that **L^{tBu}-Ag^{I}** is a tetranuclear monocarbene complex where all the Ag^{I} atoms are bound to four triazolylidenes but two silver(I)carbenes have

chlorido ancillary ligands and the other two silver(I)carbenes are bound to the nitrogen of the opposite carbazole (Figure 2.8b). The two carbazole moieties are orientated in the same direction but twisted (by 131.8(6)°) and folded towards one another with a plane fold angle of 45.5(2)°.

There is a slight difference in the length of Ag–$C_{carbene}$ bond in **L^{tBu}-Ag^{I}** whether the ancillary ligand is a Cl-atom (2.085(8) Å) or a N-atom (2.067(6) Å). The average Ag–$C_{carbene}$ bond length of 2.076(8) Å is comparable to N3-alkylated silver(I) bistriazolylidene (2.075(7) Å) reported by Crudden (**35**, Figure 2.9)[250] and an N3-alkylated silver(I) triazolylidene with a pyrrole as ancillary ligand (averaged 2.074 Å), reported by Bielawski and Sessler (**36**, Figure 2.9).[251] The average $C_{carbene}$–Ag–X (where X = Cl or N) deviates from linearity at 171.9(2)° but is comparable to those reported previously as well. The T-shaped silver(I) complex, **R^{tBu}-Ag^{I}** (Scheme 2.16) reported longer average Ag–$C_{carbene}$ bond lengths of 2.0995 Å and a significantly longer Ag–N bond length of 2.2870(11) Å compared to **L^{tBu}-Ag^{I}** (2.099 (5) Å), presumably as a result of the strained T-shape geometry.



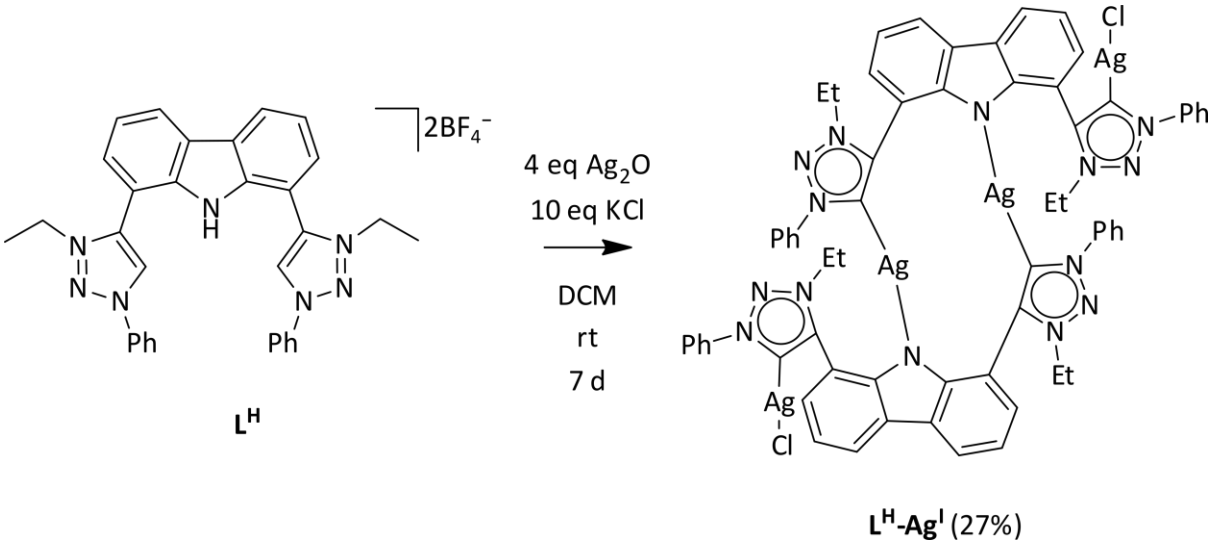
35 Dipp = 2,6-$^{i}Pr_2C_3H_6$ **36**

Figure 2.9. The first two examples of isolated N3-alkylated silver(I) triazolylidenes.[250,251]

Complex **36** (Figure 2.9) has eight silver centers, where each silver is coordinated to a triazolylidene and a nitrogen from the pyrrole moiety, with a ligand to metal ratio of 1:2. The solid-state structure also revealed strong intramolecular Ag–Ag interactions with average bond lengths of 2.843 Å (compared to the van der Waals radii of 3.440 Å for Ag^0),[244] similar to the Ag–Ag interaction reported for **L^{tBu}-Ag^{I}** of 2.9382(7) Å. The metal-metal interactions of **L^{tBu}-Ag^{I}** extend to the Ag-atoms of the neighbouring structures, specifically to the silver(I)-

chlorido moiety resulting in a polymeric structure (Figure 2.8c). Although these intermolecular Ag–Ag interactions are markedly longer (averaged 3.265(12) Å) than the intramolecular Ag–Ag bond length (2.9382(7) Å), they are still considered significant, albeit weaker, as they are shorter than 3.440 Å but longer than the Ag–Ag distance of 2.88 Å in metallic silver.[244] This structure therefore includes supported argentophilic interactions (enabled by linker ligands) as well as unsupported interactions between neighbouring molecules that result in one-dimensional polymers.[252]

The silver complex of $\mathbf{L^H}$ was also synthesized, $\mathbf{L^H\text{-}Ag^I}$, to compare to the structure of $\mathbf{L^{tBu}\text{-}Ag^I}$. As expected, the structure of $\mathbf{L^H\text{-}Ag^I}$ is virtually identical to that of $\mathbf{L^{tBu}\text{-}Ag^I}$ (Scheme 2.18) but more information was obtained in terms of characterization. For instance, for $\mathbf{L^{tBu}\text{-}Ag^I}$, no carbene resonances in the $^{13}C\{^1H\}$ NMR spectrum were observed but the carbene resonances for $\mathbf{L^H\text{-}Ag^I}$ were detected as two sets of doublet of doublets at δ_C 164.5 (J = 239.9, 17.5 Hz) and δ_C 164.4 (J = 240.6, 16.4 Hz) ppm. The carbene chemical shift for $\mathbf{L^H\text{-}Ag^I}$ is slightly upfield compared to **35** of δ_C 172 ppm (Figure 2.9)[250] and the N1,N3-diarylated T-shaped silver(I) complex $\mathbf{R^{tBu}\text{-}Ag^I}$ (δ_C 177.4 ppm (J = 185.3, 13.2 Hz) but compares closely to the reported carbene chemical shift (167.5 ppm) of a ferrocenyl N1,N3-diarylated silver(I) bistriazolylidene.[197]



Scheme 2.18. The synthesis of $\mathbf{L^H\text{-}Ag^I}$ from the direct metalation of $\mathbf{L^H}$ with silver(I) oxide and potassium chloride.

Mass spectrometry of $\mathbf{L^{tBu}\text{-}Ag^I}$ resulted in high fragmentation and only the molecular ion peak $[M+2H]^{2+}$ for the triazolium salt, $\mathbf{L^{tBu}}$, was observed. The $[M+2H]^{2+}$ molecular ion for $\mathbf{L^H\text{-}Ag^I}$ appeared but represented a structure similar to $\mathbf{L^{tBu}\text{-}Au^I}$, the gold(I) bistriazolylidene with

protonated carbazoles and $AgCl_2^-$ counterions. **L^H-Ag^I** is surprisingly unstable compared to **L^{tBu}-Ag^I** as within a few weeks at room temperature, **L^H-Ag^I** decomposed from a light-orange powder to a dark brown oil whereas no significant changes in appearance for **L^{tBu}-Ag^I** was observed over longer periods of time.

Crystals of **L^H-Ag^I** were grown from a concentrated DCM solution layered with toluene and the molecular structure is shown in Figure 2.10. Similar to **L^{tBu}-Ag^I**, also four triazolylidene silver(I) moieties are present whereby two have chlorido as ancillary ligands and the remaining two are coordinated to the nitrogen of the carbazole of the opposite ligand. The two carbazole moieties are orientated in the same direction with a plane angle of 49.5(2)° and twisted (149.9(6)°) in relation with one another. The average Ag–$C_{carbene}$ bond lengths of **L^H-Ag^I** (2.083(5) Å) is similar to that of **L^{tBu}-Ag^I** (2.076(8) Å). The Ag–$C_{carbene}$ bond length where the chlorido is an ancillary ligand is slightly longer (2.090(5) Å) than the Ag–$C_{carbene}$ bond length when the nitrogen is the ancillary ligand (2.075(5) Å). The $C_{carbene}$–Ag–X bond angle is also different: for X = Cl, the bond angle approaches linearity at 177.36(16)° and X = N, the bond angle (172.9(19)°) is more comparable to that observed for **L^{tBu}-Ag^I** (171.9(2)°). Further differences in the metal-metal interaction between the Ag–Ag atoms are also noted. For instance, the Ag1–Ag2 (Ag–Cl vs. Ag–N) bond length of 3.201(6) Å is considerably longer than the Ag2–Ag2 distance (both Ag–N) of 2.872 (8) Å, where in **L^{tBu}-Ag^I** there was no noticeable interaction between the Ag1 and Ag2 atoms, but rather to the neighbouring Ag-atom of the $C_{carbene}$–Ag–Cl (Ag1–Ag1 interaction). Metal-metal interaction between neighbouring structures are not observed for **L^H-Ag^I .**

2.3.5 Variation in wingtip functionality

The presence of a bulkier substituent on the N1 of the triazole might enforce pincer complex formation and therefore a new set of ligands were synthesized (Scheme 2.19) where the phenyl groups of **L^H** and **L^{tBu}** were replaced with the bulky aromatic 2,6-diisopropylphenyl group (Dipp). The triazole, **K^{tBu}_{dipp}** was synthesized similarly to the phenyl analogue, **L^{tBu}_{dipp}** as well as the subsequent alkylation to the triazolium salt, **L^{tBu}_{dipp}**. Unfortunately, all attempted metalation reactions with **L^{tBu}_{dipp}** were unsuccessful. Both metalation routes, i.e. the concerted free-carbene and transmetalation yielded NMR silent compounds and red-orange crystals that did not diffract.

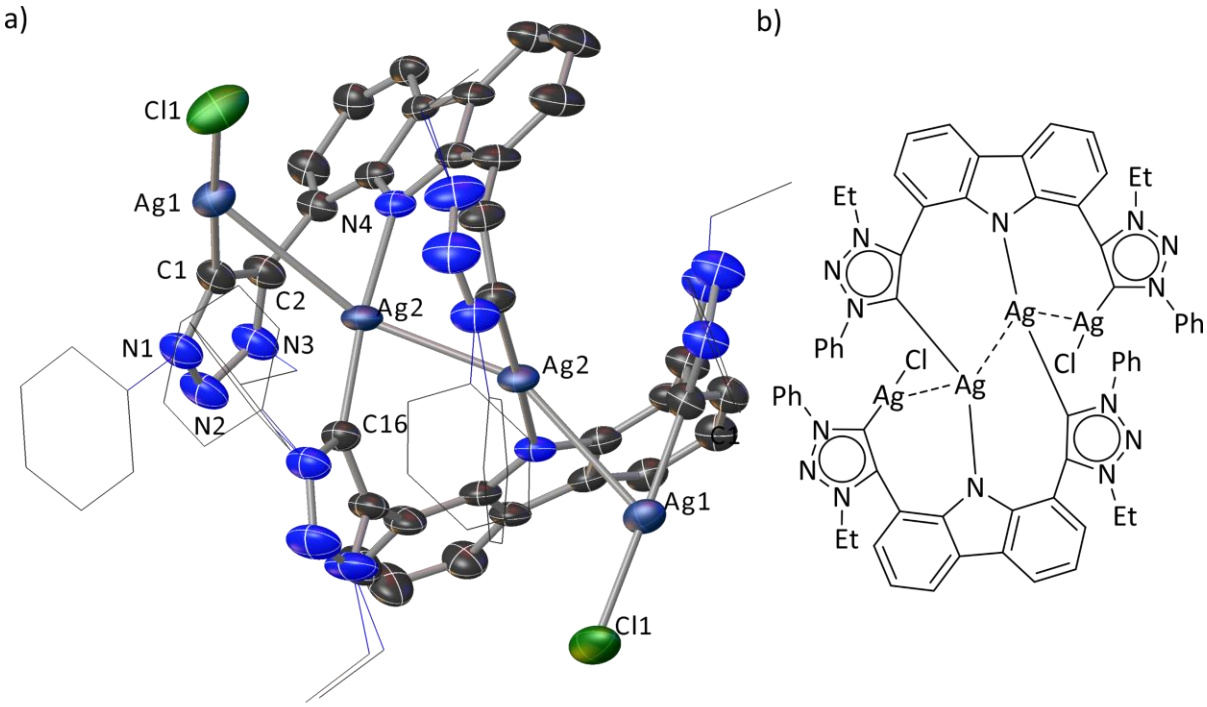


Figure 2.10. (a) Molecular structure of the **L^{H}-Ag^{I}** showing 50% probability ellipsoids and partial atom-numbering scheme. Hydrogens are omitted and the wingtip functionalities are displayed as wireframe for clarity. Selected bond lengths (Å) and angles (°): Ag1–Ag2 3.201(6), Ag2–Ag2' 2.872(8), Ag1–C1 2.090(5), Ag1–Cl1 2.337(18), Ag2–C16 2.075(5), Ag2–N4 2.099(4), C1–C2 1.391(7), C2–N3 1.371(7), N2–N3 1.318(6), N1–N2 1.323(7), N1–C1 1.378(7), N1–C1–C2 102.1(4); C1–Ag1–Cl1 177.36(16), N4–Ag2–C16 172.93(19). (b) Illustrative representation of the molecular structure of **L^{H}-Ag^{I}** .

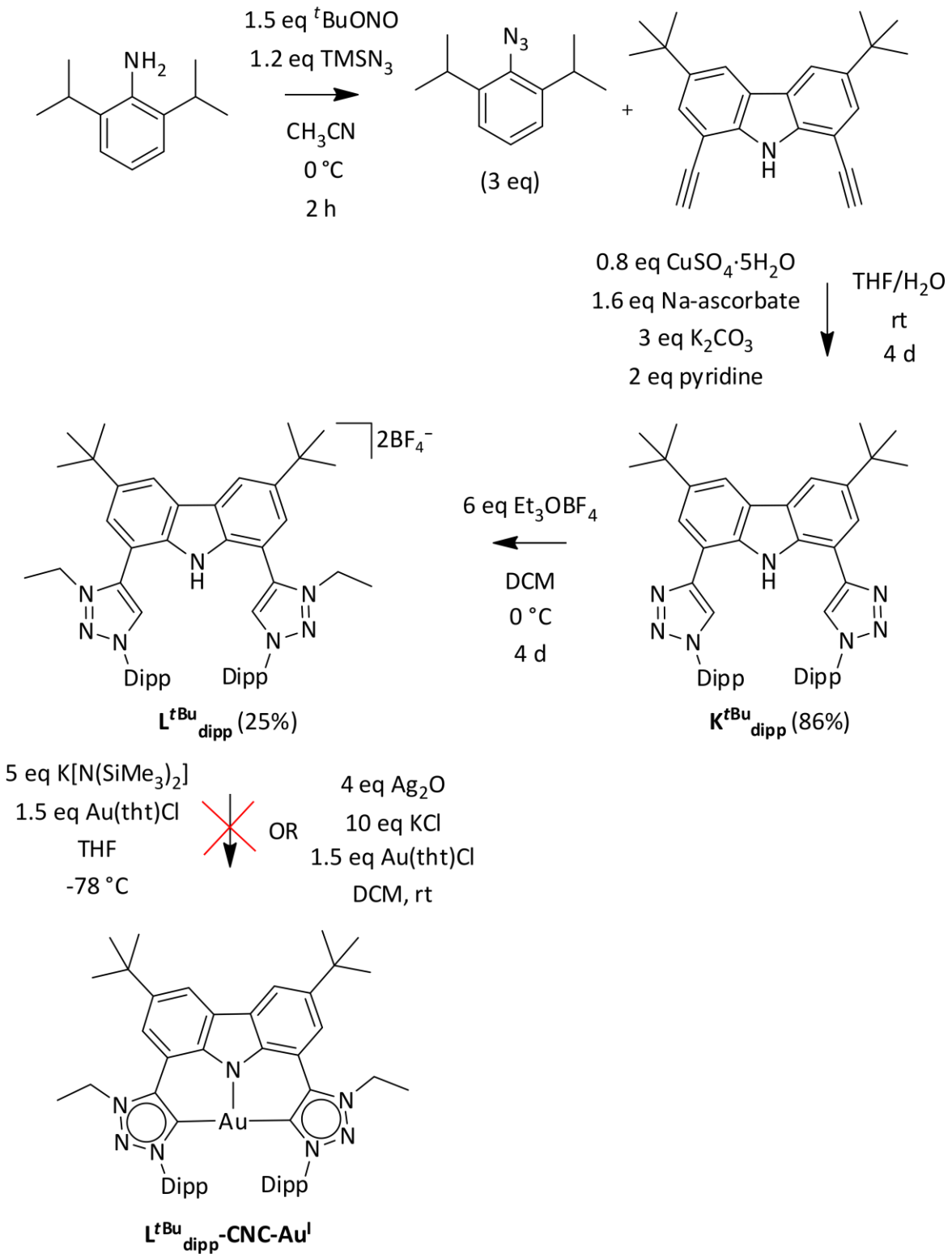
2.4 Conclusion

The synthesis of two triazolium salts **L^{H}** and **L^{tBu}** from 9*H*-carbazole are described. *tert*-Butyl functionalities were used to protect the most reactive positions of 9*H*-carbazole to functionalize the 1 and 8 positions with 1,4-substitued 1,2,3-triazole rings, resulting in two triazoles, **K^{H}** and **K^{tBu}**. The subsequent N3-alkylation yielded the 1,3,4-trisubstituted-1,2,3-triazolium tetrafluoroborate salts **L^{H}** and **L^{tBu}**, as suitable CNC precursors for the targeted pincer gold(III) complexes.

Two different metalation routes for the triazolium salts **L^{H}** and **L^{tBu}** were employed to obtain the pincer gold(I) complex. Unfortunately, the in situ deprotonation route did not succeed and the transmetalation route resulted in multinuclear metal complexes. The lack of solubility of **L^{tBu}-Au^{I}** and the lack of stability of the least sterically hindered complex, **L^{H}-Ag^{I}** will undeniably hinder further investigation of these complexes in biological media.

The successful synthesis of CNC pincer gold(I) complexes **(R^{tBu}-Au^{I}**, Scheme 2.12a), analogous to the **L^{tBu}**, have been described.[198] The **R^{tBu}** ligand scaffold had Dipp groups as both N1 and N3 substituents indicating that steric bulk might play a pivotal role in the formation of a pincer type complex. Therefore, the N1-wingtip (phenyl) of **L^{tBu}** was substituted by the bulky Dipp groups but did not yield the desired gold(I) pincer complex either. In fact, no results were obtained from the metalation reactions of **L^{tBu}_{dipp}**.

The quest for the CNC gold(III) pincer complex continues. In order to obtain the complex to evaluate its potential as an anticancer agent and investigate DNA binding ability, sterically hindered Dipp groups are seemingly necessary on both the N1 and N3 wingtips of the triazolium ring to enforce the formation of a 'pinced' complex.



Scheme 2.19. The attempted synthesis of the pincer gold(I) complex, **L^{tBu}_{dipp}-Au^{I}** by substituting the N1-wingtips of the triazole ring with bulky 2,6-diisopropylphenyl groups. The metalation of **L^{tBu}_{dipp}** was unsuccessful regardless of the metalation route employed.

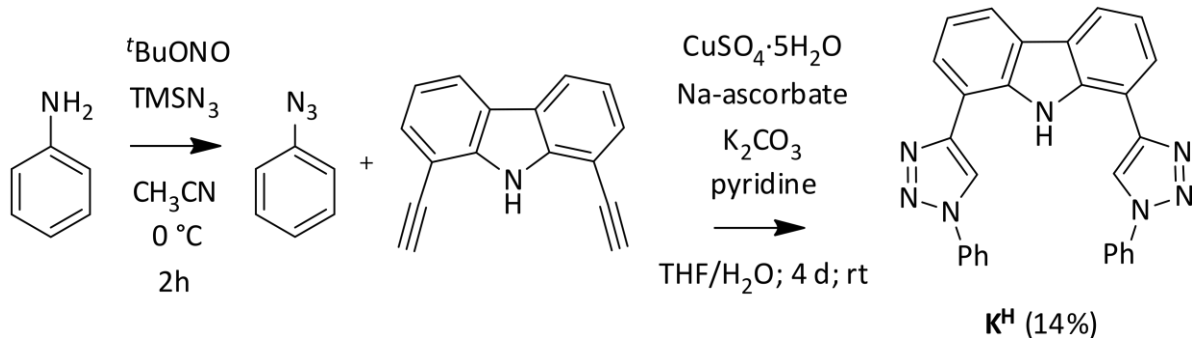
2.5 Experimental

2.5.1 General

The carbazole precursors 3,6-di(*tert*-butyl)-9*H*-carbazole,[253] 3,6-di(*tert*-butyl)-1,8-dibromo-9*H*-carbazole,[254] 3,6-di(*tert*-butyl)-1,8-bis[(trimethylsilyl)ethynyl]-9*H*-carbazole,[226] 3,6-di(*tert*-butyl)-1,8-bisethynyl-9*H*-carbazole,[226] 1,8-dibromo-9*H*-carbazole,[233] 1,8-bis[(trimethylsilyl)ethynyl]-9*H*-carbazole,[226] and 1,8-diethynyl-9*H*-carbazole[226] were all synthesized according to their literature procedures, as well as the metal precursor, chloro(tetrahydrothiophene)gold(I)[255] and Meerwein's salt, triethyloxonium tetrafluoroborate.[256] All other reagents were commercially available and used without any purification.

2.5.2 Synthesis of triazoles K^H, K^{tBu}, K^{tBu}_{dipp} and K^H_{dipp}

2.5.2.1 Synthesis and characterization of *1,8-bis-(3-phenyl-1,2,3-triazole)-9H-carbazole* (K^H)



K^H (14%)

To a solution of aniline (2.7 g, 29 mmol) in 20 mL CH_3CN at −20°C, was added dropwise *tert*-butyl nitrite (4.3 g, 42 mmol) and then trimethylsilyl azide (3.8 g, 33 mmol). After the reaction was stirred for 2 hours at room temperature, 1,8-diethynyl-9*H*-carbazole (1.0 g, 4.7 mmol) dissolved in 20 mL THF was added to the reaction mixture followed by potassium carbonate (1.9 g, 14 mmol), pyridine (0.74 g, 9.3 mmol), 20 mL aqueous copper(II)sulfate pentahydrate (0.93 g, 3.7 mmol) solution and 20 mL aqueous sodium ascorbate (1.5 g, 7.4 mmol) solution. The reaction continued for 4 days and was quenched with 0.1 M EDTA/NH_4OH. The suspension was filtered and the solid dissolved in DCM. The organic phase was extracted with DCM, dried over magnesium sulfate and concentrated in vacuo to a dark red oil, which was further purified by flash chromatography (silica gel 60, eluted with DCM), evaporated and stirred overnight in diethyl ether and filtered, affording a bright yellow solid. Yield: 0.3 g (14%). M.p. 260 °C (decomp.). ^{1}H NMR (300 MHz, $(CD_3)_2SO$) δ 12.32 (s, 1H, NH), 9.63 (s, 2H,

trz-CH), 8.28 (d, *J* = 7.6 Hz, 2H, Ar-$CH_{carbazole}$, H-1_a), 8.10 (d, *J* = 7.5 Hz, 4H, Ar-CH_{Ph}, H-2_a), 8.02 (d, *J* = 7.5 Hz, 2H, Ar-$CH_{carbazole}$, H-1_b), 7.70 (dd, *J* = 7.8, 7.8 Hz, 4H, Ar-CH_{Ph}, H-2_b), 7.57 (t, *J* = 7.4 Hz, 2H, Ar-CH_{Ph}, H-2_c), 7.40 (dd, *J* = 7.6, 7.6 Hz, 2H, Ar-$CH_{carbazole}$, H-1_c). ^{13}C {^1H} NMR (75 MHz, $(CD_3)_2SO$) δ 147.1, 136.7, 136.0 (all Ar-C_q), 130.0 (Ar-CH_{Ph}, C-2_b), 129.0 (Ar-CH_{Ph}, C-2_c), 123.4 (Ar-C_q), 123.1 (Ar-$CH_{carbazole}$, C-1_b), 120.5 (Ar-$CH_{carbazole}$, C-1_a), 120.2 (Ar-CH_{Ph}, C-2_a), 119.8 (trz-CH), 119.6 (Ar-$CH_{carbazole}$, C-1_c), 113.0 (Ar-C_q). Anal. Calcd for $C_{28}H_{19}N_7$ (+ 0.3 eq DMSO): C 72.02, H 4.40, N 20.56. Found: C 72.37, H 4.53, N 20.47. ESI-HRMS (15 V, positive mode, m/z): calcd for $[M+H]^+$: 453.1780. Found: 453.1782.

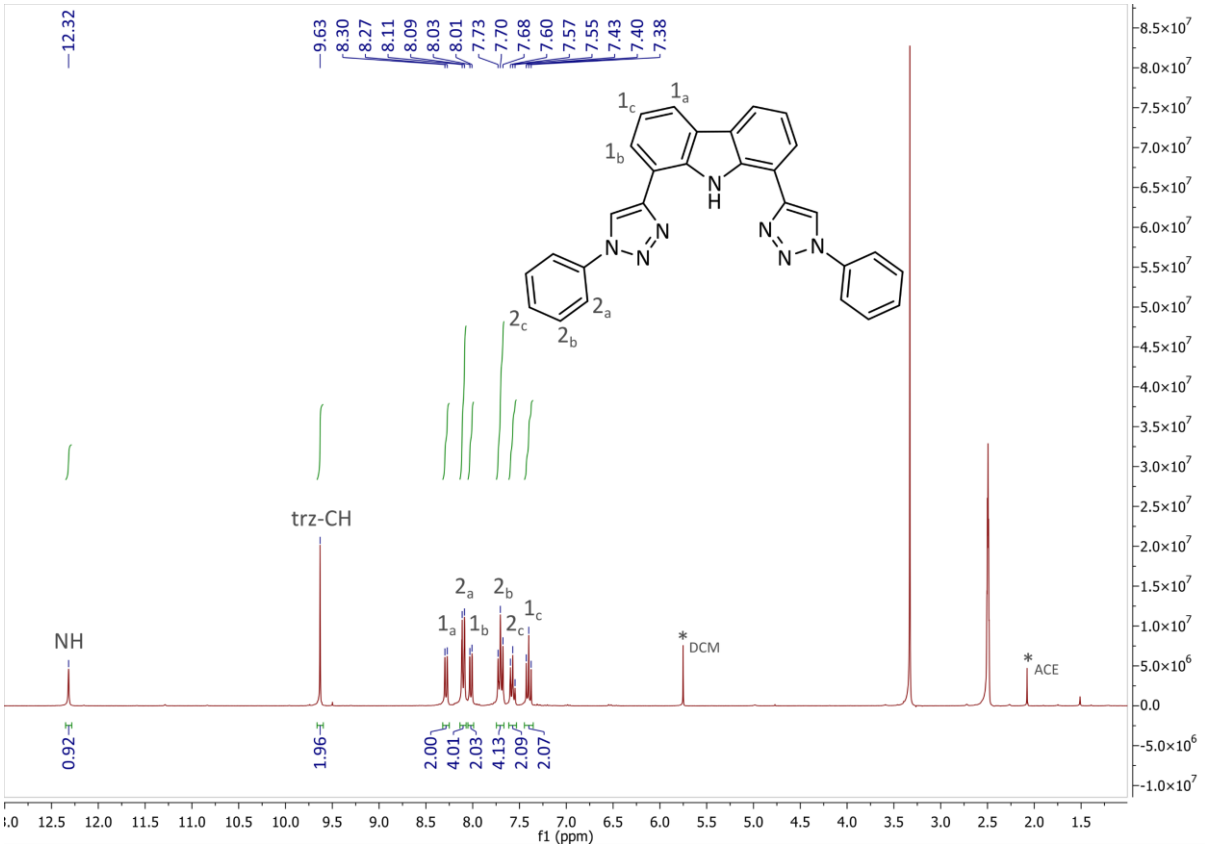


Figure 2.11. ^1H NMR spectrum of $\mathbf{K^H}$ in $(CD_3)_2SO$.

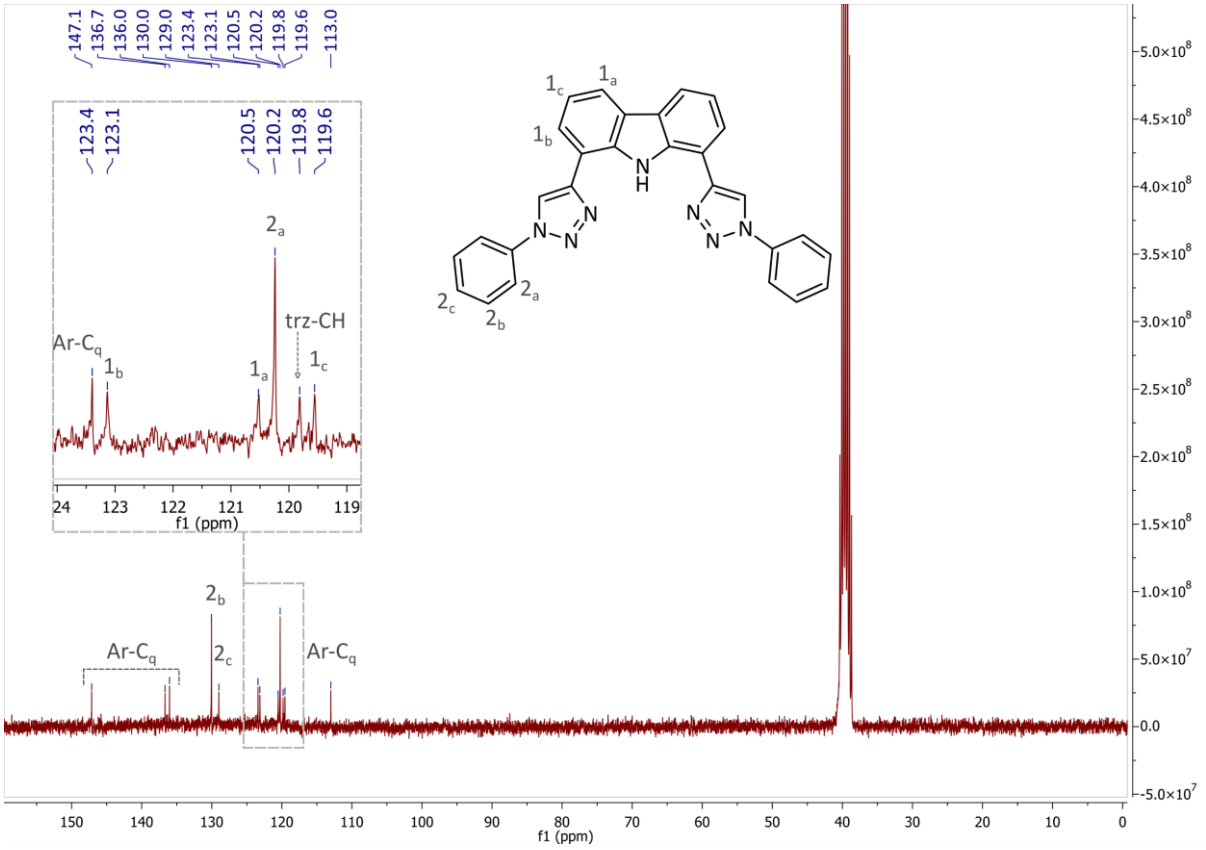
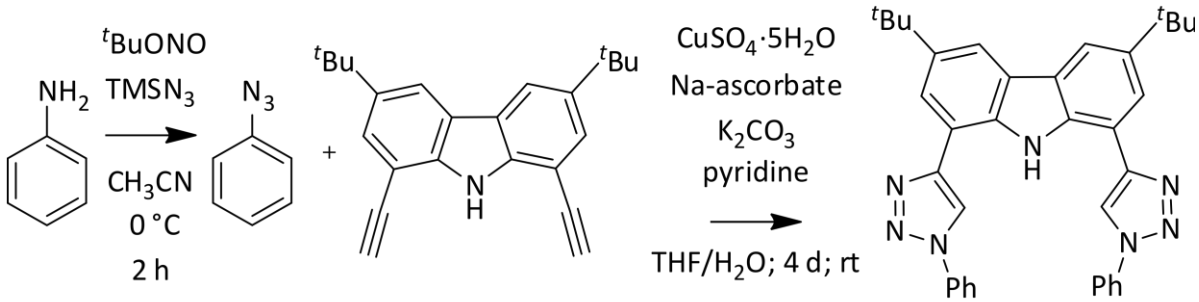


Figure 2.12. The ^{13}C {^{1}H} NMR spectrum of $\mathbf{K^{H}}$ in $(CD_3)_2SO$.

2.5.2.2 Synthesis and characterization of *3,6-di(tert-butyl)-1,8-bis-(3-phenyl-1,2,3-triazole)-9H-carbazole* ($\mathbf{K^{tBu}}$)



$\mathbf{K^{tBu}}$ (50%)

To a solution of aniline (1.7 g, 18 mmol) in 20 mL CH_3CN at -20°C, was added dropwise *tert*-butyl nitrite (2.8 g, 27 mmol) followed by trimethylsilyl azide (2.5 g, 22 mmol). After the reaction was stirred for 2 hours at room temperature, 3,6-di(*tert*-butyl)-1,8-diethynyl-9*H*-carbazole (1.0 g, 3.1 mmol) dissolved in 20 mL THF was added, followed by potassium carbonate (1.3 g, 9.1 mmol), pyridine (0.48 g, 6.1 mmol), 20 mL aqueous copper(II) sulfate pentahydrate (0.61 g, 2.4 mmol) solution and 20 mL aqueous sodium ascorbate (0.97 g, 4.9 mmol) solution. The reaction proceeded for 4 days and was quenched with 0.1 M

EDTA/NH_4OH. The organic phase was extracted with DCM, dried over magnesium sulfate, and concentrated to a dark red oil, which was further purified by flash chromatography (eluted with DCM). The solvent was evaporated and the oily solid was stirred overnight in diethyl ether and filtered, affording a bright yellow solid. Crystals suitable for XRD analysis were grown from the NMR sample in $CDCl_3$. Yield: 0.85 g (50%). ^{1}H NMR (300 MHz, $CDCl_3$) δ 11.89 (s, 1H, NH), 8.48 (s, 2H, trz-CH), 8.19 (d, *J* = 0.9 Hz, 2H, Ar-$CH_{carbazole}$, H-1_a), 7.92 (d, *J* = 7.7 Hz, 4H, Ar-CH_{Ph}, H-2_a), 7.83 (d, *J* = 1.5 Hz, 2H, Ar-$CH_{carbazole}$, H-1_b), 7.58 (dd, *J* = 7.7, 7.7 Hz, 4H, Ar-CH_{Ph}, H-2_b), 7.49 (t, *J* = 7.3 Hz, 2H, Ar-CH_{Ph}, H-2_c), 1.54 (s, 18H, ^{t}Bu-CH_3). ^{13}C {^{1}H} NMR (75 MHz, $CDCl_3$) δ 148.4, 142.1, 137.4, 136.1 (all Ar-C_q), 129.9 (Ar-CH_{Ph}, C-2_b), 128.9 (Ar-CH_{Ph}, C-2_c), 124.2 (Ar-C_q), 120.8 (Ar-CH_{Ph}, C-2_a), 120.6 (Ar-$CH_{carbazole}$, C-1_b), 117.4 (trz-CH), 116.9 (Ar-$CH_{carbazole}$, C-1_a), 112.6 (Ar-C_q), 34.9 (^{t}Bu-C_q), 32.3 (^{t}Bu-CH_3). Anal. Calcd for $C_{36}H_{35}N_7$: C 76.43, H 6.24, N 17.33. Found: C 76.81, H 6.25, N 17.69. ESI-HRMS (15 V, positive mode, m/z): calcd for $[M+H]^+$: 566.3027. Found: 566.3016.

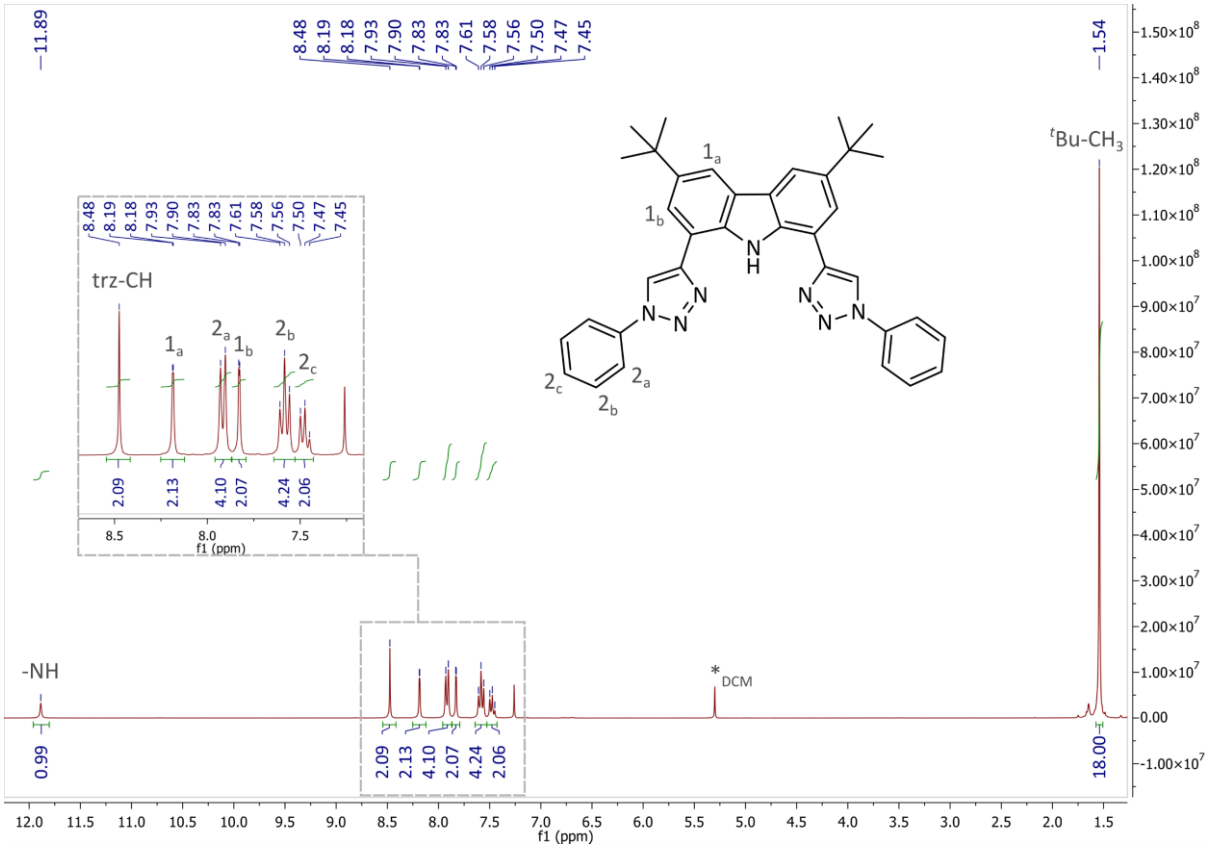


Figure 2.13. ^{1}H NMR spectrum of **K^{tBu}** in $CDCl_3$.

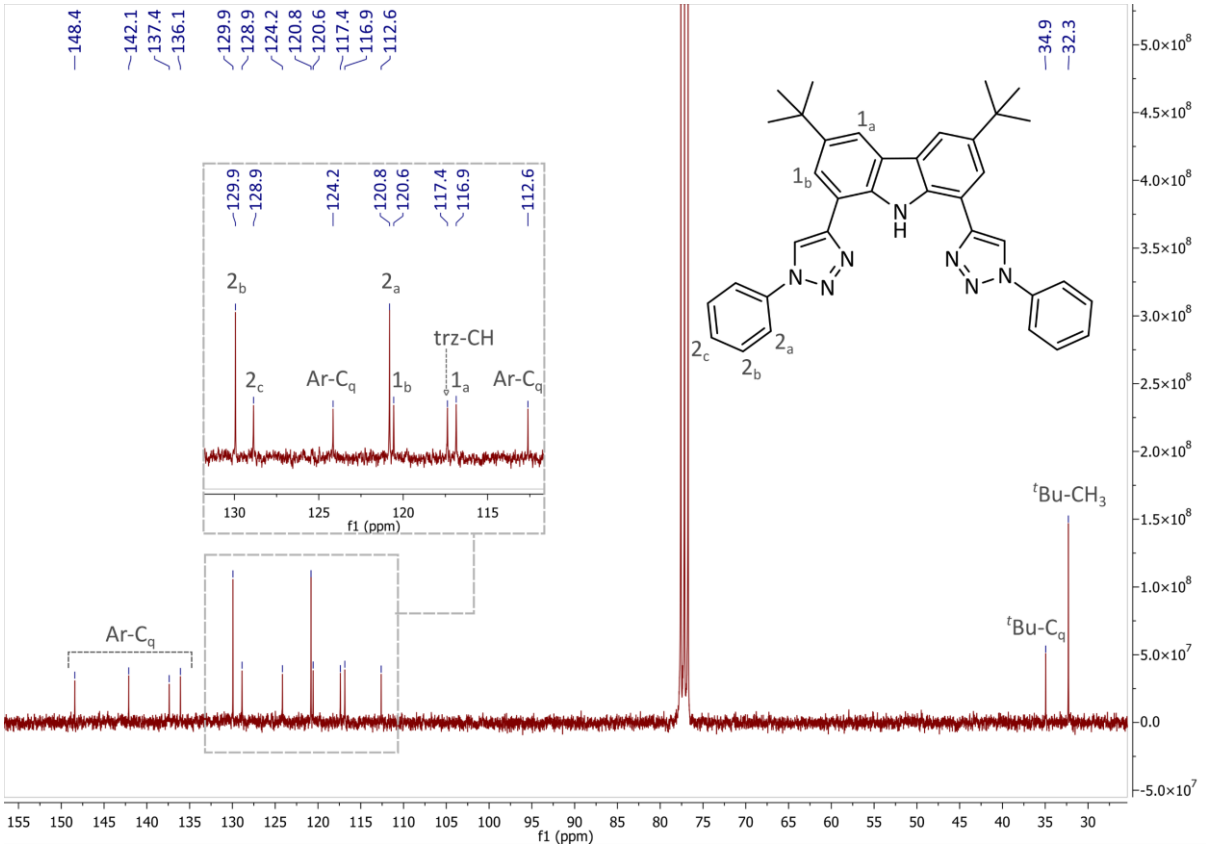
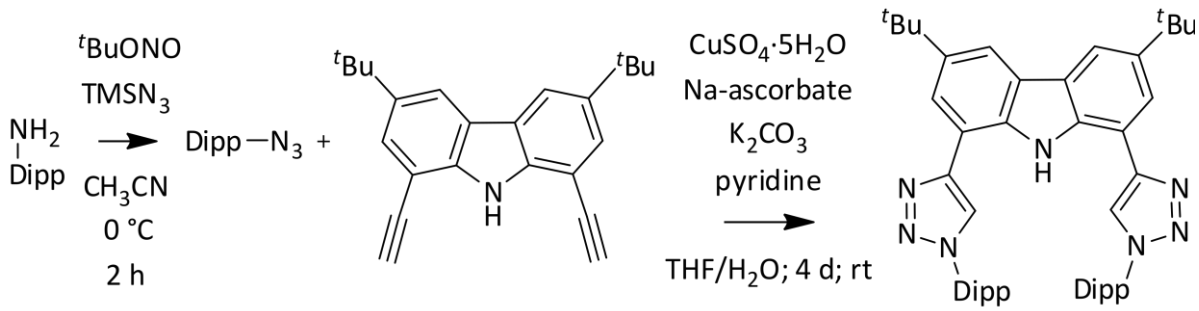


Figure 2.14. The ^{13}C {^{1}H} NMR spectrum of $\mathbf{K^{tBu}}$ in $CDCl_3$.

2.5.2.3 Synthesis and characterization of *3,6-di(tert-butyl)-1,8-bis-(3-diisopropylphenyl-1,2,3-triazole)-9H-carbazole* ($\mathbf{K^{tBu}_{dipp}}$)



Dipp = 2,6-$^{i}Pr_2C_6H_3$

$\mathbf{K^{tBu}_{dipp}}$ (86%)

To a solution of diisopropylaniline (2.4 g, 14 mmol) in 20 mL CH_3CN at −20°C, was added dropwise *tert*-butyl nitrite (2.0 g, 19 mmol) followed by trimethylsilyl azide (1.8 g, 16 mmol). After the reaction was stirred for 2 hours at room temperature, 3,6-di(*tert*-butyl)-1,8-diethynyl-9*H*-carbazole (1.1 g, 3.4 mmol) dissolved in 20 mL THF was added, followed by potassium carbonate (1.6 g, 11 mmol), pyridine (0.59 g, 7.5 mmol), 20 mL aqueous copper(II) sulfate pentahydrate (0.73 g, 2.9 mmol) solution and 20 mL aqueous sodium ascorbate (1.2 g, 5.8 mmol) solution. The reaction continued for 4 days and was quenched with 0.1 M

EDTA/NH_4OH. The organic phase was extracted with DCM, dried over magnesium sulfate, and concentrated to a red foam. The crude product was further purified by flash chromatography (eluted with DCM), after which the solvent was evaporated and the product was stirred for 20 minutes in hexane and filtered, affording a white solid. Yield: 2.2 g (86%). ^{1}H NMR (300 MHz, $CDCl_3$) δ 11.72 (s, 1H, NH), 8.20 (d, *J* = 1.8 Hz, 2H, Ar-$CH_{carbazole}$, H-1_a), 8.16 (s, 2H, trz-CH), 7.87 (d, *J* = 1.8 Hz, 2H, Ar-$CH_{carbazole}$, H-1_b), 7.52 (t, *J* = 7.7 Hz, 2H, Ar-CH_{Dipp}, H-2_a), 7.32 (d, *J* = 7.7 Hz, 4H, Ar-CH_{Dipp}, H-2_b), 2.43 (sept, *J* = 6.5 Hz, 4H, ^{i}Pr-CH, H-2_c), 1.54 (s, 18H, ^{t}Bu-CH_3), 1.19 (d, *J* = 6.9 Hz, 24H, ^{i}Pr-CH_3, H-2_d). ^{13}C {^{1}H} NMR (75 MHz, $CDCl_3$) δ 147.3, 146.4, 142.2, 136.0, 133.5 (all Ar-C_q), 130.9 (Ar-CH_{Dipp}, C-2_a), 127.1 (Ar-C_q), 124.3 (Ar-C_q), 124.0 (Ar-CH_{Dipp}, C-2_b), 122.3 (trz-CH), 120.6 (Ar-$CH_{carbazole}$, C-1_b), 116.8 (Ar-$CH_{carbazole}$, C-1_a), 112.7 (Ar-C_q), 35.0 (^{t}Bu-C_q), 32.3 (^{t}Bu-CH_3), 28.5 (^{i}Pr-CH, C-2_c), 24.5 (^{i}Pr-CH_3, C-2_d), 24.4 (^{i}Pr-CH_3, C-2_d). ESI-HRMS (15 V, positive mode, m/z): calcd for $[M+H]^+$: 734.4904. Found: 734.4890.

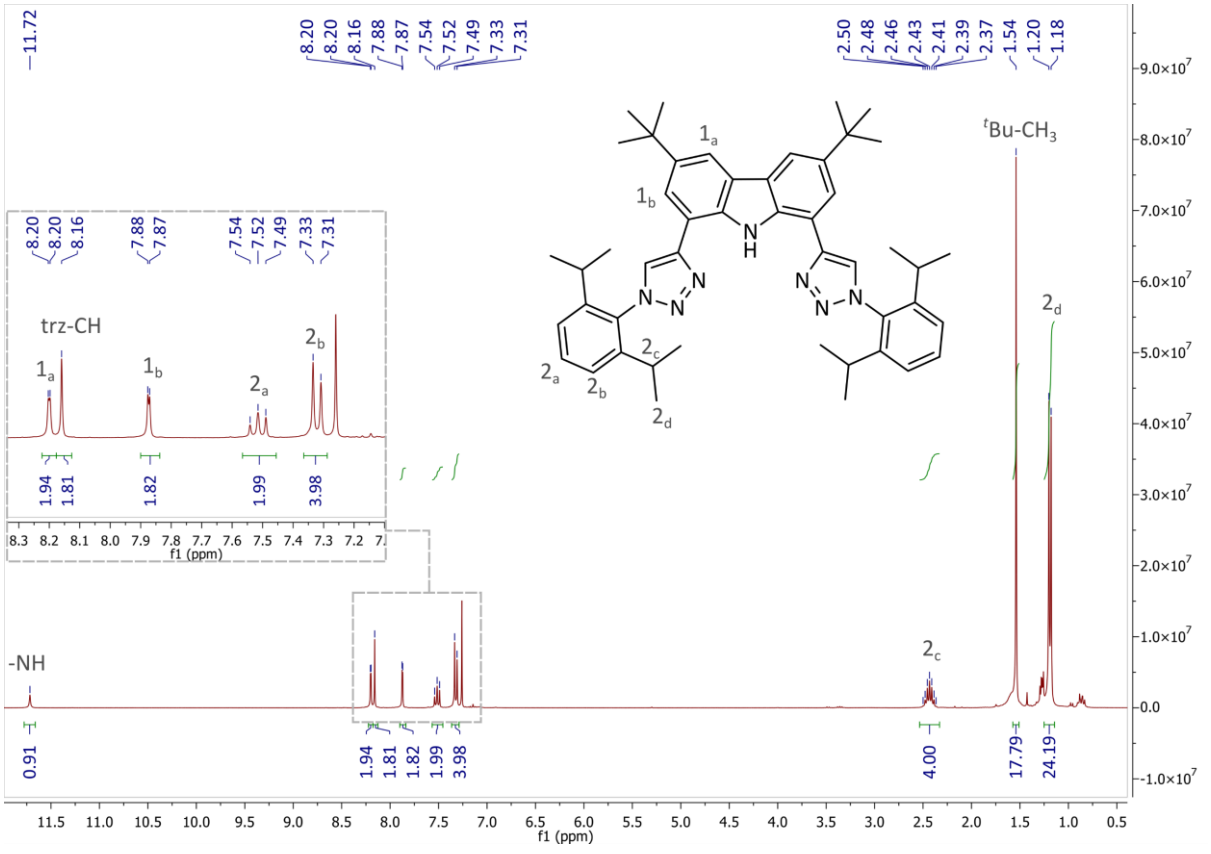


Figure 2.15. ^{1}H NMR spectrum of **K^{tBu}_{dipp}** in $CDCl_3$.

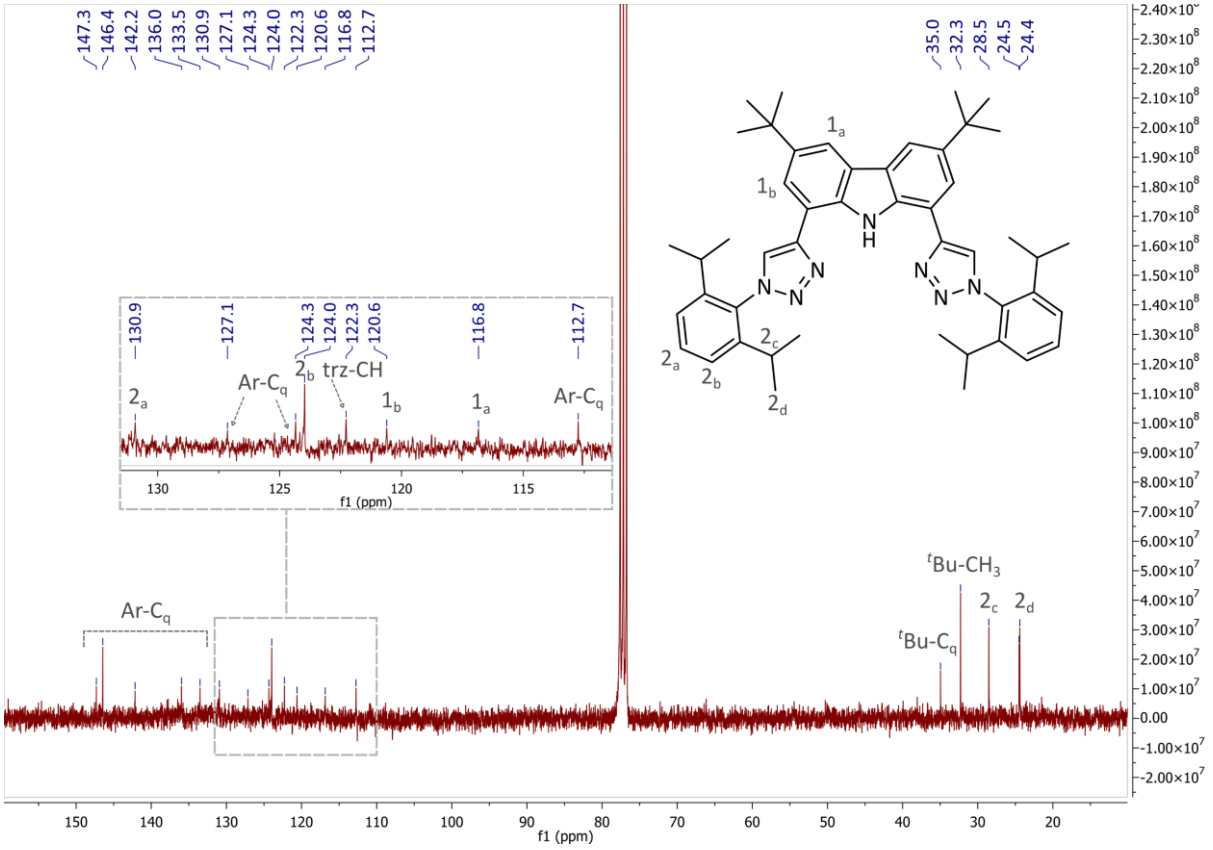
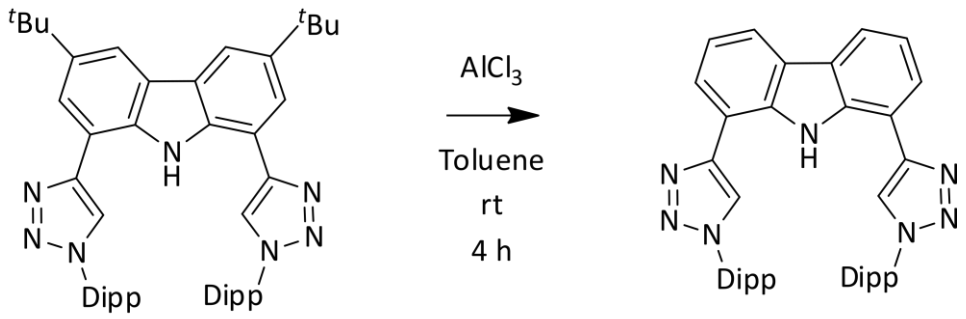


Figure 2.16. The ^{13}C {^{1}H} NMR spectrum of $\mathbf{K^{tBu}_{dipp}}$ in $CDCl_3$.

2.5.2.4 Synthesis and characterization of *1,8-bis-(3-diisopropylphenyl-1,2,3-triazole)-9H-carbazole* ($\mathbf{K^{H}_{dipp}}$)



Dipp = 2,6-$^{i}Pr_2C_6H_3$ $\mathbf{K^{H}_{dipp}}$ (71%)

The synthesis of $\mathbf{K^{H}_{dipp}}$ did not follow the conventional click route. Instead it was prepared by the deprotection of *tert*-butyl groups described for non-triazole aromatic systems.[226–228,231,232] $\mathbf{K^{tBu}_{dipp}}$ (2.0 g, 2.7 mmol) was dissolved in 50 mL of anhydrous toluene followed by the addition of anhydrous aluminium chloride (9.2 g, 69 mmol) in small amounts under a nitrogen atmosphere. The reaction mixture turned dark green and was stirred for 4 hours, after which the colour changed to orange red. The reaction was slowly quenched with water and the crude product was subsequently extracted with DCM, dried over magnesium sulfate, and

evaporated. The residue was stirred in hexane overnight and filtered, affording the product as an off-white solid. Crystals suitable for single crystal X-ray diffraction were grown from the slow evaporation of diethyl ether into a concentrated chloroform solution. Yield: 1.2 g (71%).^{1}H NMR (300 MHz, $CDCl_3$) δ 12.33 (s, 1H, NH), 8.19 (d, *J* = 7.7 Hz, 2H, Ar-$CH_{carbazole}$, H-1_a), 8.13 (s, 2H, trz-CH), 7.82 (d, *J* = 7.4 Hz, 2H, Ar-$CH_{carbazole}$, H-1_b), 7.53 (t, *J* = 7.8 Hz, Ar-CH_{Dipp}, H-2_a), 7.36 (dd, *J* = 7.6, 7.6 Hz, 2H, Ar-$CH_{carbazole}$, H-1_c), 7.33 (d, *J* = 7.8, 4H, Ar-CH_{Dipp}, H-2_b), 2.42 (sept, *J* = 6.8 Hz, 4H, ^{i}Pr-CH, H-2_c), 1.18 (t, *J* = 7.2 Hz, 24H, ^{i}Pr-CH_3, H-2_d). ^{13}C {^{1}H} NMR (75 MHz, $CDCl_3$) δ 147.1, 146.4, 137.7, 137.3, 133.4 (all Ar-C_q), 131.0 (Ar-CH_{Dipp}, C-2_a), 124.3 (Ar-C_q), 124.0 (Ar-CH_{Dipp}, C-2_b), 122.9 (Ar-$CH_{carbazole}$, C-1_c), 122.4 (Ar-$CH_{carbazole}$, C-1_b), 120.4 (trz-CH), 119.3 (Ar-$CH_{carbazole}$, C-1_a), 113.6 (Ar-C_q), 28.5 (^{i}Pr-CH, C-2_c), 24.4 (^{i}Pr-CH_3, C-2_c), 24.3 (^{i}Pr-CH_3, C-2_d). Anal. Calcd for $C_{40}H_{43}N_7$ (+ 0.1 eq hex): C 77.35, H 7.10, N 15.55. Found: C 77.77, H 7.14, N 15.18. ESI-HRMS (15 V, positive mode, m/z): calcd for $[M+H]^+$: 622.3652. Found: 622.3649.

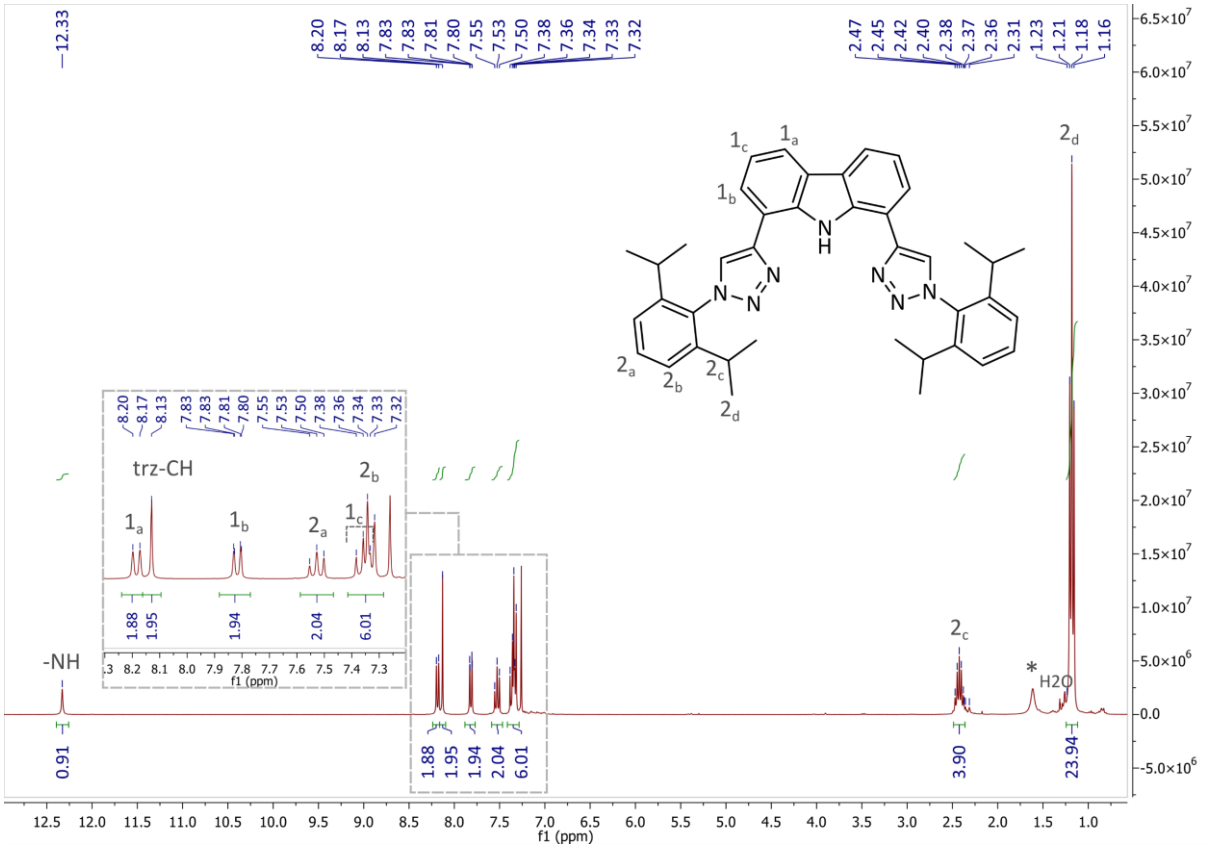


Figure 2.17. ^{1}H NMR spectrum of $\mathbf{K^{H}_{dipp}}$ in $CDCl_3$.

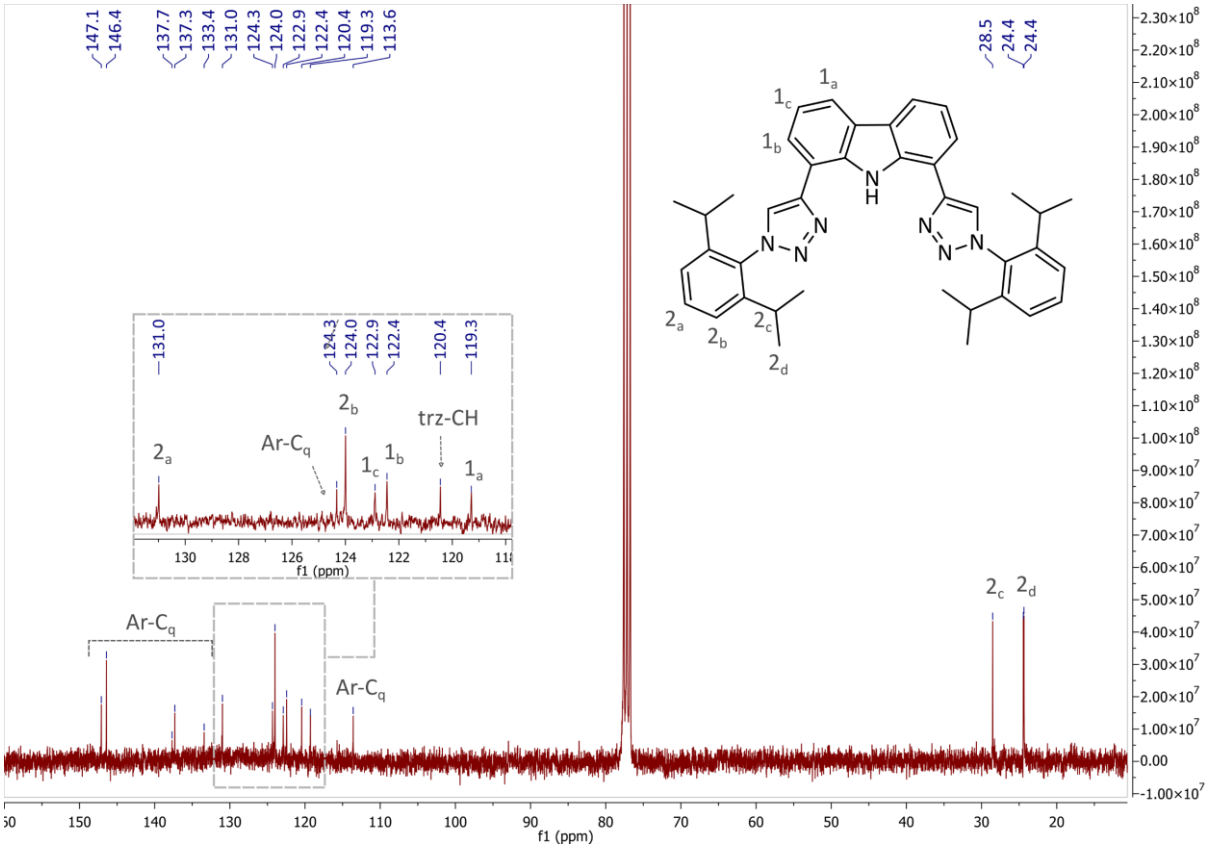
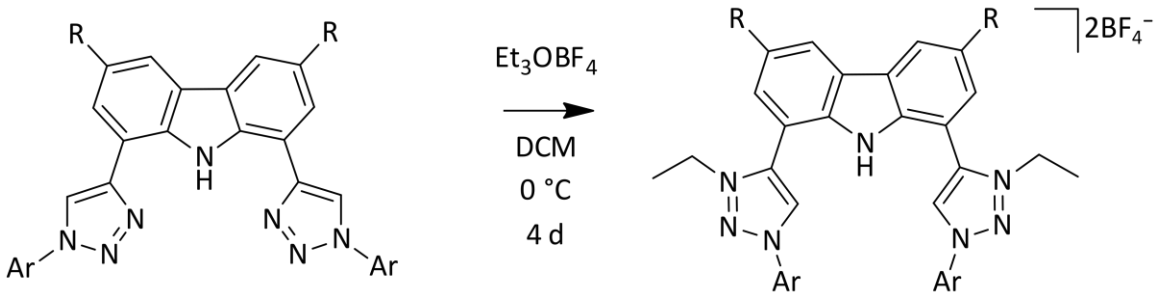


Figure 2.18. The ^{13}C {^{1}H} NMR spectrum of $\mathbf{K^{H}_{dipp}}$ in $CDCl_3$

2.5.3 Synthesis and characterization of triazolium salts, $\mathbf{L^{H}}$, $\mathbf{L^{tBu}}$ and $\mathbf{L^{tBu}_{dipp}}$

2.5.3.1 Synthesis of triazolium salts, $\mathbf{L^{H}}$, $\mathbf{L^{tBu}}$ and $\mathbf{L^{tBu}_{dipp}}$

The precursor salts, 3,6-di(R)-1,8-bis-(1-ethyl-3-Ar-1,2,3-triazolium)-9*H*-carbazole tetrafluoroborate(III), where R = H, *tert*-butyl and Ar = phenyl, diisopropylphenyl, were synthesized from their corresponding triazoles.



$\mathbf{K^{H}}$: R = H, Ar = Ph

$\mathbf{K^{tBu}}$: R = ^{t}Bu, Ar = Ph

$\mathbf{K^{tBu}_{dipp}}$: R = ^{t}Bu, Ar = Dipp (2,6-$^{i}Pr_2C_6H_3$

$\mathbf{L^{H}}$: R = H, Ar = Ph (25%)

$\mathbf{L^{tBu}}$: R = ^{t}Bu, Ar = Ph (83%)

$\mathbf{L^{tBu}_{dipp}}$: R = ^{t}Bu, Ar = Dipp (2,6-$^{i}Pr_2C_6H_3$) (25%)

To a solution of the appropriate triazole derivative in anhydrous DCM (20 mL), a solution of 6 equivalents of triethyloxonium tetrafluoroborate in DCM (10 mL) was added at −30°C and was left to reach room temperature slowly overnight, after which the reaction was stirred for an additional three days. The reaction was quenched with methanol and the solvents evaporated. The residue was dissolved in minimum acetone (4 mL) and then diethyl ether (40 mL) and the suspension was stirred for 1 h. The precipitate was filtered and dried under vacuum.

1,8-bis-(1-ethyl-3-phenyl-1,2,3-triazolium)-9H-carbazole tetrafluoroborate(III), **L^{H}**: White powder. Crystals suitable for XRD analysis were grown from the slow evaporation of diethyl ether into a concentrated DMF solution. Yield: 0.4 g (25%).^{1}H NMR (300 MHz, $(CD_3)_2SO$) δ 11.41 (s, 1H, NH), 10.04 (s, 2H, trz-CH), 8.68 (d, *J* = 7.8 Hz, 2H, Ar-$CH_{carbazole}$, H-1_a), 8.13–8.10 (m, 4H, Ar-CH_{Ph}, H-2_a), 7.85 (d, *J* = 7.5 Hz, 2H, Ar-$CH_{carbazole}$, H-1_b), 7.81–7.79 (m, 6H, Ar-CH_{Ph}, H-2_b + H-2_c), 7.63 (dd, *J* = 7.7, 7.7 Hz, 2H, Ar-$CH_{carbazole}$, H-1_c), 4.73 (q, *J* = 7.2 Hz, 4H, Et-CH_2, H-3_a), 1.53 (t, *J* = 7.2 Hz, 6H, Et-CH_3, H-3_b). ^{13}C {^{1}H} NMR (75 MHz, $(CD_3)_2SO$) δ 139.6, 138.4, 134.7 (all Ar-C_q), 132.1 (Ar-CH_{Ph}, C-2_c), 130.7 (Ar-CH_{Ph}, C-2_b), 128.9 (trz-CH), 128.7 (Ar-$CH_{carbazole}$, C-1_b), 124.7(4) (Ar-C_q), 124.7 (Ar-$CH_{carbazole}$, C-1_a), 123.8 (Ar-C_q), 121. 0 (Ar-CH_{Ph}, C-2_a), 120.5 (Ar-$CH_{carbazole}$, C-1_c), 105.4 (Ar-C_q), 47.8 (Et-CH_2, C-3_a), 13.7 (Et-CH_3, C-3_b). ^{19}F {^{1}H} NMR (376 MHz, $(CD_3)_2SO$) δ -148.35 (d, *J* = 21.2 Hz, BF_4). Anal. Calcd for $C_{36}H_{35}N_7B_2F_8$ (+ 0.15 eq hex): C 56.60, H 4.49, N 14.04. Found: C 57.02, H 4.14, N 14.33.ESI-HRMS (15 V, positive mode, m/z): calcd for M^{2+}: 255.6237. Found: 255.6251

3,6-tert-butyl-1,8-bis-(1-ethyl-3-phenyl-1,2,3-triazolium)-9H-carbazole tetrafluoroborate(III), **L^{tBu}**: White powder. Yield: 1.75 g (83%). ^{1}H NMR (300 MHz, $CDCl_3$) δ 9.80 (s, 1H, NH), 9.45 (s, 2H, trz-CH), 8.35 (d, *J* = 1.3 Hz, 2H, Ar-$CH_{carbazole}$, H-1_a), 8.00–7.97 (m, 4H, Ar-CH_{Ph}, H-2_a), 7.56–7.55 (m, 4H, Ar-CH_{Ph}, H-2_b), 7.54–7.53 (m, 2H, Ar-CH_{Ph}, H-2_c), 7.49 (d, *J* = 1.6 Hz, 2H, Ar-$CH_{carbazole}$, H-1_b), 4.62 (q, *J* = 7.3 Hz, 4H, Et-CH_2, H-3_a), 1.71 (t, *J* = 7.3 Hz, 6H, Et-CH_3, H-3_b), 1.50 (s, 18H, ^{t}Bu-CH_3). ^{13}C {^{1}H} NMR (75 MHz, $CDCl_3$) δ 143.4, 140.6, 138.0, 135.4 (all Ar-C_q), 131.7 (Ar-CH_{Ph}, C-2_c), 130.2 (Ar-CH_{Ph}, C-2_b), 128.4 (trz-CH), 124.8 (Ar-$CH_{carbazole}$, C-1_b), 124.7 (Ar-C_q), 122.3 (Ar-CH_{Ph}, C-2_a), 120.3 (Ar-$CH_{carbazole}$, C-1_a), 104.7 (Ar-C_q), 47.8 (Et-CH_2, C-3_a), 35.1 (^{t}Bu-C_q), 32.1 (^{t}Bu -CH_3), 14.4 (Et-CH_3, C-3_b). ^{19}F {^{1}H} NMR (470 MHz, $CDCl_3$) δ -152.36 (d, *J* = 24.45 Hz, BF_4). ESI-HRMS (15 V, positive mode, m/z): calcd for M^{2+}: 311.6862. Found: 311.6864.

3,6-tert-butyl-1,8-bis-(1-ethyl-3-diisopropylphenyl-1,2,3-triazolium)-9H-carbazole tetrafluoroborate(III), $\mathbf{L^{tBu}_{dipp}}$: White powder. Yield: 0.30 g (25%). ^{1}H NMR (300 MHz, $CDCl_3$) δ 9.77 (s, 1H, NH), 8.90 (s, 2H, trz-CH), 8.38 (d, *J* = 1.7 Hz, 2H, Ar-$CH_{carbazole}$, H-1_a), 7.61 (t, *J* = 7.78 Hz, 2H, Ar-CH_{Dipp}, H-2_a), 7.39 (d, *J* = 1.3 Hz, 2H, Ar-$CH_{carbazole}$, H-1_b), 7.37–7.36 (m, 4H, Ar-CH_{Dipp}, H-2_b), 4.74 (q, *J* = 7.2 Hz, 4H, Et-CH_2, H-3_a), 2.46 (p, *J* = 6.7 Hz, 4H, ^{i}Pr-CH, H-2_c), 1.69 (t, *J* = 7.1 Hz, 6H, Et-CH_3, H-3_b), 1.52 (s, 18H, ^{t}Bu-CH_3), 1.24 (d, *J* = 7.3 Hz, 12H, ^{i}Pr-CH_3, H-2_d), 1.21 (d, *J* = 7.4 Hz, 12H, ^{i}Pr-CH_3, H-2_d). ^{13}C {^{1}H} NMR (75 MHz, $CDCl_3$) δ 146.0, 143.4, 142.1, 137.8 (all Ar-C_q), 132.7 (Ar-CH_{Dipp}, C-2_a), 131.9 (trz-CH), 131.4 (Ar-C_q), 126.1 (Ar-$CH_{carbazole}$, C-1_b), 125.7 (Ar-C_q), 124.8 (Ar-CH_{Dipp}, C-2_b), 121.3 (Ar-$CH_{carbazole}$, C-1_a), 104.8 (Ar-C_q), 49.0 (Et-CH_2, C-3_a), 35.0 (^{t}Bu-C_q), 32.1 (^{t}Bu-CH_3), 28.9 (^{i}Pr-CH, C-2_c), 24.9 (^{i}Pr-CH_3, C-2_d), 23.6 (^{i}Pr-CH_3, C-2_d), 14.5 (Et-CH_3, C-3_b). ^{19}F {^{1}H} NMR (470 MHz, $CDCl_3$) δ -151.98 (d, *J* = 24.3 Hz, BF_4). ESI-HRMS (15 V, positive mode, m/z): calcd for M^{2+}: 395.7801. Found: 395.7804.

2.5.4 NMR spectra of triazolium salts, $\mathbf{L^{H}}$, $\mathbf{L^{tBu}}$ and $\mathbf{L^{tBu}_{dipp}}$

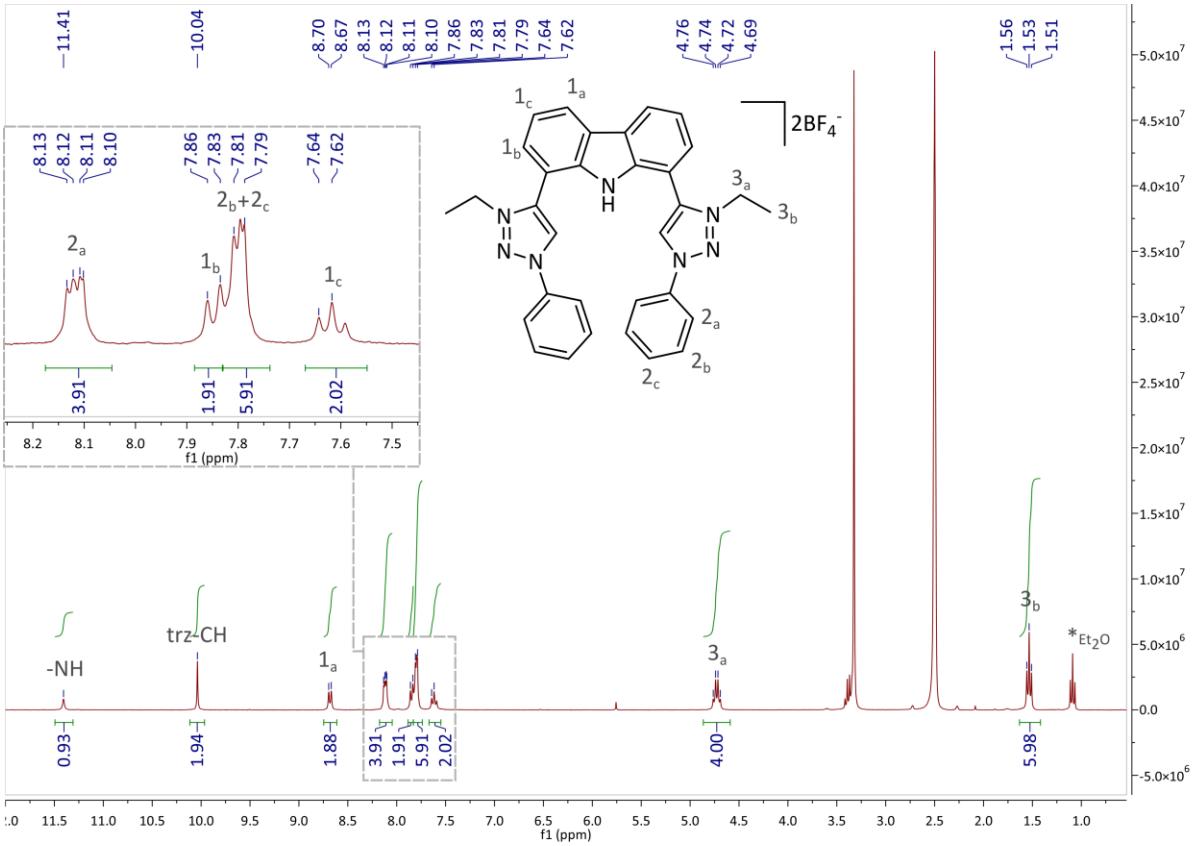


Figure 2.19. ^{1}H NMR spectrum of $\mathbf{L^{H}}$ in $(CD_3)_2SO$.

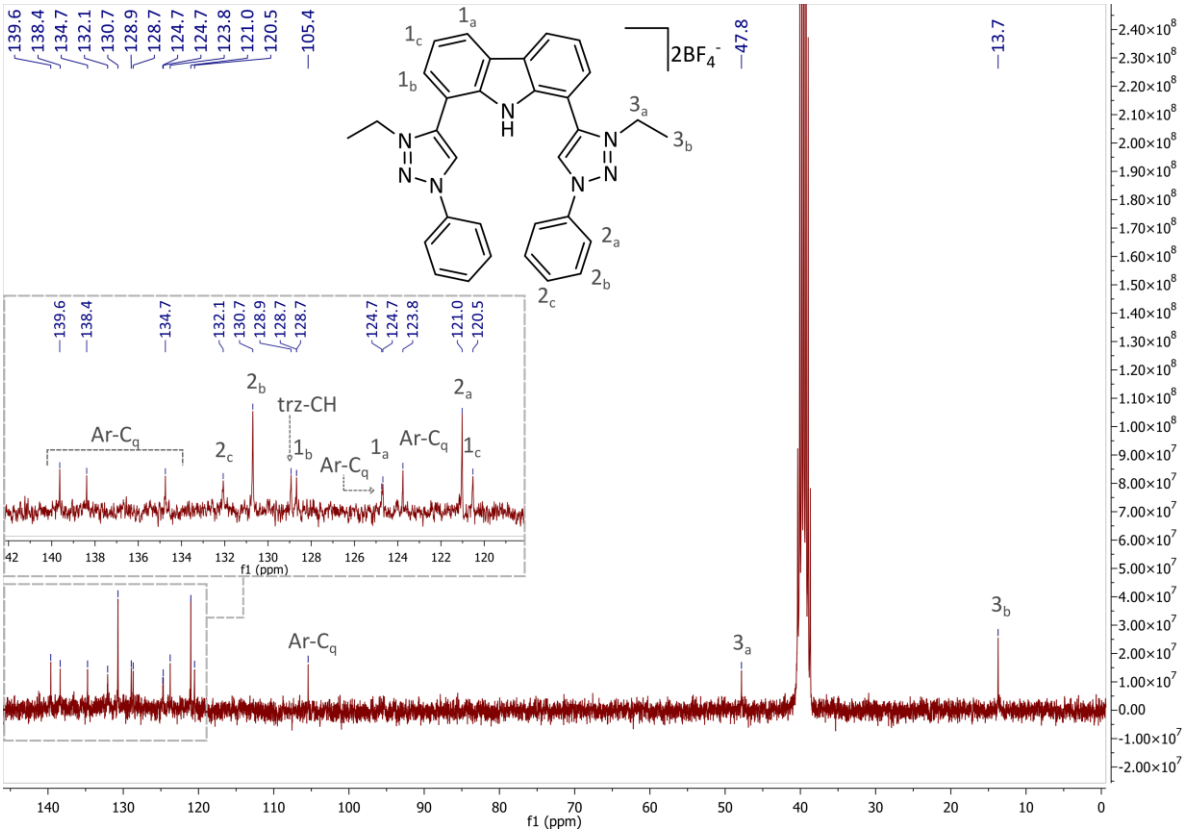


Figure 2.20. The ^{13}C {^{1}H} NMR spectrum of $\mathbf{L^{H}}$ in $(CD_3)_2SO$.

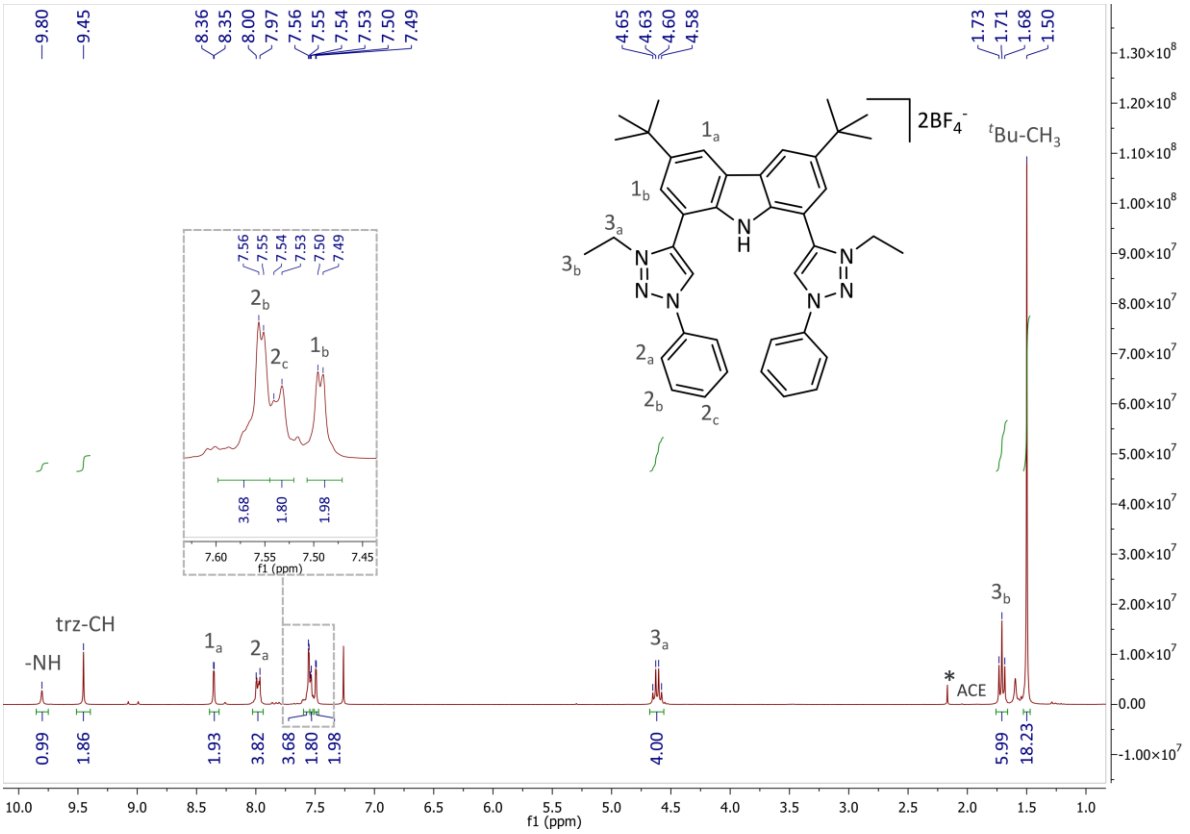


Figure 2.21. ^{1}H NMR spectrum of $\mathbf{L^{tBu}}$ in $CDCl_3$.

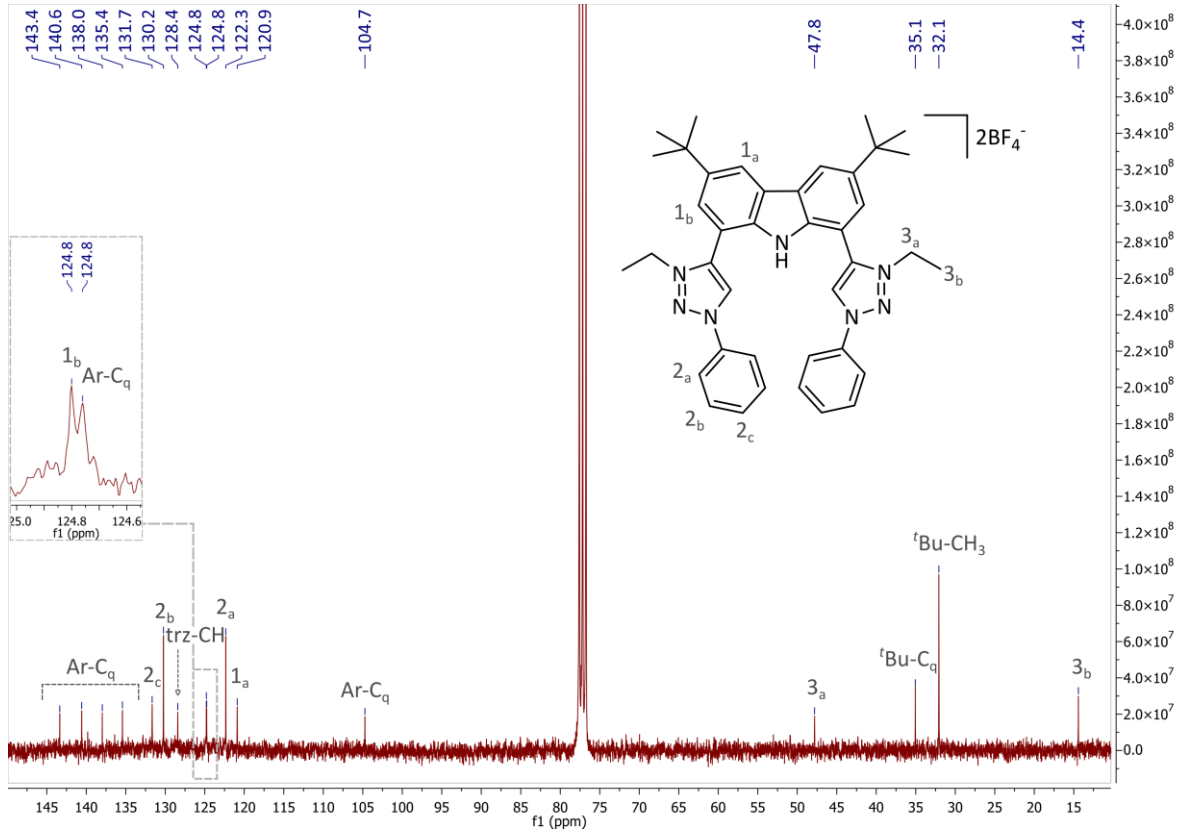


Figure 2.22. The ^{13}C {^{1}H} NMR spectrum of **L^{tBu}** in $CDCl_3$.

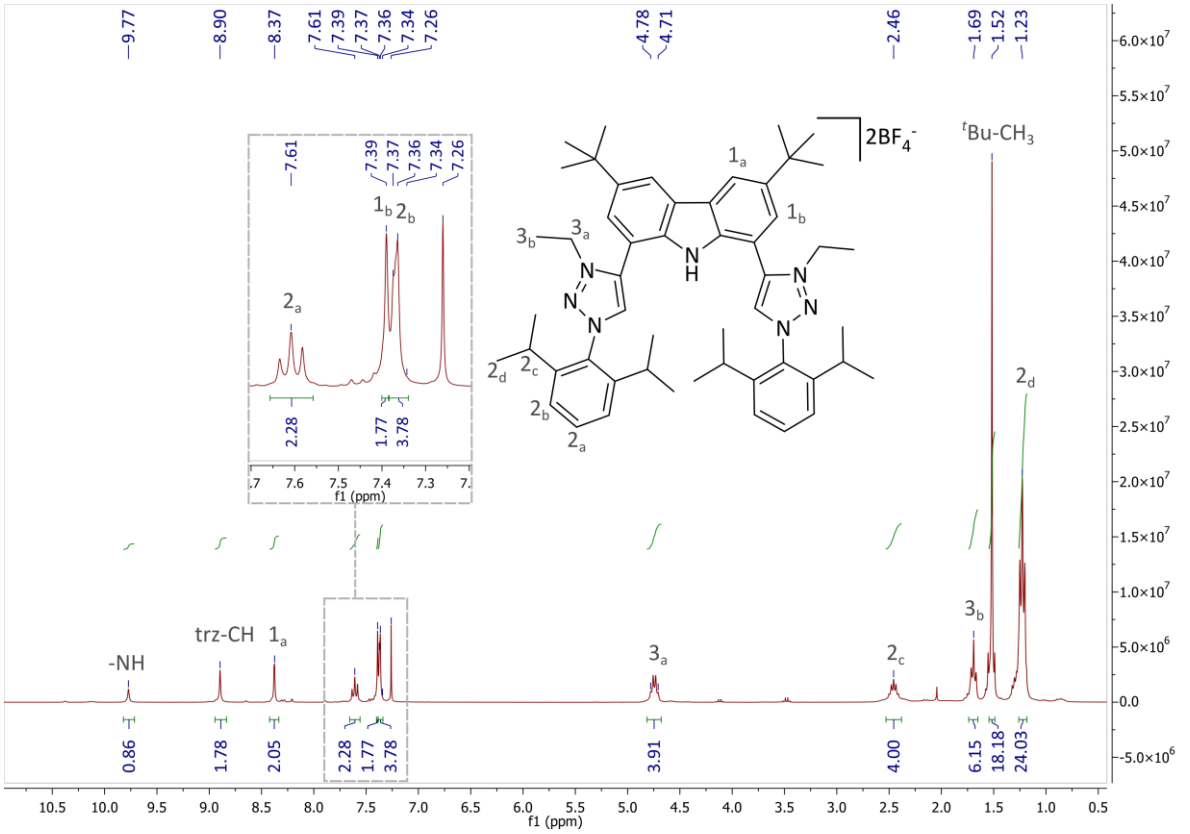


Figure 2.23. ^{1}H NMR spectrum of **L$^{tBu}_{dipp}$** in $CDCl_3$.

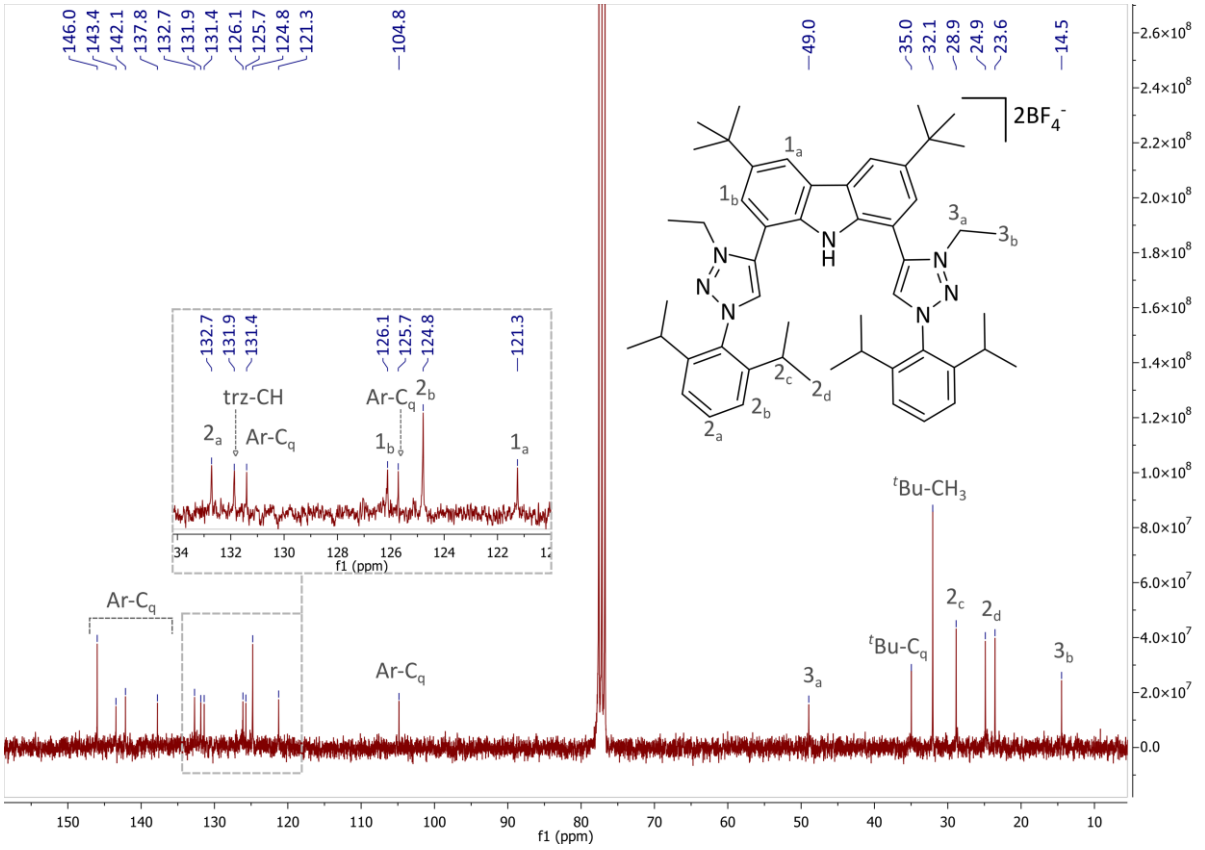
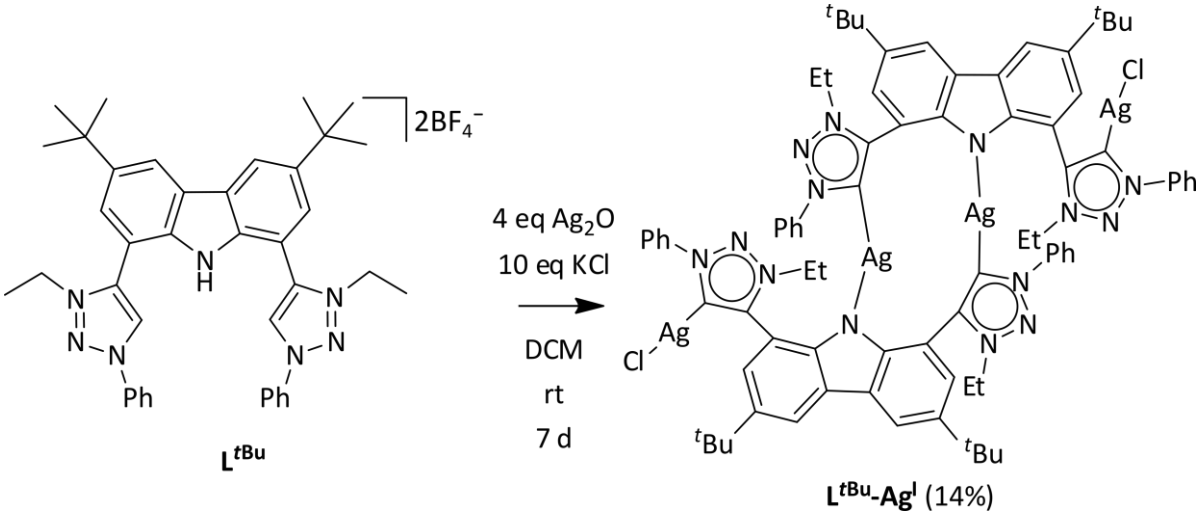


Figure 2.24. The ^{13}C {^{1}H} NMR spectrum of $\mathbf{L^{tBu}_{dipp}}$ in $CDCl_3$.

2.5.5 Synthesis of metal complexes, L^{tBu}-Ag^{I} , L^{tBu}-*N*-AgCl-Au^{I} , L^{tBu}-Au^{I} and L^{H}-Ag^{I}

2.5.5.1 Synthesis and characterization of *bis-((3,6-tert-butyl)-1-(1-ethyl-3-phenyl-1,2,3-triazo-5-lylidene silver(I) chloride)-8-(1-ethyl-3-phenyl-1-2,3-triazol-5-ylidene silver(I))-9-carbazolide)*, L^{tBu}-Ag^{I} .



To a flame dried Schlenk was added $\mathbf{L^{tBu}}$ (100 mg, 0.13 mmol), KCl (90 mg, 1.3 mmol) and Ag_2O (11 mg, 0.50 mmol) and dissolved in anhydrous DCM (10 mL). The reaction was stirred for one

week in the dark at room temperature. The solvent was evaporated, and the crude product was extracted with DCM and washed with Et_2O, affording **L^{tBu}-Ag^{I}** as a bright yellow powder. Crystals suitable for XRD analysis were grown from slow evaporation of diethyl ether in a concentrated DCM solution. Yield: 30 mg (14%). ^{1}H NMR (300 MHz, $CDCl_3$) δ 8.23 (d, *J* = 2.0 Hz, 2H, Ar-$CH_{carbazole}$, H-1_a), 8.17 (d, *J* = 2.0 Hz, 2H, Ar-$CH_{carbazole}$, H-$1_a'$), 7.49 (d, *J* = 7.9 Hz, 4H, Ar-CH_{Ph}, H-2_b), 7.40 (d, *J* = 4.2 Hz, 8H, Ar-CH_{Ph}, H-2_a), 7.33–7.30 (m, 2H, Ar-CH_{Ph}, H-2_c), 7.16–7.12 (m, 2H, Ar-CH_{Ph}, H-2_c'), 7.11 (d, *J* = 2.0 Hz, 2H, Ar-$CH_{carbazole}$, H-1_b), 7.08 (d, *J* = 2.0 Hz, 2H, Ar-$CH_{carbazole}$, H-1_b') 7.04 (dd, *J* = 7.8, 7.8 Hz, 4H, Ar-CH_{Ph}, H-2_b'), 4.37 (dq, *J* = 14.4, 7.3 Hz, 2H, Et-CH_2, H-3_a), 4.19 (dq, *J* = 14.4, 7.2 Hz, 2H, Et-CH_2, H-3_a), 3.64 (dt, *J* = 14.4, 7.3 Hz, 2H, Et-CH_2, H-3_a'), 3.25 (dq, *J* = 14.5, 7.3 Hz, 2H, Et-CH_2, H-3_a'), 1.53 (s, 18H, ^{t}Bu-CH_3), 1.47 (t, *J* = 7.3 Hz, 6H, Et-CH_3, H-3_b), 1.41 (s, 18H, ^{t}Bu-CH_3'), 0.91 (t, *J* = 7.3 Hz, Et-CH_3, H-3_b'). ^{13}C {^{1}H} NMR (100 MHz, $CDCl_3$) δ n.o. (Ag-$C_{carbene}$,), 148.7, 148.6, 148.5, 148.4, 148.1, 147.9, 147.7, 147.6, 139.7, 138.4, 138.0, 137.4, 130.0 (all Ar-C_q), 129.9 (Ar-CH_{Ph}, C-2_a),129.5 (Ar-CH_{Ph}, C-2_c), 129.4 (Ar-CH_{Ph}, C-2_c),129.0 (Ar-CH_{Ph}, C-2_b), 126.8, 126.7, 125.8, 125.7 (all Ar-C_q), 124.5 (Ar-$CH_{carbazole}$, C-1_b), 123.3 (Ar-$CH_{carbazole}$, C-$1_b'$), 122.1 (Ar-CH_{Ph}, C-2_b'), 120.9 (Ar-C_q), 120.1 (Ar-CH_{Ph}, C-2_a'), 118.5 (Ar-$CH_{carbazole}$, C-1_a), 118.2 (Ar-$CH_{carbazole}$, C-1_a'), 111.1 (Ar-C_q), 110.9 (Ar-C_q), 46.6 (Et-CH_2, C-3_a), 44.7 (Et-CH_2, C-3_a'), 34.7 (^{t}Bu-C_q), 34.6 (^{t}Bu-C_q'), 32.6 (^{t}Bu-CH_3), 32.3 (^{t}Bu-CH_3'), 16.2 (Et-CH_3, C-3_b), 15.5 (Et-CH_3, C-3_b'). Anal. Calcd for $C_{80}H_{84}N_{14}Ag_4Cl_2$ (+ 1.0 eq tetrahydrothiophene): C 55.19, H 4.85, N 10.73 S 1.75. Found: C 55.67, H 4.51, N 11.05 S 1.78

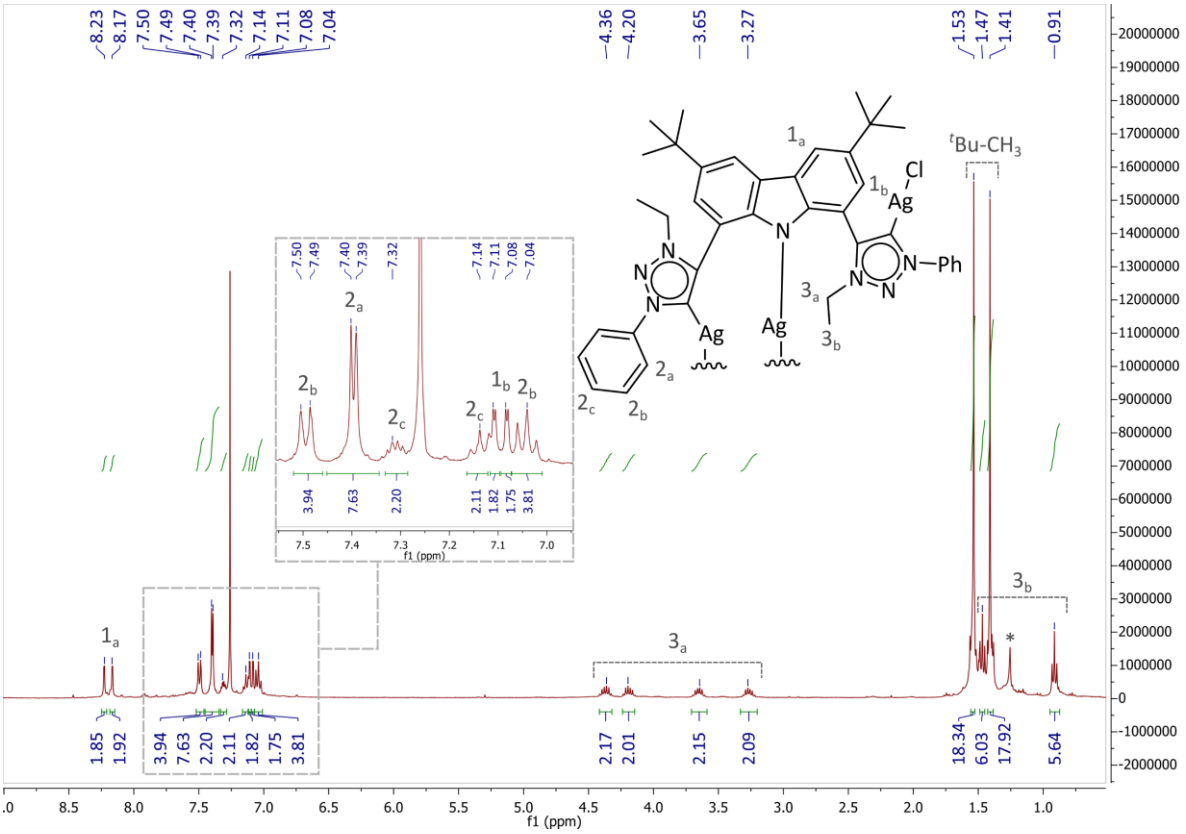


Figure 2.25. ^{1}H NMR spectrum of **L^{tBu}-Ag^{I}** in $CDCl_3$ (*grease).

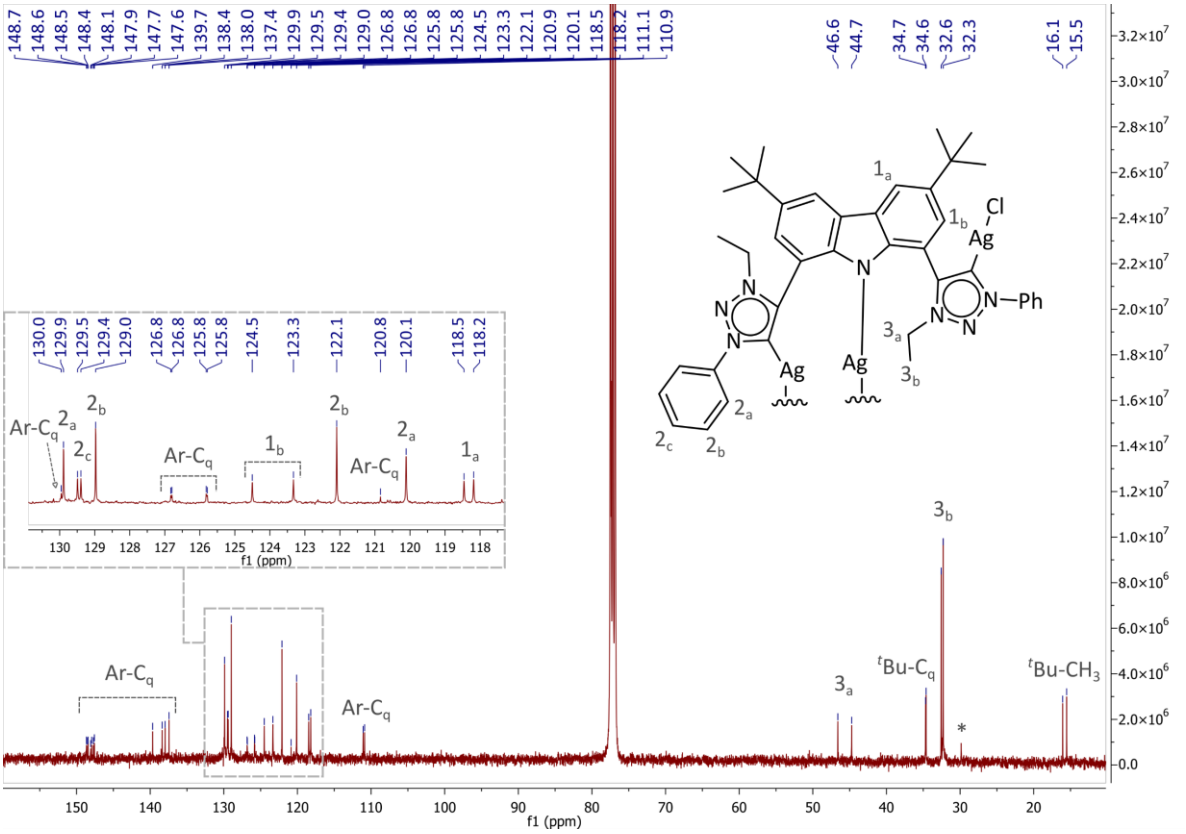
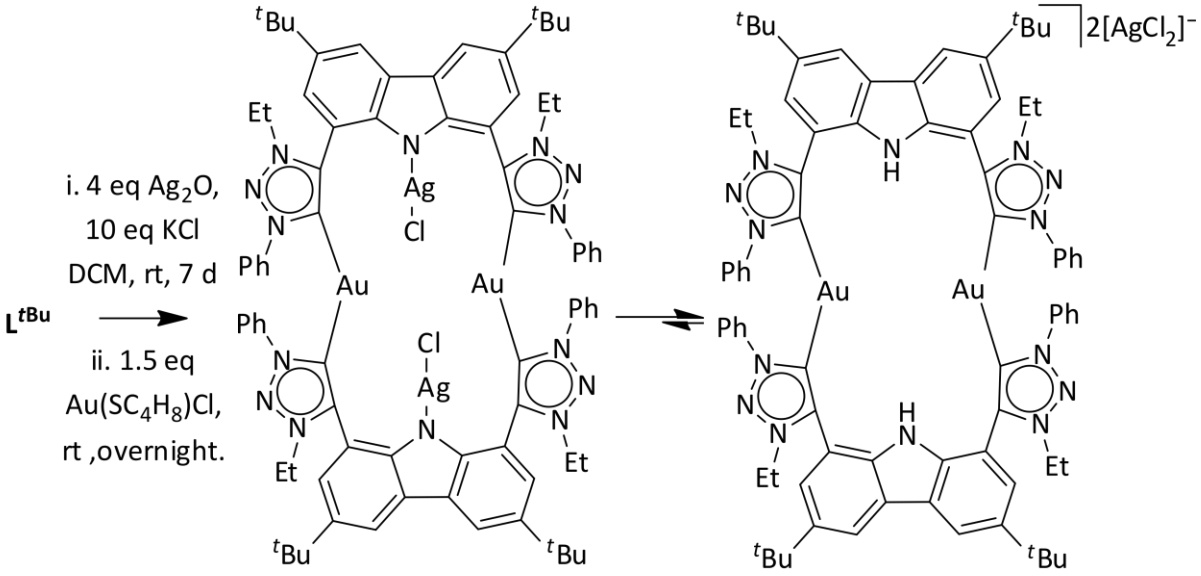


Figure 2.26. The ^{13}C {^{1}H} NMR spectrum of **L^{tBu}-Ag^{I}** in $CDCl_3$ (*grease).

2.5.5.2 Synthesis of *bis-((3,6-tert-butyl)-1,8-bis(1-ethyl-3-phenyl-1,2,3-triazol-5-ylidene gold(I)-9-silver(I) chlorido carbazolide),* L^{tBu}-*N*-AgCl-Au^{I} and *bis-((3,6-tert-butyl)-1,8-bis(1-ethyl-3-phenyl-1,2,3-triazo-5-lylidene gold(I)-9H-carbazolide dichloride-argentate(I),* L^{tBu}-Au^{I}



L^{tBu}-*N*-AgCl-Au^{I} L^{tBu}-Au^{I} (28%)

L^{tBu} (0.15 g, 0.20 mmol), 10 eq KCl (0.14 g, 1.9 mmol) and 4 eq Ag_2O (0.18 g, 0.75 mmol) were dissolved in anhydrous DCM (10 mL). The reaction was stirred for one week in the dark at room temperature. The solvent was extracted via cannula filtration and 1.5 eq Au(tht)Cl (0.90 mg, 0.28 mmol) was added. An immediate precipitate was observed, and the reaction was stirred overnight. The solvent was evaporated, and the crude reaction mixture was extracted with DCM, followed by washing with hexane. Crystals suitable for XRD analysis were grown from a concentrated DCM solution, layered with pentane. Yellow powder. Yield: 96 mg (28%). ^{1}H NMR (500 MHz, $CDCl_3$) δ 8.24 (d, *J* = 2.0 Hz, 2H, Ar-$CH_{carbazole}$, H-1_a), 8.19 (d, *J* = 2.0 Hz, 2H, Ar-$CH_{carbazole}$, H-1_a'), 7.66 (d, *J* = 8.3 Hz, 2H, Ar-CH_{Ph}, H-2_a), 7.66' (d, *J* = 8.7 Hz, 2H, Ar-CH_{Ph}, H-2_a), 7.62 (d, *J* = 7.3 Hz, 2H, Ar-CH_{Ph}, H-2_a), 7.62' (d, *J* = 8.0 Hz, 2H, Ar-CH_{Ph}, H-2_a), , 7.70 (dd, *J* = 7.6, 7.6 Hz, 4H, Ar-CH_{Ph}, H-2_b), 7.35 (t, *J* = 7.3 Hz, 2H, Ar-CH_{Ph}, H-2_c), 7.18 (t, *J* = 7.5 Hz, 2H, Ar-CH_{Ph}, H-2_c'), 7.09 (d, *J* = 2.0 Hz, 2H, Ar-$CH_{carbazole}$, H-1_b), 7.07 (m, 4H, Ar-CH_{Ph}, H-2_b'), 7.05 (d, *J* = 1.9 Hz, 2H, Ar-$CH_{carbazole}$, 2H, H-1_b'), 4.22 (dq, *J* = 14.0, 7.1 Hz, 2H, Et-CH_2, H-3_a), 4.16 (dq, *J* = 14.1, 7.1 Hz, 2H, Et-CH_2, H-3_a), 3.55 (dq, *J* = 14.1, 7.1 Hz, 2H, Et-CH_2, H-3_a'), 3.13 (dq, *J* = 14.1, 7.1 Hz, 2H, Et-CH_2, H-3_a'), 1.51 (s, 18H, ^{t}Bu-CH_3,), 1.41 (s, 18H, ^{t}Bu-CH_3'), 1.36 (t, *J* = 7.3 Hz, 6H, Et-CH_3, H-3_b), 0.90 (t, *J* = 7.3 Hz, 6H, Et-CH_3, H-3_b'). ^{13}C {^{1}H} NMR (125 MHz, $CDCl_3$) δ 157.08 (Au-$C_{carbene}$), 157.06 (Au-$C_{carbene}$'), 148.6, 148.5, 148.3(3), 148.3, 148.0, 147.9, 146.4,

139.1, 138.4, 137.8, 137.4 (all Ar-C_q), 129.8 (Ar-CH_{Ph}, C-2_b), 129.6 (Ar-CH_{Ph}, C-2_c), 129.4 (Ar-CH_{Ph}, C-2_c), 128.8 (Ar-CH_{Ph}, C-2_b), 126.6, 126.5, 125.7, 125.6 (all Ar-C_q), 124.4 (Ar-$CH_{carbazole}$, C-1_b), 123.6 (Ar-$CH_{carbazole}$, C-1_b), 123.2 (Ar-CH_{Ph}, C-2_a), 123.1 (Ar-CH_{Ph}, C-2_a), 120.4 (Ar-$CH_{carbazole}$, C-1_b), 118.4 (Ar-$CH_{carbazole}$, C-1_b), 110.8 (Ar-C_q), 110.3 (Ar-C_q), 46.4 (Et-CH_2, C-3_a), 45.1 (Et-CH_2, C-3_a), 34.7 (^{t}Bu-C_q), 34.6 (^{t}Bu-C_q), 32.6 (^{t}Bu-CH_3), 32.3 (^{t}Bu-CH_3), 16.2 (Et-CH_3, C-3_b), 15.4 (Et-CH_3, C-3_b). Anal. Calcd for $C_{80}H_{86}Au_2N_{14}Ag_2Cl_4$ (+ 1.5 eq acetone): C 48.74, H 4.60, N 9.42. Found (avg): C 48.52, H 4.51, N 9.04. ESI-HRMS (15 V, positive mode, m/z): calcd for $[M+2H]^{2+}$: 818.3240. Found: 818.3253.

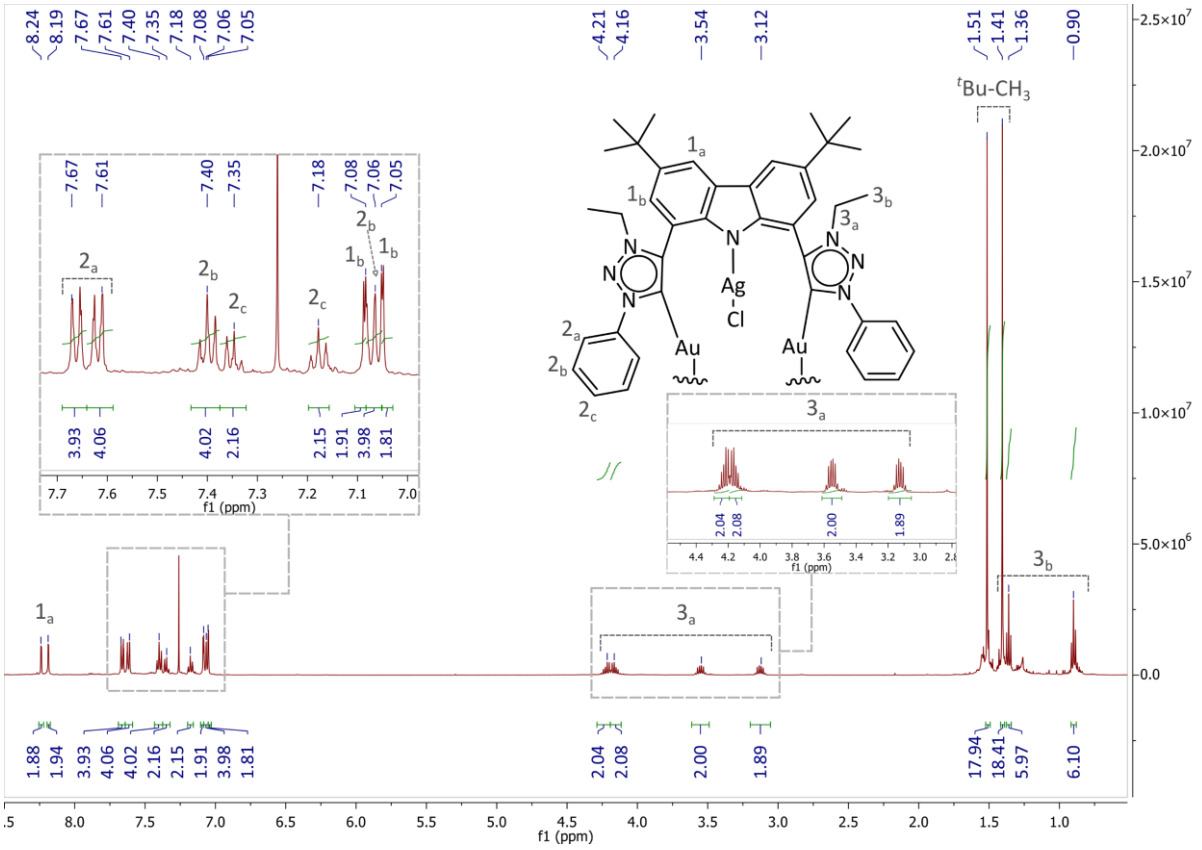


Figure 2.27. ^{1}H NMR spectrum of **L^{tBu}-*N*-AgCl-Au^I** in $CDCl_3$.

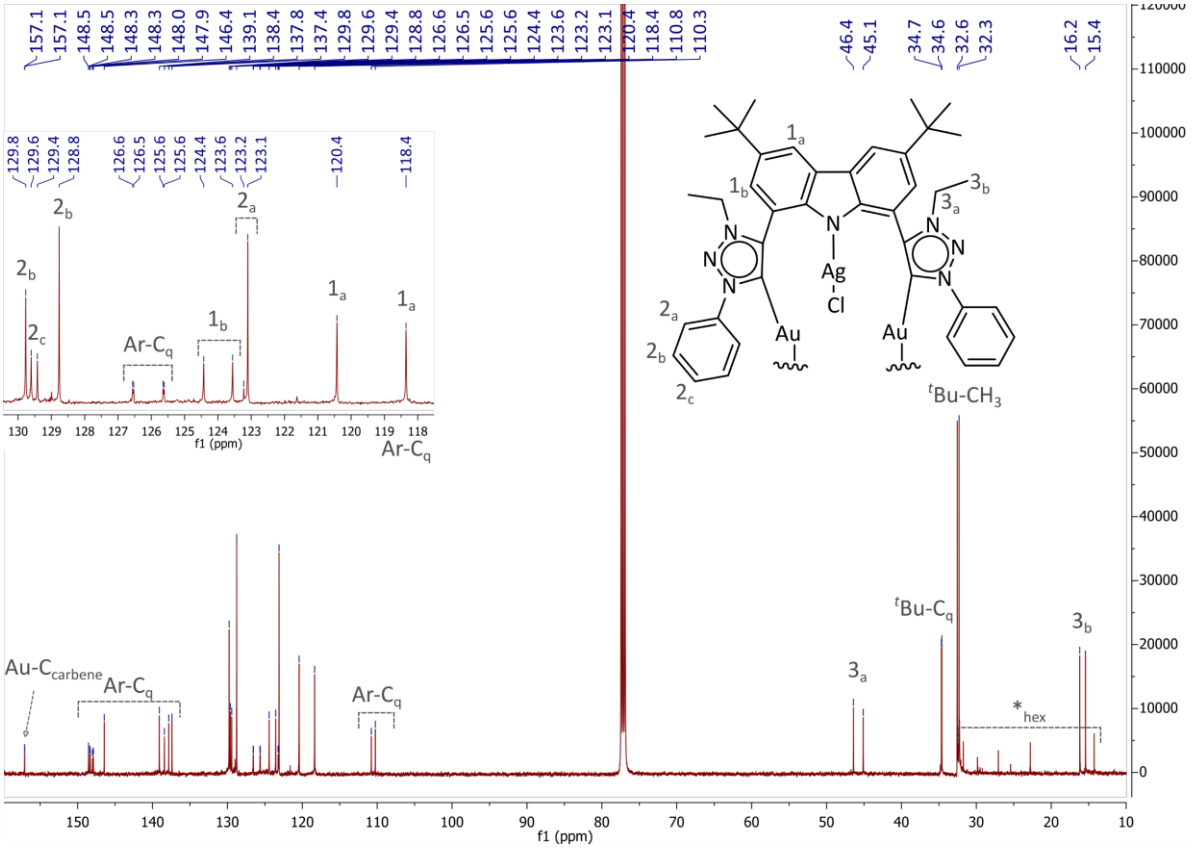
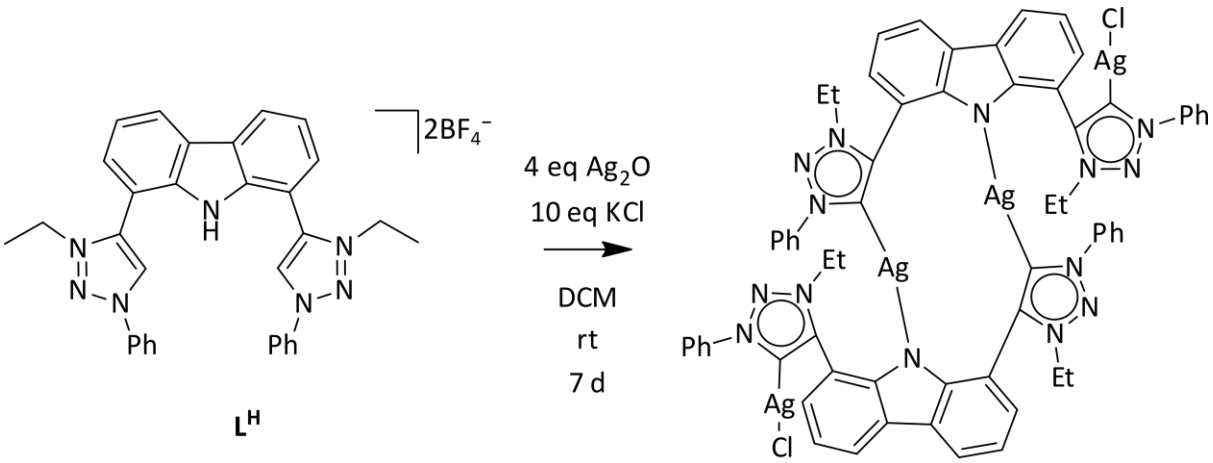


Figure 2.28. The ^{13}C {^1H} NMR spectrum of **L^{tBu}-*N*-AgCl-Au^I** in $CDCl_3$.

2.5.5.3 Synthesis of L^H-Ag^I



L^H **L^H-Ag^I** (27%)

To a flame dried Schlenk tube was added **L^H** (50 mg, 0.073 mmol), 10 eq KCl (55 mg, 0.73 mmol) and 4 eq Ag_2O (68 mg, 0.29 mmol) and the solid mixture was dissolved in anhydrous DCM (10 mL). The reaction was stirred for one week in the dark at room temperature. The solvent was evaporated, and the crude product was extracted with DCM and washed with Et_2O, affording a light orange powder. Yield: 30 mg (27 %). ^1H NMR (500 MHz, $CDCl_3$) δ 8.22

(d, J =7.6 Hz, 1H, Ar-$CH_{carbazole}$, H-1_a), 8.22′ (d, J =7.6 Hz, 1H, Ar-$CH_{carbazole}$, H-1_a), 8.19 – 8.16 (m, 2H, Ar-$CH_{carbazole}$, H-1_a′), 7.46 – 7.44 (m, 4H, Ar-CH_{Ph}, H-2_a), 7.39 – 7.35 (m, 8H, Ar-CH_{Ph}, H-2_b), 7.30 –7.28 (m, 2H, Ar-CH_{Ph}, H-2_c), 7.17 (dd, *J* = 7.4, 7.4 Hz, Ar-$CH_{carbazole}$, H-1_c), 7.12 – 7.10 (m, 4H, overlapping Ar-$CH_{carbazole}$, H-1_c′ (2H) + Ar-CH_{Ph}, H-2_c′(2H)), 7.06 – 7.04 (m, 4H, Ar-$CH_{carbazole}$, H-1_b), 7.04 – 7.00 (m, 4H, Ar-CH_{Ph}, H-2_a′), 4.41 (dq, *J* = 14.5, 7.2 Hz, 2H, Et-CH_2, H-3_a), 4.18 (dq, *J* = 14.5, 7.3 Hz, 2H, Et-CH_2, H-3_a), 3.77 (dq, *J* = 13.5, 7.4 Hz, 2H, Et-CH_2, H-3_a′), 3.26 (dq, *J* = 14.4, 7.3 Hz, 2H, Et-CH_2, H-3_a′), 1.48 (t, *J* = 7.3 Hz, 6H, Et-CH_3, H-3_b), 0.92 (t, *J* = 7.4 Hz, 6H, Et-CH_3, H-3_b′). ^{13}C {^1H} NMR (125 MHz, $CDCl_3$) δ 164.5 (dd, *J* = 239.9, 17.5 Hz, Ag-$C_{carbene}$), 164.4 (dd, *J* = 240.6, 16.4 Hz, Ag-$C_{carbene}$), 149.9(3), 149.9(1), 149.8(5), 149.8(2), 147.5, 147.4, 147.1, 147.0, 139.5, 139.1, 130.2 (all Ar-C_q), 129.9 (Ar-CH_{Ph}, C-2_b), 129.6 (Ar-CH_{Ph}, C-2_c), 129.4 (Ar-CH_{Ph}, C-2_c), 129.0 (Ar-CH_{Ph}, C-2_a), 126.9 (Ar-$CH_{carbazole}$, C-1_b), 126.0(3) (Ar-C_q), 126.0 (Ar-C_q), 125.5 (Ar-$CH_{carbazole}$, C-1_b), 122.4 (Ar-$CH_{carbazole}$, C-1_a), 122.1(3) (Ar-CH_{Ph}, C-2_a), 122.1 (Ar-$CH_{carbazole}$, C-1_a), 119.9 (Ar-CH_{Ph}, C-2_b), 115.6 (Ar-$CH_{carbazole}$, C-1_a), 115.0 (Ar-$CH_{carbazole}$, C-1_a), 111.9 (Ar-C_q), 111.7 (Ar-C_q), 46.8 (Et-CH_2, C-3_a), 45.0 (Et-CH_2, C-3_a), 15.9 (Et-CH_3, C-3_b), 14.7 (Et-CH_3, C-3_b). ESI-HRMS (15 V, positive mode, m/z): calcd for $[M+2H]^{2+}$: 617.1451. Found: 617.1380, where M = $C_{64}H_{54}Ag_2N_{14}$

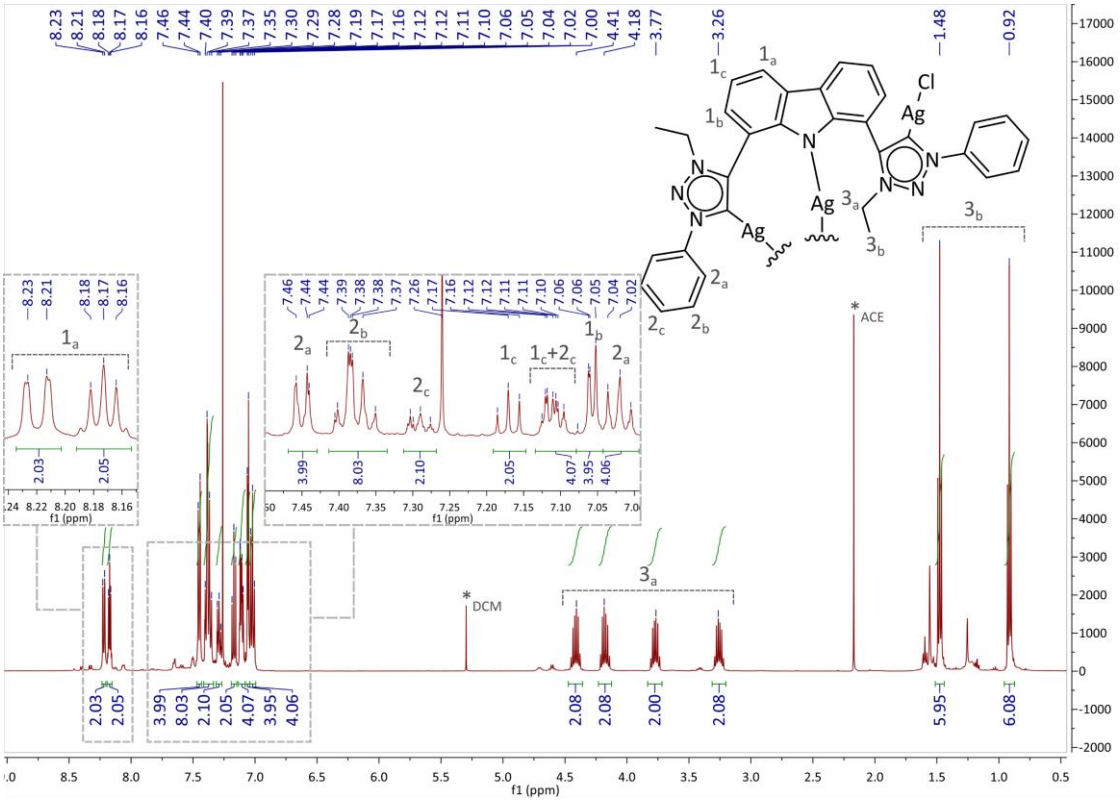


Figure 2.29. ^{1}H NMR spectrum of **L^{H}-Ag^{I}** in $CDCl_3$.

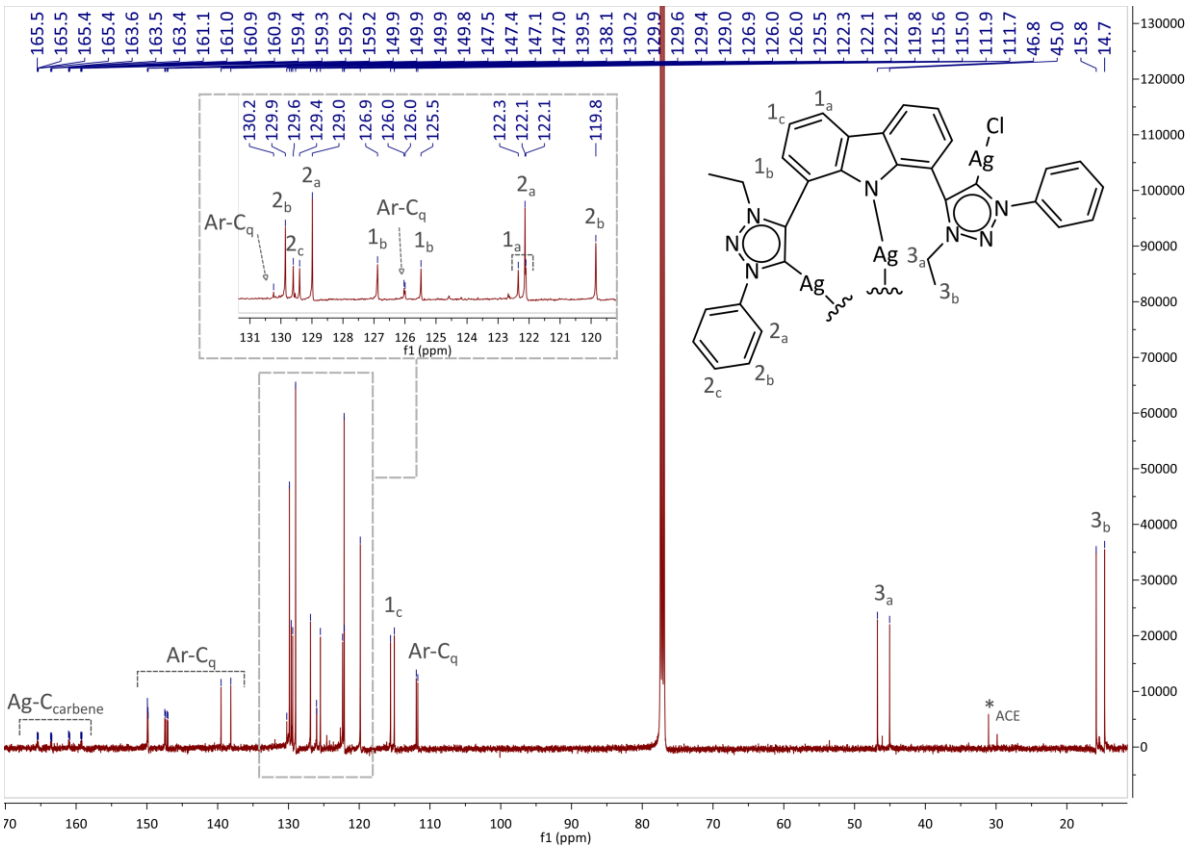
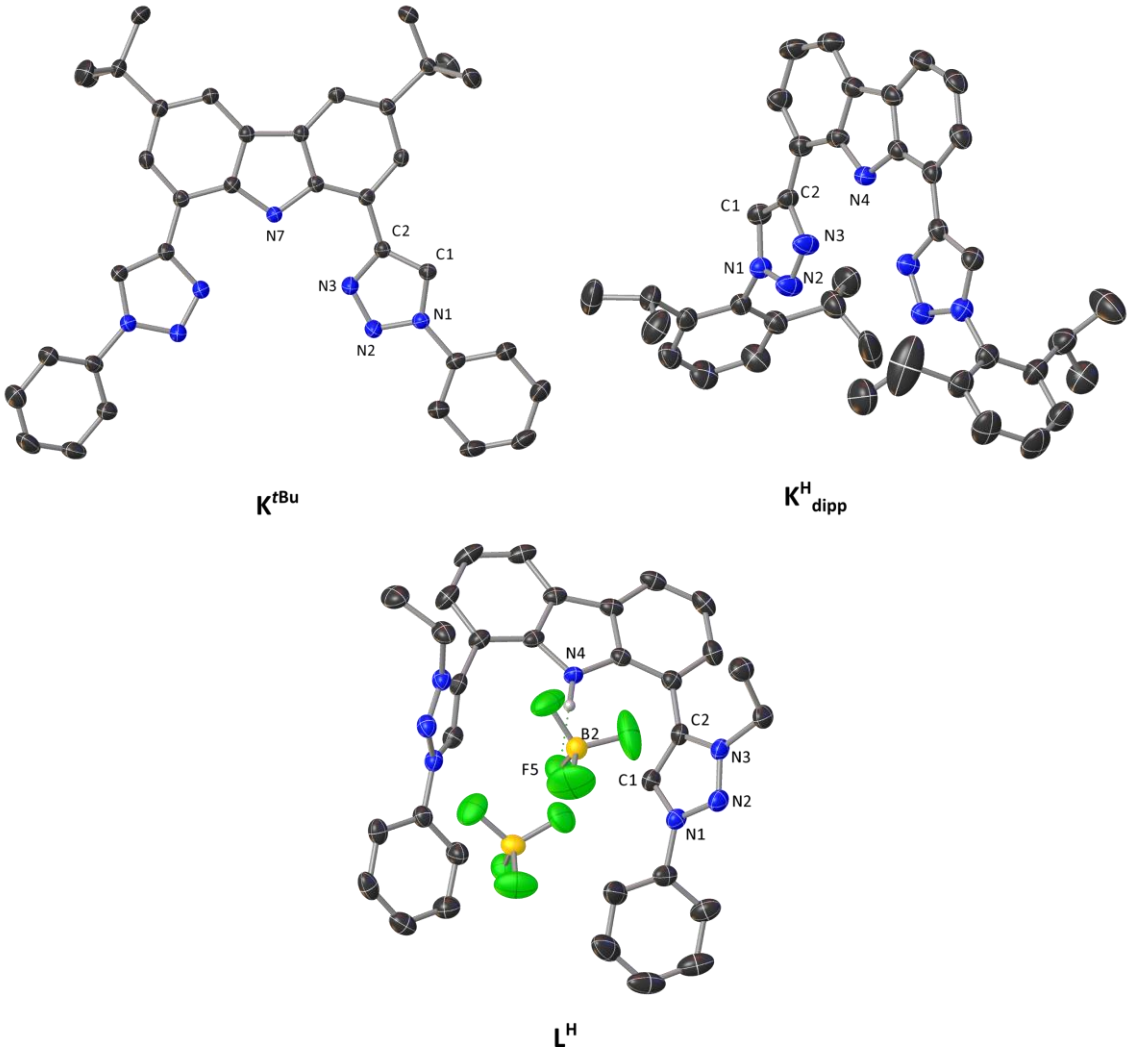


Figure 2.30. The ^{13}C {^{1}H} NMR spectrum of **L^{H}-Ag^{I}** in $CDCl_3$.

2.5.6 Single-crystal X-ray diffraction data

2.5.6.1 Crystal structure data for the triazoles, K^{tBu}, K^{H}_{dipp} and the triazolium salt, L^{H}.



K^{tBu} K^{H}_{dipp} L^{H}

Figure 2.31. Molecular structures of the triazoles K^{tBu}, K^{H}_{dipp} and the triazolium salt, L^{H}, showing 50% probability ellipsoids and partial atom-numbering scheme. Hydrogens are omitted for clarity. Selected bond lengths (Å) and angles (°) for K^{tBu}: C1–C2 1.370(2), C2–N3 1.368(2), N2–N3 1.309(2), N1–N2 1.351(2), N1–C1 1.352(2), N1–C1–C2 105.07(15); K^{H}_{dipp}: C1–C2 1.369(6), C2–N3 1.377(5), N2–N3 1.302(5), N1–N2 1.350(5), N1–C1 1.349(5), N1–C1–C2 105.3(4); L^{H}: C1–C2 1.364(3), C2–N3 1.364(2), N2–N3 1.316(2), N1–N2 1.322(2), N1–C1 1.351(2), N1–C1–C2 106.03(17)

K^{tBu}: $C_{38}H_{37}Cl_6N_7$ (M = 804.44 g/mol): orthorhombic, space group *Pbca* (no. 61), a = 23.608(2) Å, b = 12.0460(12) Å, c = 27.425(3) Å, V = 7799.3(13) Å^3, Z = 8, T = 173.15 K, μ(MoKα) = 0.479 mm^{-1}, *Dcalc* = 1.370 g/cm^3, 110764 reflections measured (2.97° ≤ 2Θ ≤ 56.478°), 9591 unique (R_{int} = 0.0377, R_{sigma} = 0.0176) which were used in all calculations. The final R_1 was 0.0480 (I > 2σ(I)) and wR_2 was 0.1285 (all data).

K^{H}_{dipp}: $C_{83}H_{90}Cl_8N_{14}$ (*M* = 1567.28 g/mol): orthorhombic, space group $P2_12_12_1$ (no. 19), *a* = 12.6789(4) Å, *b* = 13.3047(4) Å, *c* = 48.1202(15) Å, *V* = 8117.3(4) Å^3, *Z* = 4, *T* = 173.15 K, μ(MoKα) = 0.331 mm^{-1}, *Dcalc* = 1.282 g/cm^3, 80420 reflections measured (3.176° ≤ 2Θ ≤ 56.638°), 20135 unique (R_{int} = 0.0425, R_{sigma} = 0.0385) which were used in all calculations. The final R_1 was 0.0643 (I > 2σ(I)) and wR_2 was 0.1801 (all data).

L^{H}: $C_{32}H_{29}B_2F_8N_7$ (*M* = 685.24 g/mol): monoclinic, space group $P2_1/n$ (no. 14), *a* = 14.5087(3) Å, *b* = 12.1465(3) Å, *c* = 17.8754(4) Å, *β* = 102.9728(12)°, *V* = 3069.78(12) Å^3, *Z* = 4, *T* = 173.15 K, μ(MoKα) = 0.124 mm^{-1}, *Dcalc* = 1.483 g/cm^3, 37863 reflections measured (3.278° ≤ 2Θ ≤ 56°), 7404 unique (R_{int} = 0.0391, R_{sigma} = 0.0436) which were used in all calculations. The final R_1 was 0.0524 (I > 2σ(I)) and wR_2 was 0.1476 (all data).

2.5.6.2 Crystal structure data for the metal complexes, L^{tBu}-Au^{I}, L^{tBu}-*N*-AgCl-Au^{I}, L^{tBu}-Ag^{I} and L^{H}-Ag^{I}

L^{tBu}-Au^{I}: $C_{83.5}H_{93}Ag_2Au_2Cl_{11}N_{14}$ (*M* = 2292.34 g/mol): triclinic, space group *P*-1 (no. 2), *a* = 13.3806(3) Å, *b* = 15.7343(4) Å, *c* = 22.0730(5) Å, *α* = 79.6820(10)°, *β* = 77.5350(10)°, *γ* = 85.1820(10)°, *V* = 4459.23(18) Å^3, *Z* = 2, *T* = 173.15 K, μ(MoKα) = 4.094 mm^{-1}, *Dcalc* = 1.707 g/cm^3, 164663 reflections measured (2.99° ≤ 2Θ ≤ 56.832°), 22046 unique (R_{int} = 0.1075, R_{sigma} = 0.0688) which were used in all calculations. The final R_1 was 0.0369 (I > 2σ(I)) and wR_2 was 0.0955 (all data).

L^{tBu}-*N*-AgCl-Au^{I}: $C_{41.5}H_{46}AgAuCl_4N_7$ (*M* = 1089.49 g/mol): monoclinic, space group *C*2/*c* (no. 15), *a* = 20.4625(11) Å, *b* = 18.4479(12) Å, *c* = 22.5829(13) Å, *β* = 91.071(4)°, *V* = 8523.3(9) Å^3, *Z* = 8, *T* = 173.15 K, μ(MoKα) = 4.188 mm^{-1}, *Dcalc* = 1.698 g/cm^3, 48833 reflections measured (2.972° ≤ 2Θ ≤ 53.112°), 8787 unique (R_{int} = 0.2369, R_{sigma} = 0.2648) which were used in all calculations. The final R_1 was 0.0666 (I > 2σ(I)) and wR_2 was 0.1362 (all data).

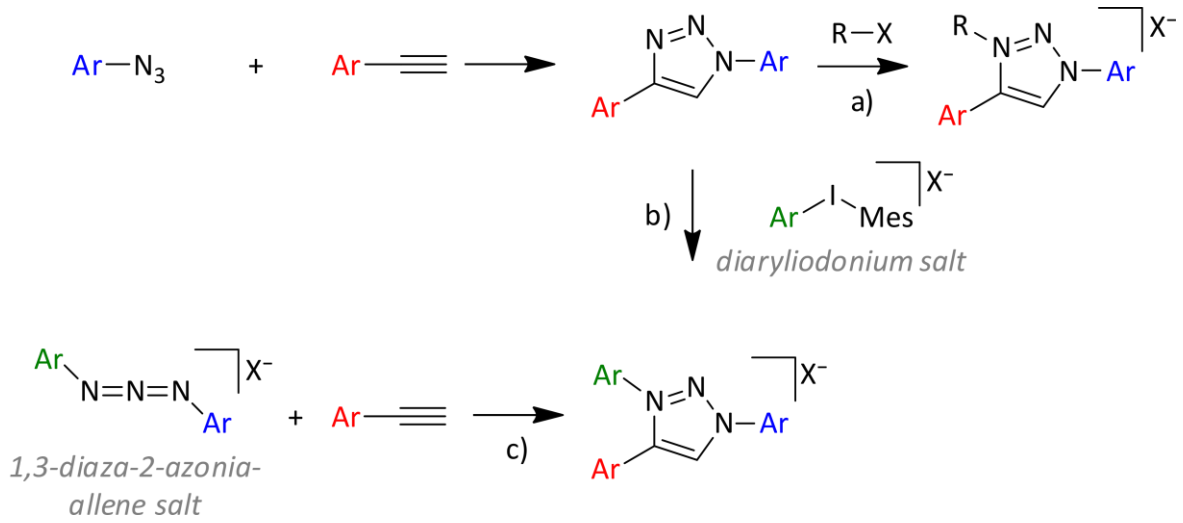
L^{tBu}-Ag^{I}: $C_{87}H_{97}Ag_4Cl_{11}N_{14}O$ (M = 2176.21 g/mol): triclinic, space group *P*-1 (no. 2), *a* = 15.3749(6) Å, *b* = 17.8182(7) Å, *c* = 19.1815(7) Å, *α* = 97.825(2)°, *β* = 112.556(2)°, *γ* = 90.804(2)°, *V* = 4795.0(3) Å3, *Z* = 2, *T* = 173.15 K, μ(MoKα) = 1.162 mm-1, *Dcalc* = 1.507 g/cm3, 86531 reflections measured (2.876° ≤ 2Θ ≤ 56.95°), 23946 unique (R_{int} = 0.0506, R_{sigma} = 0.0432) which were used in all calculations. The final R_1 was 0.0728 (I > 2σ(I)) and wR_2 was 0.2092 (all data).

L^H-Ag^I: $C_{71}H_{60}Ag_4Cl_2N_{14}$ (*M* = 1611.71 g/mol): tetragonal, space group $P4_32_12$ (no. 96), *a* = 14.6293(6) Å, *c* = 30.1142(14) Å, *V* = 6444.9(6) Å^3, *Z* = 4, *T* = 173.15 K, μ(MoKα) = 1.336 mm^{-1}, *Dcalc* = 1.661 g/cm^3, 91680 reflections measured (5.57° ≤ 2Θ ≤ 56.654°), 8030 unique (R_{int} = 0.0454, R_{sigma} = 0.0239) which were used in all calculations. The final R_1 was 0.0357 (I > 2σ(I)) and wR_2 was 0.0750 (all data).

Chapter 3: Synthesis of N1,N3-diaryl-1,2,3-triazol-5-ylidene metal complexes and their evaluation as cytotoxic agents.

3.1 Introduction

The CuAAC methodology employed for the synthesis of 1,4-disubstituted-1,2,3-triazoles allows for the introduction of an alkyl substituent on the N3 of the triazole ring to generate the N3-alkylated-1,3,4-trisubstituted-1,2,3-triazolium salts (Scheme 3.1a). The introduction of an aryl substituent on N3 in this manner is generally not accessible.[173,191] The group of Košmrlj only recently reported on the synthesis of N1,N3-diarylated-1,2,3-triazolium salts with the use of diaryliodonium salts,[257] based on the procedure described by Gao et al. for the N-arylation of imidazoles (Scheme 3.1b).[258] The more commonly used method for the synthesis of N1,N3-diarylated-1,2,3-triazolium salts however, was reported by Bertrand et al.,[221] and is based on the cycloaddition of 1,3-diaza-2-azoniaallene salts with alkynes, adapted from the synthetic procedure originally described by Wirschun and Jochims (Scheme 3.1c).[259–261]



Scheme 3.1. The various synthetic routes available for 1,2,3-triazolium salts. (a) The triazole can be alkylated with an alkyl halide or an alkyl triflate to a N3-alkylated 1,2,3-triazolium salt.[173] (b) Alternatively, an aryl substituent can be introduced on the N3 of the triazole with diaryliodonium salts.[257] (c) The more commonly used method to obtain N1,N3-diarylated triazolium salts via the cycloaddition of 1,3-diaza-2-azoniaallene salts and terminal alkynes.[221]

As mentioned previously, metalation routes of N1,N3-diarylated-1,2,3-triazolium salts can include the transmetalation and the free-carbene route; both either concerted or with the isolation of the corresponding intermediate i.e., the silver(I) trz complex or the free trz,

respectively. Due to the enhanced kinetic stability of diarylated triazolium salts as opposed to their alkylated counterparts, intramolecular rearrangement or dealkylation are suppressed during the free-carbene metalation route.[173,191]

The potential therapeutic efficacy of an anticancer agent is investigated by means of numerous in vitro cell-based methods. These methods explore the impact of the drug candidate on tumour cells mostly in terms of cell viability and proliferation, cell death and cell cycle arrest, among others.[262]

The cytotoxicity of a compound is determined as a measure of cell viability or proliferation as a response to incremental concentrations of the presumed cytotoxic agent. Cell viability is the number of healthy cells in the sample and proliferation refers to the ability of the cells to divide.[263,264]

There are various in vitro assays that determine cytotoxicity as a measure of cellular viability and/or proliferation.[265] These assays can be classified as dye exclusion-, colorimetric-, fluorometric and luminometric assays. Among these, colorimetric assays are the most employed as they are fast, reproducible, sensitive and allow for high-throughput analysis.

Originally, the trypan blue dye exclusion assay was used to assess cell viability based on the principle that viable cells, with intact cell membranes, exclude the dye, whereas dead cells take up the dye and stain blue. The viable cells are distinguished and can be counted under a microscope using a haemocytometer.[263] Although trypan blue is still used today to determine the number of viable cells in a suspension, it is not employed in cytotoxicity assessment. The dye is toxic to mammalian cells, large number of samples are difficult to process as trypsinization is required and the occurrence of counting errors is not uncommon.[265]

The MTT (3-(4,5-dimethylthiazol-2-yl)-2,5-diphenyl-2H-tetrazolium bromide)[266,267] colorimetric assay is the most widely used metabolic assay today. The assay detects the number of viable cells with active mitochondria as these cells successfully cleave MTT (yellow) into formazan, a dark blue/purple product. The absorbance of the product is measured at 570 nm with a spectrophotometer suitable for 96-well plates, allowing for a large amount of quantitative data to be obtained in a short time. The reduction of MTT, however can be influenced by nonmitochondrial dehydrogenases, presence of NADH and other reducing

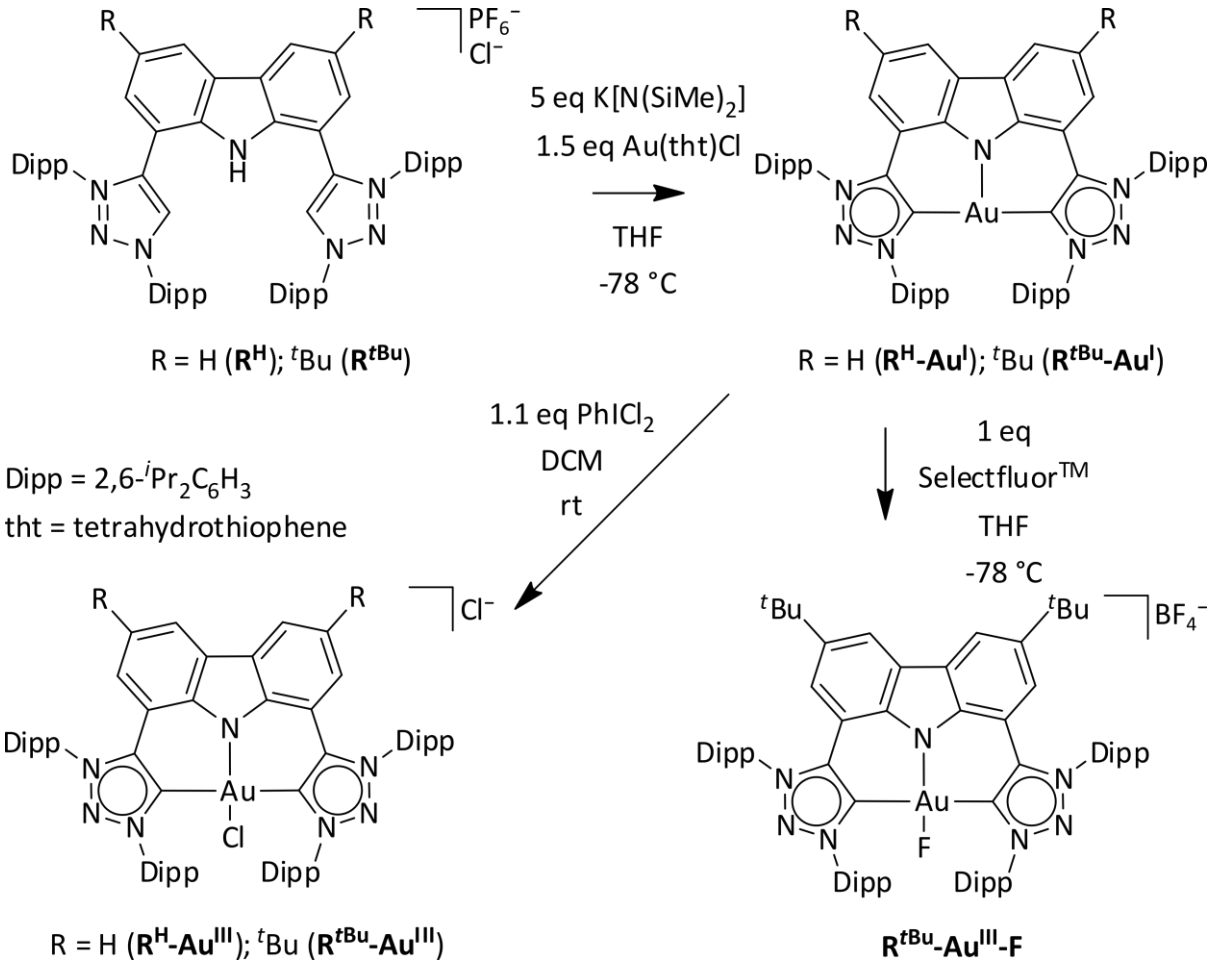
agents and any factors that affect the endocytosis of MTT and the exocytosis of MTT formazan.[268–270]

The crystal violet staining (CVS) assay is a quick and reliable colorimetric cell viability method that is independent of the metabolic products of viable cells.[271] Instead, the crystal violet dye (*N*-hexamethylpararosaniline)[264] stains the DNA and proteins of viable adherent cells (during cell death, the cells detach from cell culture plates). The absorbance of cells is directly related to the number of viable cells;[272] in fact the CVS assay was developed to determine the cell number of monolayer cultures[264,273] but has been modified as a suitable cytotoxicity assay.[274–276] In comparison to the MTT assay, the CVS assay is less influenced by the chemical nature of the drug,[269] experimental conditions (e.g. pH)[270] and has a much shorter incubation time.[272]

3.2 Aim

Following the results discussed in the previous chapter, the use of N3-alkylated-1,3,4-trisubstituted-1,2,3-triazolium salts, $\mathbf{L^{H}}$, $\mathbf{L^{tBu}}$, and $\mathbf{L^{tBu}_{dipp}}$, did not yield the anticipated CNC pincer gold(III) complexes of type **L-CNC-Au^{III}**. However, a pincer CNC gold(I) complex, $\mathbf{R^{tBu}}$-**Au^{I}** was successfully synthesized from the previously reported N1,N3-diarylated-1,3,4-trisubsituted-1,2,3-triazolium salt, $\mathbf{R^{tBu}}$ and subsequently oxidized to the pincer CNC gold(III) complex with fluoride ($\mathbf{R^{tBu}}$-**Au^{III}-F**) as an ancillary ligand (Scheme 3.2).[118,198,201] Herein is presented the synthesis of the 3,6-unfunctionalized-N1,N3-diarylated-triazolium salt ($\mathbf{R^{H}}$, **Scheme 3.2**), analogous to the known 3,6-*tert*-butyl-N1,N3-diarylated triazolium salt, $\mathbf{R^{tBu}}$. Followed by the complexation to the pincer CNC gold(I) complex ($\mathbf{R^{H}}$-**Au^{I}**, Scheme 3.2) and subsequent oxidation to the pincer CNC gold(III) complex ($\mathbf{R^{H}}$-**Au^{III}**, Scheme 3.2).

Both 1,3-diarylated triazolium salts, $\mathbf{R^{H}}$ and $\mathbf{R^{tBu}}$ and their corresponding pincer CNC gold(I) and gold(III) complexes were evaluated for their potential as cytotoxicity agents against the human breast cancer cell line, MDA-MB-231, using the CVS assay. Selectivity studies were conducted concurrently on the non-cancerous human endothelial cell line, EA.hy926.



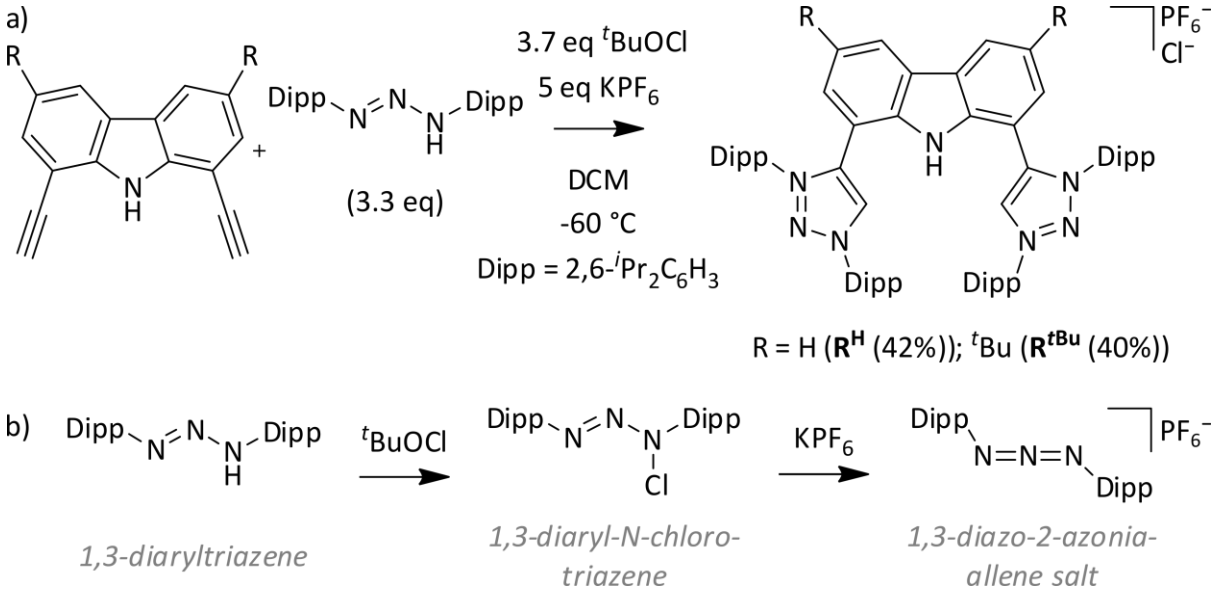
Scheme 3.2. The synthesis of the new triazolium salt, $\mathbf{R^H}$ and the corresponding gold(I) ($\mathbf{R^H}$-$\mathbf{Au^I}$) and gold(III) ($\mathbf{R^H}$-$\mathbf{Au^{III}}$) complexes are based on the synthesis previously reported for $\mathbf{R^{tBu}}$ and $\mathbf{R^{tBu}}$-$\mathbf{Au^I}$.[118,198] The gold(III)-fluorido complex, $\mathbf{R^{tBu}}$-$\mathbf{Au^{III}}$-**F** is the first example of stable monomeric cationic gold(III) fluoride,[201] while the synthesis of the gold(III) chloride complex $\mathbf{R^{tBu}}$-$\mathbf{Au^{III}}$ has not been previously described.

3.3 Results and Discussion

3.3.1 Synthesis of the triazolium salts, R^H and R^{tBu}

The N1,N3-diarylated triazolium salt, $\mathbf{R^{tBu}}$ was synthesized according to the procedure reported previously[118] and the synthesis of $\mathbf{R^H}$ was adapted accordingly (Scheme 3.3a). The syntheses of both $\mathbf{R^{tBu}}$ and $\mathbf{R^H}$ follows an adapted procedure for the cycloaddition of 1,3-diaza-2-azoniaallene and alkynes to produce N1,N3-diarylated-1,2,3-triazolium salts. The 1,3-diaza-2-azoniaallene salts required in the cycloaddition reaction are generated in situ whereby their precursors, N1,N3-diarylated triazenes are oxidized to N-chlorotriazenes with *tert*-butyl hypochlorite (Scheme 3.3b). Subsequently, the N-chlorotriazenes react with suitable Lewis

acids, such as potassium hexafluorophosphate and forms the 1,3-diaza-2-azoniaallene salts (stable under −50°C) to undergo cycloaddition with an appropriate alkyne to generate N1,N3-diarylated-1,2,3-triazolium salts.



Scheme 3.3. (a) The synthesis of $\mathbf{R^H}$ and $\mathbf{R^{tBu}}$ from their respective carbazole-based dialkynes with 1,3-diisopropylphenyltriaz-1-ene and (b) the in situ generation of the 1,3-diaza-2-azoniaallene salt from 1,3-diisopropylphenyltriaz-1-ene.[118,261]

The synthetic procedure involves the solvation of the appropriate dialkyne (3,6-*tert*-butyl-1,8-diethynyl-9H-carbazole for $\mathbf{R^{tBu}}$; 1,8-diethynyl-9H-carbazole for $\mathbf{R^H}$) and 3.7 equivalents of 1,3-bis(2,6-diisopropylphenyl)triaz-1-ene in anhydrous DCM under a nitrogen atmosphere. Excess potassium hexafluorophosphate was subsequently added and the reaction mixture was cooled down to −60 °C. Once cooled, *tert*-butyl hypochlorite was added dropwise, and the reaction mixture was kept cold for at least 6 hours following addition and was left to reach room temperature overnight. The dark red reaction mixture was filtered to remove all potassium-type salts (i.e., KPF_6, KCl) and the solvent of the filtrate was evaporated to a black solid. The crude solid was triturated with hexane followed by diethyl ether to afford $\mathbf{R^{tBu}}$ and $\mathbf{R^H}$ as white solids in 40% and 42% yield, respectively.

The ^{1}H-NMR spectrum of $\mathbf{R^H}$ in CD_3CN confirms the formation of $\mathbf{R^H}$ with the characteristic proton resonances of the carbazole amine at 13.46 ppm and the two triazolium (C5-H) proton resonances at 10.82 ppm, which is similar to those reported for the $\mathbf{R^{tBu}}$ (NH: δ_H 13.03 ppm; trz-CH: δ_H 10.95 ppm). The presence of the 2 aromatic protons (1c, Figure 3.1) and the

absence of the singlet representing the 18 protons of the *tert*-butyl groups distinguish the formation of $\mathbf{R^{H}}$ from $\mathbf{R^{tBu}}$.

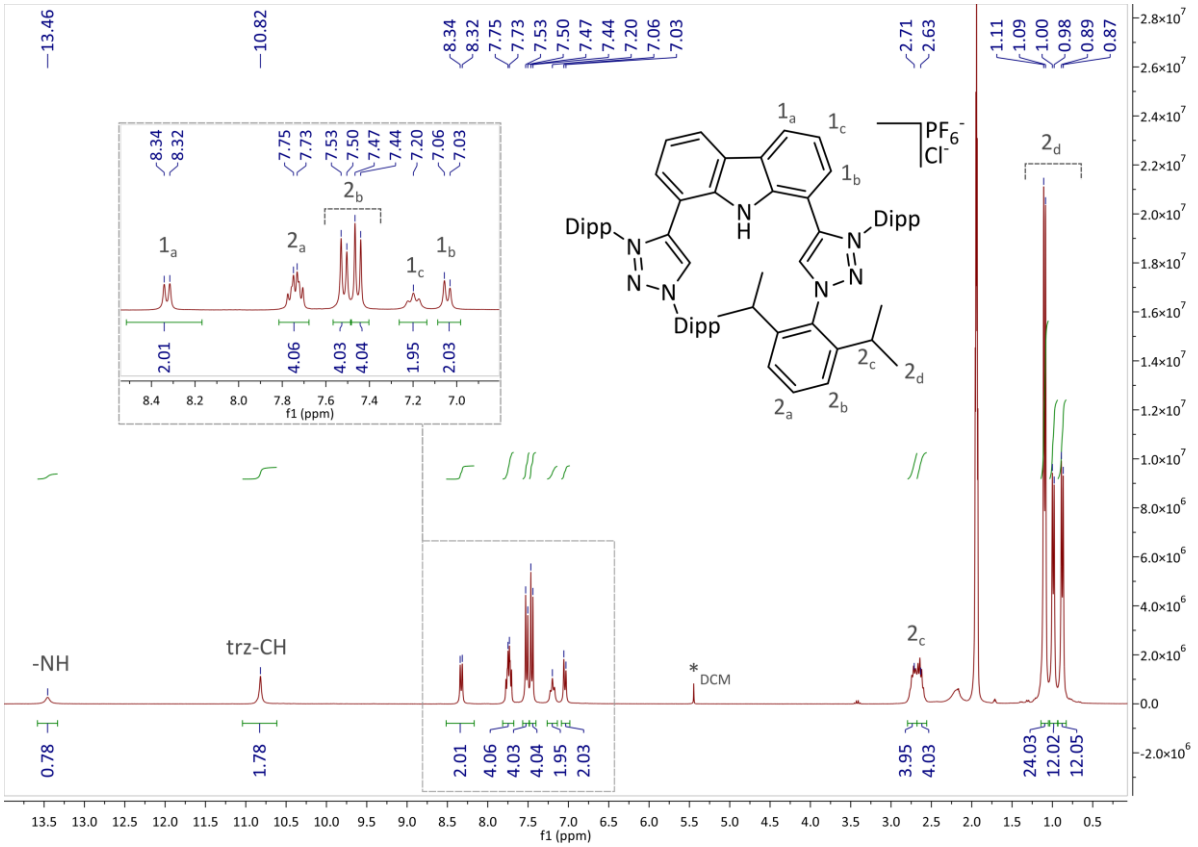
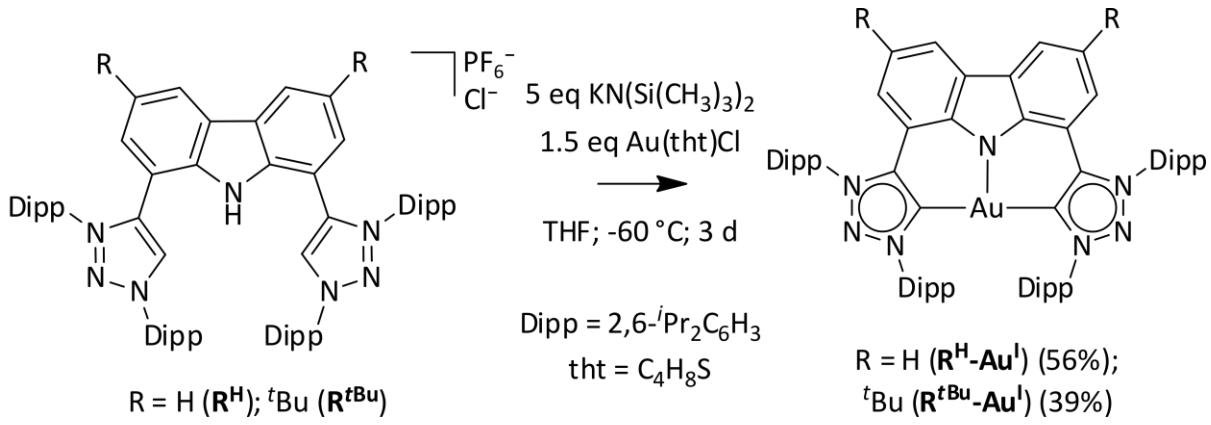


Figure 3.1. The ^{1}H NMR spectrum of $\mathbf{R^{H}}$ in CD_3CN

3.3.2 Synthesis of the CNC gold(I) complexes

Metalation of $\mathbf{R^{H}}$ and $\mathbf{R^{tBu}}$ to Au^{I} ensued via the concerted free-carbene metalation route based on the methodology reported for the synthesis of the pincer CNC gold(I) complex, $\mathbf{R^{tBu}}$-$\mathbf{Au^{I}}$ (Scheme 3.4).[198] $\mathbf{R^{H}}$ was weighed into a flame-dried Schlenk flask inside a glovebox and 5 equivalents of base, $K[Si(Me)_3)_2]$ and 1.5 equivalents of metal precursor, Au(tht)Cl, were added. Outside of the glovebox, the reaction vessel and a Schlenk flask with anhydrous THF were cooled down to −60 °C under an argon atmosphere. The cold THF was transferred to the solids, resulting in a red reaction mixture which was allowed to slowly reach room temperature overnight. When cold THF was added to $\mathbf{R^{H}}$ with base and without the presence of the metal precursor, the resulting solution was green and fluorescent, indicative of the formation of the free-carbene.[118] A clear solution of Au(tht)Cl in THF immediately changed colour to red upon the addition of the green free-carbene solution.



Scheme 3.4. The synthesis of the pincer CNC gold(I) complexes, $\mathbf{R^{H}}$-$\mathbf{Au^{I}}$ and $\mathbf{R^{tBu}}$-$\mathbf{Au^{I}}$ via the concerted free-carbene route previously reported for $\mathbf{R^{tBu}}$-$\mathbf{Au^{I}}$.[198]

The reaction continued for two more days before the solvent was evaporated. Anhydrous DCM was added to the crude solid resulting in a purple-red solution, which was subsequently filtered and evaporated. The crude solid was resuspended in diethyl ether and stirred overnight whereby the red-purple mixture changed colour to a red-orange suspension. The diethyl ether was evaporated and the solid was repeatedly washed with hexane, affording $\mathbf{R^{H}}$-$\mathbf{Au^{I}}$ as a red-orange solid in 56% yield.

Slight differences in solubilities of the gold(I) complexes, $\mathbf{R^{tBu}}$-$\mathbf{Au^{I}}$ and $\mathbf{R^{H}}$-$\mathbf{Au^{I}}$ were noted during product purification. For $\mathbf{R^{tBu}}$-$\mathbf{Au^{I}}$, the solid obtained after the evaporation of THF was re-dissolved in diethyl ether, whereas $\mathbf{R^{H}}$-$\mathbf{Au^{I}}$ was only slightly soluble in diethyl ether. Moreover, $\mathbf{R^{tBu}}$-$\mathbf{Au^{I}}$ dissolved in hexane to a greater extent than $\mathbf{R^{H}}$-$\mathbf{Au^{I}}$, resulting in a greater loss in yield during product purification than for $\mathbf{R^{H}}$-$\mathbf{Au^{I}}$. Nonetheless, $\mathbf{R^{tBu}}$-$\mathbf{Au^{I}}$ was obtained as a red solid in 39% yield.

Formation of $\mathbf{R^{H}}$-$\mathbf{Au^{I}}$ was confirmed by the disappearance of the amine and triazolium protons in the ^{1}H NMR spectrum (Figure 3.2) and the appearance of a carbene resonance at 175.0 ppm in the ^{13}C NMR spectrum in CD_2Cl_2 (inset of Figure 3.2) and 175.9 ppm in C_6D_6. The carbene carbon signal is comparable to that reported for $\mathbf{R^{tBu}}$-$\mathbf{Au^{I}}$ (δ_C 176.0 ppm in C_6D_6) and the mesityl analogue (δ_C 175.8 ppm in C_6D_6).[198] The carbene resonances of previously reported N1,N3-diarylated ferrocenyl substituted gold(I) complexes were all within the range of 183.1 ppm and 160.9 ppm ($CDCl_3$).[197]

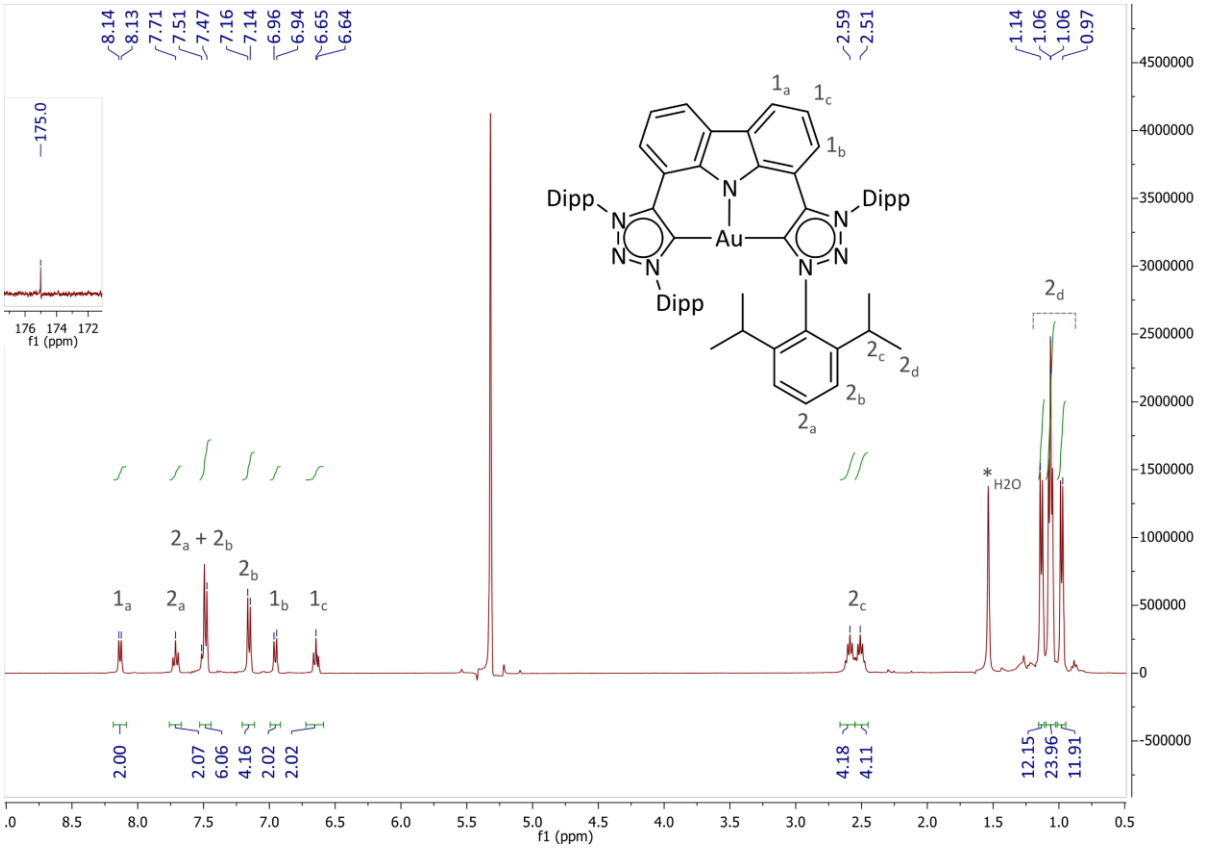


Figure 3.2. The ^{1}H NMR spectrum of **R^{H}-Au^{I}** in CD_2Cl_2. The carbene resonance of the ^{13}C NMR spectrum is included as an inset.

Crystals of **R^{H}-Au^{I}** were quite easily obtained from either an NMR sample in CD_2Cl_2 or overnight from a concentrated DCM solution layered with pentane at −20 °C. The molecular structure of **R^{H}-Au^{I}** is shown in Figure 3.3. Similar to **R^{tBu}-Au^{I}**, **R^{H}-Au^{I}** features the unusual three-coordinate T-shape. Other known three-coordinate gold(I) complexes mostly display distorted trigonal planar geometries.[198] The carbazole moiety and the $C_{carbene}$-Au-$C_{carbene}$ plane are slightly bent towards each other (Figure 3.3b). Compared to **R^{tBu}-Au^{I}**, **R^{H}-Au^{I}** is associated with a shorter Au-$C_{carbene}$ bond length (2.023(4) Å vs. 2.060 Å) and a longer Au-N_{amido} bond (2.445(3) Å vs. 2.325(2) Å). These bond lengths are in the range of other Au-$C_{carbene}$ lengths of known trz complexes (1.962–2.060 Å).[173] The $C_{carbene}$-Au-N_{amido} bond angle approach 90° with an averaged bond angle of 85.4(14)° and the $C_{carbene}$-Au-$C_{carbene}$ bond deviates from linearity with a bond angle of 169.83(15)°. The N3-Dipp substituents are orientated parallel to each other and rotated perpendicular to the carbazole plane that allow small substrates to approach the Au^{I} centre.

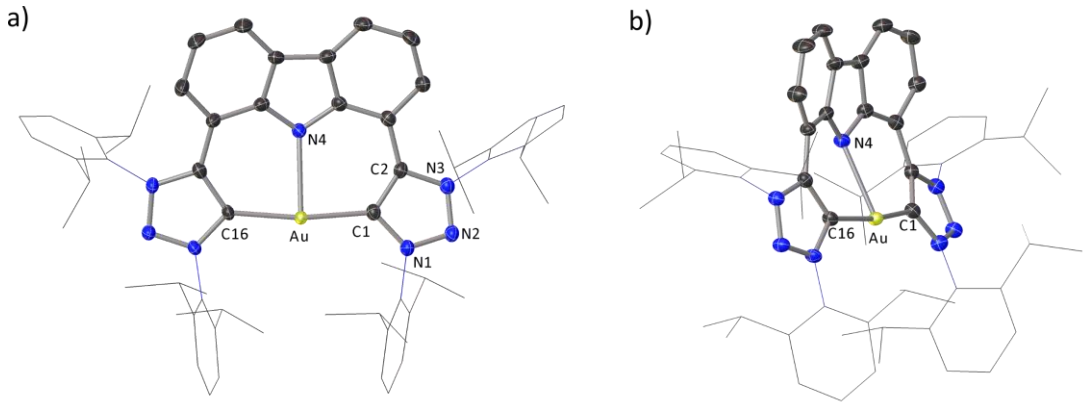
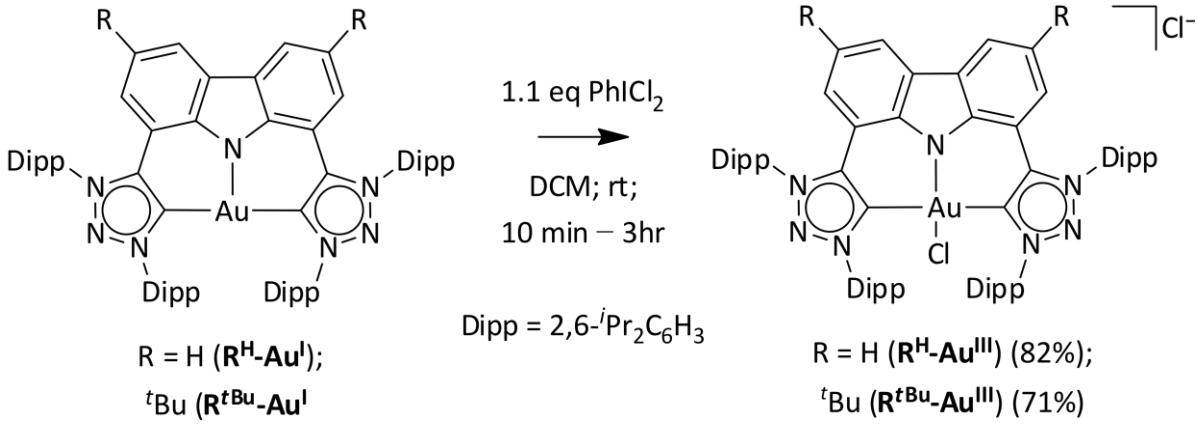


Figure 3.3. Molecular structure of $\mathbf{R^{H}}$-$\mathbf{Au^{I}}$, viewed from the (a) front and the (b) side showing 50% probability ellipsoids and partial atom-numbering scheme. Hydrogens are omitted and the wingtip functionalities are displayed as wireframes for clarity. Selected bond lengths (Å) and angles (°) for $\mathbf{R^{H}}$-$\mathbf{Au^{I}}$: Au1–C1 2.024(3), Au1–C16 2.021(3), Au1–N4 2.445(3), C1–C2 1.409(5), C1–N1 1.364(5), N1–N2 1.335(4), N2–N3 1.331(4), C2–N3 1.385(4), C1–Au1–C16 169.85(15), C1–Au1–N4 86.12(14), C16–Au1–N4 84.65(13).

3.3.3 Synthesis of the CNC gold(III) complexes

After the successful synthesis of the pincer gold(I) complexes, $\mathbf{R^{H}}$-$\mathbf{Au^{I}}$ and $\mathbf{R^{tBu}}$-$\mathbf{Au^{I}}$, the facile oxidation to their corresponding gold(III) complexes, $\mathbf{R^{H}}$-$\mathbf{Au^{III}}$ and $\mathbf{R^{tBu}}$-$\mathbf{Au^{III}}$ were performed with iodobenzene dichloride ($PhICl_2$) as oxidizing agent.[277]



Scheme 3.5. The oxidation of the pincer CNC gold(I) complexes $\mathbf{R^{H}}$-$\mathbf{Au^{I}}$ and $\mathbf{R^{tBu}}$-$\mathbf{Au^{I}}$ to their corresponding gold(III) chlorido complexes, $\mathbf{R^{H}}$-$\mathbf{Au^{III}}$ and $\mathbf{R^{tBu}}$-$\mathbf{Au^{III}}$, respectively.

The oxidation of $\mathbf{R^{H}}$-$\mathbf{Au^{I}}$ and $\mathbf{R^{tBu}}$-$\mathbf{Au^{I}}$ were carried out in anhydrous DCM in a Schlenk flask at room temperature under a nitrogen atmosphere. The oxidizing agent, $PhICl_2$ was added in stoichiometric amounts and upon addition the red solution, containing the gold(I) complex, changed colour to light orange. The oxidation of $\mathbf{R^{H}}$-$\mathbf{Au^{I}}$ to $\mathbf{R^{H}}$-$\mathbf{Au^{III}}$ continued for three more

hours, whereas the reaction of **R^{tBu}-Au^{III}** was completed within 10 minutes. The reaction mixture was filtered, and the filtrate was evaporated. The crude solid was washed with pentane to afford **R^{H}-Au^{III}** and **R^{tBu}-Au^{III}** as light orange solids in 82% and 71% yield, respectively.

Generally, the oxidation of gold(I) NHC to gold(III) NHC complexes are accompanied by an upfield carbene resonance shift of 20–30 ppm.[278] However, in the case of **R^{H}-Au^{III}** and **R^{tBu}-Au^{III}**, the expected carbene resonance upfield shift was not observed and the oxidation event, if only NMR spectroscopy is considered, was only accompanied by the disappearance of the gold(I) carbene resonance of **R^{H}-Au^{I}** and **R^{tBu}-Au^{I}**. The carbene resonance for the previously reported, **R^{tBu}-Au^{III}-F** (Scheme 3.2) was also not observed from the ^{13}C {^{1}H} NMR spectrum.[201] Although few, there are other examples of gold(III) trz complexes for which the gold(III)-carbene resonances are reported. The group of Mendoza-Espinosa reported the carbene resonances of cationic bistrz diiodo gold(III) complexes at 159.3–160.1 ppm, about 10 ppm upfield from their corresponding gold(I) complexes (δ_C 171–170.6 ppm).[279] The oxidation of the mesityl-analogue of **R^{tBu}-Au^{I}** to the corresponding gold(III) complexes with methyl and chloromethyl as ancillary ligands also reported gold(III)-carbene resonances at 146.3 and 145.7 ppm, respectively.[198]

Crystals of **R^{H}-Au^{III}** were obtained from a saturated DCM solution layered with toluene at room temperature and the solid-state structure is shown in Figure 3.4. The geometry of the Au^{III} atom is square planar with all the associated bond angles approaching 90° (avg $C_{carbene}$–Au–N: 88.94(12)°; $C_{carbene}$–Au–Cl: 91.54(10)°) and both bond angles of N–Au–Cl (172.97(9)°) and $C_{carbene}$–Au–$C_{carbene}$ (171.54(14)°) deviate slightly from linearity. The average Au-$C_{carbene}$ bond length increased slightly to 2.047(4) Å as compared to the gold(I) precursor, **R^{H}-Au^{I}** (2.023(4) Å) while the Au-N_{amido} bond length significantly decreased to 2.010(3) Å from 2.445(3) Å, as expected for a metal in higher oxidation state; the considerable change in the Au^{III}-N_{amido} bond length between the gold(I) and the gold(III) complex were also reported for the gold(III)-chloromethyl mesityl analogue of **R^{tBu}-Au^{I}** and the flourido complex, **R^{tBu}-Au^{III}-F**.[198,201] The $C_{carbene}$-Au-$C_{carbene}$ plane is slightly twisted in relation to the carbazole moiety whereby one of the triazoles rings (C1) is orientated 4.6° above the carbazole plane and the other triazole ring is 21.3(6)° below the plane of the carbazole moiety (Figure 3.4b).

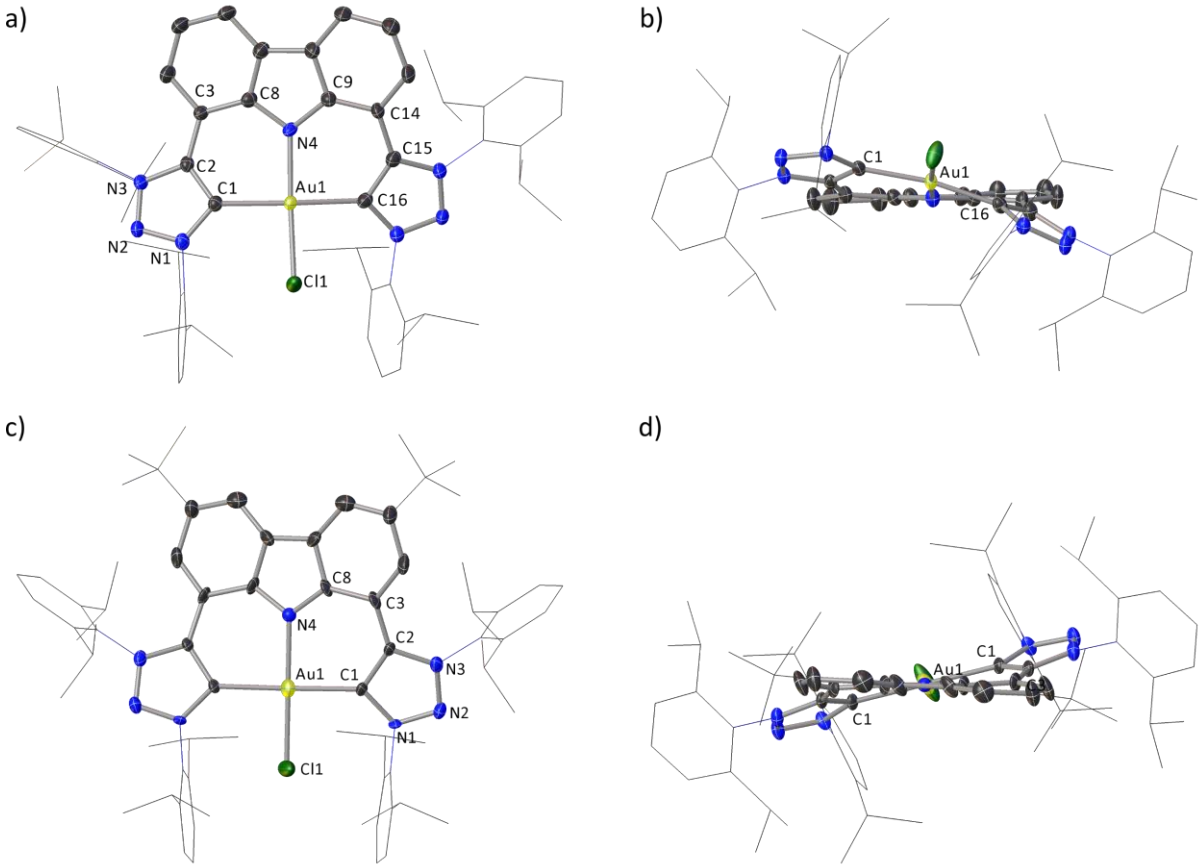


Figure 3.4. Molecular structure of $\mathbf{R^{H}}$-$\mathbf{Au^{III}}$, viewed from the (a) front and the (b) side, and $\mathbf{R^{tBu}}$-$\mathbf{Au^{III}}$ viewed from the (c) front and the (d) side, showing 50% probability ellipsoids and partial atom-numbering scheme. Hydrogens and counterions are omitted and the wingtip functionalities are displayed as wireframes for clarity. Selected bond lengths (Å) and angles (°) for $\mathbf{R^{H}}$-$\mathbf{Au^{III}}$: Au1–C1 2.054(3), Au1–C16 2.040(4), Au1–N4 2.010(3), Au1–Cl1 2.266(10), C1–C2 1.394(5), C1–N1 1.373(4), N1–N2 1.330(4), N2–N3 1.315(4), C2–N3 1.373(4), C1–Au1–C16 171.54(14), N4–Au1–Cl1 172.97(9), C1–Au1–Cl1 92.83(10), C16–Au1–Cl1 90.24(10), C1–Au1–N4 89.86(12), C16–Au1–N4 88.01(12), C1–C2–C3–C8 4.6(6), C9–C14–C15–C16 −21.3(6); for $\mathbf{R^{tBu}}$-$\mathbf{Au^{III}}$: Au1–C1 2.066(5), Au1–N4 2.045(7), Au1–Cl1 2.235(3), C1–C2 1.404(9), C1–N1 1.363(8), N1–N2 1.318(7), N2–N3 1.341(8), C2–N3 1.378(8), C1–Au1–C1' 179.0(4), N4–Au1–Cl1 180.0, C1–Au1–Cl1 90.5(2), C1–Au1–N4 89.5(2), C1–C2–C3–C8 −11.7(10).

Similar to that of $\mathbf{R^{H}}$-$\mathbf{Au^{III}}$, the geometry of the solid-state structure of $\mathbf{R^{tBu}}$-$\mathbf{Au^{III}}$ (Figure 3.4c) is also square planar with the associated bond angles around the Au^{III} atom close to 90° ($C_{carbene}$–Au–N_{amido}: 89.5(2)°; $C_{carbene}$–Au–Cl: 90.5(2)°) and 180° ($C_{carbene}$–Au-$C_{carbene}$: 179.0(4)°; N–Au–Cl 180.0°). The asymmetric unit of the molecular structure is half of that shown in Figure 3.4c, where the plane of symmetry is down the N4–Au1–Cl1 plane (C_2-symmetry). The Au–$C_{carbene}$ bond length of 2.066(5) Å and the Au-N_{amido} bond length of 2.045(7)° are both

longer than that reported for **R^H-Au^{III}** (Au–$C_{carbene}$: 2.047 Å; Au-N: 2.010(3) Å) and are within the range reported previously of Au-$C_{carbene}$ and Au-N_{amido} bond lengths reported previously.[198,201] Similar to **R^H-Au^{III}**, the $C_{carbene}$–Au–$C_{carbene}$ plane is twisted in relation to the carbazole moiety. Due to the symmetry in the solid-state structure, both triazolylidene rings are orientated 11.7(10)° above and below the plane of the carbazole moiety, respectively (Figure 3.4d).

3.3.4 Cytotoxicity studies

Preliminary cytotoxicity studies were conducted to identify active ligand precursors (**R^H** and **R^{tBu}**) and their complexes (**R^H-Au^I**, **R^{tBu}-Au^I**, **R^H-Au^{III}** and **R^{tBu}-Au^{III}**) against the breast cancer cell line, MDA-MB-231. The cancer cells were exposed to two single point concentrations of 50 µM and 5 µM for 48 h and the percentage cell viability was determined using the CVS assay.

For each compound, a 50 mM stock solution in DMSO was prepared and subsequently diluted in culture medium to concentrations of 50 and 5 µM where the maximum concentration of DMSO never exceeded 0.1%. In a 96-well plate, MDA-MB-231 cells were seeded at 5000 cells per well and allowed to adhere to the plate overnight in a humidified atmosphere at 37 °C and 5% CO_2. The medium was replaced with medium containing compounds at concentrations of 50 and 5 µM each. Conducting the experiment in a 96-well plate allowed for 6 replicates for each compound at each of the two concentrations. The cells were exposed to the compounds for 48 h in a humidified atmosphere at 37 °C and 5% CO_2, after which the cell viability was established using the CVS assay.

The CVS assay involves the removal of the treated medium and the addition of 1% glutaraldehyde to the cells as fixative. After 15 minutes of incubation, the glutaraldehyde solution is discarded, and the adhered cells were incubated with 0.1% crystal violet to stain the DNA and protein of viable adherent cells. The cells were incubated with the crystal violet stain for 30 minutes at room temperature after which the dye was removed, and the plates washed with water to rid the plates of excess dye. The plates were then left to dry overnight. The bound dye inside the wells of the 96-well plates were solubilized with 0.2% Triton-X and transferred to a 96-well reading plate. The absorbance of each well was read at 570 nm. The percentage cell viability was calculated as follows:

$$\% \text{ cell viability} = \frac{A_{treated}}{A_{control}} \times 100; \text{ where A = background corrected absorbance}$$

The results for the initial screening are shown in Figure 3.5. At 50 μM (blue bars, Figure 3.5), all compounds inhibited the growth of the cells by more than 50% except for the neutral gold(I) pincer complex, **R^{tBu}-Au^{I}**. At 5 μM (green bars, Figure 3.5), only the cells treated with the cationic gold(III) pincer complex, **R^{H}-Au^{III}** and the corresponding ligand precursor salt, **R^{H}** resulted in less than 50% cell viability. At both concentrations, **R^{H}** and **R^{H}-Au^{III}** were the best performing compounds in terms of cytotoxicity towards the cancer cells, MDA-MB-231.

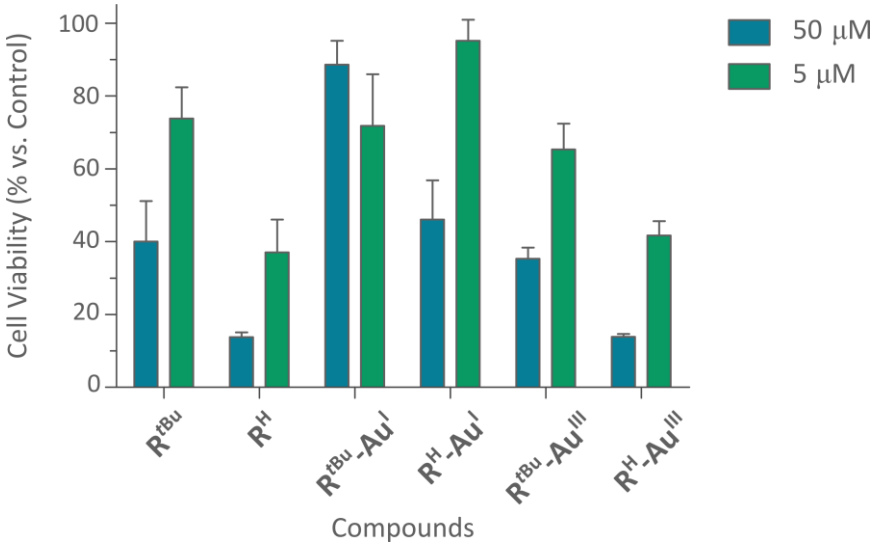


Figure 3.5. The percentage cell viability (determined by CVS assay) of MDA-MB-231 cells treated against the CNC gold(I/III) pincer complexes and their corresponding precursor ligand salts at 5 μM and 50 μM after 48 h of drug exposure compared to the control (0.1% DMSO). Data represent the average ± standard error from mean for 6 replicates of one experiment.

The solubility of the compounds had a significant impact on the results obtained from the preliminary study. The neutral gold(I) complexes, **R^{H}-Au^{I}** and **R^{tBu}-Au^{I}** exhibited low cytotoxicity and this can be attributed by their complete insolubility in DMSO. The cationic gold(III) complexes were soluble in the DMSO (**R^{H}-Au^{III}** to a greater extent than **R^{tBu}-Au^{III}**) but precipitated in the culture medium overnight. The dicationic triazolium salts, **R^{H}** and **R^{tBu}** were soluble in both DMSO and the culture medium.

DMSO is used as a carrier solvent for metal complexes and organic ligands to assist in their solubilisation in the aqueous culture medium. Too high concentrations of DMSO are toxic to cells and therefore the amount of DMSO in treatment concentrations should be kept below 1%.[280–286] During the initial screening experiments, the DMSO concentration in compound

treatments did not exceed 0.1%. Moreover, due to the nucleophilic nature of DMSO, ligand dissociation of metal complexes in DMSO is not uncommon and can impact results obtained from biological screening.[287] Therefore, the stability of **R^H-Au^{III}**, as model compound, in DMSO during 48 h and 2 months were evaluated via ^{1}H NMR spectrometry (Figure 3.6) and after 2 months in DMSO, no observable changes in the ^{1}H NMR spectrum was found.

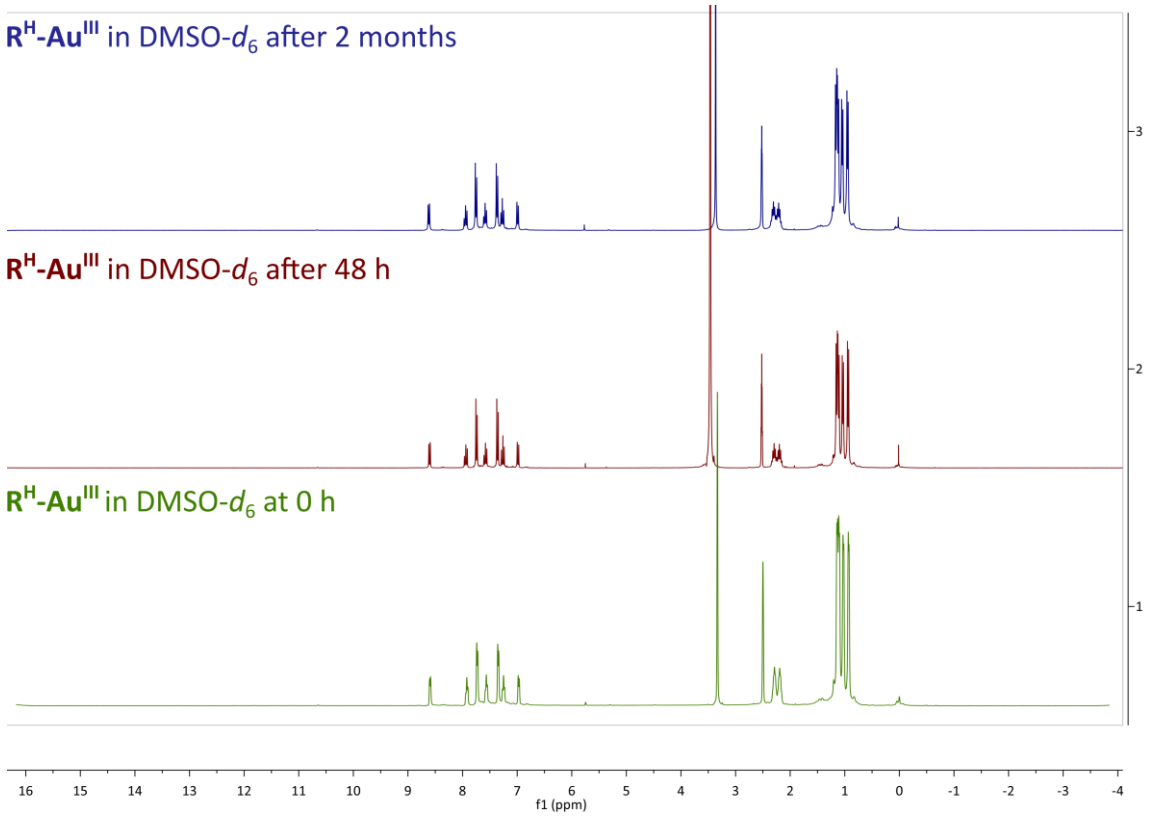


Figure 3.6. The ^{1}H NMR spectra of **R^H-Au^{III}** in $(CD_3)_2SO$ at 0 hr (green), 48 h (red) and 2 months (blue).

Since the triazolium salt, **R^H** and the corresponding gold(III) complex, **R^H-Au^{III}** decreased cell viability below 50% at both 50 and 5 µM during the preliminary experiment, these compounds were selected to undergo further screening to determine their IC_{50} (half maximal inhibitory concentration) against MDA-MB-231 cells. Selectivity towards healthy cells were also determined on the non-tumourigenic endothelial cell line, EA.hy926.

The IC_{50} values were determined using the CVS assay following the same procedure described above for the preliminary single-point concentration study. However, specific to IC_{50} experiments, incremental test concentrations in the range of 0.3 – 10 µM of each compound (**R^H** and **R^H-Au^{III}**) was prepared from their respective 50 mM stock solution in DMSO and the final DMSO concentration did not exceed 0.02%. In the case of **R^H-Au^{III}** against EA.hy926 cells, an additional concentration of 20 µM was needed to obtain an accurate IC_{50} value and as such

the highest DMSO concentration for these experiments were 0.04%. The cells were exposed to test concentrations for 48 h in a humidified atmosphere at 37 °C and 5% CO_2, after which the cell viability was calculated. The software package, *GraphPad Prism 5*, was used to calculate the IC_{50} values (Table 3.1) using non-linear regression analysis from the cell viability data obtained from the CVS assay. The dose-response curves, or more specifically, the concentration-response curves of $\mathbf{R^H\text{-}Au^{III}}$ and $\mathbf{R^H}$ against both cell lines, MDA-MB-231 (red) and EA.hy926 (blue) are shown in Figure 3.7a and b, respectively. The curves show the percentage cell viability compared to the control as response to incremental test concentrations of the compounds.

Table 3.1. The IC_{50} (± SEM) values in μM of $\mathbf{R^H\text{-}Au^{III}}$ and $\mathbf{R^H}$ against MDA-MB-231 and EA.hy926 cells

Entry	Compounds	IC_{50} (± SEM)[a]		T.I.[b]
		MDA-MB-231	EA.hy926	
1	$\mathbf{R^H\text{-}Au^{III}}$	2.3 (± 0.8)	8.6 (± 2.1)	3.8
2	$\mathbf{R^H}$	0.4 (± 0.1)	1.0 (± 0.2)	2.7

[a] Expressed as average ± standard error from mean of three independent experiments, each with 6 replicates. [b] T.I. refers to the therapeutic index and is calculated from the ratio of IC50 on the normal cells (EA.hy926) and the IC50 on tumour cells (MDA-MB-231).

The gold(III) complex, $\mathbf{R^H\text{-}Au^{III}}$ demonstrated high cytotoxic activity against the breast cancer cell line, MDA-MB-231 with a calculated IC_{50} value of 2.3 μM and a therapeutic index of 3.7 as the IC_{50} value of 8.6 μM was obtained against the normal cell line, EA.hy926 (entry 1, Table 3.1). Although direct comparison is not possible due to different incubation times, cytotoxicity assays employed, and the cell lines tested, $\mathbf{R^H\text{-}Au^{III}}$ compares well to the potency reported for other gold(III) complexes (discussed in Chapter 1; Table 1.2 and Table 1.3) where the IC_{50} values varied from 0.125 – 35 μM against various cell lines. Albeit on the lower end, the selectivity of $\mathbf{R^H\text{-}Au^{III}}$ towards cancer cells also falls within the range reported for other gold(III) complexes (T.I. 2.5 – 147; Table 1.2). Previously reported gold(I) NHC complexes with long aliphatic side-chains exhibited IC_{50} values of 3.6 – 16.8 μM specifically against MDA-MB-231 cells after 96 hours of incubation.[288] Gold(I) NHC complexes based on 4,5-diarylimidazoles exhibited higher cytotoxicity towards MDA-MB-231 cells, than the aliphatic gold(I) NHC complexes, with IC_{50} values of between 0.34 μM and 6.9 μM. The gold(III) analogues showed

potent activity in the nanomolar ranges (0.49 – 4.4 μM) after 72 hours of incubation.[130,289,290] The cytotoxicity of these complexes against normal cell lines were not investigated.

The dose-response curve of **R^H-Au^{III}** against MDA-MB-231 (represented by the red curve) and EA.hy926 cells (represented by the blue line) are shown in Figure 3.7a. Below 1 μM, the percentage cell viability of both cell lines are above 70%. At 1 μM and above, the percentage cell viability of the MDA-MB-231 cells drop to 60% with a progressive decline to 10% at the highest test concentration of 10 μM. In contrast, the percentage cell viability of the EA.hy926 cells drop below 50% around that same concentration (10 μM) and ~30% of the cells are still viable at 20 μM. The shape of both curves indicates that there is likely a minimum concentration of complex required before cytotoxicity ensues and once the limit is exceeded, the degree of cytotoxicity is accelerated.

The triazolium salt, **R^H** was much more potent than **R^H-Au^{III}** towards both cell lines with calculated IC_{50} values of 0.4 and 1.0 μM obtained for MDA-MB-231 and EA.hy926 cell lines, respectively. Some ligand precursors, including imidazolium and triazolium salts show cytotoxicity against certain cell lines. Previously reported pyridine-based triazolium salts exhibited activity towards HeLa tumour cells with IC_{50} values of 54.4 – 91.6 μM[291] and fluorine-substituted triazolium salts were significantly more cytotoxic against a wide variety of tumour cell lines with IC_{50} values as low as 1.7 μM.[292] **R^H** is considerably more toxic than previously reported triazolium salts and indicates that the ligand scaffold is quite toxic.

The dose-response curve of **R^H** against both cell lines are shown in Figure 3.7b, where the response of the MDA-MB-231 cells are represented by the red curve and the EA.hy926 cells are represented by the blue curve. Below 1 μM, the percentage cell viabilities of both cell lines are below 80%. At 1 μM, about 60% of the EA.hy926 cells are viable and the percentage cell viability of the MDA-MB-231 cells are below 50%. The two curves converge where the data points of both cell lines overlap at higher concentrations of 5 and 10 μM. For both cell lines, the change in the cell viability across increasing concentrations of **R^H** is small and results in 'flatter' curves compared to the dose-response curves of **R^H-Au^{III}**. Initially, the cytotoxicity of **R^H** at low concentrations is potent but fails to eliminate the MDA-MB-231 cells to the same extent observed with **R^H-Au^{III}**. Some selectivity of **R^H** towards the tumour cells are observed as the IC_{50} against EA.hy926 is 2.7-fold higher than the IC_{50} against the MDA-MB-231 cells, however, the dose-response curves indicate no significant separation between the responses

of the two different cell lines. The dose-response curve of **R^H-Au^{III}** do imply some selectivity as there are distinctly different responses observed for each cell line at the same concentration. These results indicate that even though the ligand precursor salt is more potent than the gold(III) complex, the ligand precursor salt is also more toxic to healthy cells than the gold(III) complex.

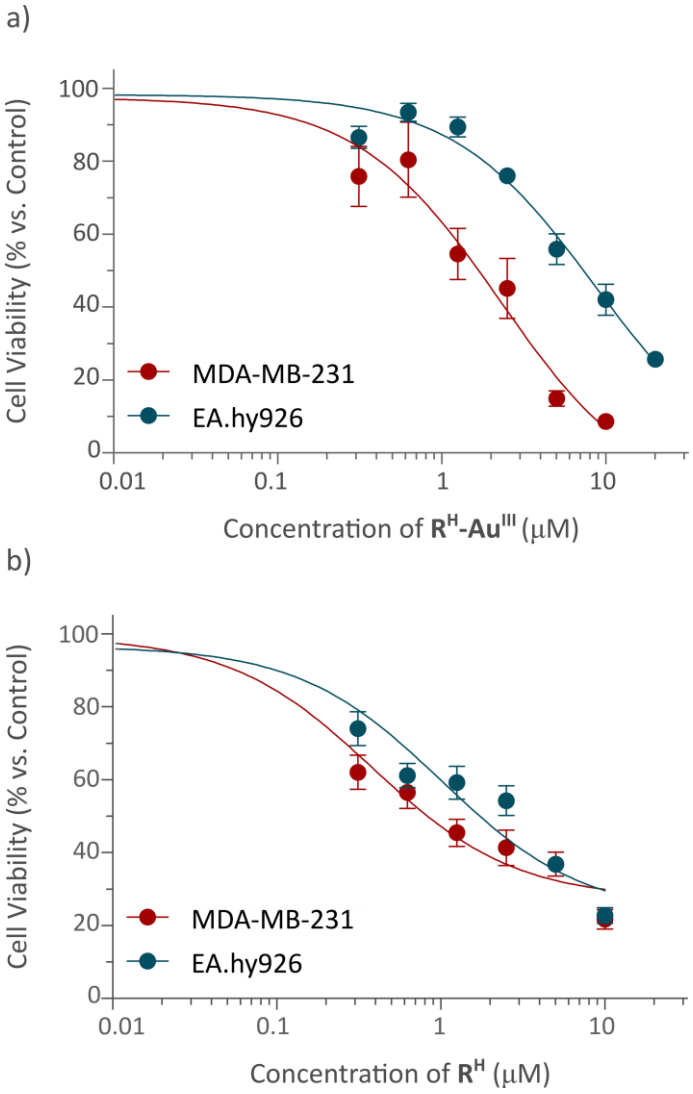


Figure 3.7. Dose-response curve of (a) **R^H-Au^{III}** and (b) **R^H** against MDA-MB-231 cells (red) and EA.hy926 (blue) cells. The graphs show the percentage cell viability compared to the control (0.02% DMSO except for **R^H-Au^{III}** and EA.hy926, which had 0.04% DMSO as vehicle control) as response to increasing concentrations of (a) **R^H-Au^{III}** and (b) **R^H**. Data represent the average ± standard error from mean for three independent experiments, each with 6 replicates.

3.4 Conclusion

The successful syntheses and characterization of a 3,6-unsubstituted analogue of $\mathbf{R^{tBu}}$, $\mathbf{R^{H}}$ was described followed by the metalation with gold(I) and oxidation to gold(III) to yield CNC pincer gold(I) and gold(III) complexes.

These compounds, ligand precursor salts and metal complexes, were subjected to cytotoxicity testing against two cell lines; the breast cancer cell line, MDA-MB-231 and the non-tumourigenic cell line, EA.hy926. Of these compounds, $\mathbf{R^{H}}$ and $\mathbf{R^{H}\text{-}Au^{III}}$ showed the most activity against MDA-MB-231 cells during preliminary screening at 50 and 5 μM and their IC_{50} values were subsequently measured. $\mathbf{R^{H}}$ proved to be potent with an IC_{50} in the nanomolar ranges but were toxic to EA.hy926 cells. Both cell lines were less sensitive to $\mathbf{R^{H}\text{-}Au^{III}}$ but the cytotoxicity and selectivity towards MDA-MB-231 cells were comparable to gold(III) complexes previously reported.

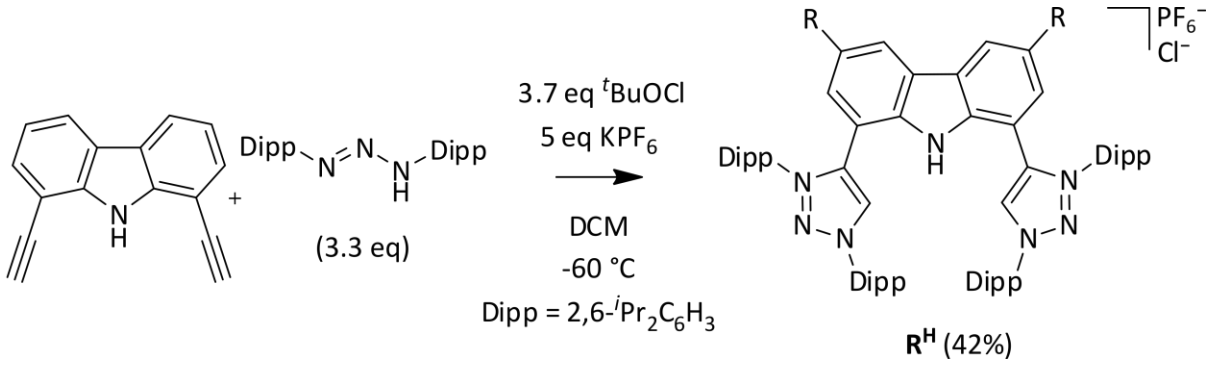
3.5 Experimental

3.5.1 General Considerations

The precursors 1,3-bis(2,6-diisopropylphenyl)triaz-1-ene,[293,294] *tert*-butyl hypochlorite[295] and dichloro iodobenzene[296] were all synthesized according to their literature procedures as well as the triazolium salt, $\mathbf{R^{tBu}}$ and the corresponding gold(I) complex, $\mathbf{R^{tBu}\text{-}Au^{I}}$.[118,198] All other reagents were commercially available and used without any purification.

Unless otherwise stated, aseptic conditions were applied throughout all in vitro procedures (including cell maintenance) and were conducted in a laminar flow cabinet. Distilled water, general glassware and pipette tips were sterilized via autoclave sterilization (120 °C at 15 psi for 20 min) and solutions were filtered-sterilized (0.22 μM pore size). The incubator and laboratory surfaces were regularly disinfected with 1% SDS (sodium dodecyl sulfate), 10% bleach and 70% ethanol. All chemicals, reagents, culture media and plastic consumable were commercially available.

3.5.2 Synthesis of the triazolium salt, 1,8-bis-(1,3-bis-(2,6-diisopropylphenyl)-1,2,3-triazolium)-9*H*-carbazole, $\mathbf{R^H}$.



$\mathbf{R^H}$ (42%)

An adapted procedure of the previously reported method for a diarylated triazolium salt synthesis was followed.[118,221] 1,8-diethynyl-9*H*-carbazole (0.9 g, 4.18 mmol, 1 eq), 1,3-bis(2,6-diisopropylphenyl)triaz-1-ene[293,294] (5.1 g, 13.96 mmol, 3.3 eq) and KPF_6 (3.85 g, 20.92 mmol, 5 eq) were dissolved in anhydrous DCM and cooled to −60 °C. In the dark, ^{t}BuOCl (1.51 g, 15.36 mmol, 3.7 eq) was added dropwise and the reaction was left overnight to warm up to room temperature. The reaction mixture was filtered, and the dark red filtrate was evaporated under reduced pressure. The crude solid product was subsequently triturated with hexane and diethyl ether affording the triazolium salt as a white solid. Yield: 2.20 g (42%). M.p. >300 °C. ^{1}H NMR (300 MHz, CD_3CN) δ 13.46 (s, 1H, NH), 10.82 (s, 2H, trz-CH), 8.33 (d, *J* = 7.7 Hz, 2H, Ar-$CH_{carbazole}$, H-1_a), 7.75 (t, *J* = 7.9 Hz, 2H, Ar-CH_{Dipp}, H-2_c), 7.73 (t, *J* = 7.9 Hz, 2H, Ar-CH_{Dipp}, H-2_c), 7.52 (d, *J* = 7.9 Hz, 4H, Ar-CH_{Dipp}, H-2_b), 7.45 (d, *J* = 7.8 Hz, 4H, Ar-CH_{Dipp}, H-2_b), 7.20 (dd, *J* = 7.8, 7.8, Hz, 2H, Ar-$CH_{carbazole}$, H-1_c), 7.04 (d, *J* = 7.8 Hz, 2H, Ar-$CH_{carbazole}$, H-1_b), 2.73 (sept, *J* = 6.7 Hz, 4H, ^{i}Pr-CH, H-2_c), 2.63 (sept, *J* = 6.6 Hz, 4H, ^{i}Pr-CH, H-2_c), 1.10 (d, *J* = 6.8 Hz, 24H), 0.99 (d, *J* = 6.7 Hz, 12H), 0.88 (d, *J* = 6.7 Hz, 12H) (all ^{i}Pr-CH_3). ^{13}C {^{1}H} NMR (75 MHz, CD_3CN) δ 146.7 (Ar-C_q), 146.6 (Ar-C_q), 134.3 (Ar-CH_{Dipp}, C-2_a), 134.1 (Ar-CH_{Dipp}, C-2_a), 131.8 (trz-CH), 130.9 (Ar-C_q), 128.0 (Ar-$CH_{carbazole}$, C-1_b), 127.4 (Ar-C_q), 126.7 (Ar-CH_{Dipp}, C-2_b), 126.1 (Ar-CH_{Dipp}, C-2_b), 125.5 (Ar-$CH_{carbazole}$, C-1_a), 121.6 (Ar-$CH_{carbazole}$, C-1_c), 108.2 (Ar-C_q), 29.9, 29.6 (all ^{i}Pr-CH, C-2_c), 25.4, 25.0, 23.8, 22.5 (all ^{i}Pr-CH_3, C-2_d). ^{19}F {^{1}H} NMR (470 MHz, CD_3CN) δ -67.63 (d, *J* = 707.7 Hz, PF_6). ^{31}P {^{1}H} NMR (202 MHz, CD_3CN) δ -139.9 (sept, *J* = 706.5 Hz, PF_6). ESI-HRMS (15 V, positive mode, m/z): calcd for M^{2+}: 471.8116. Found: 471.8117.

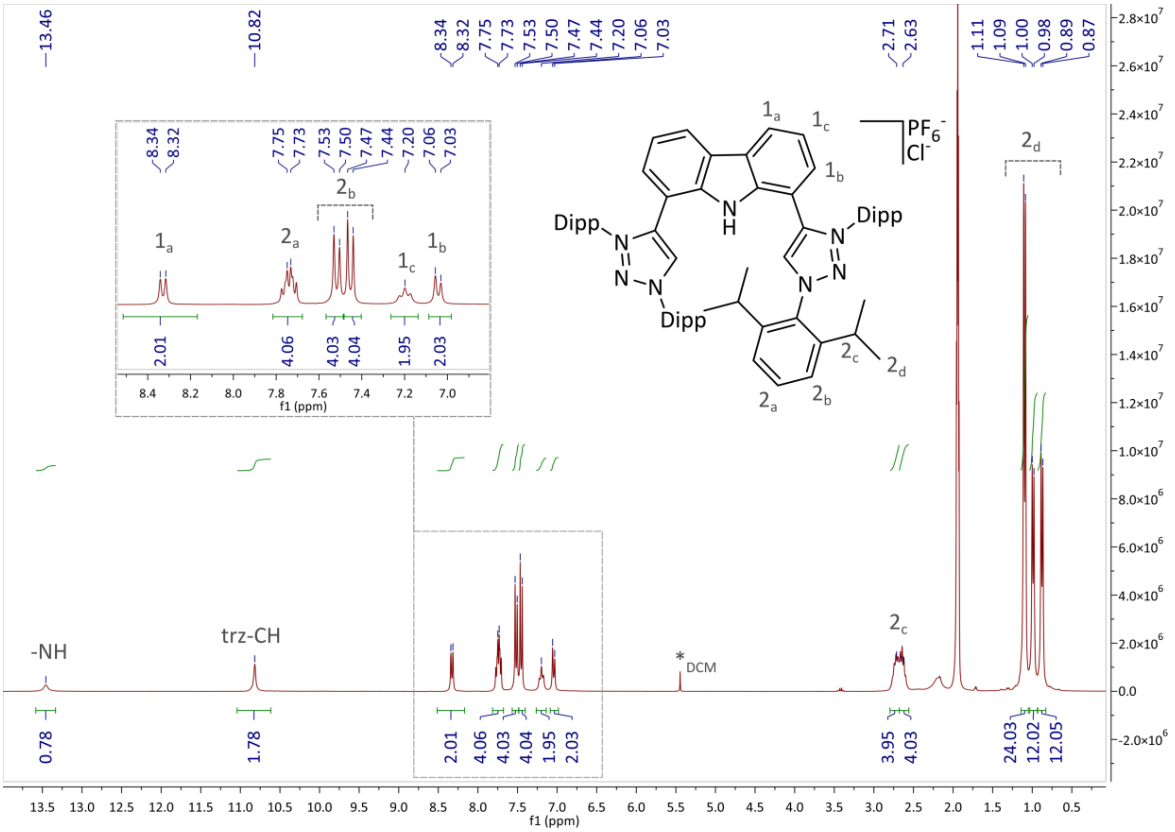


Figure 3.8. The ^{1}H NMR spectrum of $\mathbf{R^{H}}$ in CD_3CN

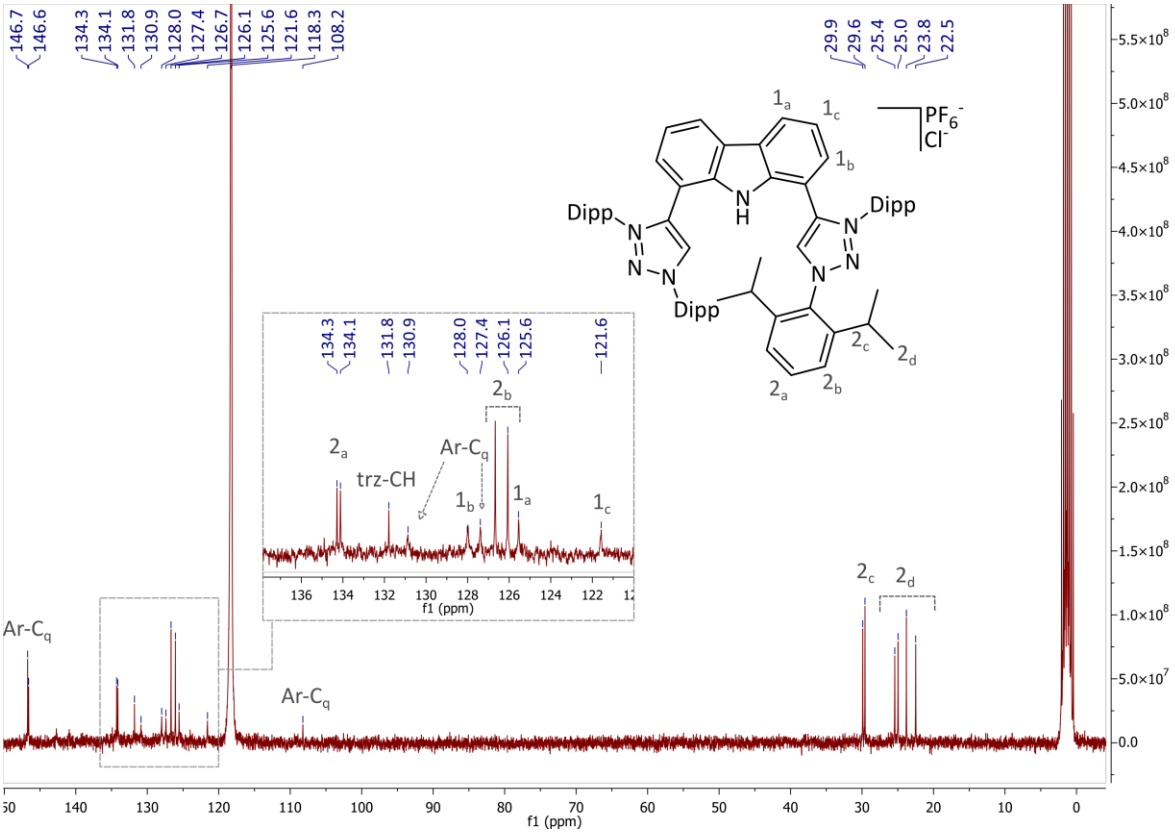
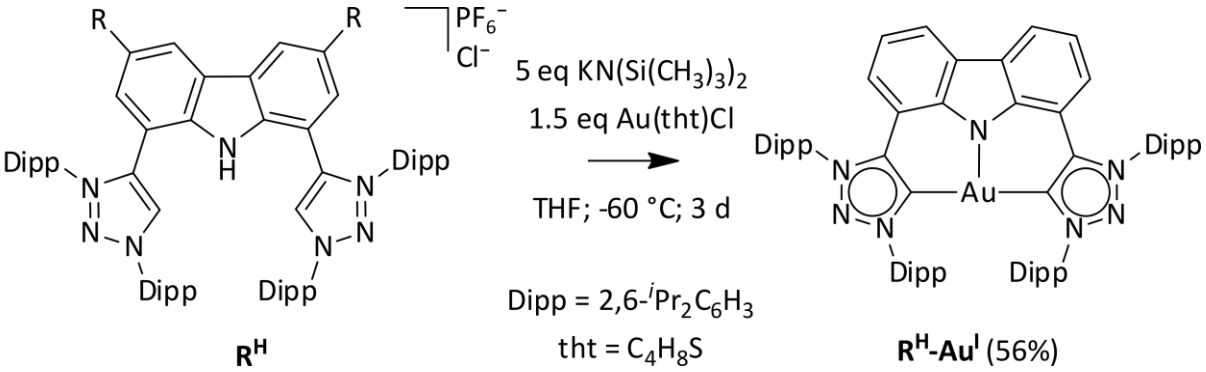


Figure 3.9. The ^{13}C {^{1}H} NMR spectrum of $\mathbf{R^{H}}$ in CD_3CN

3.5.3 Synthesis of the gold(I) pincer complex, 1,8-(bis(1,3-bis(2,6-diisopropylphenyl)-1,2,3-triazol-5-ylidene)carbazolide-CNC-gold(I), R^H-Au^I.



$\mathbf{R^H}$ $\mathbf{R^H}$-$\mathbf{Au^I}$ (56%)

The ligand precursor salt $\mathbf{R^H}$ (0.30 g, 0.24 mmol, 1 eq), $KN(Si(CH_3)_3)_2$ (0.24 g, 1.2 mmol, 5 eq) and Au(tht)Cl (0.17 g, 0.36 mmol, 1.5 eq) were weighed off into a flame-dried Schlenk flask inside the glovebox. Once removed from the glovebox and in the dark, the solids were dissolved in anhydrous THF at −60 °C and the dark red reaction mixture was left to slowly warm up to room temperature and continued for two more days. After the solvent was evaporated, the crude product was extracted with DCM and dried. The crude product was subsequently resuspended and stirred overnight in diethyl ether. The solvent was evaporated, the product was washed with hexane and dried in vacuo, affording $\mathbf{R^H}$-$\mathbf{Au^I}$ as a red solid. Crystals suitable for XRD analysis and in vitro cell culture studies were grown from a concentrated solution of DCM, layered with pentane at −20 °C. Yield: 0.16 g (56%). M.p. >300 °C. ^{1}H NMR (400 MHz, CD_2Cl_2) δ 8.13 (d, *J* = 7.4 Hz, 2H, Ar-$CH_{carbazole}$, H-1_a), 7.71 (d, *J* = 7.8 Hz, 2H, Ar-CH_{Dipp}, H-2_a), 7.51–7.47 (m, 6H, Ar-CH_{Dipp}, H-2_a (2H) + H-2_b (4H)), 7.15 (d, *J* = 7.9 Hz, 4H, Ar-CH_{Dipp}, H-2_b), 6.95 (d, *J* = 8.0 Hz, 2H, Ar-$CH_{carbazole}$, H-1_b), 6.65 (t, *J* = 7.7 Hz, 2H, Ar-$CH_{carbazole}$, H-1_c), 2.59 (sept, *J* = 6.8 Hz, 4H, ^{i}Pr-CH, H-2_c), 2.51 (sept, *J* = 6.9 Hz, 4H, ^{i}Pr-CH, H-2_c), 1.13 (d, *J* = 6.8 Hz, 12H, ^{i}Pr-CH_3, H-2_d), 1.07 (d, *J* = 7.2 Hz, 12H, ^{i}Pr-CH_3, H-2_d), 1.06 (d, *J* = 6.6 Hz, 12H, ^{i}Pr-CH_3, H-2_d), 0.98 (d, *J* = 6.8 Hz, 12H, ^{i}Pr-CH_3, H-2_d). ^{13}C {^{1}H} NMR (100 MHz, CD_2Cl_2) δ 175.0 (Au-$C_{carbene}$), 146.7, 146.6, 146.0, 145.3, 137.7, 135.4 (all Ar-C_q), 132.2 (Ar-CH_{Dipp}, C-2_a), 130.5 (Ar-CH_{Dipp}, C-2_a), 127.1 (Ar-C_q), 125.8 (Ar-CH_{Dipp}, C-2_b), 124.1 (Ar-CH_{Dipp}, C-2_b), 122.7 (Ar-$CH_{carbazole}$, C-1_b), 122.0 (Ar-$CH_{carbazole}$, C-1_a), 113.7 (Ar-$CH_{carbazole}$, C-1_c), 112.2 (Ar-C_q), 29.5, 29.2 (^{i}Pr-CH, C-2_c), 25.5, 25.0, 24.2, 23.4 (all ^{i}Pr-CH_3, C-2_d). ^{1}H NMR (400 MHz, C_6D_6) δ 8.33 (d, *J* = 7.8 Hz, 2H, Ar-$CH_{carbazole,}$ H-1_a), 7.36 (t, *J* = 7.8 Hz, 2H, Ar-CH_{Dipp}, H-2_a), 7.27 (m, 4H, (Ar-CH_{Dipp}, H-2_a (2H) + (Ar-$CH_{carbazole}$, H-1_b (2H)), 7.12 (d, *J* = 7.8 Hz, 4H, Ar-CH_{Dipp}, H-2_b), 7.10 (d, *J* = 7.8 Hz, 4H, Ar-CH_{Dipp}, H-2_b), 6.87 (dd, *J* = 7.7, 7.7 Hz, 2H, Ar-$CH_{carbazole}$, H-1_c), 2.94

(sept, *J* = 7.0 Hz, 4H, ^{i}Pr-CH, H-2$_c$), 2.68 (sept, *J* = 6.8 Hz, 4H, ^{i}Pr-CH, H-2$_c$), 1.15 (d, *J* = 6.7 Hz, 12H, ^{i}Pr-CH$_3$, H-2$_d$) 1.16 (d, *J* = 6.6 Hz, 12H, ^{i}Pr-CH$_3$, H-2$_d$), 1.05 (d, *J* = 6.8 Hz, 12H, ^{i}Pr-CH$_3$, H-2$_d$), 0.83 (d, *J* = 6.8 Hz, 12H, ^{i}Pr-CH$_3$, H-2$_d$). ^{13}C {^{1}H} NMR (100 MHz, C_6D_6) δ 175.9 (Au-C$_{carbene}$), 147.7, 147.3, 145.9, 145.3, 138.1, 135.6 (all Ar-C$_q$), 131.7 (Ar-CH$_{Dipp}$, C-2$_a$), 130.0 (Ar-CH$_{Dipp}$, C-2$_a$), 125.3 (Ar-CH$_{Dipp}$, C-2$_b$), 123.8 (Ar-CH$_{Dipp}$, C-2$_b$), 122.6 (Ar-CH$_{carbazole}$, C-1$_b$), 122.5 (Ar-CH$_{carbazole}$, C-1$_a$), 113.5 (Ar-CH$_{carbazole}$, C-1$_c$), 112.1 (Ar-C$_q$), 29.3, 29.1 (^{i}Pr-CH, C-2$_c$), 25.2, 24.7, 24.2, 23.0 (all ^{i}Pr-CH$_3$, C-2$_d$). Anal. Calcd for $C_{64}H_{74}N_7Au$ (+ 1.5 eq DCM): C 62.16, H 6.13, N 7.75. Found: C 62.22, H 6.37, N 7.35. ESI-HRMS (15 V, positive mode, m/z): calcd for $[M+H]^+$: 1138.5743. Found: 1138.5786.

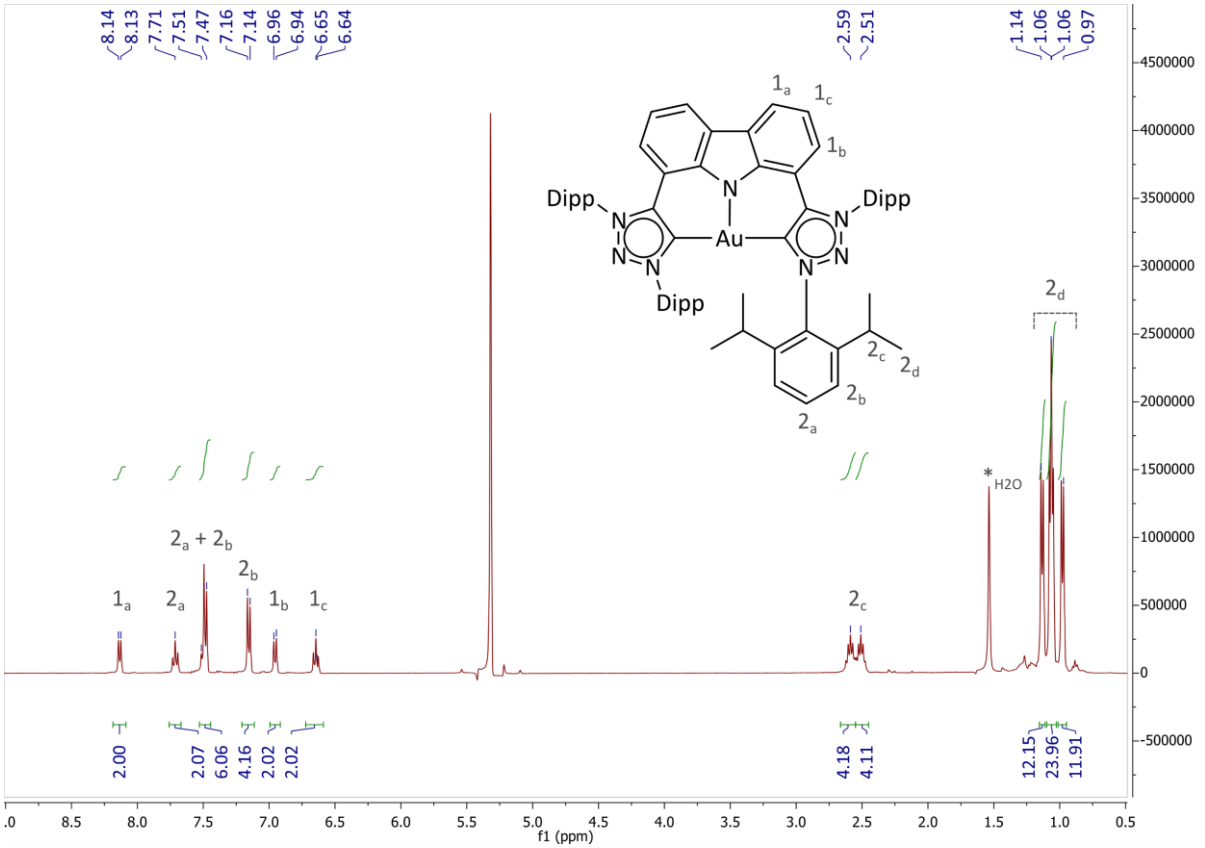


Figure 3.10. The ^{1}H NMR spectrum of **R^{H}-Au^{I}** in CD_2Cl_2.

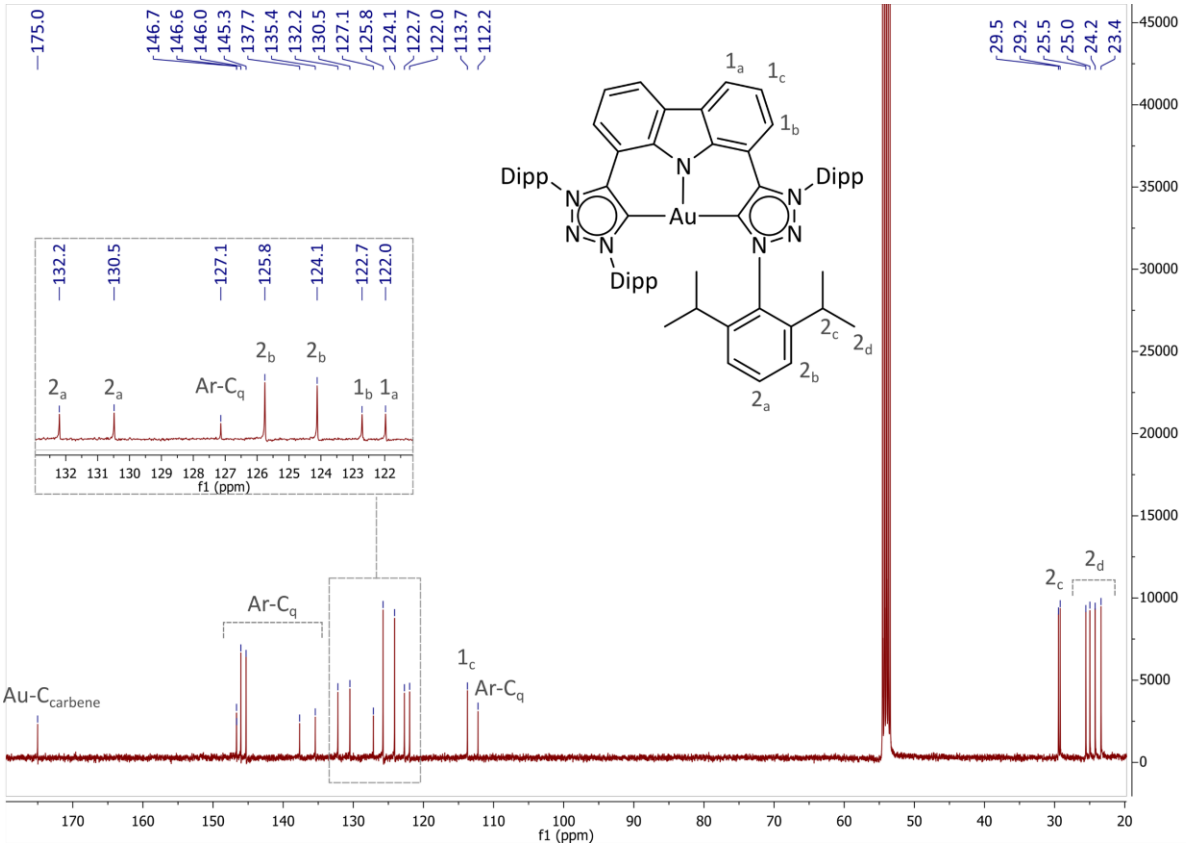
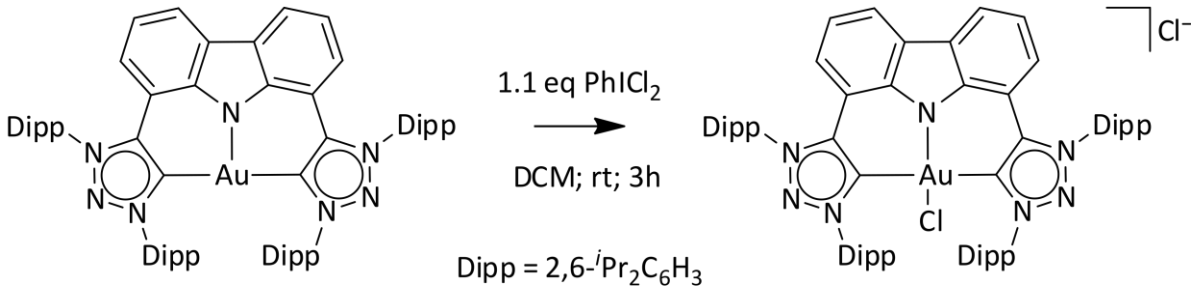


Figure 3.11. The ^{13}C {^{1}H} NMR spectrum of **R^{H}-Au^{I}** in CD_2Cl_2.

3.5.4 Synthesis of the gold(III) complexes, R^{H}-Au^{III} and R^{tBu}-Au^{III}

3.5.4.1 Synthesis of [1,8-(bis(1,3-bis(2,6-diisopropylphenyl)-1,2,3-triazol-5-ylidene) carbazolide-CNC-chlorido-gold(III)] chloride, R^{H}-Au^{III}



R^{H}-Au^{I} **R^{H}-Au^{III}** (82%)

To a solution of **R^{H}-Au^{I}** (0.10 g, 87.9 µmol, 1 eq) in anhydrous DCM, was added $PhICl_2$ (0.03 g, 94.6 µmol, 1.1 eq) and the red solution immediately turned light orange. Stirring was continued for 3 hours, after which the solvent was evaporated. The crude residue was washed with pentane and extracted with DCM, affording a light orange solid. Crystals suitable for XRD and in vitro cell culture procedures were grown from a concentrated DCM solution layered with toluene at room temperature. Yield: 87 mg (82%). M.p. 270 °C. ^{1}H NMR (300 MHz,

$(CD_3)_2SO$) δ 8.60 (d, *J* = 7.6 Hz, 2H, Ar-$CH_{carbazole}$, H-1_a), 7.92 (t, *J* = 7.8 Hz, 2H, Ar-CH_{Dipp}, H-2_a), 7.73 (d, *J* = 7.9 Hz, 4H, Ar-CH_{Dipp}, H-2_b), 7.57 (t, *J* = 7.8 Hz, 2H, Ar-CH_{Dipp}, H-2_a), 7.35 (d, *J* = 7.8 Hz, 4H, Ar-CH_{Dipp}, H-2_b), 7.25 (dd, *J* = 7.8, 7.8 Hz, 2H, Ar-$CH_{carbazole}$, H-1_c), 6.97 (d, *J* = 7.9 Hz, 2H, Ar-$CH_{carbazole}$, H-1_b), 2.29 (sept, *J* = 6.8 Hz, 4H, ^{i}Pr-CH, H-2_c), 2.19 (sept, *J* = 7.0 Hz, 4H, ^{i}Pr-CH, H-2_c), 1.14 (d, *J* = 6.8 Hz, 12H, ^{i}Pr-CH_3, H-2_d), 1.10 (d, *J* = 6.8 Hz, 12H, ^{i}Pr-CH_3, H-2_d), 1.03 (d, *J* = 6.7 Hz, 12H, ^{i}Pr-CH_3, H-2_d), 0.93 (d, *J* = 6.7 Hz, 12H, ^{i}Pr-CH_3, H-2_d). ^{13}C {^{1}H} NMR (100 MHz, $(CD_3)_2SO$) δ 144.6, 143.9, 139.1, 137.2, 136.8, 134.9 (all Ar-C_q), 133.8 (Ar-CH_{Dipp}, C-2_a), 131.5 (Ar-CH_{Dipp}, C-2_a), 131.2 (Ar-C_q), 126.2 (Ar-CH_{Dipp}, C-2_b), 124.6 (Ar-C_q), 124.3 (Ar-$CH_{carbazole}$, C-1_a), 124.2 (Ar-CH_{Dipp}, C-2_b), 121.6 (Ar-$CH_{carbazole}$, C-1_b), 119.8 (Ar-$CH_{carbazole}$, C-1_c), 108.2 (Ar-C_q), 28.9 (^{i}Pr-CH, C-2_c), 28.7 (^{i}Pr-CH, C-2_c), 24.9, 24.1, 22.9, 22.7 (all ^{i}Pr-CH_3, C-2_d). ^{1}H NMR (400 MHz, CD_2Cl_2) δ 8.37 (d, *J* = 7.5 Hz, 2H, Ar-$CH_{carbazole}$, H-1_a), 7.84 (t, *J* = 7.9 Hz, 2H, Ar-CH_{Dipp}, H-2_a), 7.57 (d, *J* = 7.9 Hz, 4H, Ar-CH_{Dipp}, H-2_b), 7.54 (t, *J* = 7.7 Hz, 2H, Ar-CH_{Dipp}, H-2_a), 7.25 (d, *J* = 7.8 Hz, 4H, Ar-CH_{Dipp}, H-2_b), 7.18 (dd, *J* = 7.8, 7.8 Hz, 2H, Ar-$CH_{carbazole}$, H-1_c), 7.05 (d, *J* = 8.0 Hz, 2H, Ar-$CH_{carbazole}$, H-1_b), 2.29 (sept, *J* = 6.7 Hz, 4H, ^{i}Pr-CH, H-2_c), 2.22 (sept, *J* = 6.7 Hz, 4H, ^{i}Pr-CH, H-2_c), 1.17 (d, *J* = 6.9 Hz, 12H, ^{i}Pr-CH_3, H-2_d), 1.18 (d, *J* = 6.8 Hz, 12H, ^{i}Pr-CH_3, H-2_d), 1.09 (d, *J* = 6.9 Hz, 12H, ^{i}Pr-CH_3, H-2_d), 0.99 (d, *J* = 6.7 Hz, 12H, ^{i}Pr-CH_3, H-2_d). ^{13}C {^{1}H} NMR (100 MHz, CD_2Cl_2) δ 145.7, 144.9, 140.1, 138.3, 138.0, 136.0 (all Ar-C_q), 134.1 (Ar-CH_{Dipp}, C-2_a), 132.4 (Ar-CH_{Dipp}, C-2_a), 132.1 (Ar-C_q), 126.5 (Ar-CH_{Dipp}, C-2_b), 125.6 (Ar-C_q), 124.7 (Ar-$CH_{carbazole}$, C-1_a), 124.3 (Ar-CH_{Dipp}, C-2_b), 122.8 (Ar-$CH_{carbazole}$, C-1_b), 120.6 (Ar-$CH_{carbazole}$, C-1_c), 109.1 (Ar-C_q), 30.0 (^{i}Pr-CH, C-2_c), 29.9 (^{i}Pr-CH, C-2_c), 25.6, 24.9, 23.6, 23.4 (all ^{i}Pr-CH_3, C-2_d). Anal. Calcd for $C_{64}H_{74}N_7AuCl_2$ (+ 0.2 eq DCM) C 62.89, H 6.12, N 8.00. Found: C 62.90, H 6.08, N 7.73. ESI-HRMS (15 V, positive mode, m/z): calcd for $[M+H]^+$: 1172.5354. Found: 1172.5390.

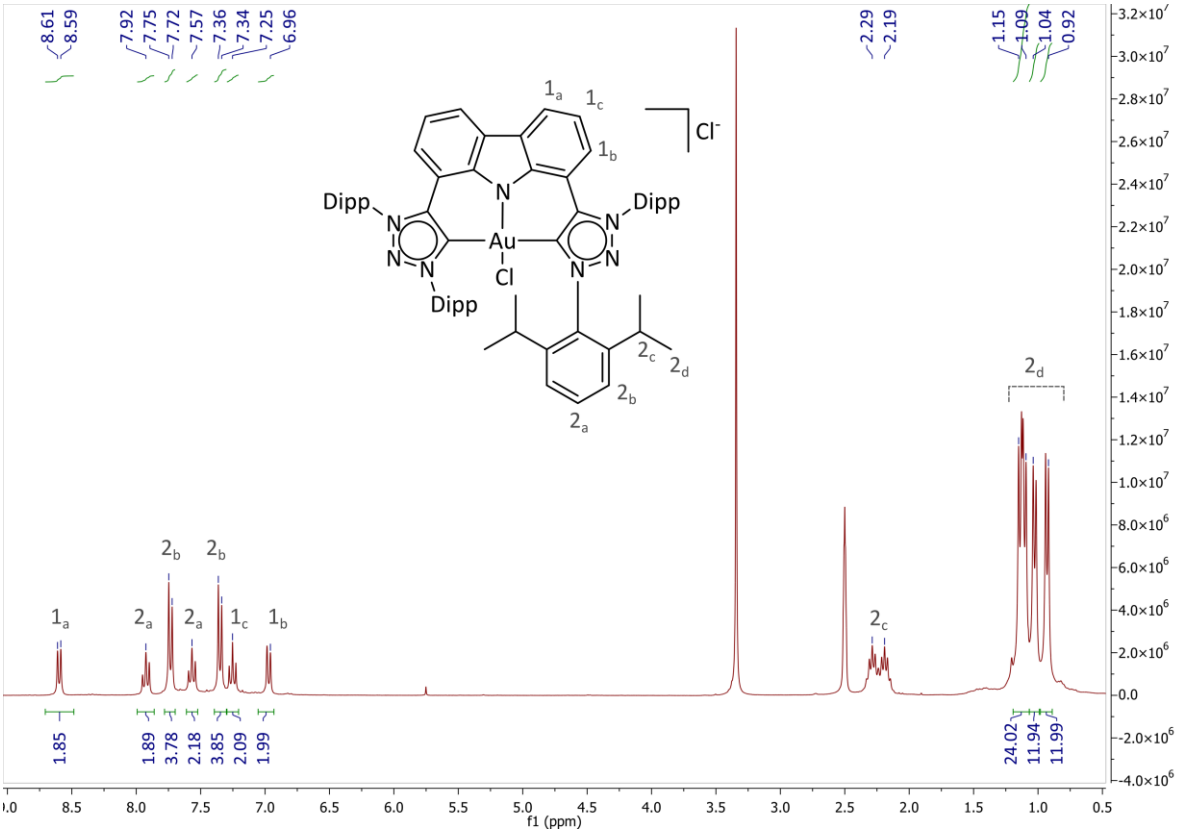


Figure 3.12. The ^{1}H NMR spectrum of **R^{H}-Au^{III}** in $(CD_3)_2SO$.

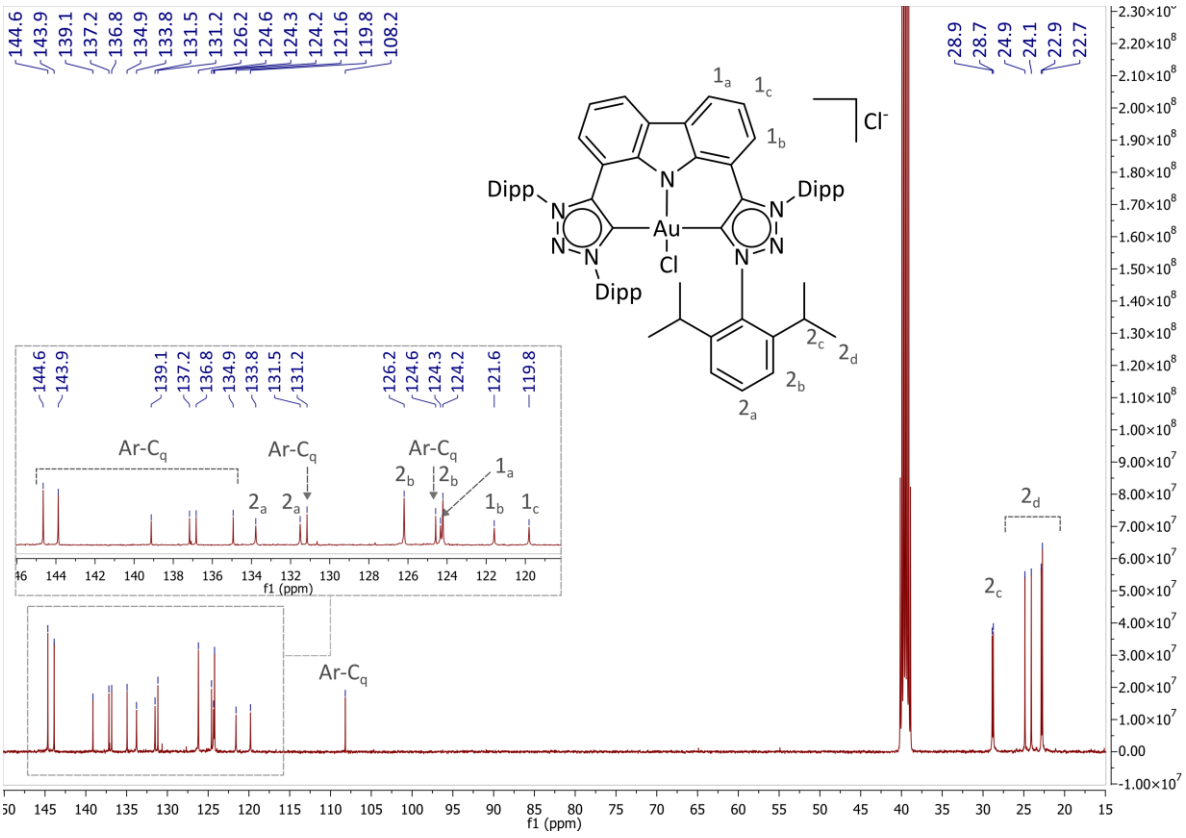
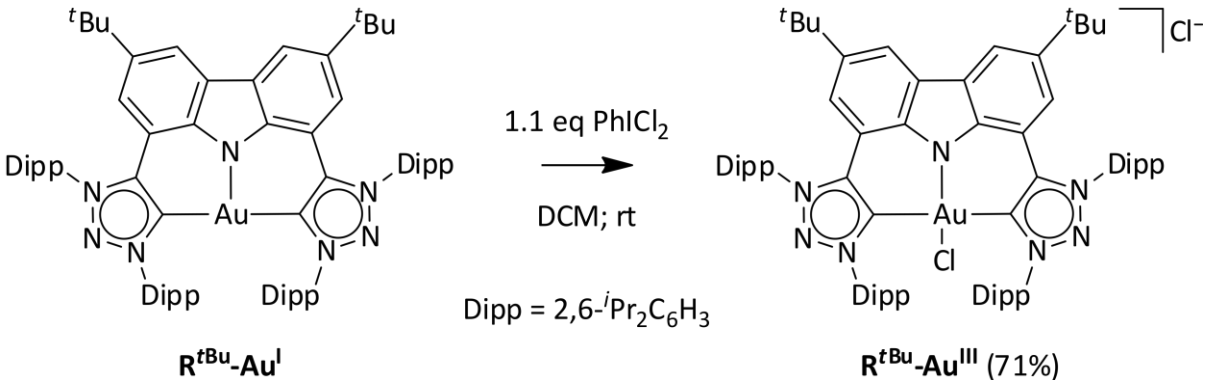


Figure 3.13. The ^{13}C {^{1}H} NMR spectrum of **R^{H}-Au^{III}** in $(CD_3)_2SO$.

3.5.4.2 Synthesis of [3,6-di-*tert*-butyl-1,8-(bis(1,3-bis(2,6-diisopropylphenyl)-1,2,3-triazol-5-ylidene) carbazolide-CNC-chlorido-gold(III)] chloride, $\mathbf{R^{tBu}\text{-}Au^{III}}$



$\mathbf{R^{tBu}\text{-}Au^{I}}$ $\mathbf{R^{tBu}\text{-}Au^{III}}$ (71%)

To a solution of $\mathbf{R^{tBu}\text{-}Au^{I}}$ (0.020 g, 15.9 µmol, 1 eq) in anhydrous DCM, was added $PhICl_2$ (4.84 mg, 17.6 µmol, 1.1 eq) and the red solution immediately turned light orange. Stirring was continued for 5 minutes, after which the solvent was evaporated. The crude residue was washed with pentane and extracted with DCM, affording a light orange solid. Crystals suitable for XRD were grown from a concentrated DCM solution layered with toluene. Yield: 15 mg (71%). ^{1}H NMR (500 MHz, $(CD_3)_2SO$) δ 8.74 (d, *J* = 1.6 Hz, 2H, Ar-$CH_{carbazole}$, H-1_a), 7.90 (t, *J* = 7.9 Hz, 2H, Ar-CH_{Dipp}, H-2_a), 7.77 (d, *J* = 7.9 Hz, 4H, Ar-CH_{Dipp}, H-2_b), 7.56 (t, *J* = 7.8 Hz, 2H, Ar-CH_{Dipp}, H-2_a), 7.33 (d, *J* = 7.8 Hz, 4H, Ar-CH_{Dipp}, H-2_b), 7.21 (d, *J* = 1.7 Hz, 2H, Ar-$CH_{carbazole}$, H-1_b), 2.27 (sept, *J* = 6.7 Hz, 4H, ^{i}Pr-CH, H-2_c), 2.21 (sept, *J* = 6.8 Hz, 4H, ^{i}Pr-CH, H-2_c), 1.14 (d, *J* = 6.7 Hz, 12H, ^{i}Pr-CH_3, H-2_d), 1.11 (d, *J* = 6.8 Hz, 12H, ^{i}Pr-CH_3, H-2_d), 1.09 (s, 18H, ^{t}Bu-CH_3), 1.03 (d, *J* = 6.8 Hz, 12H, ^{i}Pr-CH_3, H-2_d), 0.93 (d, *J* = 6.7 Hz, 12H, ^{i}Pr-CH_3, H-2_d). ^{13}C {^{1}H} NMR (125 MHz, $(CD_3)_2SO$) δ 144.7, 143.8, 142.3, 138.9, 139.1 (all Ar-C_q), 137.1 (Ar-CH_{Dipp}, C-2_a), 137.0, 135.8, 135.1 (all Ar-C_q), 133.6 (Ar-CH_{Dipp}, C-2_a), 131.5 (Ar-CH_{Dipp}, C-2_a), 131.4 (Ar-C_q), 130.6 (Ar-CH_{Dipp}, C-2_b), 127.7 (Ar-CH_{Dipp}, C-2_b), 126.4 (Ar-CH_{Dipp}, C-2_b), 124.6 (Ar-C_q), 124.1 (Ar-CH_{Dipp}, C-2_b), 121.6 (Ar-$CH_{carbazole}$, C-1_a), 119.1 (Ar-$CH_{carbazole}$, C-1_b), 107.0 (Ar-C_q), 34.3 (^{t}Bu-C_q), 31.1 (^{t}Bu-CH_3), 28.9 (^{i}Pr-CH, C-2_c), 28.8 (^{i}Pr-CH, C-2_c), 24.9, 24.2, 22.9, 22.7 (all ^{i}Pr-CH_3, C-2_d). ESI-HRMS (15 V, positive mode, m/z): calcd for $[M]^+$: 1284.6606. Found: 1284.6627.

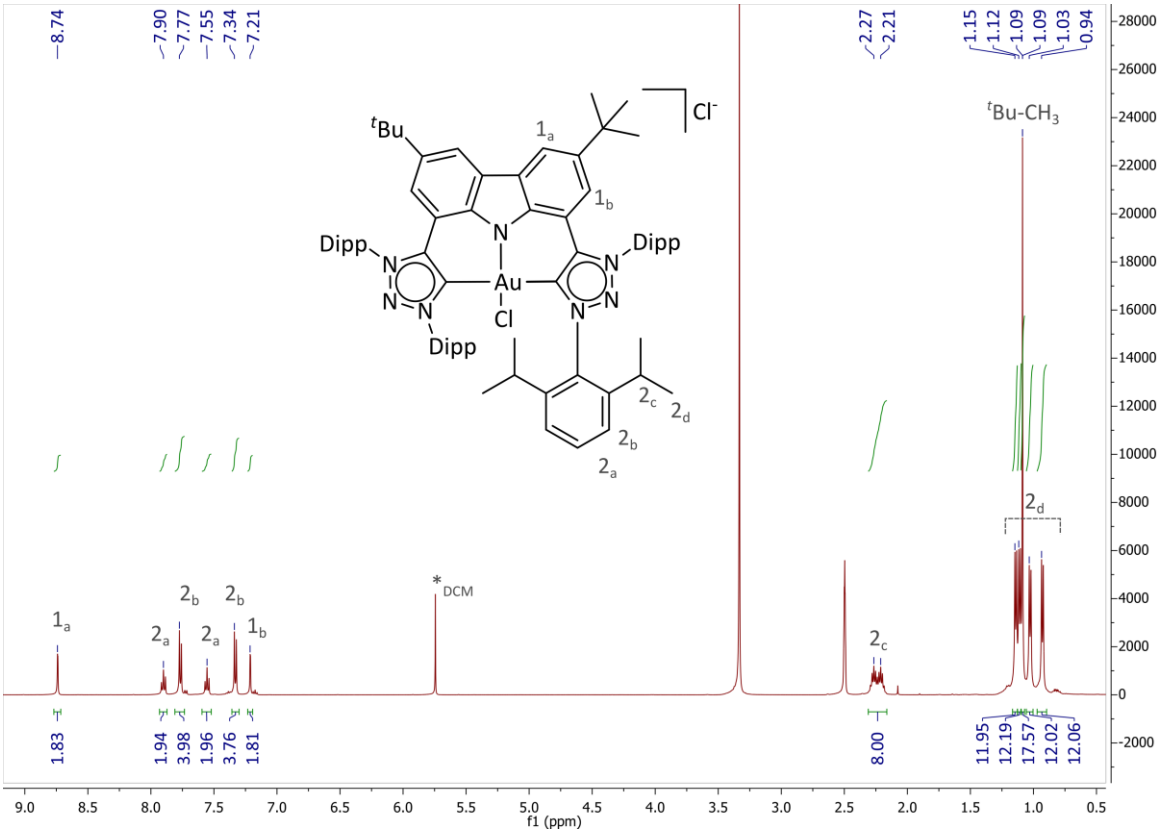


Figure 3.14. The ^{1}H NMR spectrum of **R^{tBu}-Au^{III}** in $(CD_3)_2SO$.

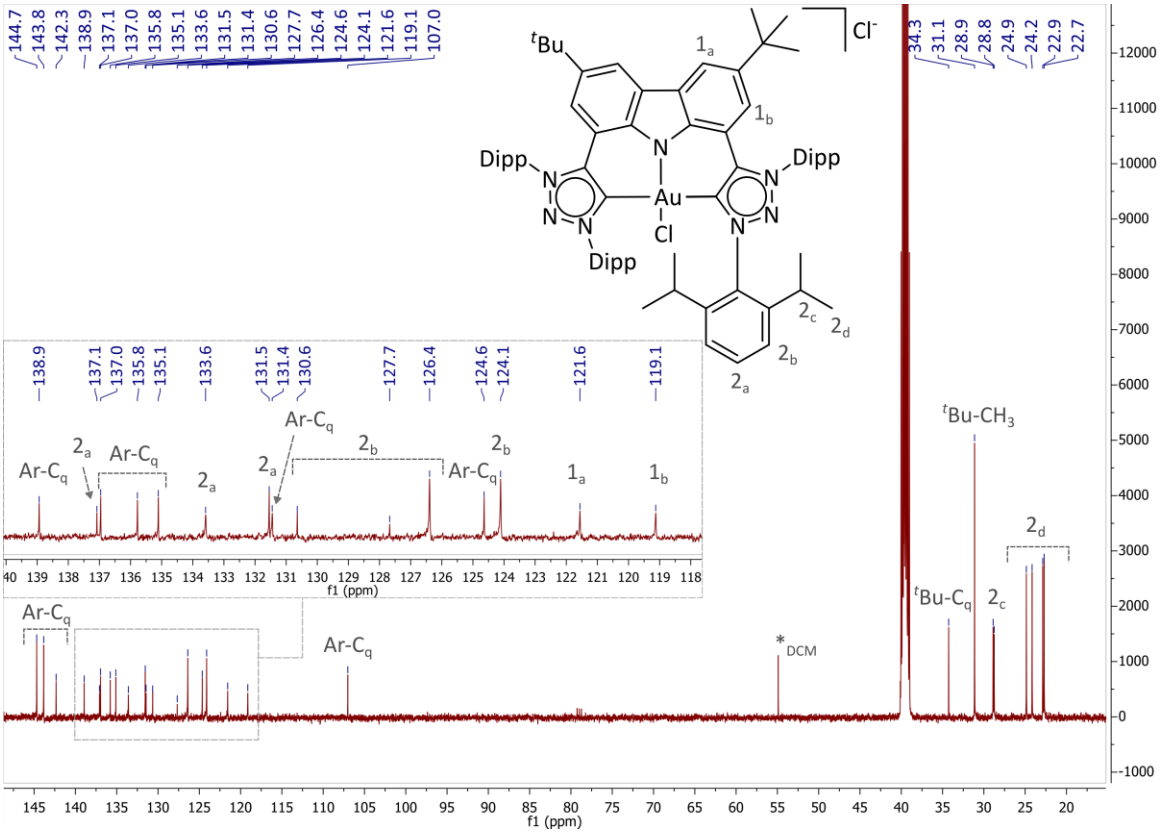


Figure 3.15. The ^{13}C {^{1}H} NMR spectrum of **R^{tBu}-Au^{III}** in $(CD_3)_2SO$.

3.5.5 Single-crystal X-ray diffraction data

3.5.5.1 Crystal structure data of R^{H}-Au^{I}, R^{H}-Au^{III} and R^{tBu}-Au^{III}

R^{H}-Au^{I}: $C_{65}H_{76}AuCl_2N_7$ (*M* = 1223.19 g/mol): tetragonal, space group *P*-42$_1$*c* (no. 114), *a* = 21.9064(10) Å, *c* = 24.9397(12) Å, *V* = 11968.3(12) Å^3, *Z* = 8, *T* = 173(2) K, μ(MoKα) = 2.593 mm^{-1}, *Dcalc* = 1.358 g/cm^3, 178479 reflections measured (5.88° ≤ 2Θ ≤ 55.998°), 14430 unique (R_{int} = 0.0538, R_{sigma} = 0.0250) which were used in all calculations. The final R_1 was 0.0232 (I > 2σ(I)) and wR_2 was 0.0508 (all data).

R^{H}-Au^{III}: $C_{163}H_{188}Au_2Cl_4N_{14}$ (*M* = 2879.00 g/mol): monoclinic, space group *P*2$_1$/*n* (no. 14), *a* = 15.2299(5) Å, *b* = 22.0990(8) Å, *c* = 21.7606(7) Å, *β* = 91.4767(11)°, *V* = 7321.4(4) Å^3, *Z* = 2, *T* = 173(2) K, μ(MoKα) = 2.130 mm^{-1}, *Dcalc* = 1.306 g/cm^3, 96491 reflections measured (2.626° ≤ 2Θ ≤ 56.808°), 18313 unique (R_{int} = 0.0786, R_{sigma} = 0.0757) which were used in all calculations. The final R_1 was 0.0396 (I > 2σ(I)) and wR_2 was 0.0914 (all data).

R^{tBu}-Au^{III}: $C_{72}H_{90}AuCl_2N_7$ (*M* = 1321.37 g/mol): monoclinic, space group *C*2/*c* (no. 15), *a* = 28.613(3) Å, *b* = 18.9492(18) Å, *c* = 19.3194(19) Å, *β* = 118.325(2)°, *V* = 9220.6(16) Å^3, *Z* = 4, *T* = 173.15 K, μ(MoKα) = 1.687 mm^{-1}, *Dcalc* = 0.952 g/cm^3, 25765 reflections measured (3.048° ≤ 2Θ ≤ 49.998°), 8102 unique (R_{int} = 0.0727, R_{sigma} = 0.0836) which were used in all calculations. The final R_1 was 0.0631 (I > 2σ(I)) and wR_2 was 0.1628 (all data).

3.5.6 Cell maintenance and in-vitro procedures

3.5.6.1 Cell lines and cell maintenance

In vitro studies were carried out on the human breast cancer cell line, MDA-MB-231[297] and the non-tumourigenic endothelial cell line, EA.hy926. Both cell lines are commercially available from the American Type Culture Collection Cell Line Bank. Both cell lines were grown and maintained in sterile 25 or 75 cm^2 tissue culture flasks in a humidified atmosphere at 37 °C and 5% CO_2 using Iscove's Modified Dulbecco's Medium (IMDM) supplemented with 10% heat inactivated foetal calf serum, 100 U/mL penicillin G, 100 µg/mL streptomycin and 250 µg/L fungizone. Growth medium was replaced every two to three days and if confluent, the cells were trypsinized; cells were incubated with trypsin (1–3 min at 37 °C) following the removal of the growth medium and several washes with 0.01 M 1× PBS (8 mM NaH_2PO_4, 2 mM KH_2PO_4, 0.14 M NaCl, 10 mM KCl). Thereafter the flasks were tapped against gloved

hands and inspected under the microscope to observe if the cells were rounded and detached from the cell culture flask surface. The trypsinization was quenched with the addition of medium and collected in 15 mL tubes. The suspension was centrifuged at 3000 rpm for 5 minutes and the supernatant was removed. The pellet was resuspended in fresh medium and was either divided into subcultures, counted for seeding purposes or frozen away in cryotubes at −78 °C (1 000 000 cells/mL in 10% DMSO in IMDM).

3.5.6.2 Seeding for in vitro procedures

The pellet obtained from a trypsinized cell suspension was resuspended in fresh medium and 20 µL of this suspension was added to 60 µL medium and 20 µL trypan blue dye. The stained cells (10 µL) were counted on a haemocytometer and the average count of 5 or 10 squares were taken, multiplied by the dilution factor (x5) and 10 000 to obtain the number of viable cells per millilitre. The volume of cell suspension required to ensure the right number of cells per experiment is obtained by dividing the required number of cells by the cells counted per millilitre

3.5.6.3 Crystal Violet Assay

The cytotoxicity of the compounds was evaluated on both MDA-MD-231 and EA.hy926 cell lines using the CVS assay. Stock solutions (50 mM) of the compounds were made in DMSO and test concentrations (20 µM – 0.3125 µM) for the CVS assay were prepared by diluting the compounds in cell culture medium. The vehicle control represented the highest DMSO concentration (never exceeding 0.04%) relevant to the test conditions. Cells were seeded at 5000 cells per well in a 96 well plate and allowed to adhere to the plate overnight in a humidified incubator at 37 °C and 5% CO_2. The attachment medium was discarded, and the cells were exposed to incremental concentrations of the compounds for 48 h in a humidified incubator at 37 °C and 5% CO_2. After 48 h, the medium was removed and 100 µL of 1% glutaraldehyde was added to each well and incubated for 15 min at room temperature, followed by the removal of glutaraldehyde and the addition of 0.1% crystal violet solution (0.1 g of gentian violet dissolved in 1% ethanol solution). The plates were incubated for 30 min at room temperature. The crystal violet dye was removed by submerging the plates under running water and left overnight to dry. The following day, 0.2% Triton-X (200 µL) was added to each well and allowed to incubate on a plate shaker for 60–90 min, after which 100 µL of the solubilised dye was transferred to a 96-well reading plate. The absorbances of each well

were measured at 570 nm using a ELX800 Universal Microplate Reader. Six data points were obtained for a single concentration and three replicate experiments were performed.

The absorbance values were corrected against the background (absorbance of empty wells) and were expressed as percentage cell viability. The percentage cell viability is calculated by expressing the absorbance of the treated cells as a percentage of the untreated cells. The IC_{50} values were obtained by using the non-linear regression analysis of *GraphPad Prism 5* software.

Chapter 4: Interaction of the 1,3-diarylated-CNC-gold(III) complex with biological macromolecules.

4.1 Introduction

There are various experimental techniques available to elucidate the potential binding of metal complexes to biological macromolecules such as DNA and proteins. These methods can either be direct such as MS, SC XRD, NMR spectroscopy, and viscosity measurements or indirect which involve the use of optical-based approaches such as UV spectroscopy or electrophoretic mobility shift assays (EMSA) to infer binding between metallodrugs and macromolecules.[298]

Historically, XRD has delivered a wealth of knowledge on a fundamental level on the very biological macromolecules that are investigated as potential drug targets. Indeed, it was the seminal XRD photograph of B-DNA taken by Rosalind Franklin that played a pivotal role in clarifying the double-helical structure of DNA.[299] Presently, XRD offers validation on how metallodrugs bind to macromolecules when predicted by other high-resolution methods such as NMR spectroscopy and MS. The crystal structure of cisplatin covalently bound to DNA, at two adjacent guanine residues (on N7) on the same strand (1,2-intrastrand crosslink), effectively demonstrated the bend of duplex DNA towards the major groove (**A**, Figure 4.1) induced by cisplatin**.**[300] Previous NMR solution structure studies performed on the different types of cisplatin-DNA adducts on varying lengths of single- or double-stranded DNA were hereby corroborated.[301,302]

There are few crystal structures reported of gold complexes bound to DNA and most of the examples available are associated with telomeric G-quadruplexes. ESI-MS revealed adducts of telomeric DNA (23 nucleotide sequence) with an intact biscarbene gold(I) complex derived from caffeine (**12**, Figure 4.1). XRD studies further revealed that the gold(I) complex interacts non-covalently between stacks of telomeric sequences (**B**, Figure 4.1)[37,303]

Many more examples of crystal structures exist with gold bound to proteins.[304] Some of the first examples include the antirheumatic drug myocrisin, of which the gold(I) is covalently bound to a cysteine residue (Cys25) in the active site of the protein, cathepsin K (**C**, Figure 4.2). The malate ligand does not dissociate and participates in hydrogen bonding with the nearby residues.[305]

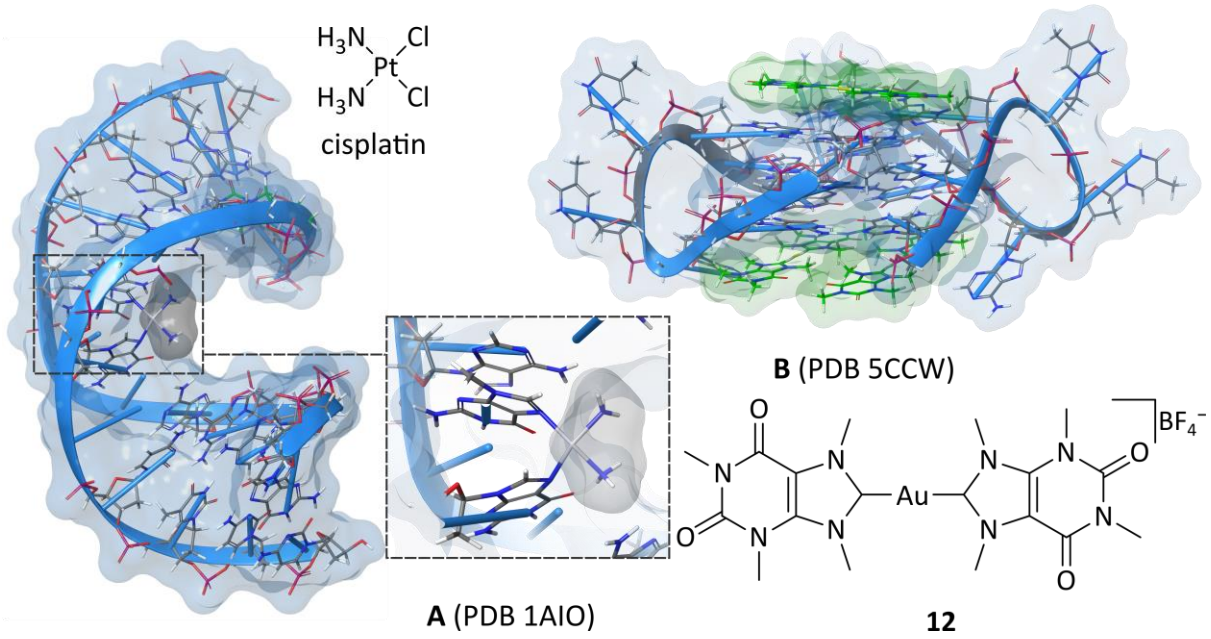


Figure 4.1. The crystal structures of cisplatin covalently bound to two N7-atoms of two adjacent guanine residues of duplex DNA (**A**, PDB 1AIO) and a gold(I) biscarbene complex, **12**, interacting with telomeric G-quadruplex DNA in a non-covalent manner (**B**, PDB 5CCW).[300,303]

As previously mentioned, the Au^{I} of auranofin binds to the cysteine residue (Cys34) of human serum albumin (HSA) and although a great deal of experimental evidence indicates that this is true, the first structural evidence of Cys34 being a gold-binding site has only just been reported (**D,** Figure 4.2). [306,307] Messori and co-workers crystallized BSA (bovine serum albumin) with a gold(III) dithiocarbamate complex, **37** (Figure 4.2). Upon binding to the protein, the Au^{III} is reduced to Au^{I} with a concurrent loss of ligands, resulting in a naked Au^{I} bound to Cys34 of BSA. Independent ESI-MS experiments confirm the formation of protein adducts with a single Au^{I} atom and NMR spectroscopic results indicate the loss of signal from the gold(III) dithiocarbamate complex with the appearance of the signals associated with ligand degradation in the presence of BSA.

Hen egg-white lysozyme (HEWL) is often used as a model protein to probe the interaction between metal complexes and proteins.[304] From the work reported by Messori et al., gold(III) complexes undergo reduction to Au^{I} with the associated loss of ligands to coordinate to an exposed histidine residue (His15) of HEWL.[308] A representative crystal structure is shown as **E** in Figure 4.2; an adduct from one of the gold(III) complexes in the Auoxo family, namely Auoxo3, complex **38.** Interestingly, two Au^{I} ions are bound to His15, whereby one Au^{I} has a

nearby asparagine residue (Asn93) as ancillary ligand and the second Au^{I} is bound to water in a bidentate coordination.[309]

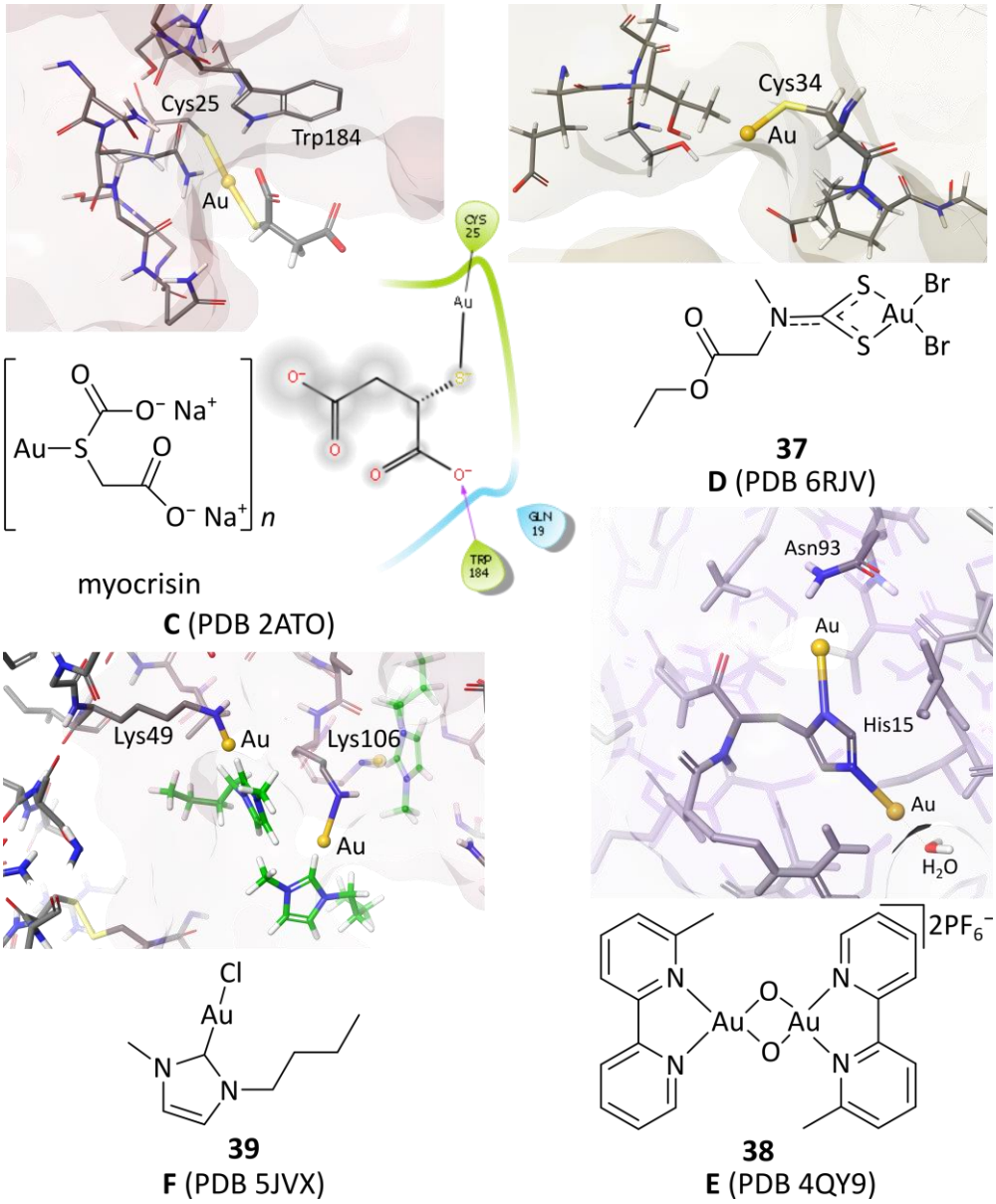


Figure 4.2. Crystal structures of gold-protein adducts. **C**: adduct of aurothiomalate with Cys25 residue of cathepsin K. Below the crystal structure, the ligand interaction diagram shows the covalent bond to Cys25 and a hydrogen bond between the malate ligand and Trp184.[305] **D**: The Au^{I} of the gold(III) dithiocarbamate complex bound to Cys34 of BSA.[307] **E**: The two Au^{I} ions of Auoxo3 complex bound to the ND2 and NE2 nitrogen atoms of His15, while either Au^{I} ion interacts with Asn93 or water.[309] **F**: The gold(I) NHC complex, each bound to a lysine residue (Lys49, Lys106) of thaumatin.[310] Structures generated with *Maestro*.[311]

Lastly, the solid-state structure of the first gold(I) NHC complex-protein adduct has recently been reported (**F**, Figure 4.2).[310] The adduct involves the model protein thaumatin with no

free cysteine and histidine residues. The gold(I) NHC complex, where NHC = 1-butyl-3-methylimidazole-2-ylidene (**39**, Figure 4.2), binds to many lysine and arginine residues as well as the N-terminal amine. In most of the binding sites, the NHC-moiety is retained.

Crystal structures of gold-protein adducts reveal that gold complexes bind to exposed cysteine more often than not, and, to a lesser extent, histidine residues, of proteins as naked Au^{I} ions, regardless if the gold ion of the complex was in oxidation state +3. The direct methods – SC XRD, MS, and NMR – are complementary in offering conclusive evidence surrounding the interaction of metal complexes with proteins and DNA, the latter two methods being especially important when crystals suitable for XRD are difficult to grow.

The use of UV-vis spectroscopy, to investigate the interaction between complexes and macromolecules, is considered an indirect approach as the results obtained from these experiments are usually compared to the results obtained from organic or inorganic compounds with known binding modes to DNA or proteins. Other than direct coordination as the case with cisplatin, non-covalent binding modes to DNA are frequently observed. DNA intercalators, such as ethidium bromide (Figure 4.3) are usually associated with at least one planar aromatic moiety to insert between adjacent nucleotide bases. The DNA helix lengthens, stiffens and unwinds to accommodate the intercalator.[312,313] Minor groove binders are often characterized by their crescent shape and protonated amines such as Hoechst 33258 (**G**, Figure 4.3)[314] and does not induce as strong a conformational change to the DNA as intercalators.[315] External electrostatic binding to the negatively charged phosphate backbone occurs with small ions such as Na^{+}, transition metal ions (Ag^{+}, Hg^{2+} etc.) and cationic polyamines. Electrostatic binding is unspecific and does not change the structure of the DNA.[316] Binding to the major groove (e.g. methyl green, Figure 4.3)[317] and direct coordination to the phosphate backbone (e.g. TriplatinNC, **H**, Figure 4.3)[318] are also possible but are seen less frequently.

UV-vis spectroscopy offers an abundance of experimental methodologies to elucidate the binding between metallodrugs and macromolecules. Among them are absorbance titration studies, DNA thermal denaturation studies and dichroism. During absorbance titration studies, the effect of incremental amounts of DNA or protein on the UV-vis absorbance spectrum of a free drug is investigated. If binding occurs, the induced UV-vis spectrum will most commonly be associated with a decrease in intensity (hypochromic effect) and

bathochromic shifts (also termed red-shift; towards longer wavelengths) of the absorbance maxima of the free drug.[319]

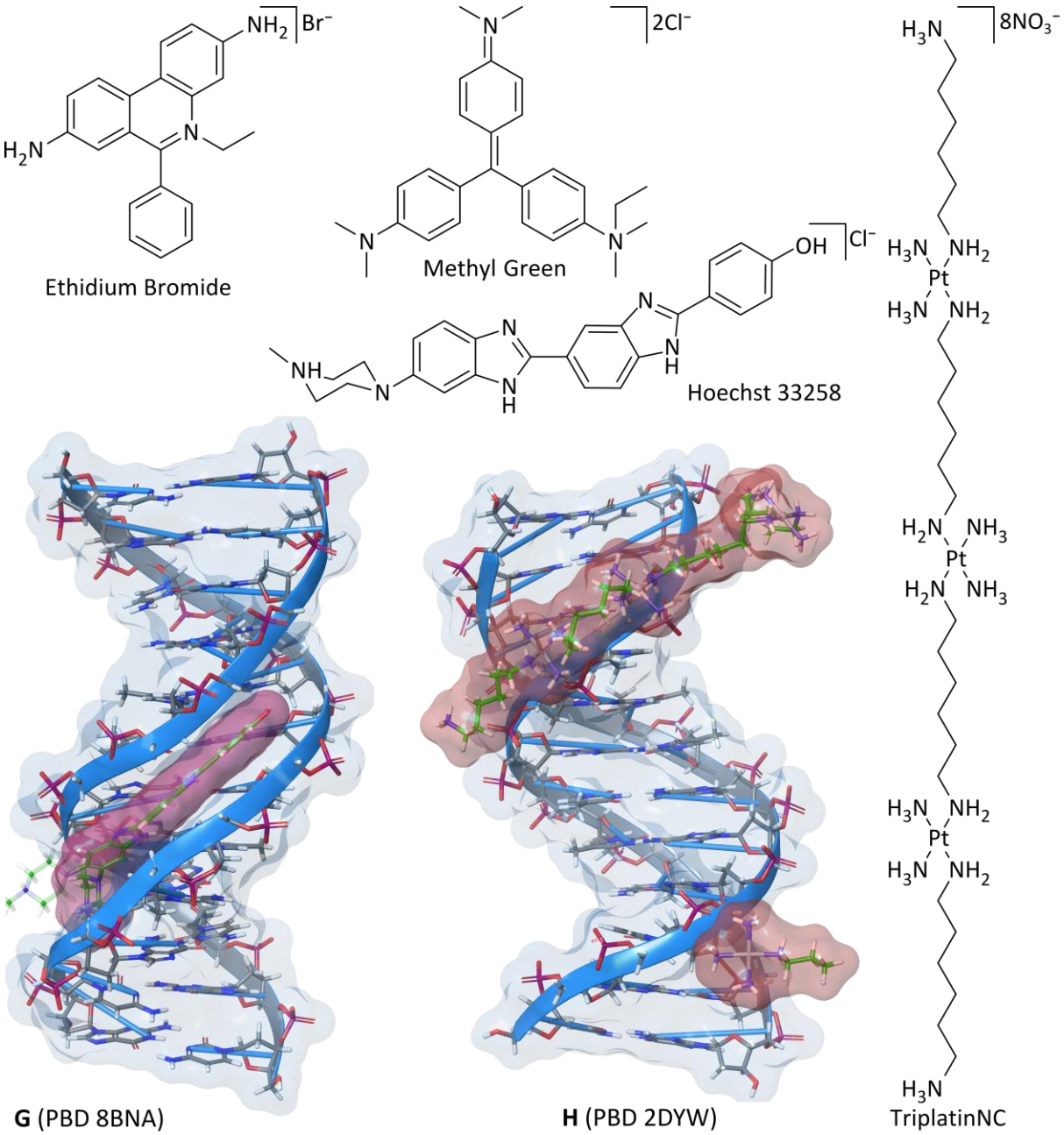


Figure 4.3. The chemical structures of DNA-binding compounds: ethidium bromide, methyl green, Hoechst 33258 and TriplatinNC. The crystal structure of Hoechst 33258 bound to the minor groove of DNA is shown (**G**)[314] and the crystal structure of TriplatinNC interacting with the phosphate backbone of DNA is shown (**H**)[318]. Crystal structures generated with *Maestro*.[311]

UV-vis absorption can also be used to investigate the change in the denaturation temperature of DNA in the presence of the drug. DNA thermal studies are based on changes in the helix-to-coil transition temperature of DNA ($T_{m:}$ the temperature at which half of the helical

structure is altered or lost) upon binding of drugs and is monitored by observing the change in the absorbance of DNA as a function of temperature. Interactions such as intercalators and groove-binders stabilize the double-helix and increase the T_m of DNA, while the T_m decreases when destabilizing interactions are present.[20] The change in T_m also gives insight into the strength of the DNA-drug interactions as significant changes in T_m indicates a strong interaction.[20,298,320]

Circular dichroism (CD) is the difference in the absorbance of two different rays of light as a result of passing through an optically active substance, whereas linear dichroism (LD) the difference in the absorbance of light travelling parallel and perpendicular relative to an orientation axis, e.g. the DNA helical axis. DNA and proteins are large, chiral biomolecules and both CD and LD experiments can be used to detect conformation changes to DNA or proteins due to ligand interactions. DNA-binding drugs are often achiral and small and will lack an active CD and LD spectrum of their own. The interaction with DNA will induce CD and LD activity and is therefore indicative of an interaction.[20,298,321–325]

DNA viscosity measurement is a non-optical method used to determine the type of binding mode. This technique is based on the principle that the viscosity of DNA is altered depending on the type of interaction between the metallodrug and DNA. Covalent binders such as cisplatin bend the DNA, thereby shortening the axial length of the helix, resulting in a decreased viscosity. Intercalators cause a lengthening of the helix and therefore the viscosity of DNA increases. Groove-binders do not distort the structure of DNA significantly enough to induce any changes in the viscosity of DNA.[313,315]

Gel electrophoresis is a familiar technique initially used as a tool to separate and purify nucleic acids[326–328] but can also be used to investigate the effect of a complex or drug on the migration of DNA. DNA is negatively charged due to the anionic phosphate groups associated with each nucleotide. As the mass of DNA increases with the addition of nucleotides, so does the charge of the molecule. Therefore, the charge to mass ratio of nucleic acids remains approximately constant, provided that the nucleotides are the same length.[329] During electrophoresis of plasmid DNA, separation of the different topological forms takes place on the basis of size. Plasmid DNA contains supercoiled (SC), nicked-open circular (NOC) and linear (Lin) DNA (Figure 4.4). The SC form experiences the least resistance through the gel matrix and will therefore migrate the fastest towards the anode. Due to the relaxed topology of the NOC

form, the NOC band will migrate the slowest. Gel electrophoresis can also be used to detect damage to DNA by a drug/complex as cleaved DNA will result in different fragments moving at different rates towards the anode[37] and DNA intercalators are often identified by Topo I-mediated DNA relaxation assays.[153,202]

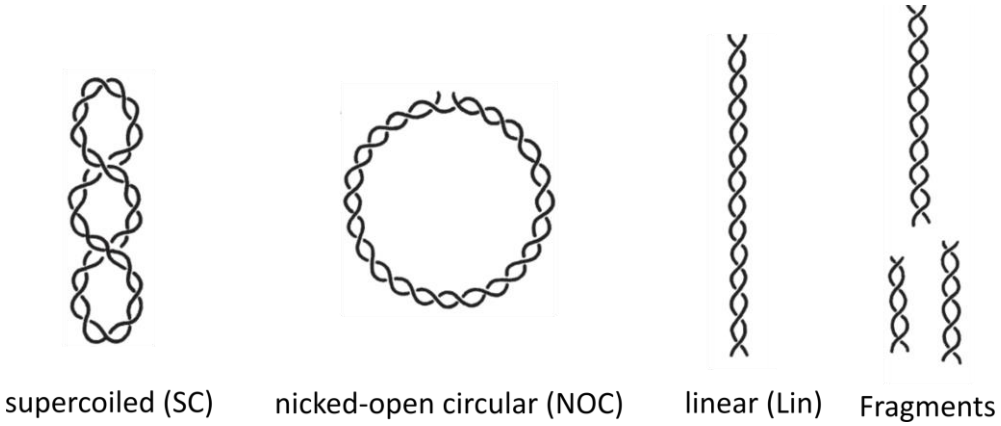


Figure 4.4. The different topological forms of plasmid DNA used in EMSA. Image is reproduced from original publication.[20]

There are many more experimental techniques to explain the binding of potential metallodrugs to biological macromolecules and only some examples are discussed above. As a starting point, to determine if any binding to DNA occurs, UV-absorption titration studies, DNA thermal denaturation studies, and EMSAs can be used. To determine the type of binding mode to DNA, techniques such as dichroism and DNA viscosity measurements are recommended. The methods discussed above can easily be adapted for binding to proteins as well, where additional techniques such as SC XRD, NMR spectroscopy and ESI-MS can be utilized to determine the amino acid residue and the associated protein-drug interactions involved.

4.2 Aim

The triazolium salt, **R^H** and the corresponding gold(III) complex, **R^H-Au^{III}** were found to be the most cytotoxic compounds against the breast cancer cell line, MDA-MB-231. However, the gold(III) complex, **R^H-Au^{III}** exhibited better selectivity against the non-tumourigenic cell line, EA.hy926. Indications of the mode of action of the gold(III) complex can potentially be given by evaluating the ability of **R^H-Au^{III}** to bind to biological macromolecules. Initially, the interaction of **R^H-Au^{III}** with DNA was evaluated with a range of UV-vis spectroscopy methodologies, viscometrical and EMSA studies. Similarly, the interaction with **R^H-Au^{III}** and

proteins such as HEWL and HSA were investigated by UV-vis titration studies. Finally, the redox stability of **R^H-Au^{III}** in the presence of GSH was investigated by ESI-MS spectrometry and ^{1}H-NMR and UV-vis spectroscopy.

4.3 Results and Discussion

4.3.1 Electronic structure of R^H-Au^{III}

Prior to investigating the ability of **R^H-Au^{III}** to bind to DNA and proteins via UV-vis titration studies, the electronic structure of **R^H-Au^{III}** in DMSO (Figure 4.5a) and in 1× PBS with 10% DMSO was characterized (Figure 4.5b). In DMSO, four absorption maxima are observed at 303 nm ($\varepsilon = 14036$ M^{-1} cm^{-1}), 336 nm ($\varepsilon = 8699$ M^{-1} cm^{-1}), 363 nm ($\varepsilon = 8798$ M^{-1} cm^{-1}) and 398 nm ($\varepsilon = 7494$ M^{-1} cm^{-1}). These values correspond well to those previously reported for the fluorinated analogue in THF (**R^{tBu}-Au^{III}-F**, Scheme 3.2).[201] By comparison, the absorbance maxima of **R^H-Au^{III}** in 1× PBS (10% DMSO) were similarly located at 298 nm ($\varepsilon = 14023$ M^{-1} cm^{-1}), 362 nm ($\varepsilon = 9166$ M^{-1} cm^{-1}) and 399 nm ($\varepsilon = 8177$ M^{-1} cm^{-1}). An additional peak at 264 nm ($\varepsilon = 30385$ M^{-1} cm^{-1}) was identified in 1× PBS due to the extended solvent window of water (190 – 1100 nm) as opposed to DMSO (268 – 1100 nm) and the absorbance maxima of 336 nm (present in DMSO) was not apparent in the UV-vis spectrum of **R^H-Au^{III}** in 1× PBS.

The transitions in DMSO were assigned according to TD-DFT calculations at the B3LYP-D3/Def-2-SVP[330–334] level of theory using *Gaussian 9.0 E*[335] and the calculated UV-vis spectrum of **R^H-Au^{III}** in DMSO (polarizable continuum model)[336–338] is shown as an inset to Figure 4.5a. The predicted absorption maxima and the major contributions to each transition are presented in Table 4.1. Due to the limited solvent window of DMSO, the calculated absorbance peak at 271 nm is not experimentally observed in DMSO but is observed in 1× PBS (10% DMSO) at 264 nm. The predicted UV-vis peaks of 389 nm and 372 nm agree with the actual absorbance maxima of 398 nm and 363 nm, respectively. The experimental peak of 336 nm is explained by two predicted band maxima at 325 nm and 338 nm of which have equal intensity (oscillator strengths).

The frontier molecular orbitals are involved in the lower energy transitions of 336 – 398 nm. Specifically, the excitation of an electron from the HOMO to the LUMO+1 and the LUMO+2 contributes to the transitions at 398 and 363 nm, respectively. The major contributor to the peak at 336 nm is from the excitation from HOMO−1 to LUMO+1 and LUMO+2. The HOMO

and HOMO−1 are bonding orbitals spanning across the carbazole moiety, whereas the LUMO+1 and the LUMO+2 orbitals are antibonding in nature (π^*) and predominantly localized on the trz (Figure 4.5c). Therefore, the lower energy transitions may be assigned to intraligand charge transfer (ILCT) with dominant $\pi^* \leftarrow \pi$ character.

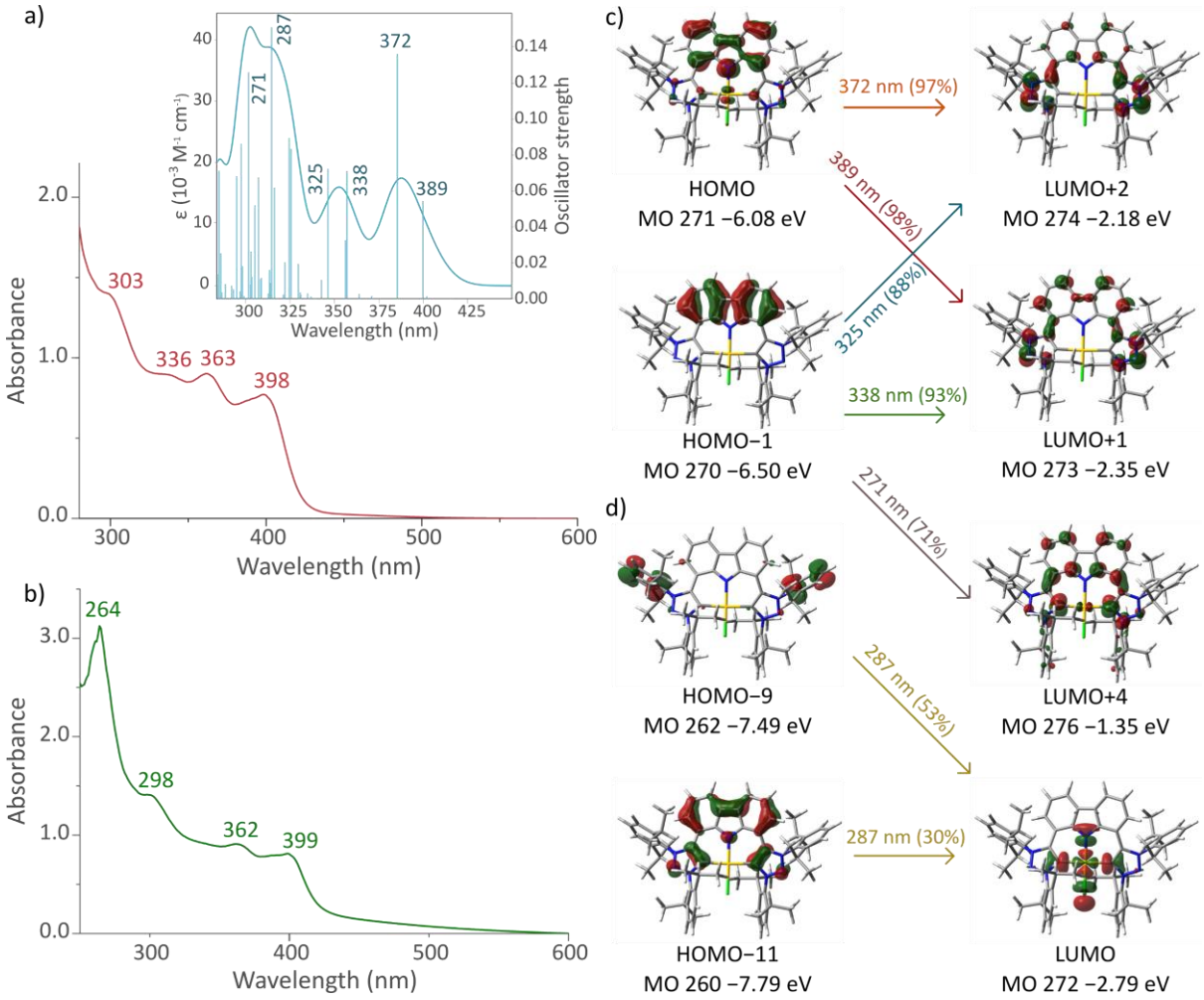


Figure 4.5. (a) The UV-vis absorption spectrum of **R^H-Au^{III}** in DMSO where the absorption maxima (λ_{max}) are indicated at 303, 336, 363 and 398 nm. The TD-DFT calculated spectrum of **R^H-Au^{III}** in DMSO is shown in the inset. (b) The UV-vis absorption spectrum of **R^H-Au^{III}** in 1× PBS (10% DMSO) where the absorption maxima (λ_{max}) are indicated at 264, 298, 362 and 399 nm. Views of the molecular orbitals for **R^H-Au^{III}** at an isosurface of 0.04 a.u that contribute mainly to the predicted (c) lower and (d) higher energy transitions in the UV-vis spectrum of **R^H-Au^{III}** in DMSO as calculated by *Gaussian09* at the B3LYP-D3/Def-2-SVP level of theory using the solvent polarizable continuum model (DMSO). The TD-DFT spectrum was generated with *GaussSum 3.0*.[339]

The higher energy transitions of 271 nm and 287 nm (the latter corresponding to the experimental peak observed at 303 nm) involve the excitation of an electron from HOMO-1 to LUMO+4 and from both HOMO−9 and HOMO−11 to the frontier LUMO, respectively (Figure

4.5d). More specifically, the transition at 271 nm is attributed to the transfer of an electron from a π bonding orbital localized on the carbazole moiety to an π antibonding (π*) orbital localized on the carbazole ring system and triazolylidene rings (ILCT $\pi^* \leftarrow \pi$). The main transition contributing to the peak at 303 nm involves the excitation from the Dipp wingtip groups (HOMO−9) and the conjugated ring system spanning across the carbazole and trz (HOMO−11) to the LUMO located on the Au^{III} ion (σ* MO derived from the 5dx^2–y^2 atomic orbital) and the nearby bonding atoms i.e., the nitrogen from the carbazole amido, the two carbene carbons and the ancillary chlorido ligand. The band is therefore assigned as a ligand to metal charge transfer (LMCT $\sigma^* \leftarrow \pi$).

Table 4.1. Experimental UV-vis absorption maxima and DFT-calculated absorbance data with major contributions to key transitions of **R^H-Au^{III}** in DMSO.

Electronic absorption bands (nm) (ε / M^{-1} cm^{-1})	**Calculated electronic absorption bands (λ_{max}/nm) (f, oscillator strength)**	**Major Contributions (> 20%) to electronic transitions**
n.o[a]	271 (0.127)	LUMO+4 ← HOMO−1
303 (14036)	287 (0.152)	LUMO ← HOMO−9 LUMO ← HOMO−11
336 (8699)	325 (0.073) 338 (0.071)	LUMO+2 ← HOMO−1 LUMO+1 ← HOMO−1
363 (8798)	372 (0.137)	LUMO+2 ← HOMO
398 (7494)	389 (0.056)	LUMO+1 ← HOMO

[a] not observed (falls outside the measured window).

4.3.2 DNA Binding Studies

4.3.2.1 Electrophoretic Mobility Shift Assays (EMSA)

The interaction of **R^H-Au^{III}** with plasmid DNA (pUC57) was investigated with gel electrophoresis. The gel was prepared by adding agarose gel (1.2% w/v) to 1× TAE (40 mM Tris-acetate and 1 mM EDTA, pH 8.3) buffer and heated until boiling. Once the gel solution cooled down to 60 °C, the gel was poured into the mould and left to set for at least 30 minutes. The samples were prepared by adding different stock concentrations of the test compounds

in DMSO to the pUC57 plasmid DNA in 1× TAE buffer in such a way that the concentration of DMSO in the samples was held constant at the maximum of 10%. The solutions of pUC57 DNA and the test compounds were incubated at 37 °C for 30 minutes. Once the samples were loaded into the wells, the gels ran for 120 min at 65 mV in 1× TAE. Subsequently, the gels were removed from the electrophoresis chamber and stained with 0.5 μg/μL ethidium bromide to aid the visualization of the DNA bands. The ethidium bromide stain was removed with Type 1 ultrapure water. The gels were then visualized and photographed. The experiments were repeated at least three times and the representative assay is given in Figure 4.6.

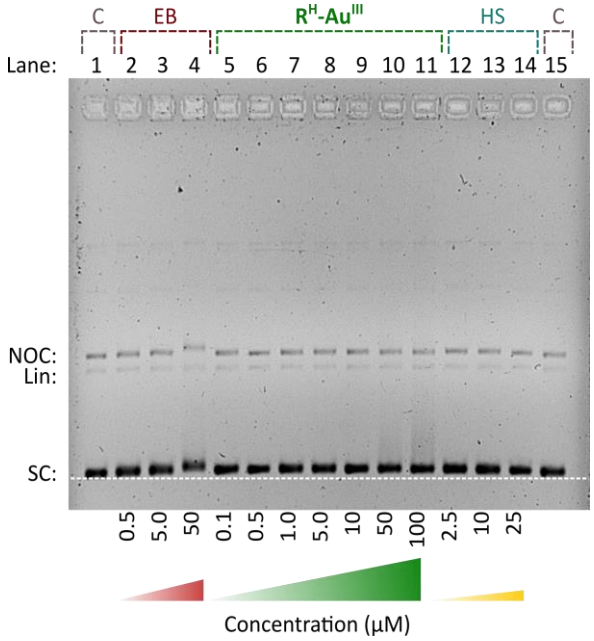


Figure 4.6. EMSA of **R^H-Au^{III}** with pUC57 plasmid DNA (2.5 ng/well, 1× TAE buffer (10% DMSO) that have SC, NOC and Lin DNA. The lanes contain pUC57 DNA only (C, lanes 1 and 15), increasing concentrations of ethidium bromide (EB, lanes 2–4), **R^H-Au^{III}** (lanes 5–11) and Hoechst 33258 (HS, lanes 12–14). Experiments were done in triplicate and the representative assay is shown.

In lanes 1 and 15, pUC57 in 10% DMSO in 1× TAE buffer was run, labelled C (for the control). In these lanes, the different topological forms of plasmid DNA i.e., SC, Lin and NOC are observed and their relative migration distance through the gel, under the experimental conditions employed, are observed. To compare the migration of the different DNA bands in the presence of a known DNA intercalator and a minor groove binder to the migration of DNA in the presence of **R^H-Au^{III}**, increasing concentrations of ethidium bromide (EB) and Hoechst 33258 (HS) were run in lanes 2–4 (labelled EB) and 12–14 (labelled HS), respectively.

Already at the low concentration of 0.5 μM EB (lane 2), a slight retardation in migration of all three bands are observed. The difference is amplified at 50 μM (lane 4), whereby all three bands migrated significantly slower than the control and a slight streak of the SC band is observed. When EB interacts with DNA, the double helix unwinds to accommodate the intercalator, increasing hydrodynamic drag which retards the mobility of the DNA in the gel.[340] By contrast, the minor groove binder, HS, does not induce these structural changes and no observable changes in the mobility of the DNA is noted in lanes 12–14, except for a very slight increase in the mobility of the DNA at increasing concentrations of HS.

No change in the mobility of any bands were observed for **R^H-Au^{III}** until 10 μM (lanes 5–9, Figure 4.6). At 50 μM and above, noticeable streaking of the SC band is observed (lanes 10, 11), similar and slightly more distinguished than EB at 50 μM (lane 4). The streaking represents a small amount of DNA of which the mobility was affected by **R^H-Au^{III}** and hints at the potential interaction of DNA with **R^H-Au^{III}**. However, the mobility of the bulk DNA of all topological forms were not as strongly affected such as the case with the organic intercalator, EB.

4.3.2.2 UV-vis titration experiments

UV-vis absorption titration studies with **R^H-Au^{III}** and calf thymus DNA (ctDNA) were carried out to investigate the potential binding between **R^H-Au^{III}** and DNA. The titration studies involved adding small incremental amounts of a high concentration stock solution of ctDNA to a fixed concentration of **R^H-Au^{III}** in a quartz cuvette with a pathlength of 1 cm. Any changes observed in the absorption spectrum of **R^H-Au^{III}** over the course of the experiment is potentially due to the interaction of ctDNA with **R^H-Au^{III}**.

The titration study was initially carried out in 1× TAE with 10% DMSO. However, after only a few additions of ctDNA to **R^H-Au^{III}** precipitation in the cuvette occurred. Changing the buffer to 1× PBS (10% DMSO) did allow for more additions of ctDNA without precipitation interfering with the absorption spectrum and therefore the repeat UV-vis titration studies were conducted in 1× PBS (10% DMSO). To a fixed concentration of **R^H-Au^{III}** (30.8 – 31.6 μM) in 1× PBS (10% DMSO) were added incremental amounts ranging from 5 – 50 μL of a stock ctDNA solution with a concentration of 1.47(2) mM bp. The concentration of the ctDNA stock solution was determined by using the molar absorptivity coefficient of 13200 bp M^{-1} cm^{-1}. Samples were incubated for 10 minutes at 28 °C (± 2 °C) before the measurements were

performed. Figure 4.7a shows the change in the absorption spectrum of **R^H-Au^{III}** of a representative experiment of three replicates.

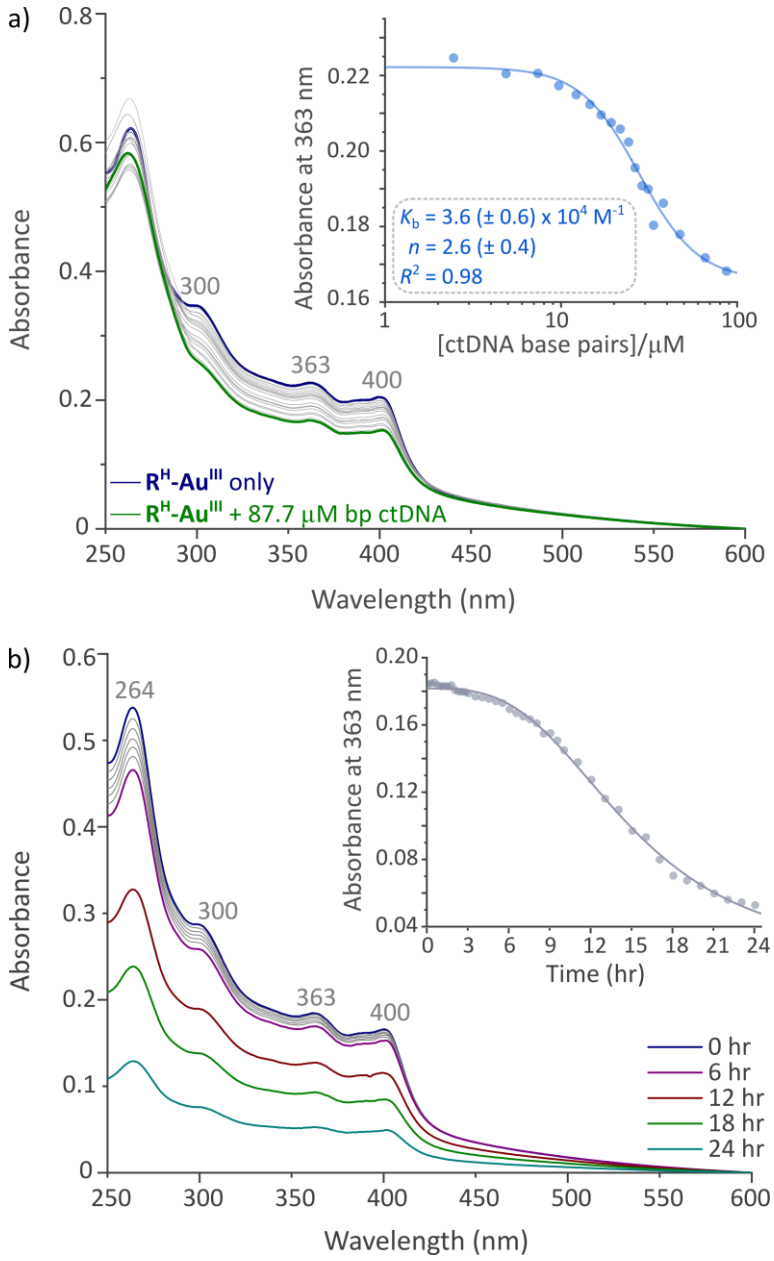


Figure 4.7. (a) The UV-vis absorption spectra of **R^H-Au^{III}** in 1× PBS and 10% DMSO before (30.8 µM, blue spectrum) and after sequential additions of ctDNA (final [ctDNA] = 87.7 µM bp, green spectrum). Inset of (a) shows the change in the absorbance at 363 nm as a function of [ctDNA] fitted to the Hill model. (b) The change in the UV-vis absorption spectrum of **R^H-Au^{III}** in PBS and 10% DMSO over 24 h The inset of (b) shows the change in absorption at 363 nm as a function of time.

The highest ratio of [ctDNA]:[**R^H-Au^{III}**] obtained, before visible precipitation occurred during the titration experiments, was 3:1. The spectrum illuminated with blue represents the absorbance spectrum of **R^H-Au^{III}** prior to the addition of ctDNA. The green spectrum

represents the absorbance spectrum of **R^H-Au^{III}** in the presence of 87.7 μM bp ctDNA, after incremental additions of ctDNA over time (represented in grey).

A decrease in absorbance intensity is observed across the characteristic maxima peaks of 300, 363 and 400 nm by approximately 25%. No significant shift in the peaks occurred and no isosbestic points had appeared during the titration experiments. The change in the UV-vis spectrum of **R^H-Au^{III}** upon the addition of ctDNA resemble that of the slow precipitation of **R^H-Au^{III}** only in 1× PBS (10% DMSO) over 24 hours (Figure 4.7b). The precipitation of **R^H-Au^{III}** in 1× PBS (10% DMSO) is also characterized by an equal drop in intensity of all the absorbance maxima. The hypochromicity at 363 nm as a function of time is shown in the inset of (Figure 4.7b). The changes observed in the UV-vis spectrum of **R^H-Au^{III}** and ctDNA is therefore due to the precipitation of the gold(III) complex. However, the rate of precipitation is clearly accelerated in the presence of ctDNA as the absorbance at 363 nm decreased by 25% (inset of Figure 4.7a) while the absorbance at 363 nm of **R^H-Au^{III}** in 1× PBS (10% DMSO) without ctDNA, during the first 6 hours (the duration of a typical titration experiment), only decreased by 8%. The significant drop in hypochromicity of **R^H-Au^{III}** during titrations with ctDNA, as opposed to without ctDNA, can potentially be attributed to a binding event, where the binding event itself is unable to contribute to the spectroscopic changes expected (such as bathochromatic shifts etc.) due to precipitation from solution.

The decrease in absorbance at 363 nm during the titration with ctDNA was fitted to the Hill model[341] with an R^2 value of 0.9 and random residual distribution around the x-axis; indicative of a relatively good fit (inset of Figure 4.7a). Using the Hill model, the affinity of **R^H-Au^{III}** for ctDNA was quantified by calculating an averaged (three replicates) binding constant (K_b) of $3.6 \pm (0.1) \times 10^4\ M^{-1}$. The K_b of EB to ctDNA in Tris-HCl buffer at 23 °C is reported to be between $2.5 \times 10^6 - 8.2 \times 10^4\ M^{-1}$, depending on the salt concentration.[342] Psoralen, a tricyclic aromatic compound on which extensive DNA-binding studies have been conducted, has a calculated K_b of $9.75 \times 10^3\ M^{-1}$ and other acridine-derivatives, which are known DNA intercalators have K_b values of 1.74×10^4 to $1.0 \times 10^6\ M^{-1}$.[343,344] The K_b for minor groove binders are usually slightly higher than intercalators with K_b values reported between 10^5 and $10^8\ M^{-1}$.[314,345] The metallointercalators, the CNC-gold(III) complexes, **25c** and **27b** (Figure 4.8), have reported K_b values of 4.5×10^5 and $5.4 \times 10^5\ M^{-1}$, respectively.[150,153] Ruthenium(II) polypyridyl complexes have long been under investigation for their DNA-binding abilities as they can be used as DNA

probes due to their luminescent properties.[346,347] The ruthenium complex, $[Ru(phen)_3]^{2+}$, **40**, Figure 4.8) binds to DNA via a semi-intercalative binding mode and induces a kink in the DNA. Substitution of one of the phen ligands with a ligand that can permeate deeper between base pairs such as dppz (-dipyrido[3,2-a:2',3'-c] phenazine, **41**, Figure 4.8), results in a significantly stronger binding constant (from 6.2×10^3 M^{-1} to 3.2×10^6 M^{-1}), with extended versions of the dppz ligands (of type **42**, Figure 4.8) reporting K_b values as high as 2.7×10^7 M^{-1}.[348–350] Interestingly, the latter complexes (of type **42**) and **40** do not show the associated changes in the UV-vis absorption spectrum during titration experiments with DNA and instead an overall decrease in hypochromicity and the absence of isosbestic points are observed; similar to that observed for $\mathbf{R^H\text{-}Au^{III}}$ and ctDNA during UV-vis titration studies. Moreover, a binding bite size (i.e., the number of DNA base pairs that is involved in the interaction between the metal complex and DNA) of n = 2.3 (±0.3) was calculated for $\mathbf{R^H\text{-}Au^{III}}$ and ctDNA and is similar to the n values reported for the extended dppz ruthenium complexes of type **42** (n = 2.1–2.3).

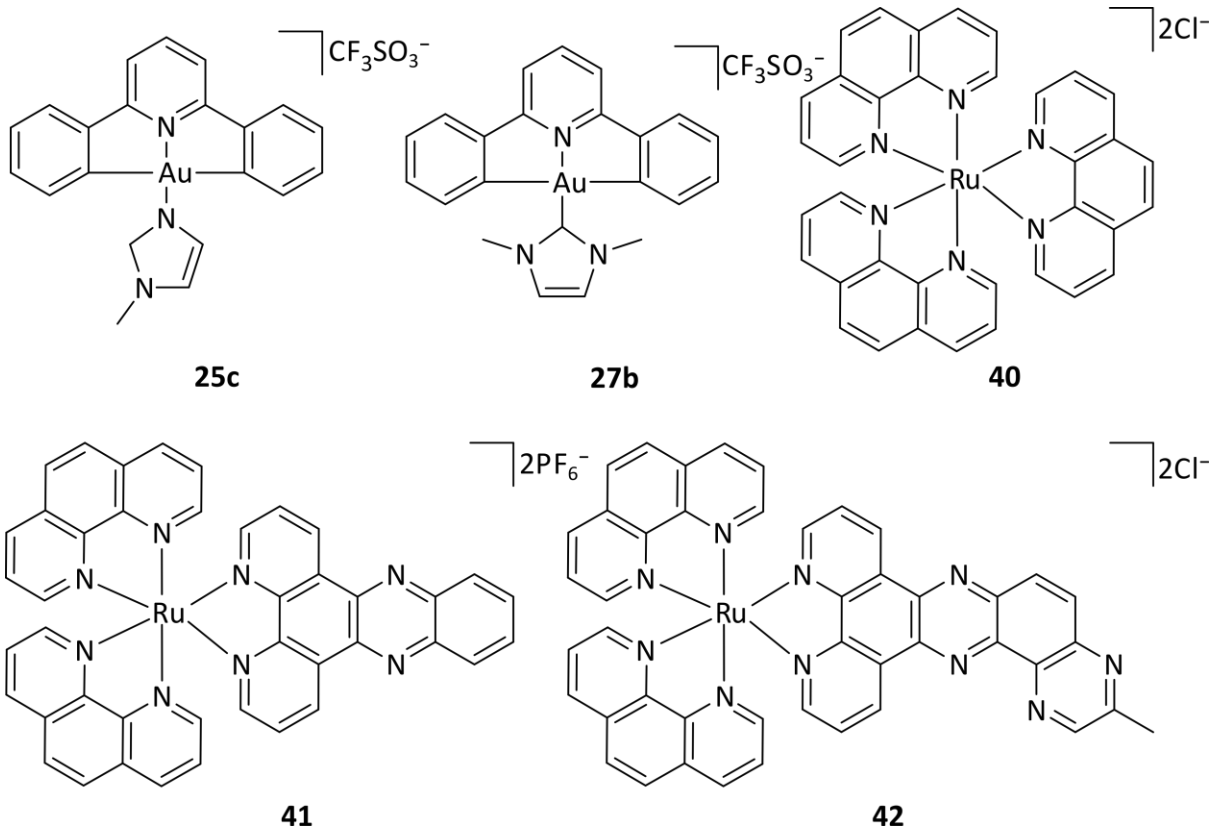


Figure 4.8. Selected examples of metal complexes with known DNA binding motifs proposed by extensive DNA-binding studies.

The K_b of **R^H-Au^{III}** falls into the lower end of the range of binding constants for known intercalators and compares well to the K_b obtained for the semi-intercalative Ru(II) complex, **40**. The EMSA results suggested weak intercalative interaction between **R^H-Au^{III}** and plasmid DNA (compared to EB) and the calculated K_b of **R^H-Au^{III}** supports a semi-intercalative binding motif. Results from further DNA binding studies such as viscometry and thermal denaturation studies are necessary to confirm binding between **R^H-Au^{III}** and DNA and aid the elucidation into the binding motif.

4.3.2.3 Viscometry

The influence of **R^H-Au^{III}** on the viscosity of ctDNA was investigated and compared to the changes in the viscosity of ctDNA induced by EB and HS under similar experimental conditions. Stock solutions of **R^H-Au^{III}**, EB and HS of varying concentrations with 1 μM, 5 μM or 50 μM ctDNA in PBS (10% DMSO) were prepared and incubated for at least 30 minutes at 37 °C prior to measurements. Using a rolling-ball viscometer, each sample (100 μL) was injected into a thin tube followed by the addition of a gold ball. The tube was placed inside the viscometer and the viscosity of the samples were measured according to the Höppler principle: the time taken for the ball to travel under gravity through a specified distance in the sample fluid at an incline of 80°.[351] For each sample, three independent measurements were recorded, and each experiment was repeated at least twice. The results are plotted as a graph (Figure 4.9) that shows the change in the relative viscosity of ctDNA (compared to the viscosity of ctDNA in 1× PBS and 10% DMSO, η_0) against increasing molar ratios of **R^H-Au^{III}**, EB and HS.

The experiments with EB, HS and **R^H-Au^{III}** were all initially conducted with 1 μM ctDNA. While the viscosity of ctDNA did not change in the presence of HS (Figure 4.9, blue triangles), the expected increase in viscosity due to EB, at this low DNA concentration, did not occur. Instead, as the molar ratio of [EB]:[ctDNA] increased, the viscosity of the samples decreased. The same was observed when the experiments were conducted with 5 μM ctDNA. The decrease in viscosity at such low concentrations of ctDNA can be attributed to the likelihood that the viscosity of EB solutions themselves were measured with negligible amounts of DNA. The expected increase in viscosity was observed when the concentration of ctDNA was increased to 50 μM where the relative viscosity of ctDNA increased with increased EB concentration and the results are comparable to what is reported (Figure 4.9, green squares).[315,352] Repeating the same experiment with 50 μM ctDNA and **R^H-Au^{III}** could not be managed due to severe

precipitation at already low molar ratios (≥ [$\mathbf{R^H\text{-}Au^{III}}$]:[ctDNA] = 1). Viscometry measurements are sensitive to any obstructions inside the tube since the movement of the ball is significantly impacted by air bubbles and precipitated material etc. Therefore, the viscosity of these samples was difficult to measure and even more so to repeat for reproducibility purposes. As such, the change in the relative viscosity of 5 µM ctDNA and increasing amounts of $\mathbf{R^H\text{-}Au^{III}}$ is shown in Figure 4.9 (red circles) alongside the effect of EB with 50 µM ctDNA (green squares) and HS (blue triangles) with 1 µM ctDNA.

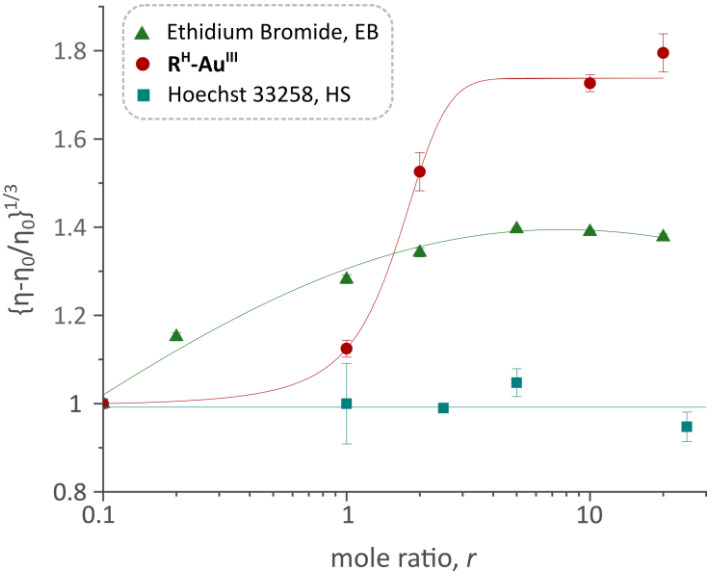


Figure 4.9. The change in the relative viscosity of ctDNA in the presence of $\mathbf{R^H\text{-}Au^{III}}$ (red circles), EB (green squares) and HS (blue triangles) as a function of increasing molar ratios of compound to ctDNA (in base pairs) at 37 °C in 1× PBS (10% DMSO). Triplicate measurements of dynamic viscosity (η, mPa s) were averaged and used to calculate the relative viscosity of the solution, $\{\eta\text{-}\eta_0/\eta_0\}^{1/3}$, where η_0 represents the dynamic viscosity of ctDNA in 1× PBS and 10% DMSO.

The most striking observation is the significant increase in the viscosity of ctDNA induced by $\mathbf{R^H\text{-}Au^{III}}$ compared to EB and indicates that $\mathbf{R^H\text{-}Au^{III}}$ is indeed interacting with ctDNA. The binding of $\mathbf{R^H\text{-}Au^{III}}$ causes a lengthening of the helix resulting in a noteworthy increase in the viscosity of ctDNA as induced by known DNA intercalators. The increase in viscosity of ctDNA with increasing molar ratio of [$\mathbf{R^H\text{-}Au^{III}}$]:[ctDNA] follows a sigmoidal relationship where the viscosity increases slowly at low molar ratios and is rapidly increased between molar ratios of 1 and 10. Beyond the molar ratio of 10, the viscosity does not increase significantly and binding saturation is likely reached. The increase in viscosity due to EB is gradual; an increase in viscosity is immediately evident at low molar ratios, whereafter a steady increase is

observed. Binding saturation with EB is reached sooner than with **R^H-Au^{III}** at a molar ratio of about 4.

The viscosity of DNA is sensitive to changes in the axial length of the DNA helix. Classical intercalators (e.g. EB) insert between the base pairs, the latter being separated to accommodate the intercalator. The helical axis unwinds, lengthens, and stiffens as a result and the viscosity is increased concomitantly. Groove-binders (e.g. HS) do not induce the same hydrodynamic changes and relatively no change in the viscosity of DNA is observed.[313,315] The metallointercalators, the polypyridyl Ru^{II}-analogues of $[Ru(phen)_2dppz]^{2+}$ (of type **42**, Figure 4.8) increase the viscosity of DNA linearly with increasing complex concentrations.[348] The same linear increase was also observed for the CNC-gold(III) DNA intercalators, **25c** and **27b** (Figure 4.8).[150,153] In contrast, the viscosity of DNA decreases in the presence of partial intercalators such as $[Ru(phen)_3]^{2+}$ (**40**, Figure 4.8) and the organic insecticide acetamiprid (ACT), as they can act as a wedge by splaying the bases at the intercalation site on one strand, leading to a partial inward collapse of the base pair on the complementary strand.[352–354] The result is a bend in the DNA and a shortening of the effective length of the helix. The same effect is induced by the covalent binder, cisplatin.[20,298]

The significant non-linear increase in the viscosity of ctDNA induced by **R^H-Au^{III}** is unique, corresponding to neither behaviour of a classical intercalator nor that of a conventional partial intercalator. Furthermore, none of the collective evidence is consistent with minor groove binding.

4.3.2.4 Thermal Denaturation

The interaction between **R^H-Au^{III}** and ctDNA was further validated by investigating the change in the melting temperature of ctDNA due to **R^H-Au^{III}** and compared to EB. The change in the melting temperature (T_m) of ctDNA in the presence of **R^H-Au^{III}** was investigated concurrently. The T_m is the temperature at which 50% of the duplex has dissociated into two single strands and is monitored by an increase in absorbance at 260 nm as a function of temperature. Usually, ΔT_m offers useful insight into the strength of the interaction; duplex DNA will require more energy (higher temperature) to separate into two strands when a drug is bound that stabilizes the duplex and therefore increases the T_m of the drug-DNA complex compared to the T_m of the native DNA.[20,298]

Initially, the thermal melt curves of ctDNA and **R^{H}-Au^{III}** were conducted at a molar ratio of 1:3 ([ctDNA]:[**R^{H}-Au^{III}**]) to ensure that binding is saturated without the occurrence of precipitation. Unfortunately, as 100 µM is the maximum concentration of **R^{H}-Au^{III}** that can be reached in 1x PBS (10% DMSO), the maximum concentration of ctDNA used was only 35 µM. Under these experimental conditions, the absorbance at 260 nm were too scattered to make accurate calculations, especially since the **R^{H}-Au^{III}** also has an absorbance maximum close to 260 nm (264 nm). The molar ratio was inverted (3:1, [ctDNA]:[**R^{H}-Au^{III}**]) to gain reliable information regarding the thermal denaturation of ctDNA in the presence of **R^{H}-Au^{III}** under non-saturating conditions. For comparison, the same experimental conditions were used to measure the effect of EB on the thermal denaturation of ctDNA.

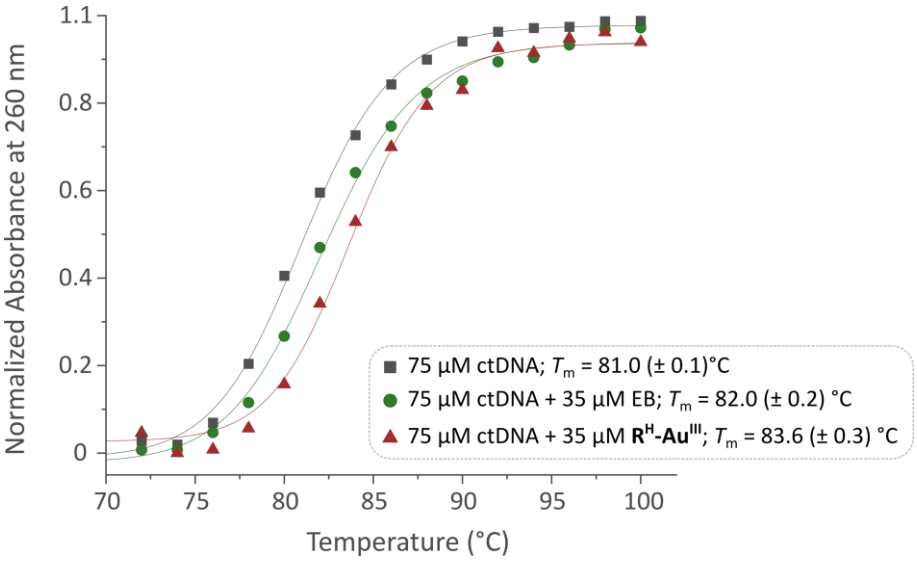


Figure 4.10. The thermal denaturation curves of 75 µM bp ctDNA measured as the change in the absorbance at 260 nm as a function of time in the presence of 35 µM **R^{H}-Au^{III}** or 35 µM EB at 37 °C in 1× PBS (10% DMSO). The data are fitted to Boltzmann sigmoidal functions.[355]

At the [ctDNA]:[**R^{H}-Au^{III}**] ratio of 3:1, **R^{H}-Au^{III}** induced a ΔT_m of +2.7 °C, while under the same experimental conditions, EB induced a slightly smaller ΔT_m of +1.8 °C (Figure 4.10). Under these conditions, the interaction between **R^{H}-Au^{III}** and ctDNA is slightly stronger than the interaction between EB and ctDNA. The results correspond partly to the viscosity data, where **R^{H}-Au^{III}** did increase the viscosity of the DNA more than EB.

The ΔT_m is dependent on the ratio of DNA to drug investigated. The ΔT_m of the polypyridyl Ru^{II} complexes (of type **42**, Figure 4.8) increased as the concentration of complex to DNA increased. At DNA:[Ru^{II}] ratios of 10:1 an increase in T_m of more than 6 °C were described

whereas at a ratio of 20:1, ΔT_m of 1.2 – 2.0 °C were reported for the complexes.[348] A significant increase in the T_m of 16.5 °C of ctDNA was induced by the CNC-gold(III)-complex, **25c** at a 1:1 molar ratio.[150] The degree to which partial intercalators change the T_m also varies. For instance, the $[Ru(phen)_3]^{2+}$ complex, **40** induces a maximum ΔT_m of 20 °C at a ratio of 6:1 ($\Delta T_{m^{max}}$)[356] whereas the organic insecticide, ACT, only increased the T_m by 3 °C at a [ctDNA]:[ACT] ratio of 3:1.[353] The latter comparing well to the ΔT_m obtained for **R^H-Au^{III}**.

The K_b calculated from the UV-vis titration study and the results from EMSA suggest that **R^H-Au^{III}** is interacting with DNA via partial intercalation while the thermal melt analysis reveal that **R^H-Au^{III}** stabilizes double-stranded DNA enough to increase the melting temperature, even more than ethidium bromide under the same conditions. Conversely, the viscosity data contradict this binding motif as partial intercalators decrease the viscosity of DNA, provided that they induce a kink/bend in the helical axis. It is possible that **R^H-Au^{III}** is binding to ctDNA via partial intercalation that does not result in the shortening of the helix and hints towards a non-conventional partial intercalative binding motif.

4.3.2.5 Linear Dichroism

Linear dichroism is a UV-vis spectroscopy technique based on the absorption of polarized light. Polarized light is absorbed by a molecule during a transition when a transition moment dipole exist that can interact with the polarized electric field vector and as a result, change the direction of the light.[325]

Linear dichroism (LD) is the difference between the absorbance (A) of polarized light travelling parallel (A_{par}, A_{II}) and perpendicular (A_{per}, $A_{\perp}$) relative to an orientation axis (Eq. 1). For the purpose of measuring the LD of drug-DNA interactions, the orientation axis is equivalent to the helical axis of the DNA (Figure 4.11a). A Couette cell can be used for measurements to orientate the DNA with hydrodynamic flow. The inner cylinder of the Couette cell rotates at a certain speed (e.g. 1000 rpm) creating a flow that aligns large molecules like DNA easily (Figure 4.11a). The extent of the LD signal is dependent on two parameters: S and $cos^2\alpha$, where S is the orientation factor and α is the angle between the transition moment dipoles and the helical axis (Eq. 2). A perfectly aligned DNA helix parallel to the flow is represented by $S = 1$ and details that the DNA is stiff, straight, and easy to orientate. An orientation factor nearing 0 indicates that the DNA molecules have become flexible, kinked or shortened.

Furthermore, the LD spectrum of DNA is negative (Figure 4.11b) since the transition moments of the base pairs are 90° aligned relative to the helical axis ($\alpha = 90°$).[357]

$$LD(\lambda) = A_{par}(\lambda) - A_{per}(\lambda) \quad (1)$$

$$LD^r = \frac{LD(\lambda)}{A_{iso}(\lambda)} = S \times \frac{3}{2} \times (3cos^2\alpha - 1) \quad (2)$$

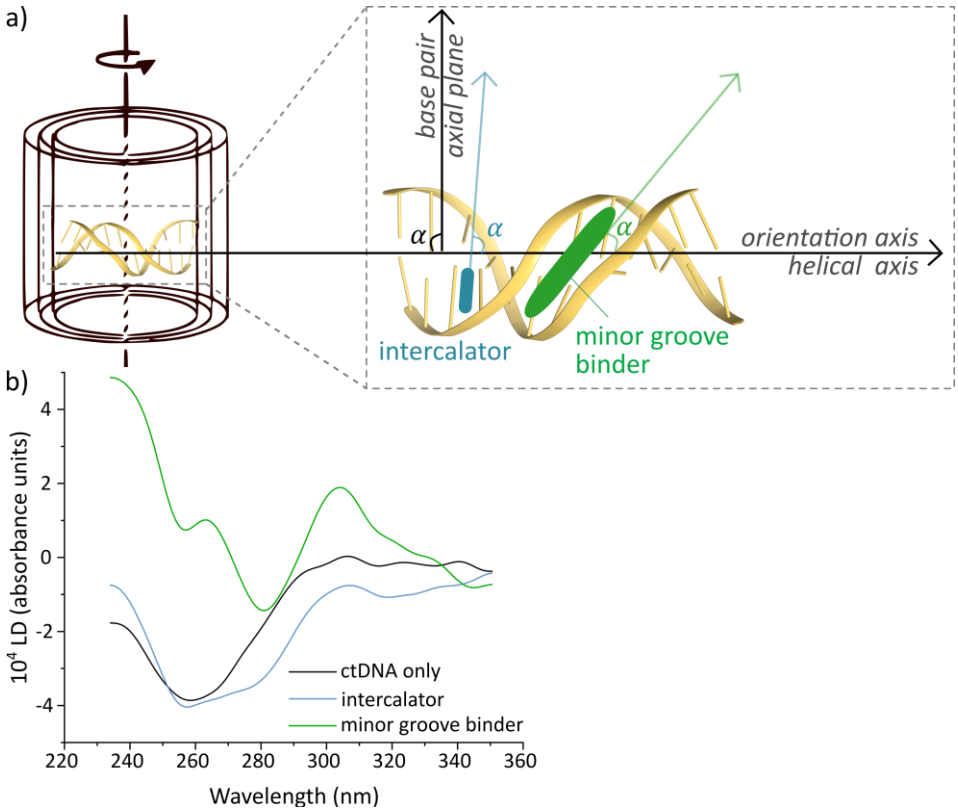


Figure 4.11. (a) A schematic illustration of a Couette cell aligning DNA molecules so that the orientation axis is equivalent to the helical axis of the DNA and the plane of the base pairs are orientated ~ 90° relative to the orientation axes. (b) The LD spectrum of ctDNA alone (black) is negative (peak at ~ 260 nm) due to the perpendicular orientation of the base pair plane and the helical axis. In the presence of the intercalator (EB, [drug]:[ctDNA] = 1), the LD spectrum of ctDNA is of the same sign and magnitude. In the presence of a minor groove binder (HS, [drug]:[ctDNA] = 1), the LD spectrum of ctDNA is positive.

The sign of the LD spectra of DNA provides additional insight as to what type of interaction is involved when small molecules are bound. Usually, DNA intercalators have their $\pi^* \leftarrow \pi$ transition moments parallel to the plane of the base pairs and perpendicular to the helical axis ($\alpha = 90°$) and will produce a LD signal of the same sign and magnitude as DNA itself

(Figure 4.11b). Typically, the transition moments of minor groove binders have their long axis transition moments aligned < 55° (~ 45°) relative to the helical axis and will produce a positive LD spectrum (Figure 4.11b). Small molecules (i.e. drugs) rarely have LD activity since they are difficult to orientate (S ~ 0). The appearance of LD activity for a drug (i.e. induced LD, ΔLD) due to DNA is an immediate indication of a binding event since the drug is now aligned and the electronic transition dipole moments of the two chromophores are coupled.[325,357]

LD spectra of **R^H-Au^{III}** and ctDNA were measured at increasing molar ratios of **R^H-Au^{III}** (40 – 2.5 μM) to a fixed concentration of ctDNA (10 μM.bp) at 37 °C using a Couette cell tube rotating at 900 rpm in 1× PBS (10% DMSO). For comparison, the CD and LD spectra of EB and HS were measured at a 1:1 molar ratio of [drug]:[ctDNA] (Figure 4.11b). The ΔLD spectra of EB and HS are shown in Figure 4.12a and Figure 4.12c, respectively. ΔLD spectra are obtained by subtracting the LD of ctDNA alone from the LD spectrum of the drug-DNA spectrum, thus obtaining the change in the LD of the drug due to DNA.

Both EB and HS did not exhibit LD spectra of their own, as expected. However, upon binding with DNA, both EB and HS displayed active LD spectra due to their interaction with DNA. For EB, all three peaks of 260, 285 and 322 are negative and the spectrum changes sign to positive below 250 nm. Both transition dipole moments of EB at 300 nm and 450–500 nm are orientated parallel to the base pair plane and are thus perpendicular to the helical plane (Figure 4.12b).[325] The sign of the ΔLD is negative since α is close to 90° and signifies that EB is indeed an intercalator. Below 250 nm, the LD spectrum of ctDNA alone is more negative that the LD spectrum of DNA and EB (Figure 4.11b) and could explain the increase in the positive signal observed below 250 nm in the ΔLD spectrum. The ΔLD spectrum of HS shows strong positive induced LD signals at 242, 260, 303 nm, where the peak at 285 nm is just above 0. The transition moment dipoles of HS are likely across its long axis (similar to other minor groove binders).[325] Within the minor groove pocket, the long axis of HS is oriented ~ 45° relative to the base pair plane and helical axis (Figure 4.12d), accounting for the significantly positive ΔLD spectrum.

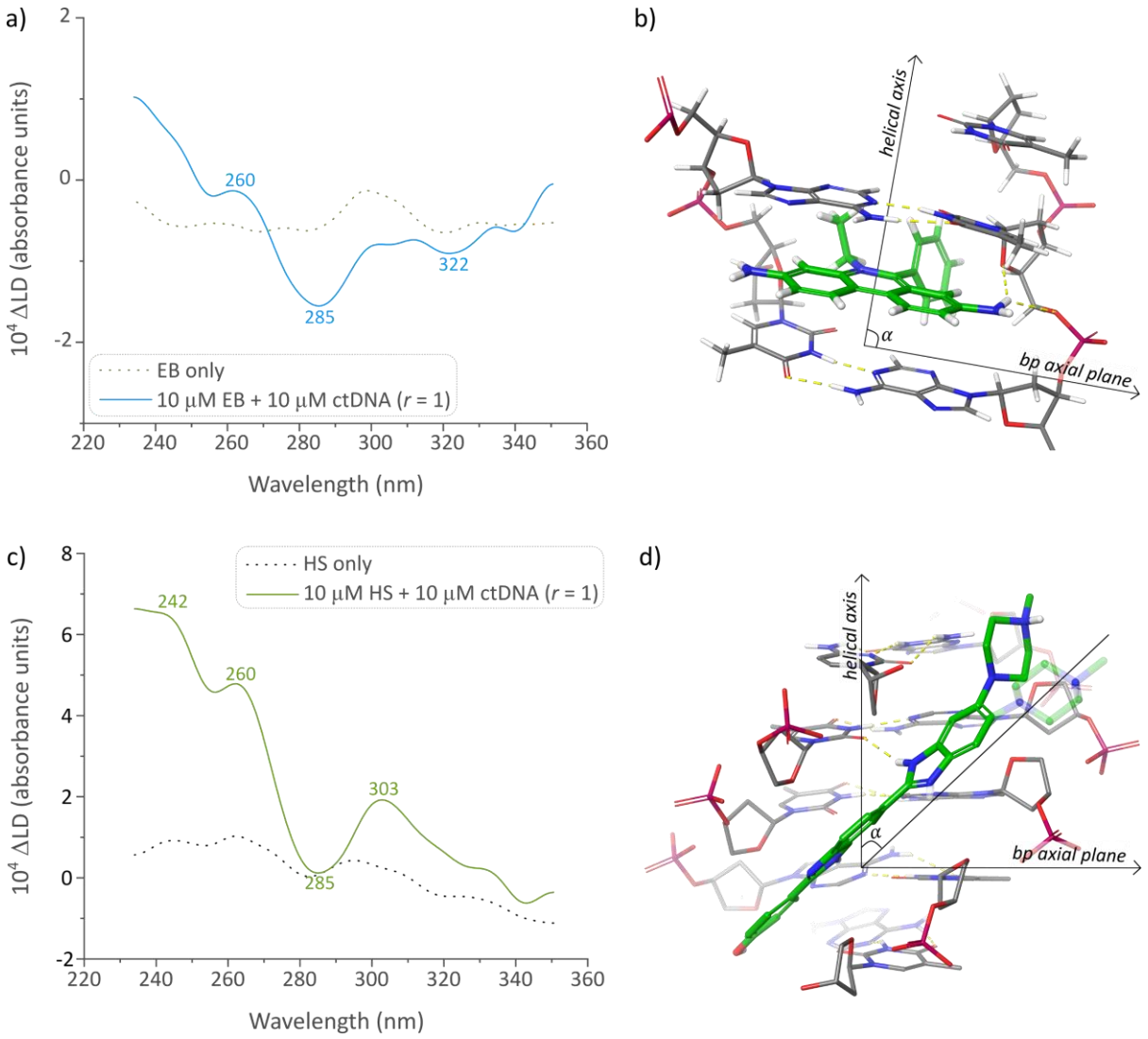


Figure 4.12. (a) The *Δ*LD spectrum of EB with ctDNA at a *r* = 1 where *r* is the molar ratio of drug to ctDNA. b) a docking pose generated of EB intercalated with double stranded DNA (PDB: 2O1I).[358] (c) The *Δ*LD spectrum of HS with ctDNA at a *r* = 1. (d) The crystal structure of HS in the minor groove of DNA (PDB: 8BNA).[314]

The *Δ*LD spectrum of **R^H-Au^{III}** is shown in Figure 4.13 at increasing [**R^H-Au^{III}**]:[ctDNA] ratios while the [ctDNA] was kept constant at 10 μM. Similar to EB and HS, the gold(III) complex did not display a LD spectrum of its own (dotted line, Figure 4.13). At small molar ratios of **R^H-Au^{III}** (*r* = 0.25, 0.50), the *Δ*LD spectrum of **R^H-Au^{III}** with ctDNA did not show significant changes in the shape of the curve and instead shifted position to more positive (*r* = 0.25) and more negative (*r* = 0.5). At low binding ratios, the interaction between **R^H-Au^{III}** between ctDNA is presumably too weak for sufficient alignment of the necessary electronic transition moments of **R^H-Au^{III}** and the DNA, hence the irregular "positions" of the *Δ*LD spectra at *r* = 0.25 and 0.5.

However, at higher molar ratios of $r \geq 1$, a definite peak at 262 nm is observed and grows in intensity as r is increased. At r = 4, the peak has shifted to 253 nm and the sign is positive. Moreover, at r = 4, two strong negative peaks at 295 and 303 nm are observed, and where the development of these peak was apparent already at r = 1.

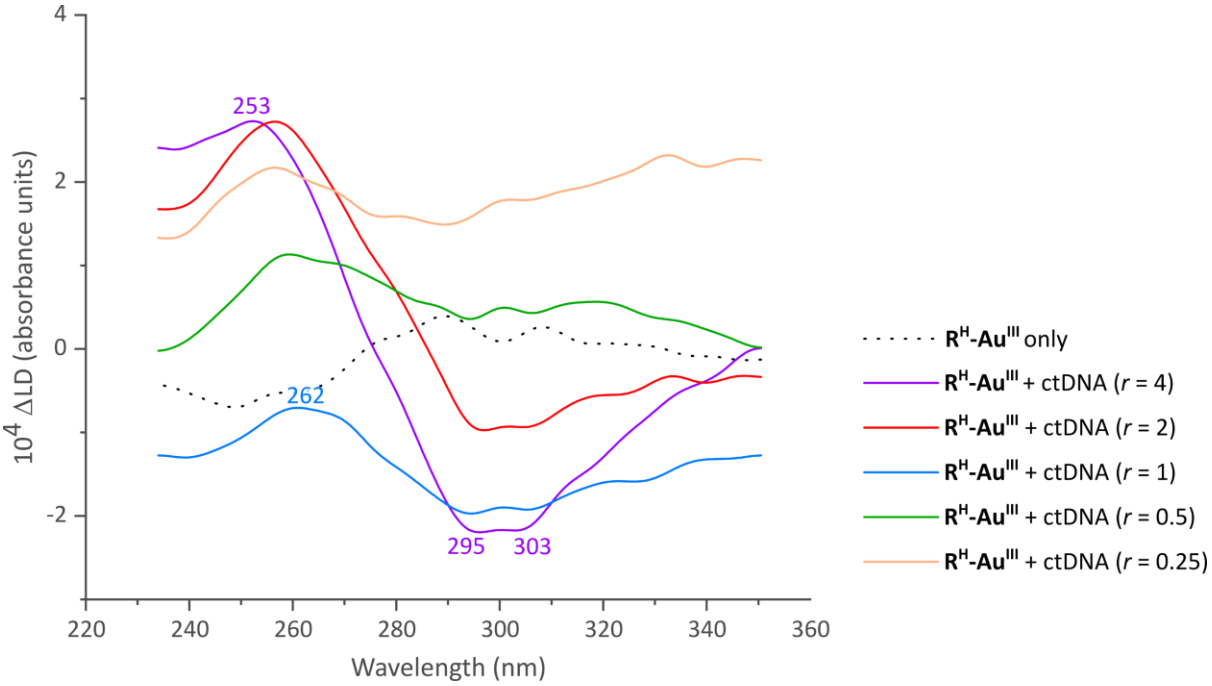


Figure 4.13. The ΔLD spectrum of **R^H-Au^{III}** with 10 µM ctDNA at increasing [**R^H-Au^{III}**]:[ctDNA] ratios (r) of 0.25 – 4 in 1× PBS (10% DMSO) at 37 °C.

DNA does induce a change in the LD of **R^H-Au^{III}** and therefore indicates that there is an interaction between the two molecules, albeit more significant at higher molar ratios. Further inspection of the ΔLD spectrum of **R^H-Au^{III}** suggests that $\pi \rightarrow \pi^*$ transition moments of the **R^H-Au^{III}** are perpendicular to the helical axis evidenced by a sharp negative ΔLD signal at 295 and 303 nm. EB at r =1 had similar peaks located negatively at 285 and 322 nm (Figure 4.12a). At r = 1 for **R^H-Au^{III}**, the peak at 262 nm is slightly more negative than the same peak for EB. Unlike EB, **R^H-Au^{III}** is not a planar molecule and it is likely that separate $\pi^* \leftarrow \pi$ transition moments of **R^H-Au^{III}** are orientated $\sim 90°$ relative to the $\pi^* \leftarrow \pi$ transition moments contributing to the negative signals at 295 nm and 303 nm. These out-of-plane transition moments are likely contributing to the sharp increase and shift observed in the 262 nm peak at higher molar ratios. However, the positive ΔLD signal at 253 nm at the highest molar ratio (r = 4) is smaller than that of the 242 and the 260 nm peaks observed on the ΔLD spectrum of HS at r =1.

The ΔLD spectra of **R^H-Au^{III}** at increasing molar ratios indicates that **R^H-Au^{III}** is interacting with DNA. At lower ratios, the binding is weak and negligible but as the molar ratio of **R^H-Au^{III}** increase, a noteworthy interaction is observed. When interaction between **R^H-Au^{III}** and DNA occurs, the resulting ΔLD spectra suggest an intercalation binding motif due to similarity to that of the ΔLD spectrum of EB. In contrast, the strong positive ΔLD spectrum of HS with DNA across all wavelengths is not observed for **R^H-Au^{III}**, except for the peaks below 260 nm that positively increase to approximately half the intensity of the 242 and 260 nm peaks of HS at higher molar ratios (r = 2, 4 for **R^H-Au^{III}** vs. r = 1 for HS). Due to the significant differences in the ΔLD spectra of **R^H-Au^{III}** and HS at longer wavelengths, a complete minor groove binding motif for **R^H-Au^{III}** can be ruled out. However, the LD experiments do support the finding that a partial intercalative binding motif for **R^H-Au^{III}** and DNA is operative, as suggested by the other biomolecular methods employed and discussed above.

4.3.2.6 Biomolecular simulations

Molecular docking is used to find the best alignment between two molecules with respect to each other. The process of biomolecular docking involves the docking of a ligand into a binding site of a biological macromolecule (e.g. DNA). Under standard docking protocols, the binding site of the biomolecule was held rigid while the translational and rotational degrees of freedom of the ligand is taken into consideration when generating a suitable pose of the ligand within the binding site. Furthermore, a scoring function (ΔG_{score}) is generated that represents the binding affinity of the ligand and the interaction site for a particular pose.[359]

In an attempt to explain the interaction between **R^H-Au^{III}** and DNA, molecular docking of **R^H-Au^{III}** with several DNA targets were performed using *Glide 5.0* standard precision (SP)[360–362] and the OPLS3e force field[363] from the *Schrödinger 2020-3* software suite with published X-ray structures of DNA targets found on the RSCB protein data bank (www.rcsb.org). Docking experiments were run on DFT-optimized structures of **R^H-Au^{III}** and EB. Binding sites were directed with grid boxes of varying sizes (12 – 40 Å) and default docking settings were employed.

The space-filled DFT optimized structure of **R^H-Au^{III}** is displayed in Figure 4.14 and clearly shows that, due to the sterically demanding wingtip groups (Dipp), the carbazole is only partially exposed for potential intercalation into DNA. As a result, *Glide* could produce relatively few poses of **R^H-Au^{III}** bound to standard intercalation sites.

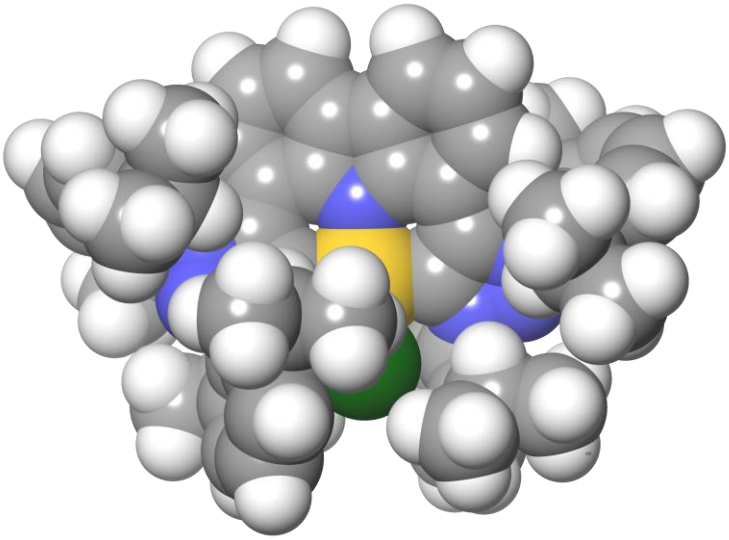


Figure 4.14. The space-filled DFT-optimized structure of $\mathbf{R^H\text{-}Au^{III}}$ showing how the bulky Dipp wingtip groups restrict access to the carbazole moiety.

However, an example of the partial intercalative binding mode of $\mathbf{R^H\text{-}Au^{III}}$ was obtained by using a palindromic DNA sequence (PDB:4E1U) of 5′-d(CGGAAAATTACCG)-3′.[358] $\mathbf{R^H\text{-}Au^{III}}$ was able to target the central 5′-AT-3′ step with a modest *Glide* docking score of −7.93 kcal mol^{-1}. To give some perspective on the docking score, the docking score obtained for EB and the same palindromic DNA sequence was −8.77 kcal mol^{-1} while EB intercalated with double stranded mismatched DNA (PDB: 2O1I, Figure 4.12b) was scored at −10.52 kcal mol^{-1}. The docking pose of $\mathbf{R^H\text{-}Au^{III}}$ within the 5′-AT-3′ site is shown in Figure 4.15 at different viewing angles. The docking pose is viewed 'head on', from the side and from the top respectively in Figure 4.15. From these views, it is apparent that the carbazole ring insert between the base pairs while the rest of the gold(III) complex i.e., the triazolylidenes and associated wingtip groups are extended beyond the intercalation site into the minor groove.

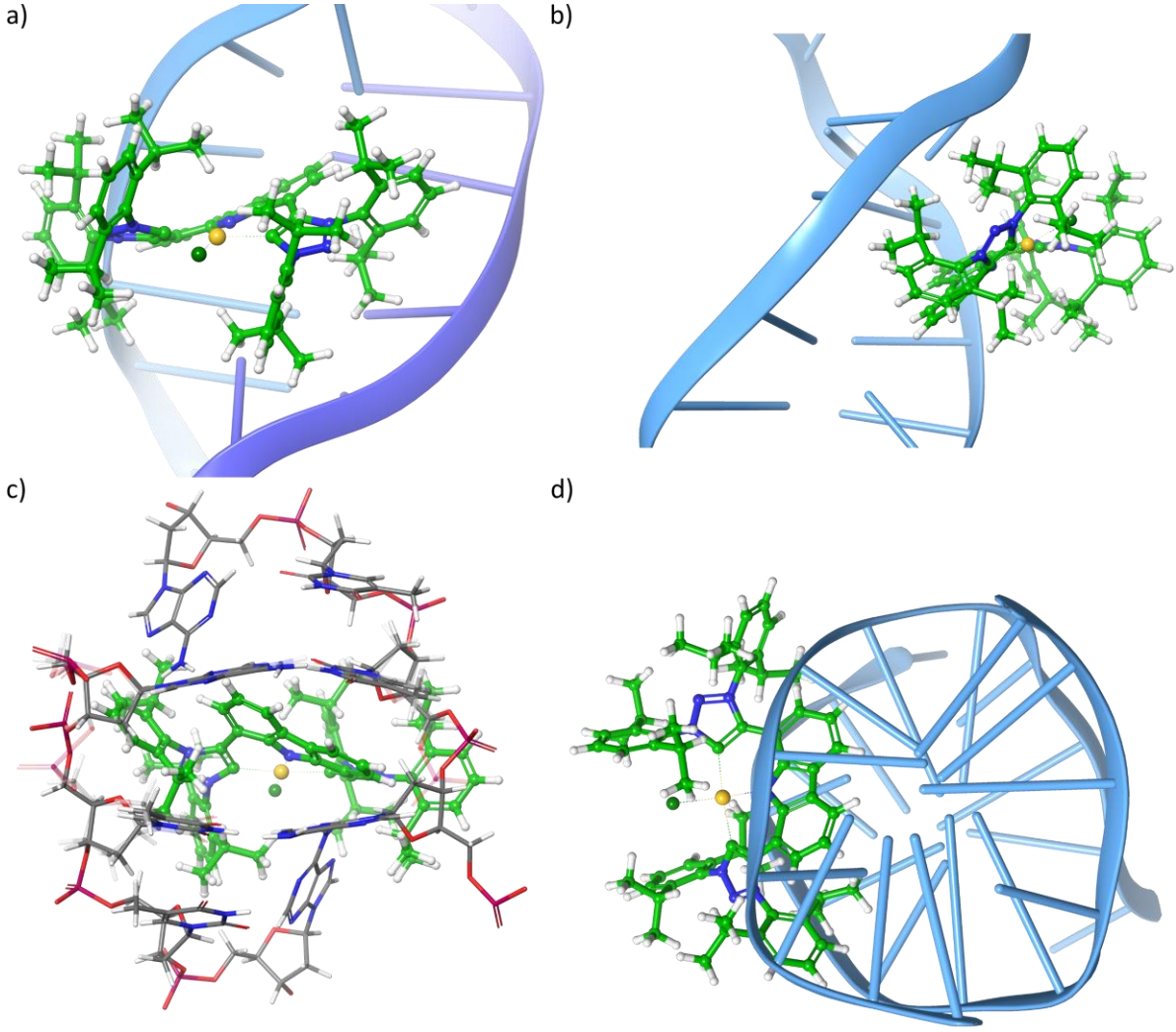


Figure 4.15. The lowest-energy docking pose of **R^H-Au^{III}** within the central 5′-AT-3′ step of the 5′-D(CGGAAAATTACCG)-3′ DNA sequence. The position of **R^H-Au^{III}** at the intercalation site is shown head on at both a) and c), whereas c) shows the chemical detail of the nucleic acid residues, A and T. The DNA strand as viewed from b) the side and from d) the top.

The partial-intercalative/minor groove hybrid docking pose of **R^H-Au^{III}** partly explain the experimental results obtained from the biomolecular methods described above. However, the docking results fail to explain the effect of **R^H-Au^{III}** on the viscosity of ctDNA, especially compared to a conventional organic intercalator. The dose-responsive increase in the viscosity of DNA with **R^H-Au^{III}** could suggest that **R^H-Au^{III}** is involved in crosslinking or entangling DNA strands and thereby increasing the polymeric nature of the biomolecule. To investigate this, **R^H-Au^{III}** was docked into a DNA three-way junction (Figure 4.16) reported by Oleksi et al. (PDB 3I1D).[364]

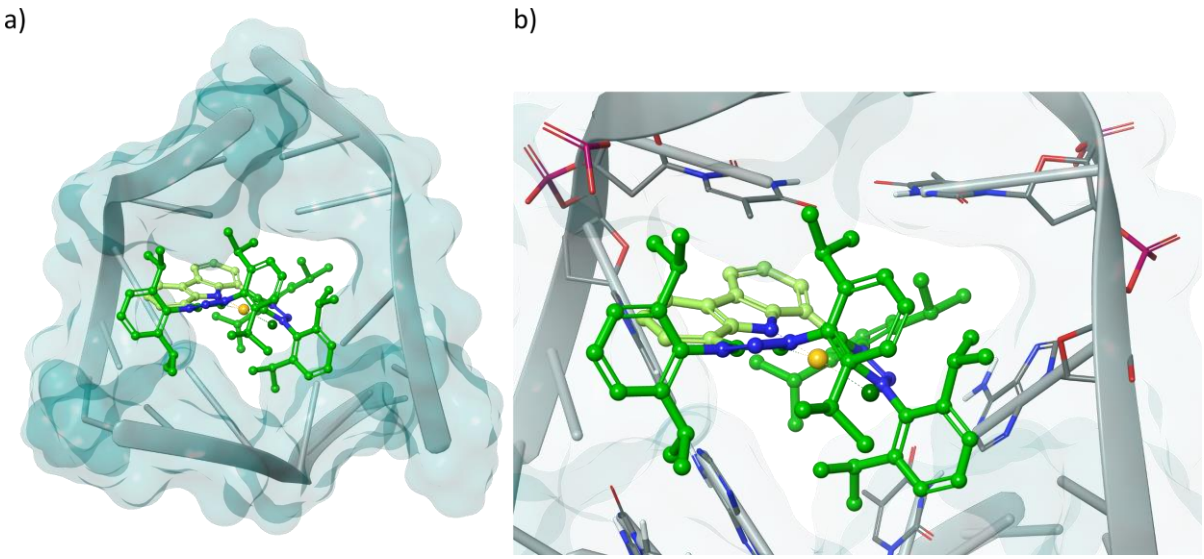


Figure 4.16. The docking pose of **R^H-Au^{III}** with a palindromic hexameric three-way junction with the sequence 5′-d(CGTACG)-3′. (a) illustrates the centrally located binding site occupied by **R^H-Au^{III}**. (b) shows the position of **R^H-Au^{III}** relative the nucleotide residues within the interaction site.

The structure of the three-way junction comprises of three nucleotide strands, each 6 nucleotides long with a sequence of 5′-d(CGTACG)-3′. The junction is centrally located in between the 5′-TA-3′ steps of all three strands. At first glance, the shape of **R^H-Au^{III}** is complimentary to the binding site and forms a stable, non-covalent adduct with a favourable binding score of −11.89 kcal/mol^{-1} (Figure 4.16a). On further inspection, the generated pose reveal that the carbazole moiety is located in between the adenine and thymine bases of the 5′-TA-3′ step of one strand, orientated parallel to the thymine ring at 3.8 Å apart, which is slightly longer than the typical $\pi - \pi$ stacking interactions of between 3.4 – 3.6 Å (Figure 4.16b).[365]

Three and four-way DNA junctions are vital intermediate structures during DNA replication. Unlike four-way junctions, the spontaneous in vitro formation of three-way junctions in solution are unknown.[366] Therefore, the docking results remain speculative and require experimental verification with oligonucleotides that are known to form three-way junctions. Nonetheless, the biomolecular simulations have revealed that it is both theoretically possible and thermodynamically favourable for **R^H-Au^{III}** to interact with a DNA target despite its steric bulk. Moreover, the binding of **R^H-Au^{III}** might be involved in the stabilization of secondary DNA structures that are formed during genomic processes that are an uncontrolled occurrence in cancer cells.

4.3.3 Protein Binding Studies

Gold(III) complexes are known to preferentially bind to proteins instead of DNA.[127] In particular, the Auoxo family of gold complexes (e.g. complex **38**, Figure 4.2) are widely known to bind to proteins such as HSA and HEWL via the Au^{I} ion as a result of reduction of Au^{III} to Au^{I} and associated loss of ligands.[308,309]

UV-vis absorption titration studies of $\mathbf{R^{H}\text{-}Au^{III}}$ in the presence of HEWL and HSA were conducted. During the titration experiments with $\mathbf{R^{H}\text{-}Au^{III}}$ and ctDNA, the DNA was added in small increments to a fixed concentration of metal complex. However, when the process was repeated for HEWL whereby a small amount of a stock concentration of HEWL was added to $\mathbf{R^{H}\text{-}Au^{III}}$ in the cuvette, precipitation occurred immediately. The titration studies with the proteins were therefore conducted in reverse, whereby a stock concentration of $\mathbf{R^{H}\text{-}Au^{III}}$ were added to a fixed concentration of protein. The changes in the absorbance spectra for both HEWL and HSA were studied at 280 nm (Figure 4.17).

The absorption spectrum of HSA titrated against $\mathbf{R^{H}\text{-}Au^{III}}$ is shown in Figure 4.17a. The spectrum of HSA before addition and in the presence of 6.5 μM $\mathbf{R^{H}\text{-}Au^{III}}$ is elucidated with blue and green, respectively. The spectral changes during the titrations due to several additions of $\mathbf{R^{H}\text{-}Au^{III}}$ to HSA are represented in grey. No changes in the spectrum of HSA is observed except for the appearance of the $\mathbf{R^{H}\text{-}Au^{III}}$ chromophore along with the characteristic peak maxima at 363 and 398 nm. The addition of beyond 6.5 μM $\mathbf{R^{H}\text{-}Au^{III}}$ resulted in precipitation. Likewise, with HEWL (Figure 4.17b), concentrations higher than 17 μM $\mathbf{R^{H}\text{-}Au^{III}}$ was sufficient to cause precipitation with no change in the spectra of HEWL. The precipitation is likely of the protein alone since the intensity of the UV-vis absorbance maxima of $\mathbf{R^{H}\text{-}Au^{III}}$ increased in tandem with added aliquots of $\mathbf{R^{H}\text{-}Au^{III}}$ to the cuvette. Solutions of $\mathbf{R^{H}\text{-}Au^{III}}$ and HEWL were incubated overnight at 37 °C and subjected to mass spectrometry. No adducts were observed and the molecular ion peaks associated with HEWL and $\mathbf{R^{H}\text{-}Au^{III}}$ remained unaltered.

The results obtained from the UV-vis titration studies and the ESI-MS experiments conducted with $\mathbf{R^{H}\text{-}Au^{III}}$ and HEWL, indicate that $\mathbf{R^{H}\text{-}Au^{III}}$ does not bind to proteins. This lack of reactivity can be attributed to the steric bulk offered by the Dipp groups in crowding the Au^{III} (Figure 4.14) from forming covalent bonds with surface amino acid residues of the proteins. Considering the fact that HEWL has an exposed histidine residue (N-donor) as a binding site

for gold ions, the inability of **R^H-Au^{III}** to form covalent interactions with N-donors (e.g. nucleotides) from large biomolecules can loosely imply that binding between **R^H-Au^{III}** and ctDNA is not covalent either.

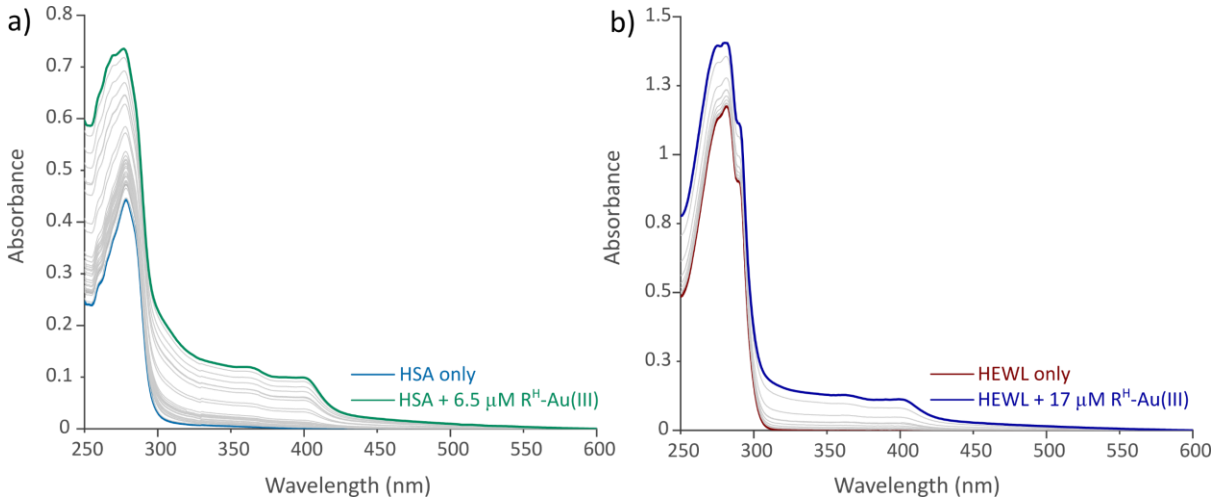


Figure 4.17. (a) The UV-vis absorption spectra of HSA in 1× PBS and 10% DMSO before (12.5 µM, blue spectrum) and after sequential additions of **R^H-Au^{III}** (final [**R^H-Au^{III}**] = 6.5 µM, green spectrum). (b) The UV-vis absorption spectra of HEWL in 1× PBS and 10% DMSO before (30.7 µM, red spectrum) and after sequential additions of **R^H-Au^{III}** (final [**R^H-Au^{III}**] = 17.0 µM, blue spectrum). The titration experiments were repeated in triplicate at 37(±0.2)°C.

4.3.4 Stability Studies with GSH

The stability of **R^H-Au^{III}** in the presence of the intracellular reductant, reduced glutathione (GSH) was evaluated. A solution of GSH (100 mM, D_2O) was added to an NMR sample of **R^H-Au^{III}** (10 mg, $(CD_3)_2SO$, ~ 14 mM) to obtain a final excess [GSH] of ~ 20 mM. ^1H NMR spectra were recorded at certain time intervals for 24 hours at room temperature. The ^1H NMR spectra of the gold(III) complex in the presence of excess GSH at T = 0 h and T = 24 h are presented in Figure 4.18a**.** After 24 hours, each disappearing peak in the aromatic region (6.5 – 9.0) is accompanied by a new additional peak which is either slightly shifted upfield from the original peak or overlapped. The same is observed in the aliphatic region upfield of 1.5 ppm with an additional pair of doublets at 0.6 and 0.4 ppm.

Specifically, 15 minutes after the addition of excess GSH in D_2O to the NMR sample, small shoulder peaks are observed for the carbazole protons H1a, H1b and H1c along with the development of a new doublet between the Dipp protons, H2a and H2b at ~7.8 ppm. These peaks all grow progressively in intensity with the accompanied dampening of the original

proton signals. These slight peak shifts suggest the formation of a new gold(III) complex. Reduction to gold(I) did not occur as no colour change to red or precipitation of the insoluble gold(I) complex, **R^{H}-Au^{I}**, was observed, nor were the significant differences in the resonances of the carbazole backbone protons expected for complexes containing a Au^{I} and Au^{III} central metal, observed. The absence of the acidic triazolium protons in the ^{1}H NMR rule out demetalation of the complex.

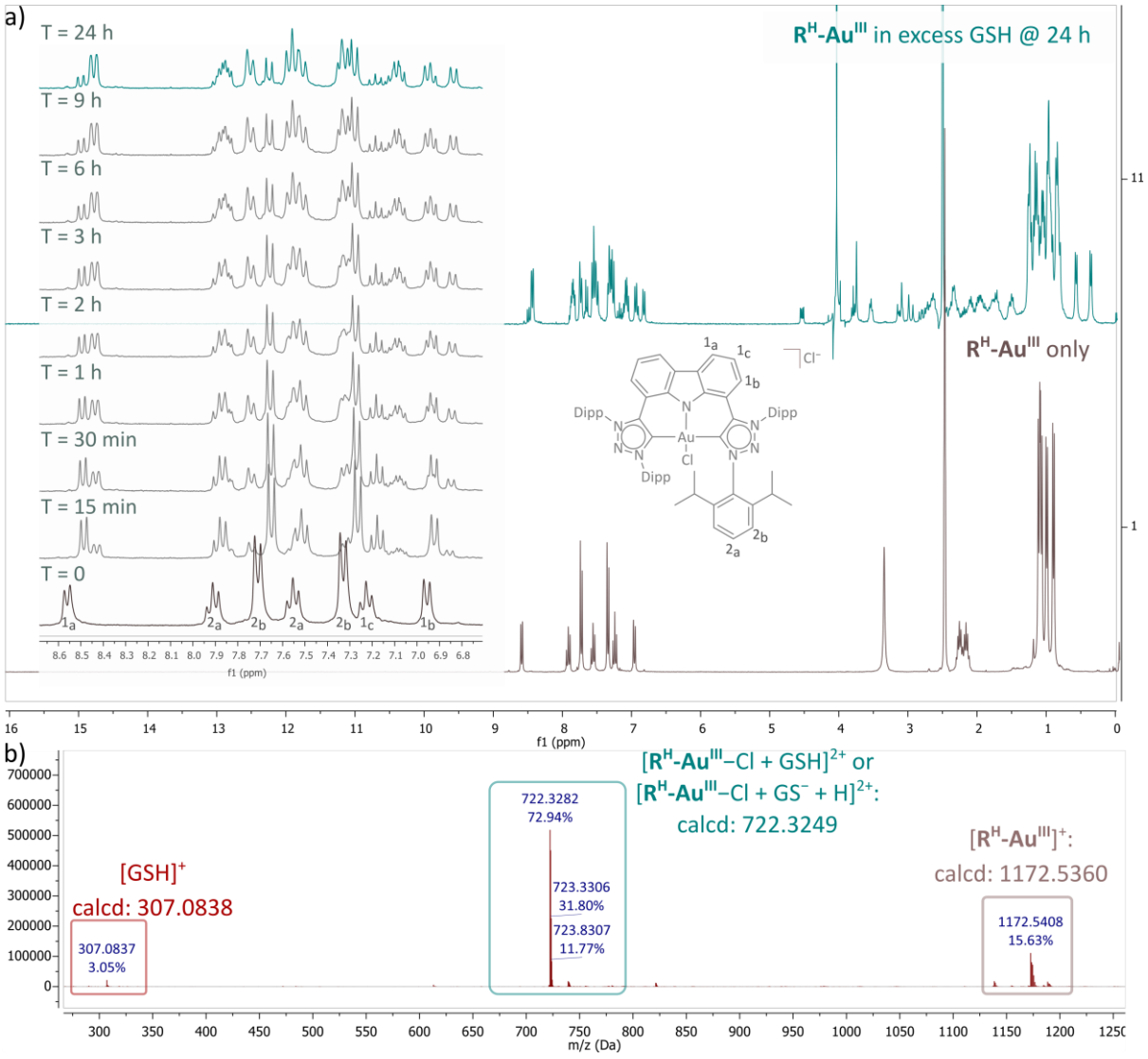


Figure 4.18. (a) The ^{1}H NMR spectra of **R^{H}-Au^{III}** in the presence of excess GSH at T = 24 h (top, blue) and **R^{H}-Au^{III}** before addition of GSH for comparison (bottom spectrum, brown) in $(CD_3)_2SO$ at room temperature. The inset magnifies the changes in the aromatic region upon the addition of GSH at certain time intervals. (b) The ESI-MS spectrum of **R^{H}-Au^{III}** in the presence of excess GSH after 48 h.

The ^{1}H NMR sample was analysed by ESI-MS and confirms the formation of a new gold(III)-GSH adduct (Figure 4.18b). The ion cluster peak at the *m/*2 value of 722.3282 corresponds to

the doubly charged molecular ion peak of the gold(III)-GSH adduct of either $[M - Cl + GSH]^{2+}$ or $[M - Cl + GS^- + H^+]^{2+}$, for isotopic mass of M = **R^H-Au^{III}**. The chlorido ligand of the gold(III) complex is displaced either by a deprotonated form of GSH (GS^-) accompanied by M+H adduct formation (i.e., protonation elsewhere on the complex), or a protonated form of GSH. The ion cluster peaks at *m/z* values of 307.0838 and 1172.5408 are attributed to the unreacted GSH and **R^H-Au^{III}**, respectively.

The reactivity of **R^H-Au^{III}** and GSH was also confirmed by UV-vis spectroscopy. The UV-vis spectrum (Figure 4.19**)** shows the reaction of **R^H-Au^{III}**:GSH at a 1:7 molar ratio in DMSO (5% H_2O). The brown line represents 15 µM of **R^H-Au^{III}** at T = 0 and the blue-green line represents the newly formed **R^H-Au^{III}-GSH** adduct at T = 600 min, after reacting with 100 µM of GSH. The change in the UV-vis spectrum of **R^H-Au^{III}** to **R^H-Au^{III}-GSH** is associated with the appearance of five isosbestic points at 305, 311, 370, 384 and 404 nm. The absorbance maxima of **R^H-Au^{III}** at 363 nm decrease in intensity and undergoes a 9 nm red-shift to a new peak at 372 nm. Similarly, the peak of 399 nm decreases accordingly and a new peak at 415 nm is formed.

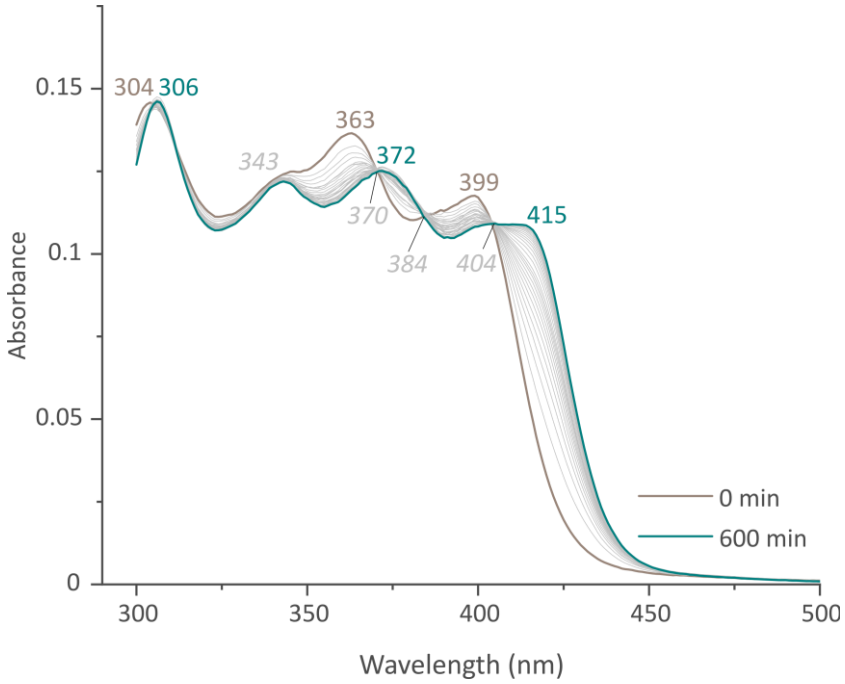


Figure 4.19. The UV-vis absorption spectra of **R^H-Au^{III}** in DMSO and GSH over 10 h at a molar ratio of 1:7 representing [**R^H-Au^{III}**]:[GSH].

Interestingly, at lower concentrations of GSH (~ 8 mM) no changes in the ^{1}H NMR of **R^H-Au^{III}** (~ 14 mM) spectrum is observed, where the molar ratio of **R^H-Au^{III}** to GSH is 2:1. Only once

the molar ratio is shifted to at least 1:2, does formation of the gold(III)-adduct become apparent (as observed in the top ^{1}H NMR spectrum of Figure 4.18a).

The reactivity of **R^{H}-Au^{III}** towards GSH is dependent on GSH being present in excess. GSH levels are often elevated in cancer cells to defend against oxidative damage.[367] The possibility that the cytotoxicity of **R^{H}-Au^{III}** is dependent on an intracellular mode of action, so that the complex undergoes ligand substitution and sequesters GSH inside the cancer cells and induces ROS-mediated cell death cannot be excluded. Indeed, the mechanism of action of previously reported gold(III) complexes that form GSH adducts are related to intracellular oxidative stress,[147,149] and might indicate that the mode-of-action of **R^{H}-Au^{III}**, if intracellular, might be similarly related. However, GSH is also found in the blood (1–10 μM) and can potentially deactivate the cytotoxicity of **R^{H}-Au^{III}** similar to that of auranofin.[83,116]

4.4 Conclusion

The interaction of **R^{H}-Au^{III}** with biological macromolecules was investigated in attempt to explain the cytotoxicity of **R^{H}-Au^{III}** against cancer cells. The DNA binding studies involved various UV-vis spectrometric methods, EMSA, viscosity and molecular docking approaches. Binding to proteins i.e., HEWL, HSA and the tripeptide GSH, was investigated by UV-Vis titration studies, ESI-MS and ^{1}H NMR spectroscopy.

As a preliminary experiment, the ability of **R^{H}-Au^{III}** to bind or interact with DNA was investigated with EMSA. **R^{H}-Au^{III}** induced a slight streak in the SC form of plasmid DNA during EMSA studies that indicated that the mobility of a small amount of DNA was affected by **R^{H}-Au^{III}**. During UV-vis titration studies, **R^{H}-Au^{III}** was found to interact weakly with ctDNA as the calculated binding constant was in the lower range of other known intercalators. Moreover, the spectroscopic changes associated with binding was not observed during the titration experiment due the precipitation of either **R^{H}-Au^{III}** and/or **R^{H}-Au^{III}-DNA** complex. Thermal melting analysis revealed that the interaction of **R^{H}-Au^{III}** does stabilize the duplex resulting in an increase in the melting temperature of ctDNA. Moreover, **R^{H}-Au^{III}** exhibits a predominantly negative induced LD signal in the presence of ctDNA. Results from the collective experimental methods indicate that **R^{H}-Au^{III}** interacts with DNA via either an intercalative or partial intercalative binding mode. However, the effect of **R^{H}-Au^{III}** on the viscosity of the ctDNA is unique and implies that the interaction is non-conventional. **R^{H}-Au^{III}** might increase the

polymeric nature of the DNA by stabilizing the formation of higher-order structures of DNA. Indeed, molecular docking suggested that, theoretically, **R^H-Au^{III}** would be capable of targeting three-way junctions but direct experimental evidence will be key to corroborate the docking results.

Surprisingly, **R^H-Au^{III}** was unreactive towards the proteins, HSA and HEWL, presumably due to the steric bulk of the diarylated wingtip groups crowding the Au^{III} ion. Gratifyingly, the ligand scaffold effectively redox-stabilized the Au^{III} ion from reduction and demetallation in the presence of excess GSH. Instead, a spectroscopically distinct gold(III)-GSH, **R^H-Au^{III}-GSH** adduct forms.

4.5 Experimental

4.5.1 Electronic Structure of R^H-Au^{III}

The molar absorptivities at the wavelength maxima of **R^H-Au^{III}** in DMSO and in 1x PBS (10% DMSO) were determined according to the Beer-Lambert Law. For the Beer-Lambert titration a 2.0×10^{-4} M **R^H-Au^{III}** sample was prepared in a quartz cuvette and subsequently diluted to known lower concentrations of 1.0×10^{-4} M, 5×10^{-5} M, 2.5×10^{-5} M, 1.0×10^{-5} M and 5×10^{-6} M. The absorbances at 303, 336, 363 and 398 nm were plotted as a function of the concentration of **R^H-Au^{III}** and the slopes (molar absorptivity) were calculated with linear regression analysis.

The TD-DFT calculations were done according to the computational details reported for the previously reported **R^{tBu}-Au^{III}-F** complex.[201] The **R^H-Au^{III}** structure was optimized from the crystal structure data at B3LYP-D3[330–333] level of theory using def2-SVP[334] basis set for all atoms in *Gaussian 09*[335]. At the same DFT level, TD-DFT calculations were conducted using the polarizable continuum model (PCM)[336–338] for DMSO and the first 60 excited states were considered (using the first 30 states were not sufficient due to the presence of only weak oscillator frequencies at longer wavelengths (>350 nm) and the assignment of transitions was ambiguous. Transitions at >350 nm with stronger oscillator frequencies were identified when the number of excited states were increased to 60).

4.5.2 Electrophoretic Mobility Shift Assays

Stock solutions of each test compound were prepared in DMSO. For **R^H** and **R^H-Au^{III}** the concentrations were 1000, 500, 100, 50, 10, 5 and 1 μM. From the stock solutions, 1 μL was added to 1 μL pUC57 in 1 μL 10× TAE (40 mM Tris-acetate and 1 mM EDTA, pH 8.3) and 7 μL Type 1 ultrapure water. These samples were incubated at 37°C for 30 minutes before each successive EMSA experiment. Meanwhile, 0.437 g of agarose gel was added to 37 mL 1× TAE and brought to the boil. The gel solution was cooled down 60 °C, poured into the electrophoretic mould and allowed to set for at least 30 minutes. After incubation, 2 μL of loading dye (bromophenol blue and xylene cyanol FF) was added and 6 μL of each sample was loaded into a well. The gels were placed in the Mini-Sub-Cell GT® Agarose Gel Electrophoresis System (Bio-Rad) with 1× TAE and ran for 120 minutes at 65 mV. After the run was completed, the gels were stained with ethidium bromide (5 mg/L) for at least 30 minutes and de-stained with Type 1 ultrapure water for at least 10 minutes. The gels were visualized using a G:Box Chemi XRQ gel doc system (Syngene) with midwave UV transillumination and a UV filter (GeneSys 1.4.6.0). Experiments were repeated at least three times.

4.5.3 UV-vis spectroscopy

The DNA titration experiments were performed at 28 °C (± 2 °C) in 1× PBS (0.01 M, phosphate buffered solution) and 10% DMSO. Samples were prepared with a fixed concentration of **R^H-Au^{III}** ($3.08 \times 10^{-5} – 3.16 \times 10^{-5}$ M) to which incremental amounts (5 – 50 μL) of ctDNA (0.0014 M bp, ε_{260} = 13 200 bp M^{-1} cm^{-1}) were added until a 3:1 ratio of [ctDNA]:[**R^H-Au^{III}**] was obtained. The samples were incubated for 10 minutes prior to the measurement of the absorption spectrum. Experiments were repeated in triplicate.

The change in the absorbance at 363 nm as a function of [ctDNA] were plotted and fitted to the Hill model,[341] a non-linear regression algorithm, using the software *OriginPro2019*. The Hill formula is shown as equation 3 (below), where *K* is the dissociation constant (Michealis constant) and *n* the number of cooperative sites.

$$y = \frac{y_{max} \cdot x^n}{K^n + x^n} \quad (3)$$

The fitting parameters and correlation matrix of the representative experiment (Hill plot inset in Figure 4.7) is shown in Table 4.2.

Table 4.2. The fitting parameters and correlation matrix of the fitted Hill plot of change in absorbance at 363 nm as a function of [ctDNA base pairs] from a representative UV-vis titration (shown in Figure 4.7) experiment with ctDNA and RH-AuIII generated from OriginPro2019.

Hill Equation (*OriginPro2019*): $y = \frac{(START + (END - START) .x^n}{k^n + x^n}$

Fitting Parameters

	Value	**Standard error**	**95% LCL[a]**	**95% UCL[b]**
START	0.22221	0.00182	0.21833	0.22609
END	0.16576	0.00351	0.15827	0.17325
K	2.77726E-5	1.7267E-6	2.40922E-5	3.14529E-5
n	2.58798	0.39793	1.73981	3.43615

Correlation Matrix

	START	***END***	***K***	***n***
START	1	-0.36818	-0.14137	-0.64704
END	-0.36818	1	-0.77713	0.75685
K	-0.14137	-0.77713	1	-0.43072
n	-0.64704	0.75685	-0.43072	1

[a] upper confidence limit. [b] lower confidence limit

LD spectra were recorded concurrently (two detection channels) at 37 °C using a thermostatted cylindrical quartz Couette cell accessory in the range of 200–650 nm at a rotation rate of 900 rpm. The concentration of ctDNA in 1× PBS solution (10% DMSO) was kept constant at 10 μM bp, while varying the molar concentration ratio (*r*) of **R^H-Au^{III}** relative to ctDNA to give solutions with *r* = 0.25, 0.5, 1.0, 2.0 and 4.0.

Melting curves were recorded in 1× PBS (10% DMSO) at a ctDNA concentration of 75 μM bp. The melting profile of ctDNA in the presence of EB and **R^H-Au^{III}** (both at 35 μM) were investigated by monitoring the change in absorbance at 260 nm, as samples were continuously heated at a rate of 2 °C/min in 2 °C intervals over a temperature range of 40–105 °C.

4.5.4 Viscosity

The change in viscosity of a buffered solution of ctDNA was evaluated as a function of the concentration of **R^H-Au^{III}**, EB, and HS added to a fixed concentration of sheared ctDNA at 37 °C in 1× PBS (10% DMSO). Compounds were incubated with the DNA target for 30 – 60 min at 37 °C prior to performing viscosity measurements. The ctDNA concentrations were typically 1.0, 5.0, 50 μM for these experiments, which were performed in a PCTFE capillary with a diameter of 1.62 mm containing 100 μL aliquots of solution in a rolling ball Lovis 2000 M microviscometer (Anton Paar). All measurements were performed with a 1.5 mm diameter gold-coated steel ball (4 μm thick layer) in triplicate (the minimum number of repetitions). After recording the dynamic viscosity (mPa s) of ctDNA alone in the DMSO-buffer solution (η_0), the dynamic viscosity for each analyte-ctDNA mixture (η) was measured. Analyte compound concentrations ranged from 0.50 μM to 1000 μM, depending on solubility and whether DNA precipitation was evident or not. HS, for example, is limited to a maximum concentration of ~ 30 μM in the buffer system used with DNA precipitation occurring at higher concentrations. Data from triplicate measurements were averaged and used to calculate a dimensionless relative viscosity for the solution, $\{(\eta - \eta_0)/\eta_0\}^{(1/3)}$, which was plotted as the relative change in viscosity, $\Delta\{(\eta - \eta_0)/\eta_0\}^{(1/3)}$, against *r*, where *r* is the analyte to ctDNA base pair mole ratio (i.e. [analyte]/[ctDNA base pairs]).

4.5.5 Molecular Docking

Docking studies were carried out with *Schrödinger 2020-3* using *Glide 5.0 SP*.[360–362] Grid files for DNA targets were first created from the X-ray structures of interest downloaded from the RCSB PDB. Macromolecules were prepared for simulations by calculating protonation and metal charge states for pH 7.0 ± 2.0 with *Epik*,[368,369] assigning bond orders automatically, and refining all added H atom positions. Crystal mates were used to create complete macromolecular assemblies for simulations. Grid files for docking were produced using standard settings and box sizes for ligand location ranging from 12 Å^3 (ordinary DNA intercalation sites) to 40 Å^3 (DNA four-way junctions). Docking experiments were conducted on **R^H-Au^{III}**, EB and HS with the DFT-calculated geometries and refined with the OPLS3e force field.[363]

Table 4.3. Summary of *Glide* docking results showing the best pose docking scores (in kcal mol^{-1})

DNA target	PDB code	Sequence	R^H-Au^{III}	EB	HS
3-way junction	3I1D	CGTACG	-10,839	-7,676	-7,052
		CGTACG	-11,888[a]	-7,723	0,000
	2ET0	CGTACG	-8,363	-8,598	-6,842
	3FX8	CGTACG	0,000	-8,545	0,000
dsDNA oligo intercalation	2O1I	CGGAAATTCCCG	0,000	-10,524	-7,431
site at center	3GSJ	CGGAAATTACCG	0,000	0,000	-7,621
		CGGAAATTACCG[b]	0,000	-7,958	0,000
		CGGAAATTACCG [c,d]	-7,933	0,000	0,000
	4E1U	CGGAAATTACCG[e,f]	-7,746	0,000	0,000
		CGGAAATTACCG[g]	0,000	-8,771	0,000
		CGGAAATTACCG[h]	0,000	0,000	0,000

[a] result form best docking run; parameters unique. All other entries use identical parameters. [b] tight grid, site 1. [c] loose grid1. [d] best pose is part intercalation, part minor groove binding. [e] loose grid2. [f] all sites open for binding. [g] tight grid, site 3. [h] tight grid, site 5.

The docking runs employed flexible ligand torsion angles, the OPLS2005 force field for ligand pose refinement, no torsion angle bias, a dielectric constant of 2.0 Debye, and no additional restrictions (such as heightened planarization of π-conjugated ring systems) or enhancements (such as including aromatic CH and halogen H-bond donors and acceptors, respectively). The same strategy was used throughout for each macromolecular target. Initial tests with several combinations of parameters showed that the default settings in *Schrödinger* for *Glide* were reliable, though we elected to remove any torsion angle biases for the screening procedure. (Docking scores for poses, and thus ligand binding orders, were very sensitive to the selection of parameters used for the screens, requiring a careful choice and fixed set of parameters for all runs to enable screening uniformity and comparison of data obtained from different runs and DNA targets.)

4.5.6 Protein Binding

Protein binding experiments with **R^H-Au^{III}** were performed at 37 °C (± 0.2 °C) in 1× PBS (0.01 M) and 10% DMSO. Samples were prepared with a fixed HEWL concentration of 3.07 – 3.30 × 10^{-5} M (ε_{260} = 37970 M^{-1} cm^{-1}) or a fixed HSA concentration of 1.2 – 1.3 × 10^{-5} M (ε_{260} = 35700 M^{-1} cm^{-1}) to which incremental amounts of **R^H-Au^{III}** stock solutions were added (1000 – 10 µM, 5 – 20 µL). The samples were incubated for 2 minutes prior to the measurement of the absorption spectrum and experiments were repeated in triplicate.

For ESI-MS studies of **R^H-Au^{III}** with HEWL, multiple samples were prepared at various molar ratios of **R^H-Au^{III}** and HEWL in 1× PBS (10% DMSO). Samples were either incubated at 37 °C or room temperature overnight. Some samples were left to incubate for longer. No ESI-MS adducts between **R^H-Au^{III}** and HEWL were found. Above is a representative ESI-MS spectrum of a 10:1 molar ratio of HEWL to **R^H-Au^{III}** after four weeks of incubation at room temperature.

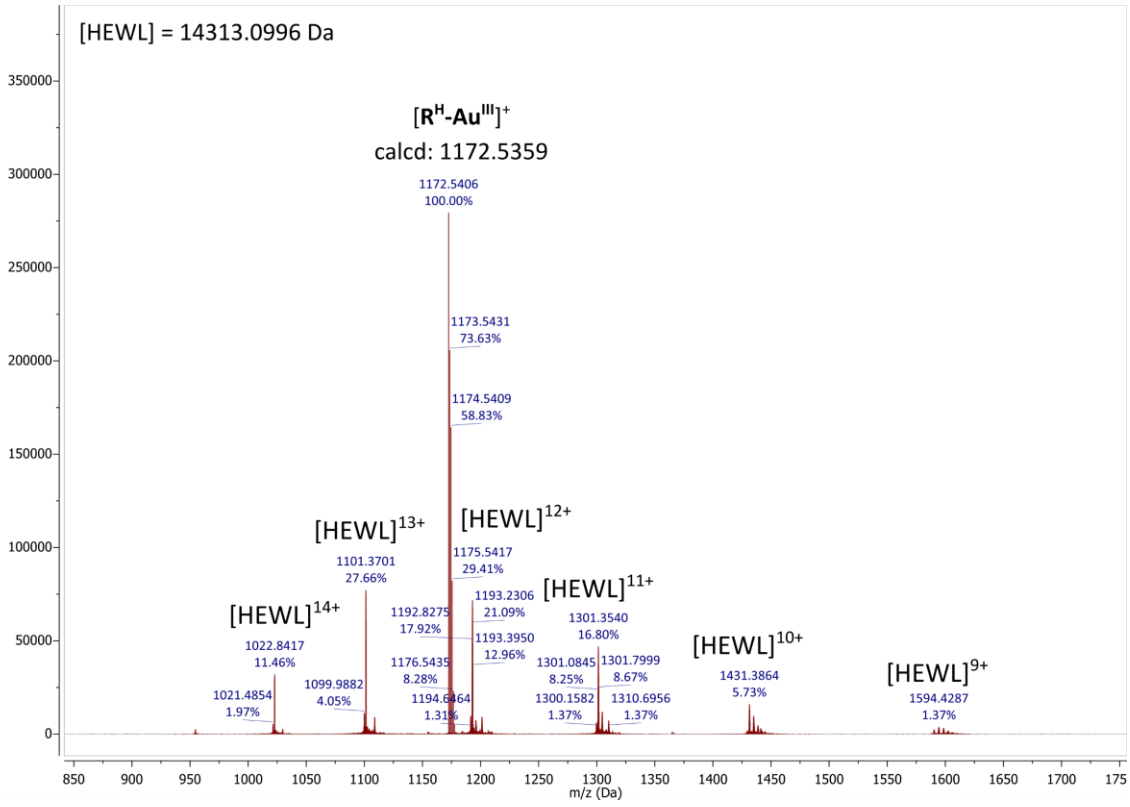


Figure 4.20. A representative ESI-MS of **R^H-Au^{III}** with HEWL at a molar ratio of 10:1 (HEWL: **R^H-Au^{III}**) after 28 days in solution (1× PBS, 10% DMSO).

4.5.7 Interaction with GSH

The stability of **R^H-Au^{III}** in the presence of GSH was evaluated with ^{1}H NMR. A solution of GSH (100 mM, D_2O) was added to an NMR sample of **R^H-Au^{III}** (10 mg, $(CD_3)_2SO$) to obtain a final GSH concentration of 8 mM or 20 mM in the sample. The ^{1}H NMR spectra were measured at certain time intervals for 48 hs. After 48 h 10 µL of the NMR sample were added to 990 µL acetonitrile (HPLC grade) for MS analysis.

The interaction of GSH with different molar ratios as a function of time were also conducted by UV-vis spectroscopy. Final concentrations (100, 50 and 25 µM) of **R^H-Au^{III}** in DMSO were prepared and 100 µL solution of GSH in ultrapure type 1 water was added so that the final concentrations of **R^H-Au^{III}** and GSH in the cuvette were 100 µM, 50 µM or 25 µM for **R^H-Au^{III}** and 50 µM for GSH in 5% H_2O in DMSO. The reactions were monitored for at 24 hours at 15 min intervals for the first 3 hours, 30-minute intervals until 10 hours followed by hourly intervals until 24 hours.

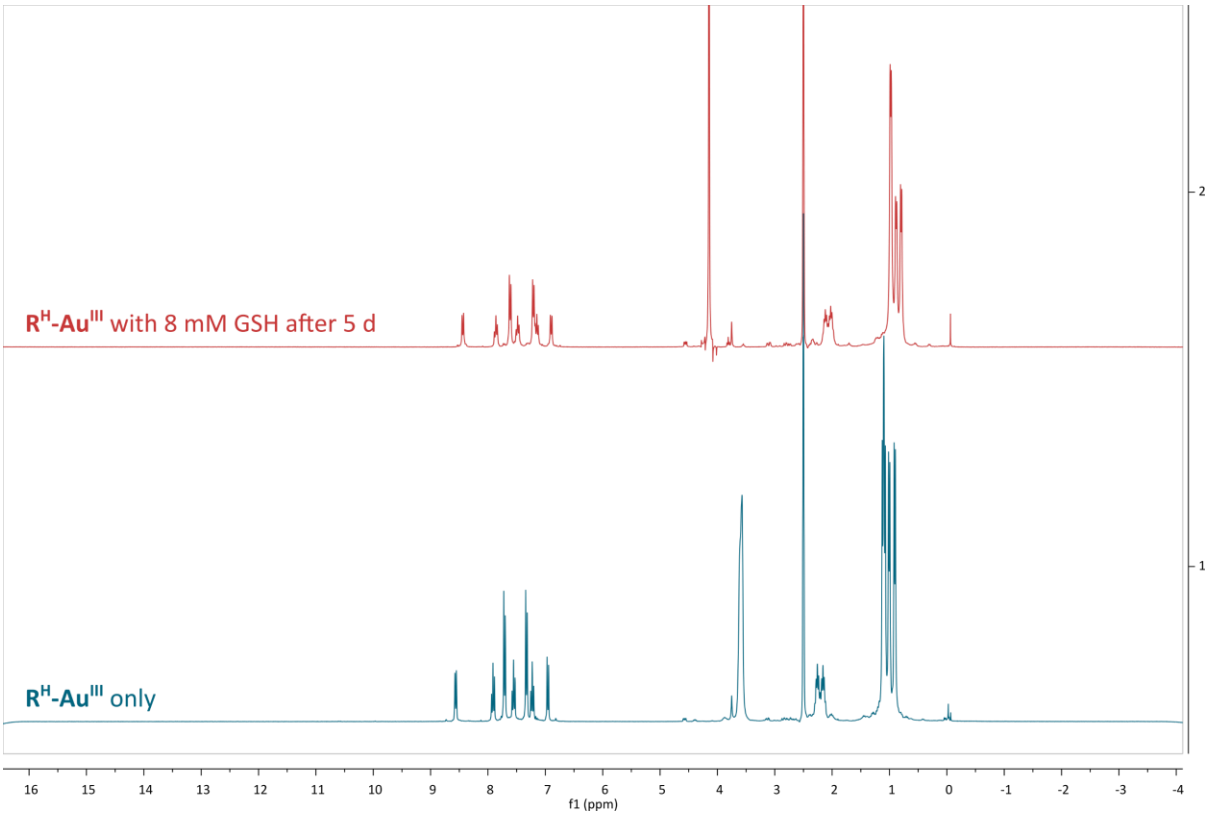


Figure 4.21. The ^{1}H NMR spectrum of **R^H-Au^{III}** in $(CD_3)_2SO$ before the addition of GSH (bottom, blue) and after 5 days in the presence of 8 mM GSH (top, red). The slight shift in the peaks is attributed to the addition of D_2O to aid the solvation of GSH in $(CD_3)_2SO$.

Chapter 5: Conclusion

5.1 Rationale of study hypothesis

The therapeutic qualities of metals have been known for ages.[69,70] The more recent expansion into the development of metallodrugs is inspired by the potent anticancer properties of cisplatin[39–42] and the antirheumatic drugs, auranofin and myocrisin.[56] Metal complexes offer attractive attributes to the field of drug design with their wide range of coordination numbers, geometries, and redox states. This diversity allows for the potential to target one or more different biological targets, permitting the design of a metallodrug for a multi-faceted approach.[20,22,37,38,62–66]

Gold(I) compounds interact preferentially with sulfur and phosphine ligands and therefore can bind to, and subsequently inactivate proteins with cysteine (-thiol) and selenocysteine (-selenium) residues, leading to cell death induced by mitochondrial dysfunction.[118–124] Gold(III) complexes favour nitrogen and oxygen donors and since gold(III) salts were historically used to stain nucleic acids for electron microscopy imaging,[67] the mode of action of gold(III) anticancer drugs were thought to be similar to that of cisplatin. Gold(III) complexes have recently re-emerged as a class of compounds with potent cytotoxicity against cancer cells. More evidence reveals that the mechanism of action of most gold(III) complexes are independent of DNA. If the Au^{III} ion is stabilized by an appropriate multidentate ligand scaffold, in particular, porphyrin[147,202] and CNC[83,113,150–152,154] pincer ligands, the resultant gold(III) complexes are remarkably stable against intracellular reductants. The complexes also elicit strong cytotoxicity against cancer cells and can bind to DNA via intercalative modes of binding - DNA being one of many targets for these gold(III) complexes.

Selectivity of these complexes towards cancer cells remain a challenge and is improved by the use of non-toxic ligands such as NHCs. Moreover, NHCs are strong σ-donors and have shown to effectively stabilize both Au^{I} and Au^{III} under physiological conditions.[125–129] For drug design, the use of 1,2,3-triazol-5-ylidenes are an attractive class of ligands for their ease of modulation, high functional group tolerance and ability to stabilize metals in both high and low oxidation states.[173,191–194,203] Surprisingly, few reports on the anticancer potential of 1,2,3-triazolylidenes exist.[195–197,370]

The monoanionic CNC pincer ligand, based on a carbazole backbone with two flanking 1,2,3-triazol-5-ylidenes (**R^{tBu}**) was previously synthesised in our labs and has been shown to successfully stabilize reactive first row late transition metals.[118] The gold analogues could be oxidized to a range of robust gold(III) complexes.[198,201] The enhanced redox stability and the planar aromatic carbazole present ideal features to be explored further for DNA binding ability and cytotoxicity towards cancer cells.

5.2 Summary of study

The aim of this study was to explore the anticancer potential of gold(III) pincer complexes of which the synthetic design was inspired by the bistrz carbazole ligand scaffold, **R^{tBu}**. The modified design involved replacing the 2,6-diisopropylphenyl wingtip groups with ethyl and phenyl substituents and removing the *tert*-butyl groups from the carbazole, in order to reduce steric hindrance to facilitate DNA binding via intercalation.

All attempts to synthesize the CNC pincer complexes of the modified precursor salts, **L^{H}** and **L^{tBu}** were unsuccessful. Instead, the coordination of the two new bis(1,2,3-triazolium)carbazole salts **L^{H}** and **L^{tBu}** to coinage metals(I) (Au^{I} and Ag^{I}), yielded novel complexes with different coordination modes when using a transmetalation (Ag^{I} to Au^{I}) approach. These included the heterometallic tetranuclear **L^{tBu}-*N*-AgCl-Au^{I}** which over time decomposes to the homometallic dinuclear biscarbene 'cage' complex **L^{tBu}-Au^{I}** where the ligand serves as a bridge between two Au^{I} centers coordinated by the trz ligands. Investigation of the synthetic route using the silver(I) precursor only, did not yield the desired pincer complexes; instead homometallic tetranuclear Ag^{I} complexes (**L^{H}-Ag^{I}** or **L^{tBu}-Ag^{I}**) with two bridging ligands were isolated displaying either intra- (**L^{H}-Ag^{I}**) or intermolecular (**L^{tBu}-Ag^{I}**) argentophilic interactions.

The concerted free carbene route as access to mononuclear tridentate pincer complexes of gold(I) (**R^{H}-Au^{I}** and the known **R^{tBu}-Au^{I}**), and subsequent oxidation to gold(III) (**R^{H}-Au^{III}** and **R^{tBu}-Au^{III}**) were only possible if diarylated triazolium precursors **R^{H}** and **R^{tBu}** were employed. Of the diarylated compounds, the precursor salt, **R^{H}** and corresponding gold(III) complex, **R^{H}-Au^{III}** exhibited the strongest cytotoxicity against the breast cancer cell line, MDA-MB-231. **R^{H}** proved to be potent with an IC_{50} in the nanomolar ranges but were toxic to the non-

tumourgenic EA.hy926 cells. Although both cell lines were less sensitive to **R^H-Au^{III}** than the precursor salt, **R^H-Au^{III}** presented higher selectivity towards the cancer cells.

During binding studies with DNA, **R^H-Au^{III}** was found to interact modestly with ctDNA and from the various UV-vis spectroscopic methods that were employed indicated that **R^H-Au^{III}** is a partial-intercalator. However, the unusually marked dose-responsive increase in the viscosity of ctDNA induced by **R^H-Au^{III}** points to an unconventional interaction when compared with known partial- or complete DNA intercalators. Indeed, the sterically demanding Dipp groups crowd the aromatic planar carbazole ring system in the complex and hinder classical modes of DNA intercalation. To explain the experimental findings, biomolecular simulations revealed that **R^H-Au^{III}** may selectively target DNA three-way junctions over double-stranded DNA in silico.

Furthermore, **R^H-Au^{III}** does not reduce to Au^I or demetalate in the presence of excess glutathione (GSH) and is evidently redox stabilized by the bulky ligand scaffold. Instead, a stable gold(III)-GSH adduct forms upon substitution of the chloride ligand by GSH. From the reactivity of **R^H-Au^{III}** with proteins and GSH, the cytotoxicity of **R^H-Au^{III}** is most likely due to the intact metal complex.

5.3 Evaluation of study impact

Drug design is dependent on the synthetic feasibility of the intended drug, as eloquently illustrated in this study. Not only did the use of 1,2,3-triazolylidenes as C-donor ligands sufficiently stabilize the gold(III) under physiological conditions (as hypothesized) but also enabled the facile modification of the wingtip groups upon the finding that alkylated analogues were not feasible with the synthetic methodologies employed. As a result, the potential of this class of gold(III) pincer complexes as suitable anticancer agents were demonstrated.

Although the objective of the project was to investigate the cytotoxicity and potential for DNA intercalation on a set of complexes that had reduced bulk, the sterically encumbered gold(III) complex, **R^H-Au^{III}** was found to be cytotoxic to cancer cells and interact with DNA. In fact, docking results showcased the potential of **R^H-Au^{III}** to target higher order DNA structures that are important intermediates during DNA replication. If the binding of **R^H-Au^{III}** to three-way junctions are proven experimentally with oligonucleotides that can from three-way junctions

and verified, the results intimate towards the reason for cytotoxic selectivity, as cancer cells should form more of these three-way junctions due to the accelerated rate of replication.

The study accounts how a less-than-ideal, but accessible candidate, **R^H-Au^{III}** was subjected to biological studies due to its synthetic feasibility, and how **R^H-Au^{III}** turned out to be a promising anticancer agent in its own right. In contrast to most gold(III) complexes reported, the anticancer properties and interaction with biological macromolecules are likely due to the intact metal complex, with the ancillary chlorido ligand available for exchange. Most importantly, it was unforeseen that the "unwanted" steric bulk ultimately drives the selective interaction with these biological macromolecules to the extent that discrimination between different DNA structures can be attributed to the selectivity of **R^H-Au^{III}** towards cancer cells.

5.4 Future perspectives

From a synthetic point of view, modifications in the wingtips of the 1,2,3-triazol-5-ylidenes of the original ligand scaffold, **R^H** can be explored further in attempt to improve the solubility of these compounds in aqueous growth media that are used for in vitro studies and aqueous buffers employed in DNA and protein binding experiments. Moreover, the role of the metal in the cytotoxicity is to be evaluated by synthesizing silver, copper or platinum analogues. Concurrently, the ability of the ligand to stabilize high oxidation states of these metals (i.e., Cu^{II}, Ag^{III}, Pt^{IV}) can be investigated. An extensive study into the potential formation of pincer complexes of the alkylated analogues, **L^H** and **L^{tBu}**, can be conducted by considering alternative synthetic routes, other metal precursors and theoretical calculations.

The cytotoxicity of the **R^H-Au^{III}** can be further evaluated with more cancer cell lines. The use of flow cytometry to investigate if **R^H-Au^{III}** induces cell cycle arrest during the DNA replication phase of cancer cells (strengthening DNA three-way junctions as suitable drug target for **R^H-Au^{III}**) is a logical next step. Since **R^H-Au^{III}** forms a gold(III)-GSH adduct, further in vitro studies can be conducted to evaluate the ability of **R^H-Au^{III}** to enter cells and generate ROS-mediated cell death, as an alternative mode of action (other than DNA binding).

The reactivity of **R^H-Au^{III}** towards GSH is unique since **R^H-Au^{III}** undergoes ligand substitution only when GSH is in excess. Future kinetic studies into the formation of the **R^H-Au^{III}-GSH** adduct should prove insightful in elucidating the reaction mechanism.

In terms of bioinorganic experiments, the interaction of **R^H-Au^{III}** with other higher order DNA targets should be experimentally explored to verify the results obtained from molecular docking studies. Moreover, the isolation of the **R^H-Au^{III}-GSH** adduct and subsequent interaction and cytotoxicity studies can provide additional information regarding the 'active' biological complex.

General Methodology and Instrumentation

Materials

All synthetic procedures sensitive to air and moisture were conducted under inert atmosphere (either under nitrogen or argon gas) using standard Schlenk or vacuum line techniques. Air sensitive solids were stored and handled in a PureLab HE glove box. All synthetic procedures resulting in novel compounds were performed at least twice to confirm reproducibility. Anhydrous THF, diethyl ether, toluene and *n*-hexane were distilled over sodium metal under N_2 (g). DCM and acetonitrile were dried by distillation over CaH_2, under N_2 (g). Triethylamine were purified by distillation over potassium hydroxide. Deuterated dimethyl sulfoxide was stored in a Schlenk tube over activated 4 Å molecular sieves.

Nuclear magnetic resonance (NMR)

NMR spectra were acquired on either a Bruker Avance-III-300, operating at 300.13 MHz for ^{1}H, 75.47 MHz for ^{13}C, 121.49 MHz for ^{31}P and 282.40 MHz for ^{19}F, or a Bruker Avance-III-400, operating at 400.21 MHz for ^{1}H, 100.64 MHz for ^{13}C, 162.01 MHz for ^{31}P and 376.57 MHz for ^{19}F, or a Avance-III-500, operating at 500.13 MHz for ^{1}H, 125.31 MHz for ^{13}C, 202.46 MHz for ^{31}P and 470.59 MHz for ^{19}F, spectrometer. Standard Bruker pulse programs at 298 K were used in the experiments. Chemical shifts are reported in δ (in ppm) relative to the deuterated solvent signal. For $CDCl_3$, C_6D_6, CD_3CN and $(CD_3)_2SO$ the δ H was referenced at 7.26, 7.16, 1.94 and 2.50 ppm, respectively and the δ ^{13}C $\{^{1}H\}$ was referenced at 77.16 128.1, 118.26 and 39.52 ppm, respectively. The spectra were analysed with *MestReNova Software (9.0.1)*. The spectral coupling patterns are abbreviated as follows: s - singlet; d - double; t - triplet; q - quartet; sept – septet; m – multiplet; br s – broad signal. Proton coupling constants (*J*) are given in hertz (Hz). An asterisk (*) denotes solvent impurities in the NMR spectra[371] and quaternary carbons are represented by the symbol C_q in ^{13}C $\{^{1}H\}$ NMR spectra. The multiplicities of the ^{13}C signal in ^{13}C $\{^{1}H\}$ NMR spectra were deduced from DEPT-135 $\{^{1}H\}$ experiments. Assignment of non-quaternary carbons were confirmed with 2D heteronuclear (^{13}C-^{1}H) single quantum coherence (HSQC) experiments.

Crystal structure determination

SC XRD analyses were performed on a Bruker Apex II-CCD detector/ Crystals were mounted under oil on nylon loops and the crystals were kept at 173(±2) K during data collection. Using

Olex2,[372] the structures were solved with the ShelXT[373] structure solution program using Intrinsic Phasing and refined with ShelXL[374] refinement package using Least Squares minimization. CCDC 2048088 (for **K^{tBu}**), 2048089 (for **L^{tBu}-*N*-AgCl-Au^{I}**), 2048090 (for **L^{tBu}-Ag^{I}**), 2048091 (for **K$^{H}_{dipp}$**), 2048092 (**L^{H}-Ag^{I}**), 2048093 (**R^{H}-Au^{I}**), 2048094 (**R^{tBu}-Au^{III}**), 2048095 (**L^{tBu}-Au^{I}**), 2048096 (**R^{H}-Au^{III}**) and 2048097 (**L^{H}**) contain the supplementary crystallographic data for this thesis. The data can be obtained free of charge via www.ccdc.cam.ac.uk/data_request/cif, by email: data_request@ccdc.cam.ac.uk or by contacting The Cambridge Crystallographic Data Centre, 12 Union Road, Cambridge CB2 1EZ, UK, Fax: +44 1223 336033.

Mass spectrometry, elemental analysis and melting points

Mass spectral analyses were performed on a Bruker Compact Q-TOF high resolution mass spectrometer by direct infusion at a flow rate of 5 µL/min for 1 min using Bruker Daltronics HyStar 3.2 SR4 software and 5 mM sodium formate for calibration. Positive electron spray was employed as the ionization technique over a m/z range of 150-3000. Measurements were either prepared in Merck Millipore® purified water or HPLC-grade acetonitrile. Chromatograms were analysed with *Bruker Compass DataAnalysis software (Version 4.3)* and possible molecular ion adducts were identified with the aid of the mass spectrometry calculator developed by Fiehn Lab which is based on the spectral data reported by Siegel et al.[375]

Elemental analyses were carried out using an Elementar varioELcube CHNS-O analyser.

Melting points were measured using a Stuart SMP10 melting point apparatus.

Ultraviolet (UV) spectrometry

Absorbance experiments were conducted using either a Specord 210® Plus (analytik jena) using WinASPECT Plus version 4.2.0.0 equipped with a double 8-cell changer unit and a Peltier thermostat system or a PerkinElmer UV/VIS Lambda 365 spectrometer fitted with a Peltier Temp. multicell unit and Peltier controller. Quartz cuvettes with 10 mm pathlength were used and measurements were done at either 28°C or 37°C. Melting curves and linear dichroism were measured on a Jasco J-1500 CD spectrometer.

References

1 L. A. Torre, R. L. Siegel, E. M. Ward and A. Jemal, *Cancer Epidemiol. Biomarkers Prev.*, 2016, **25**, 16–27.

2 F. Bray, A. Jemal, N. Grey, J. Ferlay and D. Forman, *Lancet Oncol.*, 2012, **13**, 790–801.

3 N. A. Campbell, J. B. Reece, L. A. Urry, M. L. Cain, S. A. Wasserman, P. V. Minorsky and R. B. Jackson, *Biology, 8th Edition*, Pearson Benjamin Cummings, 8th edn., 2008.

4 K. Collins, T. Jacks and N. P. Pavletich, *Proc. Natl. Acad. Sci.*, 1997, **94**, 2776–2778.

5 G. M. Cooper and R. E. Hausman, *The cell: A Molecular Approach*, ASM Press, Washington, 4th edn., 2007.

6 C. J. Sherr, *Science.*, 1996, **274**, 1672–1674.

7 D. Hanahan and R. A. Weinberg, *Cell*, 2000, **100**, 57–70.

8 D. Hanahan and R. A. Weinberg, *Cell*, 2011, **144**, 646–674.

9 E. Stefan and K. Bister, in *Viruses, Genes, and Cancer.*, eds. E. Hunter and K. Bister, Springer, Cambridge, 2017, vol. 407, pp. 117–151.

10 P. Bachireddy, P. K. Bendapudi and D. W. Felsher, *Clin. Cancer Res.*, 2005, **11**, 4278–4281.

11 C. Braicu, M. Buse, C. Busuioc, R. Drula, D. Gulei, L. Raduly, A. Rusu, A. Irimie, A. G. Atanasov, O. Slaby, C. Ionescu and I. Berindan-Neagoe, *Cancers (Basel).*, 2019, **11**, 1–25.

12 V. Labi and M. Erlacher, *Cell Death Dis.*, 2015, **6**, e1675–e1675.

13 K. Murphy, *Janeway's Immunobiology*, Garland Science, 8th edn., 2011.

14 Z. Jin and W. S. El-Deiry, *Cancer Biol. Ther.*, 2005, **4**, 147–171.

15 K. Kannan and S. K. Jain, *Pathophysiology*, 2000, **7**, 153–163.

16 S. Elmore, *Toxicol. Pathol.*, 2007, **35**, 495–516.

17 G. Kroemer, L. Galluzzi, P. Vandenabeele, J. Abrams, E. S. Alnemri, E. H. Baehrecke, M. V Blagosklonny, W. S. El-Deiry, P. Golstein, D. R. Green, M. Hengartner, R. A. Knight, S. Kumar, S. A. Lipton, W. Malorni, G. Nuñez, M. E. Peter, J. Tschopp, J. Yuan, M. Piacentini, B. Zhivotovsky and G. Melino, *Cell Death Differ.*, 2009, **16**, 3–11.

18 K. W. Kohn, *Cancer Res.*, 1996, **56**, 5533–46.

19 L. H. Hurley, *Nat. Rev. Cancer*, 2002, **2**, 188–200.

20 N. Farrell, in *Advances in Inorganic Chemistry*, 1989, vol. 75, pp. 8–45.

21 R. R. Sinden, in *DNA Structure and Function*, Elsevier, 1994, pp. 1–57.

22 B. J. Pages, D. L. Ang, E. P. Wright and J. R. Aldrich-Wright, *Dalton. Trans.*, 2015, **44**, 3505–3526.

23 Y. Huang and L. Li, *Transl. Cancer Res.*, 2013, **2**, 144–154.

24 A. Eastman, in *Cisplatin: Chemistry and Biochemistry of a Leading Anticancer Drug*, ed. B. Lippert, Wiley, 1999, pp. 111–134.

25 M. D'Incalci and C. M. Galmarini, *Mol. Cancer Ther.*, 2010, **9**, 2157–2163.

26 J. C. Dabrowiak, in *Metals in Medicine*, John Wiley & Sons Ltd, 2017, pp. 91–156.

27 S. J. Berners-Price, L. Ronconi and P. J. Sadler, *Prog. Nucl. Magn. Reson. Spectrosc.*, 2006, **49**, 65–98.

28 D. Wang and S. J. Lippard, *Nat. Rev. Drug Discov.*, 2005, **4**, 307–320.

29 T. W. Hambley, *J. Chem. Soc. Dalt. Trans.*, 2001, 2711–2718.

30 C. A. Rabik and M. E. Dolan, *Cancer Treat. Rev.*, 2007, **33**, 9–23.

31 Z. H. Siddik, *Oncogene*, 2003, **22**, 7265–7279.

32 T. Makovec, *Radiol. Oncol.*, 2019, **53**, 148–158.

33 E. R. Jamieson and S. J. Lippard, *Chem. Rev.*, 1999, **99**, 2467–2498.

34 V. N. Iyer and W. Szybalski, *Proc. Natl. Acad. Sci.*, 1963, **50**, 355–362.

35 M. Tomasz, R. Lipman, D. Chowdary, J. Pawlak, G. Verdine and K. Nakanishi, *Science.*, 1987, **235**, 1204–1208.

36 J. J. Champoux, *Annu. Rev. Biochem.*, 2001, **70**, 369–413.

37 Ö. Karaca, S. M. Meier-Menches, A. Casini and F. E. Kühn, *Chem. Commun.*, 2017, **53**, 8249–8260.

38 A. Łęczkowska and R. Vilar, *Annu. Reports Sect. 'A' (Inorganic Chem.*, 2013, **109**, 299.

39 B. Rosenberg, L. Van Camp and T. Krigas, *Nature*, 1965, **205**, 698–699.

40 B. Rosenberg, L. Van Camp, J. E. Trosko and V. H. Mansour, *Nature*, 1969, **222**, 385–386.

41 L. Kelland, *Nat. Rev. Cancer*, 2007, **7**, 573–584.

42 S. Dasari and P. Bernard Tchounwou, *Eur. J. Pharmacol.*, 2014, **740**, 364–378.

43 N. J. Wheate, S. Walker, G. E. Craig and R. Oun, *Dalton. Trans.*, 2010, **39**, 8113.

44 K. D. Mjos and C. Orvig, *Chem. Rev.*, 2014, **114**, 4540–4563.

45 M. Frezza, S. Hindo, D. Chen, A. Davenport, S. Schmitt, D. Tomco and Q. Ping Dou, *Curr. Pharm. Des.*, 2010, **16**, 1813–1825.

46 S. Komeda and A. Casini, *Curr. Top. Med. Chem.*, 2012, **12**, 219–235.

47 A. Vessières, S. Top, W. Beck, E. Hillard and G. Jaouen, *Dalton. Trans.*, 2006, 529–541.

48 N. Muhammad and Z. Guo, *Curr. Opin. Chem. Biol.*, 2014, **19**, 144–153.

49 D. Chen, V. Milacic, M. Frezza and Q. Dou, *Curr. Pharm. Des.*, 2009, **15**, 777–791.

50 P. C. Bruijnincx and P. J. Sadler, *Curr. Opin. Chem. Biol.*, 2008, **12**, 197–206.

51 R. F. Ozols, *Cancer Treat. Rev.*, 1991, **18**, 77–83.

52 R. F. Ozols, T. C. Hamilton, E. Reed, M. C. Poirier, H. Masuda, G. Lai and R. C. Young, in *Platinum and Other Metal Coordination Compounds in Cancer Chemotherapy*, Springer US, Boston, MA, 1988, pp. 197–206.

53 G. Sava, S. Pacor, G. Mestroni and E. Alessio, *Clin. Exp. Metastasis*, 1992, **10**, 273–280.

54 W. Peti, T. Pieper, M. Sommer, B. K. Keppler and G. Giester, *Eur. J. Inorg. Chem.*, 1999, **1999**, 1551–1555.

55 E. Alessio and L. Messori, *Molecules*, 2019, **24**, 1–20.

56 P. Pedrosa, A. Carvalho, P. V. Baptista and A. R. Fernandes, *Basic Concepts Viewed from Front. Inorg. Coord. Chem.*, , DOI:10.5772/intechopen.80233.

57 P. J. Barnard and S. J. Berners-Price, *Coord. Chem. Rev.*, 2007, **251**, 1889–1902.

58 S. J. Berners-Price and A. Filipovska, *Metallomics*, 2011, **3**, 863–873.

59 I. Ott, *Coord. Chem. Rev.*, 2009, **253**, 1670–1681.

60 R. Garg, L. G. Benedetti, M. B. Abera, H. Wang, M. Abba and M. G. Kazanietz, *Oncogene*, 2014, **33**, 5225–5237.

61 A. P. Fields and R. P. Regala, *Pharmacol. Res.*, 2007, **55**, 487–497.

62 P. V. Simpson, N. M. Desai, I. Casari, M. Massi and M. Falasca, *Future Med. Chem.*, 2019, **11**, 119–135.

63 U. Ndagi, N. Mhlongo and M. E. Soliman, *Drug Des. Devel. Ther.*, 2017, **11**, 599–616.

64 C. S. Allardyce and P. J. Dyson, *Dalton. Trans.*, 2016, **45**, 3201–3209.

65 T. Gianferrara, I. Bratsos and E. Alessio, *Dalton. Trans.*, 2009, 7588–7598.

66 S. P. Fricker, *Dalton. Trans.*, 2007, 4903–4917.

67 P. J. Sadler, *Gold Bull.*, 1976, **9**, 110–118.

68 T. Zou, C. T. Lum, C.-N. Lok, J.-J. Zhang and C.-M. Che, *Chem. Soc. Rev.*, 2015, **44**, 8786–8801.

69 H. Zhao and Y. Ning, *Gold Bull.*, 2001, **34**, 24–29.

70 G. J. Higby, *Gold Bull.*, 1982, **15**, 130–140.

71 S. P. Pricker, *Gold Bull.*, 1996, **29**, 53–60.

72 P. J. Sadler and R. E. Sue, *Met. Based. Drugs*, 1994, **1**, 107–144.

73 B. M. Sutton, *Gold Bull.*, 1986, **19**, 15–16.

74 B. M. Sutton, E. McGusty, D. T. Walz and M. J. DiMartino, *J. Med. Chem.*, 1972, **15**, 1095–1098.

75 T. M. Simon, D. H. Kunishima, G. J. Vibert and A. Lorber, *Cancer*, 1979, **44**, 1965–1975.

76 C. Marzano, V. Gandin, A. Folda, G. Scutari, A. Bindoli and M. P. Rigobello, *Free Radic. Biol. Med.*, 2007, **42**, 872–881.

77 S. T. Crooke and C. K. Mirabelli, *Am. J. Med.*, 1983, **75**, 109–113.

78 C. Roder and M. J. Thomson, *Drugs R D*, 2015, **15**, 13–20.

79 T. M. Simon, D. H. Kunishima, G. J. Vibert and A. Lorber, *Cancer Res.*, 1981, **41**, 94–97.

80 C. K. Mirabelli, R. K. Johnson, C. M. Sung, L. Faucette, K. Muirhead and S. T. Crooke, *Cancer Res.*, 1985, **45**, 32–39.

81 D. T. Felson, J. J. Anderson and R. F. Meenan, *Arthritis Rheum.*, 1990, **33**, 1449–1461.

82 G. Fanali, A. Di Masi, V. Trezza, M. Marino, M. Fasano and P. Ascenzi, *Mol. Aspects Med.*, 2012, **33**, 209–290.

83 D. Hu, C.-N. Lok and C.-M. Che, in *Metal-based Anticancer Agents*, 2019, pp. 120–142.

84 I. Ott, in *Inorganic and Organometallic Transition Metal Complexes with Biological Molecules and Living Cells*, Elsevier, 2017, pp. 147–179.

85 J. Zhang, X. Li, X. Han, R. Liu and J. Fang, *Trends Pharmacol. Sci.*, 2017, **38**, 794–808.

86 J. Huang and L. Zhong, *Adv. Top. Sci. Technol. China*, 2012, **8**, 41–64.

87 P. Nguyen, R. T. Awwad, D. D. K. Smart, D. R. Spitz and D. Gius, *Cancer Lett.*, 2006, **236**, 164–174.

88 S. Gromer, L. D. Arscott, C. H. Williams, R. H. Schirmeri and K. Becker, *J. Biol. Chem.*, 1998, **273**, 20096–20101.

89 V. Scalcon, A. Bindoli and M. P. Rigobello, *Free Radic. Biol. Med.*, 2018, **127**, 62–79.

90 K. M. Debatin, D. Poncet and G. Kroemer, *Oncogene*, 2002, **21**, 8786–8803.

91 G. Ferrin, C. I. Linares and J. Muntane, *Curr.*

Pharm. Des., 2011, **17**, 2002–2016.

92 A. S. Humphreys, A. Filipovska, S. J. Berners-Price, G. A. Koutsantonis, B. W. Skelton and A. H. White, *Dalton. Trans.*, 2007, 4943–4950.

93 O. Rackham, S. J. Nichols, P. J. Leedman, S. J. Berners-Price and A. Filipovska, *Biochem. Pharmacol.*, 2007, **74**, 992–1002.

94 M. V. Baker, P. J. Barnard, S. J. Berners-Price, S. K. Brayshaw, J. L. Hickey, B. W. Skelton and A. H. White, *Dalton. Trans.*, 2006, **6**, 3708–3715.

95 J. L. Hickey, R. A. Ruhayel, P. J. Barnard, M. V. Baker, S. J. Berners-Price and A. Filipovska, *J. Am. Chem. Soc.*, 2008, **130**, 12570–12571.

96 S. Trapp and R. W. Horobin, *Eur. Biophys. J.*, 2005, **34**, 959–966.

97 I. Kandela, W. Lee and G. L. Indig, *Biotech. Histochem.*, 2003, **78**, 157–169.

98 S. J. Berners-Price and P. J. Sadler, in *Bioinorganic Chemistry. Structure and Bonding. Vol 70.*, Springer Berlin Heidelberg, 1988, pp. 27–102.

99 S. J. Berners-Price, C. K. Mirabelli, R. K. Johnson, M. R. Mattern, F. L. McCabe, L. F. Faucette, C. M. Sung, S. M. Mong, P. J. Sadler and S. T. Crooke, *Cancer Res.*, 1986, **46**, 5486–5493.

100 M. J. McKeage, S. J. Berners-Price, P. Galettis, R. J. Bowen, W. Brouwer, L. Ding, L. Zhuang and B. C. Baguley, *Cancer Chemother. Pharmacol.*, 2000, **46**, 343–350.

101 S. B. Aher, P. N. Muskawar, K. Thenmozhi and P. R. Bhagat, *Eur. J. Med. Chem.*, 2014, **81**, 408–419.

102 W. Liu and R. Gust, *Chem. Soc. Rev.*, 2013, **42**, 755–773.

103 G. Gasser, I. Ott and N. Metzler-Nolte, *J. Med. Chem.*, 2011, **54**, 3–25.

104 S. Jürgens and A. Casini, *Chim. Int. J. Chem.*, 2017, **71**, 92–101.

105 A. Gautier and F. Cisnetti, *Metallomics*, 2012, **4**, 23–32.

106 S. Y. Hussaini, R. A. Haque and M. R. Razali, *J. Organomet. Chem.*, 2019, **882**, 96–111.

107 P. O. Wagers, M. J. Panzner, M. R. Southerland, M. A. DeBord, M. C. Deblock, C. A. Tessier, C. L. Cannon and W. J. Youngs, in *N-Heterocyclic Carbenes: From Laboratory Curiosities to Efficient Synthetic Tools 2nd Edition*, ed. S. Díez-González, Royal Society of Chemistry, Cambridge, 2nd edn., 2016, pp. 567–595.

108 T. Zou, C.-N. Lok, P.-K. Wan, Z.-F. Zhang, S.-K. Fung and C.-M. Che, *Curr. Opin. Chem. Biol.*, 2018, **43**, 30–36.

109 L. Oehninger, R. Rubbiani and I. Ott, *Dalton. Trans.*, 2013, **42**, 3269–3284.

110 R. Rubbiani, I. Kitanovic, H. Alborzinia, S. Can, A. Kitanovic, L. A. Onambele, M. Stefanopoulou, Y. Geldmacher, W. S. Sheldrick, G. Wolber, A. Prokop, S. Wölfl and I. Ott, *J. Med. Chem.*, 2010, **53**, 8608–8618.

111 A. Pratesi, C. Gabbiani, E. Michelucci, M. Ginanneschi, A. M. Papini, R. Rubbiani, I. Ott and L. Messori, *J. Inorg. Biochem.*, 2014, **136**, 161–169.

112 R. Rubbiani, S. Can, I. Kitanovic, H. Alborzinia, M. Stefanopoulou, M. Kokoschka, S. Mönchgesang, W. S. Sheldrick, S. Wölfl and I. Ott, *J. Med. Chem.*, 2011, **54**, 8646–8657.

113 K. Yan, C. N. Lok, K. Bierla and C. M. Che, *Chem. Commun.*, 2010, **46**, 7691–7693.

114 A. Meyer, C. P. Bagowski, M. Kokoschka, M. Stefanopoulou, H. Alborzinia, S. Can, D. H. Vlecken, W. S. Sheldrick, S. Wölfl and I. Ott, *Angew. Chem. Int. Ed.*, 2012, **51**, 8895–8899.

115 A. Meyer, L. Oehninger, Y. Geldmacher, H. Alborzinia, S. Wölfl, W. S. Sheldrick and I. Ott, *ChemMedChem*, 2014, **9**, 1794–1800.

116 T. Zou, C. T. Lum, C.-N. N. Lok, W.-P. P. To, K.-H. H. Low and C.-M. M. Che, *Angew. Chem. Int. Ed.*, 2014, **53**, 5810–5814.

117 B. Bertrand, L. Stefan, M. Pirrotta, D. Monchaud, E. Bodio, P. Richard, P. Le Gendre, E. Warmerdam, M. H. De Jager, G. M. M. Groothuis, M. Picquet and A. Casini, *Inorg. Chem.*, 2014, **53**, 2296–2303.

118 D. I. Bezuidenhout, G. Kleinhans, G. Guisado-Barrios, D. C. Liles, G. Ung and G. Bertrand, *Chem. Commun.*, 2014, **50**, 2431.

119 A. Casini and L. Messori, *Curr. Top. Med. Chem.*, 2011, **11**, 2647–2660.

120 S. Nobili, E. Mini, I. Landini, C. Gabbiani, A. Casini and L. Messori, *Med. Res. Rev.*, 2010, **30**, 550–580.

121 E. R. T. Tiekink, *Inflammopharmacology*, 2008, **16**, 138–142.

122 V. Milacic, D. Fregona and Q. P. Dou, *Histol. Histopathol.*, 2008, **23**, 101–8.

123 E. R. T. Tiekink, *Gold Bull.*, 2003, **36**, 117–124.

124 C. F. I. Shaw, *Chem. Rev.*, 1999, **99**, 2589–2600.

125 N. Cutillas, G. S. Yellol, C. De Haro, C. Vicente, V. Rodríguez and J. Ruiz, *Coord. Chem. Rev.*, 2013, **257**, 2784–2797.

126 B. Bertrand, M. R. M. Williams and M. Bochmann, *Chem. Eur. J.*, 2018, **24**, 11840–11851.

127 A. Casini, C. Hartinger, C. Gabbiani, E. Mini, P. J. Dyson, B. K. Keppler and L. Messori, *J. Inorg.*

Biochem., 2008, **102**, 564–575.

128 C. Gabbiani, A. Casini and L. Messori, *Gold Bull.*, 2007, **40**, 73–81.

129 X. Wang and Z. Guo, *Dalton. Trans.*, 2008, 1521–1532.

130 W. Liu, K. Bensdorf, M. Proetto, U. Abram, A. Hagenbach and R. Gust, *J. Med. Chem.*, 2011, **54**, 8605–8615.

131 T. Zou, C. T. Lum, S. S. Y. Chui and C. M. Che, *Angew. Chem. Int. Ed.*, 2013, **52**, 2930–2933.

132 B. Bertrand, E. Bodio, P. Richard, M. Picquet, P. Le Gendre and A. Casini, *J. Organomet. Chem.*, 2015, **775**, 124–129.

133 V. Gandin, A. P. Fernandes, M. P. Rigobello, B. Dani, F. Sorrentino, F. Tisato, M. Björnstedt, A. Bindoli, A. Sturaro, R. Rella and C. Marzano, *Biochem. Pharmacol.*, 2010, **79**, 90–101.

134 P. J. Sadler, M. Nasr and V. L. Narayanan, *Platin. Coord. Complexes Cancer Chemother.*, 1984, 290–304.

135 E. R. T. Tiekink, *Crit. Rev. Oncol. Hematol.*, 2002, **42**, 225–248.

136 C. K. Mirabelli, C. M. Sung, J. P. Zimmerman, D. T. Hill, S. Mong and S. T. Crooke, *Biochem. Pharmacol.*, 1986, **35**, 1427–1433.

137 C. F. Shaw, in *Metal Compounds in Cancer Therapy*, ed. S. P. Fricker, Springer Netherlands, Dordrecht, 1994, pp. 46–64.

138 R. V Parish, R. G. Buckley, S. P. Fricker, J. Mack, L. Hargreaves, J. P. Wright, A. M. Elsome and B. R. C. Theobald, *J. Chem. Soc. Dalt. Trans.*, 1996, 69–74.

139 J. Vicente, M. T. Chicote and M. D. Bermúdez, *J. Organomet. Chem.*, 1984, **268**, 191–195.

140 R. G. Buckley, A. M. Elsome, S. P. Fricker, G. R. Henderson, B. R. C. Theobald, R. V. Parish, B. P. Howe and L. R. Kelland, *J. Med. Chem.*, 1996, **39**, 5208–5214.

141 R. V. Parish, B. P. Howe, J. P. Wright, J. Mack, R. G. Pritchard, R. G. Buckley, A. M. Elsome and S. P. Fricker, *Inorg. Chem.*, 1996, **35**, 1659–1666.

142 P. Calamai, S. Carotti, A. Guerri, L. Messori, E. Mini, P. Orioli and G. Paolo Speroni, *J. Inorg. Biochem.*, 1997, **66**, 103–109.

143 L. Messori, F. Abbate, G. Marcon, P. Orioli, M. Fontani, E. Mini, T. Mazzei, S. Carotti, T. O'Connell and P. Zanello, *J. Med. Chem.*, 2000, **43**, 3541–3548.

144 A. Casini, M. A. Cinellu, G. Minghetti, C. Gabbiani, M. Coronnello, E. Mini and L. Messori, *J. Med. Chem.*, 2006, **49**, 5524–5531.

145 M. Coronnello, E. Mini, B. Caciagli, M. A. Cinellu, A. Bindoli, C. Gabbiani and L. Messori, *J. Med. Chem.*, 2005, **48**, 6761–6765.

146 R. D. Teo, H. B. Gray, P. Lim, J. Termini, E. Domeshek and Z. Gross, *Chem. Commun.*, 2014, **50**, 13789–13792.

147 C.-M. Che, R. W.-Y. Sun, W.-Y. Yu, C.-B. Ko, N. Zhu and H. Sun, *Chem. Commun.*, 2003, 1718–9.

148 G. Marcon, S. Carotti, M. Coronnello, L. Messori, E. Mini, P. Orioli, T. Mazzei, M. A. Cinellu and G. Minghetti, *J. Med. Chem.*, 2002, **45**, 1672–1677.

149 J.-J. J. Zhang, R. W.-Y. Y. Sun and C.-M. M. Che, *Chem. Commun.*, 2012, **48**, 3388.

150 C. K.-L. Li, R. W.-Y. Sun, S. C.-F. Kui, N. Zhu and C.-M. Che, *Chem. Eur. J.*, 2006, **12**, 5253–5266.

151 B. Bertrand, M. Bochmann, J. Fernandez-Cestau and L. Rocchigiani, in *Pincer Compounds: Chemistry and Applications*, 2018, pp. 673–699.

152 R. W. Y. Sun, C. N. Lok, T. T. H. Fong, C. K. L. Li, Z. F. Yang, A. F. M. Siu and C. M. Che, *Chem. Sci.*, 2013, **4**, 1979–1988.

153 J. J. Yan, A. L. F. Chow, C. H. Leung, R. W. Y. Sun, D. L. Ma and C. M. Che, *Chem. Commun.*, 2010, **46**, 3893–3895.

154 B. Bertrand, J. Fernandez-Cestau, J. Angulo, M. M. D. Cominetti, Z. A. E. Waller, M. Searcey, M. A. O'Connell and M. Bochmann, *Inorg. Chem.*, 2017, **56**, 5728–5740.

155 S. K. Fung, T. Zou, B. Cao, P. Y. Lee, Y. M. E. Fung, D. Hu, C. N. Lok and C. M. Che, *Angew. Chem. Int. Ed.*, 2017, **56**, 3892–3896.

156 H. V. Huynh, *The Organometallic Chemistry of N-heterocyclic Carbenes*, John Wiley & Sons, Ltd, Chichester, UK, First., 2017.

157 S. Diez-Gonzalez, Ed., *N-Heterocyclic Carbenes: From Laboratory Curiosities to Efficient Synthetic Tools: Edition 2*, Royal Society of Chemistry, Cambridge, 2016.

158 S. Diez-Gonzalez, Ed., *N-Heterocyclic Carbenes: From Laboratory Curiosities to Efficient Synthetic Tools*, Royal Society of Chemistry, Cambridge, 2010.

159 C. S. J. Cazin, Ed., *N-Heterocyclic Carbenes in Transition Metal Catalysis and Organocatalysis*, Springer Netherlands, Dordrecht, 2011, vol. 32.

160 A. T. Biju, *N-Heterocyclic Carbenes in Organocatalysis*, Wiley-VCH Verlag GmbH & Co. KGaA, Weinheim, Germany, 2018.

161 M.-L. Teyssot, A.-S. Jarrousse, M. Manin, A. Chevry, S. Roche, F. Norre, C. Beaudoin, L. Morel, D. Boyer, R. Mahiou and A. Gautier, *Dalton. Trans.*, 2009, 6894.

162 M. Mora, M. C. Gimeno and R. Visbal, *Chem. Soc. Rev.*, 2019, **48**, 447–462.

163 K. M. Hindi, M. J. Panzner, C. A. Tessier, C. L.

Cannon and W. J. Youngs, *Chem. Rev.*, 2009, **109**, 3859–3884.

164 M. C. Deblock, M. J. Panzner, C. A. Tessier, C. L. Cannon and W. J. Youngs, in *N-Heterocyclic Carbenes: From Laboratory Curiosities to Efficient Synthetic Tools*, ed. S. Díez-González, Royal Society of Chemistry, Cambridge, 2011, pp. 119–133.

165 L. Mercs and M. Albrecht, *Chem. Soc. Rev.*, 2010, **39**, 1903–1912.

166 W. Liu and R. Gust, *Coord. Chem. Rev.*, 2016, **329**, 191–213.

167 M. Albrecht, in *Advances in Organometallic Chemistry*, Elsevier Inc., 1st edn., 2014, vol. 62, pp. 111–158.

168 M. Albrecht, *Chem. Commun.*, 2008, 3601.

169 P. L. Arnold and S. Pearson, *Coord. Chem. Rev.*, 2007, **251**, 596–609.

170 O. Schuster, L. Yang, H. G. Raubenheimer and M. Albrecht, *Chem. Rev.*, 2009, **109**, 3445–3478.

171 S. Gründemann, A. Kovacevic, M. Albrecht, J. W. Faller Robert, H. Crabtree, J. W. Faller, R. H. Crabtree, J. W. Faller Robert and H. Crabtree, *Chem. Commun.*, 2001, **4**, 2274.

172 A. Krüger and M. Albrecht, in *N-Heterocyclic Carbenes: From Laboratory Curiosities to Efficient Synthetic Tools*, ed. S. Díez-González, Royal Society of Chemistry, Cambridge, 2011, pp. 134–165.

173 Á. Vivancos, C. Segarra and M. Albrecht, *Chem. Rev.*, 2018, **118**, 9493–9586.

174 R. H. Crabtree, *Coord. Chem. Rev.*, 2013, **257**, 755–766.

175 S. Gründemann, A. Kovacevic, M. Albrecht, J. W. Faller and R. H. Crabtree, *J. Am. Chem. Soc.*, 2002, **124**, 10473–10481.

176 G. Sini, O. Eisenstein and R. H. Crabtree, *Inorg. Chem.*, 2002, **41**, 602–604.

177 A. M. Magill and B. F. Yates, *Aust. J. Chem.*, 2004, **57**, 1205–1210.

178 P. Mathew, A. Neels and M. Albrecht, *J. Am. Chem. Soc.*, 2008, **130**, 13534–13535.

179 A. J. Arduengo, R. L. Harlow and M. Kline, *J. Am. Chem. Soc.*, 1991, **113**, 361–363.

180 H.-J. Schönherr and H.-W. Wanzlick, *Justus Liebigs Ann. Chem.*, 1970, **731**, 176–179.

181 H.-J. Schönherr and H.-W. Wanzlick, *Chem. Ber.*, 1970, **103**, 1037–1046.

182 E. Aldeco-Perez, A. J. Rosenthal, B. Donnadieu, P. Parameswaran, G. Frenking and G. Bertrand, *Science.*, 2009, **326**, 556–559.

183 G. Guisado-Barrios, J. Bouffard, B. Donnadieu and G. Bertrand, *Angew. Chem. Int. Ed.*, 2010, **49**, 4759–4762.

184 D. Bourissou, O. Guerret, F. P. Gabbaï and G. Bertrand, *Chem. Rev.*, 2000, **100**, 39–92.

185 D. Munz, *Organometallics*, 2018, **37**, 275–289.

186 H. V. Huynh, *Chem. Rev.*, 2018, **118**, 9457–9492.

187 A. Levens, F. An, M. Breugst, H. Mayr and D. W. Lupton, *Org. Lett.*, 2016, **18**, 3566–3569.

188 L.-A. Schaper, L. Graser, X. Wei, R. Zhong, K. Öfele, A. Pöthig, M. Cokoja, B. Bechlars, W. a. Herrmann and F. E. Kühn, *Inorg. Chem.*, 2013, **52**, 6142–6152.

189 L.-A. Schaper, X. Wei, S. J. Hock, A. Pöthig, K. Öfele, M. Cokoja, W. a. Herrmann and F. E. Kühn, *Organometallics*, 2013, **32**, 3376–3384.

190 L.-A. Schaper, K. Öfele, R. Kadyrov, B. Bechlars, M. Drees, M. Cokoja, W. A. Herrmann and F. E. Kühn, *Chem. Commun.*, 2012, **48**, 3857.

191 G. Guisado-Barrios, M. Soleilhavoup and G. Bertrand, *Acc. Chem. Res.*, 2018, **51**, 3236–3244.

192 D. Schweinfurth, L. Hettmanczyk, L. Suntrup and B. Sarkar, *Z. Anorg. Allg. Chem.*, 2017, 643, 554–584.

193 K. O. Marichev, S. A. Patil and A. Bugarin, *Tetrahedron*, 2018, **74**, 2523–2546.

194 K. F. Donnelly, A. Petronilho and M. Albrecht, *Chem. Commun.*, 2013, **49**, 1145–1159.

195 K. J. Kilpin, S. Crot, T. Riedel, J. A. Kitchen and P. J. Dyson, *Dalton. Trans.*, 2014, **43**, 1443–1448.

196 S. Vanicek, M. Podewitz, J. Stubbe, D. Schulze, H. Kopacka, K. Wurst, T. Müller, P. Lippmann, S. Haslinger, H. Schottenberger, K. R. Liedl, I. Ott, B. Sarkar and B. Bildstein, *Chem. Eur. J.*, 2018, **24**, 3742–3753.

197 D. Aucamp, S. V. Kumar, D. C. Liles, M. A. Fernandes, L. Harmse and D. I. Bezuidenhout, *Dalton. Trans.*, 2018, **47**, 16072–16081.

198 G. Kleinhans, M. M. Hansmann, G. Guisado-Barrios, D. C. Liles, G. Bertrand and D. I. Bezuidenhout, *J. Am. Chem. Soc.*, 2016, **138**, 15873–15876.

199 G. Kleinhans, G. Guisado-Barrios, D. C. Liles, G. Bertrand and D. I. Bezuidenhout, *Chem. Commun.*, 2016, **52**, 3504–3507.

200 G. Kleinhans, G. Guisado-Barrios, E. Peris and D. I. Bezuidenhout, *Polyhedron*, 2018, **143**, 43–48.

201 G. Kleinhans, A. K.-W. Chan, M.-Y. Leung, D. C. Liles, M. A. Fernandes, V. W. -W. Yam, I. Fernández and D. I. Bezuidenhout, *Chem. – A Eur. J.*, 2020, **26**, 6993–6998.

202 K. J. Akerman, A. M. Fagenson, V. Cyril, M. Taylor, M. T. Muller, M. P. Akerman and O. Q. Munro, *J. Am. Chem. Soc.*, 2014, **136**, 5670–

5682.

203 J. D. Crowley, A. L. Lee and K. J. Kilpin, *Aust. J. Chem.*, 2011, **64**, 1118–1132.

204 H. C. Kolb, M. G. Finn and K. B. Sharpless, *Angew. Chem. Int. Ed.*, 2001, **40**, 2004–2021.

205 R. Huisgen, *Angew. Chem. Int. Ed. English*, 1963, **2**, 633–645.

206 R. Huisgen, *Angew. Chem. Int. Ed. English*, 1963, **2**, 565–598.

207 V. V. Rostovtsev, L. G. Green, V. V. Fokin and K. B. Sharpless, *Angew. Chem. Int. Ed.*, 2002, **41**, 2596–2599.

208 C. W. Tornøe, C. Christensen and M. Meldal, *J. Org. Chem.*, 2002, **67**, 3057–3064.

209 J. E. Moses and A. D. Moorhouse, *Chem. Soc. Rev.*, 2007, **36**, 1249–1262.

210 J. D. Crowley, S. M. Goldup, A.-L. Lee, D. A. Leigh and R. T. McBurney, *Chem. Soc. Rev.*, 2009, **38**, 1530.

211 J. M. Holub and K. Kirshenbaum, *Chem. Soc. Rev.*, 2010, **39**, 1325.

212 Y. Hua and A. H. Flood, *Chem. Soc. Rev.*, 2010, **39**, 1262.

213 C. Le Droumaguet, C. Wang and Q. Wang, *Chem. Soc. Rev.*, 2010, **39**, 1233–1239.

214 K. D. Hänni and D. A. Leigh, *Chem. Soc. Rev.*, 2010, **39**, 1240–1251.

215 M. Meldal and C. W. Tornøe, *Chem. Rev.*, 2008, **108**, 2952–3015.

216 L. Zhang, X. Chen, P. Xue, H. H. Y. Sun, I. D. Williams, K. B. Sharpless, V. V. Fokin and G. Jia, *J. Am. Chem. Soc.*, 2005, **127**, 15998–15999.

217 Y.-C. Wang, Y.-Y. Xie, H.-E. Qu, H.-S. Wang, Y.-M. Pan and F.-P. Huang, *J. Org. Chem.*, 2014, **79**, 4463–4469.

218 S. W. Kwok, J. R. Fotsing, R. J. Fraser, V. O. Rodionov and V. V Fokin, *Org. Lett.*, 2010, **12**, 4217–4219.

219 P. Mathew, A. Neels and M. Albrecht, *J. Am. Chem. Soc.*, 2008, **130**, 13534–13535.

220 H. V. Huynh, in *The Organometallic Chemistry of N-heterocyclic Carbenes*, John Wiley & Sons, Ltd, Chichester, UK, 2017, pp. 52–98.

221 J. Bouffard, B. K. Keitz, R. Tonner, G. Guisado-Barrios, G. Frenking, R. H. Grubbs, G. Bertrand, V. Lavallo, G. Guisado-Barrios, G. Frenking, R. H. Grubbs and G. Bertrand, *Organometallics*, 2011, **30**, 2617–2627.

222 P. de Frémont, N. Marion and S. P. Nolan, *Coord. Chem. Rev.*, 2009, **253**, 862–892.

223 M. S. Mudadu, A. N. Singh and R. P. Thummel, *J. Org. Chem.*, 2008, **73**, 6513–6520.

224 A. Dangsopon, N. Poomsuk, K. Siriwong, T. Vilaivan and C. Suparpprom, *RSC Adv.*, 2016, **6**, 74314–74322.

225 T. Suzuki, A. Kinoshita, H. Kawada and M. Nakada, *Synlett*, 2003, 570–572.

226 M. S. Bennington, H. L. C. C. Feltham, Z. J. Buxton, N. G. White and S. Brooker, *Dalton. Trans.*, 2017, **46**, 4696–4710.

227 M. Tashiro and T. Yamato, *Synthesis (Stuttg).*, 1979, 48–50.

228 M. Tashiro, *Synthesis (Stuttg).*, 1979, **1979**, 921–936.

229 Y. Liu, M. Nishiura, Y. Wang and Z. Hou, *J. Am. Chem. Soc.*, 2006, **128**, 5592–5593.

230 E. Jürgens, K. N. Buys, A. T. Schmidt, S. K. Furfari, M. L. Cole, M. Moser, F. Rominger and D. Kunz, *New J. Chem.*, 2016, **40**, 9160–9169.

231 S. Saleh and L. Tashtoush, *Tetrahedron*, 1998, **54**, 14157–14177.

232 N. Lewis and I. Morgan, *Synth. Commun.*, 1988, **18**, 1783–1793.

233 S. J. Malthus, S. A. Cameron and S. Brooker, *Inorg. Chem.*, 2018, **57**, 2480–2488.

234 R. Chinchilla and C. Nájera, *Chem. Rev.*, 2007, **107**, 874–922.

235 H. Gilman, A. G. Brook and L. S. Miller, *J. Am. Chem. Soc.*, 1953, **75**, 4531–4534.

236 N. V. Tzouras, F. Nahra, L. Falivene, L. Cavallo, M. Saab, K. Van Hecke, A. Collado, C. J. Collett, A. D. Smith, C. S. J. Cazin and S. P. Nolan, *Chem. Eur. J.*, 2020, 4515–4519.

237 V. D. Bock, H. Hiemstra and J. H. van Maarseveen, *Eur. J. Org. Chem.*, 2006, **2006**, 51–68.

238 B. T. Worrell, J. A. Malik and V. V. Fokin, *Science.*, 2013, **340**, 457–460.

239 L. Jin, D. R. Tolentino, M. Melaimi and G. Bertrand, *Sci. Adv.*, , DOI:10.1126/sciadv.1500304.

240 G. Guisado-Barrios, J. Bouffard, B. Donnadieu and G. Bertrand, *Organometallics*, 2011, **30**, 6017–6021.

241 K. Barral, A. D. Moorhouse and J. E. Moses, *Org. Lett.*, 2007, **9**, 1809–1811.

242 J. T. Fletcher, B. J. Bumgarner, N. D. Engels and D. A. Skoglund, *Organometallics*, 2008, **27**, 5430–5433.

243 E. Jürgens, O. Back, J. J. Mayer, K. Heinze and D. Kunz, *Zeitschrift fur Naturforsch. - Sect. B J. Chem. Sci.*, 2016, **71**, 1011–1018.

244 J. C. Garrison and W. J. Youngs, *Chem. Rev.*, 2005, **105**, 3978–4008.

245 J. M. Hayes, M. Viciano, E. Peris, G. Ujaque and A. Lledós, *Organometallics*, 2007, **26**, 6170–6183.

246 D. Canseco-Gonzalez, A. Petronilho, H. Mueller-Bunz, K. Ohmatsu, T. Ooi and M. Albrecht, *J. Am. Chem. Soc.*, 2013, **135**, 13193–13203.

247 M. Contel, J. Garrido, M. C. Gimeno, J. Jiménez, P. G. Jones, A. Laguna and M. Laguna, *Inorg. Chim. Acta*, 1997, **254**, 157–161.

248 J. A. Cabeza, I. Fernández, P. García-Álvarez and C. J. Laglera-Gándara, *Dalton. Trans.*, 2019, **48**, 13273–13280.

249 J. I. Van Der Vlugt, M. A. Siegler, M. Janssen, D. Vogt and A. L. Spek, *Organometallics*, 2009, **28**, 7025–7032.

250 E. C. Keske, O. V. Zenkina, R. Wang and C. M. Crudden, *Organometallics*, 2012, **31**, 456–461.

251 J. Cai, X. Yang, K. Arumugam, C. W. Bielawski and J. L. Sessler, *Organometallics*, 2011, **30**, 5033–5037.

252 H. Schmidbaur and A. Schier, *Chem. Soc. Rev.*, 2012, **41**, 370–412.

253 Y. Liu, M. Nishiura, Y. Wang and Z. Hou, *J. Am. Chem. Soc.*, 2006, **128**, 5592–5593.

254 V. C. Gibson, S. K. Spitzmesser, A. J. P. White and D. J. Williams, *Dalton. Trans.*, 2003, **3**, 2718.

255 R. Uson, A. Laguna and M. Laguna, in *Inorganic Syntheses*, ed. H. D. Kaesz, John Wiley & Sons Ltd, 1989, vol. 26, p. 86.

256 H. Meerwein, *Org. Synth.*, 1966, **46**, 113.

257 M. Virant and J. Košmrlj, *J. Org. Chem.*, 2019, **84**, 14030–14044.

258 T. Lv, Z. Wang, J. You, J. Lan and G. Gao, *J. Org. Chem.*, 2013, **78**, 5723–5730.

259 W. Wirschun, M. Winkler, K. Lutz and J. C. Jochims, *J. Chem. Soc. Perkin Trans. 1*, 1998, 1755–1761.

260 W. Wirschun, *J. fur Prakt. Chem.*, 1998, **340**, 300–308.

261 W. Wirschun and J. C. Jochims, *Synthesis (Stuttg).*, 1997, **1997**, 233–241.

262 J. L. Gordon, M. A. Brown and M. M. Reynolds, *Diseases*, 2018, **6**, 85.

263 M. J. Stoddart, in *Methods in Molecular Biology*, ed. M. J. Stoddart, Humana Press, Totowa, NJ, 2011, vol. 740, p. p.7-12.

264 R. J. Gillies, N. Didier and M. Denton, *Anal. Biochem.*, 1986, **159**, 109–113.

265 Ö. S. Aslantürk, in *Genotoxicity - A Predictable Risk to Our Actual World*, InTech, 2018, pp. 1–18.

266 T. Mosmann, *J. Immunol. Methods*, 1983, **65**, 55–63.

267 M. Nikš and M. Otto, *J. Immunol. Methods*, 1990, **130**, 149–151.

268 Y. Liu, D. A. Peterson, H. Kimura and D. Schubert, *J. Neurochem.*, 2002, **69**, 581–593.

269 L. Śliwka, K. Wiktorska, P. Suchocki, M. Milczarek, S. Mielczarek, K. Lubelska, T. Cierpiał, P. Łyżwa, P. Kiełbasiński, A. Jaromin, A. Flis and Z. Chilmonczyk, *PLoS One*, 2016, **11**, e0155772.

270 K. Chiba, K. Kawakami and K. Tohyama, *Toxicol. Vitr.*, 1998, **12**, 251–258.

271 M. Feoktistova, P. Geserick and M. Leverkus, *Cold Spring Harb. Protoc.*, 2016, **2016**, pdb.prot087379.

272 K. Saotome, H. Morita and M. Umeda, *Toxicol. Vitr.*, 1989, **3**, 317–321.

273 W. Kueng, E. Silber and U. Eppenberger, *Anal. Biochem.*, 1989, **182**, 16–19.

274 D. A. Flick and G. E. Gifford, *J. Immunol. Methods*, 1984, **68**, 167–175.

275 S. W. Rothman, *J. Clin. Pathol.*, 1986, **39**, 672–676.

276 E. Vega-Avila and M. K. Pugsley, *Proc. West. Pharmacol. Soc.*, 2011, **54**, 10–14.

277 M. Pažický, A. Loos, M. J. Ferreira, D. Serra, N. Vinokurov, F. Rominger, C. Jäkel, A. S. K. Hashmi and M. Limbach, *Organometallics*, 2010, **29**, 4448–4458.

278 J. C. Y. Lin, R. T. W. Huang, C. S. Lee, A. Bhattacharyya, W. S. Hwang and I. J. B. Lin, *Chem. Rev.*, 2009, **109**, 3561–3598.

279 D. Mendoza-Espinosa, D. Rendón-Nava, A. Alvarez-Hernández, D. Angeles-Beltrán, G. E. Negrón-Silva and O. R. Suárez-Castillo, *Chem. Asian J.*, 2017, **12**, 203–207.

280 M. Timm, L. Saaby, L. Moesby and E. W. Hansen, *Cytotechnology*, 2013, **65**, 887–894.

281 M. Singh, K. Mckenzie and X. Ma, *J. Biotech Res.*, 2017, **8**, 78–82.

282 L. Jamalzadeh, H. Ghafoori, R. Sariri, H. Rabuti, J. Nasirzade, H. Hasani and M. R. Aghamaali, *Avicenna J. Med. Biochem.*, 2016, **In press**, 1–49.

283 F. Hajighasemi and S. Tajik, *Iran. J. Blood Cancer*, 2017, **9**, 48–53.

284 L. De Abreu Costa, M. H. F. Ottoni, M. G. Dos Santos, A. B. Meireles, V. G. De Almeida, W. De Fátima Pereira, B. A. De Avelar-Freitas and G. E. A. Brito-Melo, *Molecules*, 2017, **22**, 1–10.

285 L. Zapór, J. Skowroń and M. Gołofit-Szymczak, *Int. J. Occup. Saf. Ergon.*, 2002, **8**, 121–129.

286 J. Galvao, B. Davis, M. Tilley, E. Normando, M. R. Duchen and M. F. Cordeiro, *FASEB J.*, 2014, **28**, 1317–1330.

287 M. Patra, T. Joshi, V. Pierroz, K. Ingram, M. Kaiser, S. Ferrari, B. Spingler, J. Keiser and G. Gasser, *Chem. Eur. J.*, 2013, **19**, 14768–14772.

288 J. Arcau, V. Andermark, M. Rodrigues, I. Giannicchi, L. Pérez-Garcia, I. Ott and L. Rodríguez, *Eur. J. Inorg. Chem.*, 2014, **2014**, 6117–6125.

289 W. Liu, K. Bensdorf, M. Proetto, A. Hagenbach, U. Abram and R. Gust, *J. Med. Chem.*, 2012, **55**, 3713–3724.

290 M. Porchia, M. Pellei, M. Marinelli, F. Tisato, F. Del Bello and C. Santini, *Eur. J. Med. Chem.*, 2018, **146**, 709–746.

291 I. Steiner, N. Stojanovic, A. Bolje, A. Brozovic, D. Polancec, A. Ambriovic-Ristov, M. R. Stojkovic, I. Piantanida, D. Eljuga, J. Kosmrlj and M. Osmak, *Radiol. Oncol.*, 2016, **50**, 280–288.

292 J.-M. Liu, M. Wang, Y.-J. Zhou, J.-M. Yan, L.-J. Yang, Y. Li, H.-B. Zhang and X.-D. Yang, *RSC Adv.*, 2015, **5**, 63936–63944.

293 N. Nimitsiriwat, V. C. Gibson, E. L. Marshall, P. Takolpuckdee, A. K. Tomov, A. J. P. White, D. J. Williams, M. R. J. Elsegood and S. H. Dale, *Inorg. Chem.*, 2007, **46**, 9988–9997.

294 A. G. M. Barrett, M. R. Crimmin, M. S. Hill, P. B. Hitchcock, G. Kociok-Köhn and P. A. Procopiou, *Inorg. Chem.*, 2008, **47**, 7366–7376.

295 M. J. Mintz and C. Walling, *Org. Synth.*, 1969, **49**, 9.

296 X. F. Zhao and C. Zhang, *Synthesis (Stuttg).*, 2007, 551–557.

297 S. E. Burdall, A. M. Hanby, M. R. J. Lansdown and V. Speirs, *Breast Cancer Res.*, 2003, **5**, 89.

298 A. Kellett, Z. Molphy, C. Slator, V. McKee and N. P. Farrell, *Chem. Soc. Rev.*, 2019, **48**, 971–988.

299 R. E. Franklin and R. G. Gosling, *Nature*, 1953, **171**, 740–741.

300 P. M. Takahara, A. C. Rosenzweig, C. A. Frederick and S. J. Lippard, *Nature*, 1995, **377**, 649–652.

301 J. H. J. Den Hartog, C. Altona, J. H. Van Boom, G. A. Van Der Marel, C. A. G. Haasnoot and J. Reedijk, *J. Biomol. Struct. Dyn.*, 1985, **2**, 1137–1155.

302 A. M. J. Fichtinger-Schepman, P. H. M. Lohman, J. L. van der Veer, J. H. J. den Hartog and J. Reedijk, *Biochemistry*, 1985, **24**, 707–713.

303 C. Bazzicalupi, M. Ferraroni, F. Papi, L. Massai, B. Bertrand, L. Messori, P. Gratteri and A. Casini, *Angew. Chem. Int. Ed.*, 2016, **55**, 4256–4259.

304 A. Giorgio and A. Merlino, *Coord. Chem. Rev.*, 2020, **407**, 213175.

305 E. Weidauer, Y. Yasuda, B. K. Biswal, M. Cherny, M. N. G. James and D. Brömme, *Biol. Chem.*, 2007, **388**, 331–336.

306 M. T. Coffer, C. F. Shaw, M. K. Eidsness, J. W. Watkins and R. C. Elder, *Inorg. Chem.*, 1986, **25**, 333–339.

307 A. Pratesi, D. Cirri, D. Fregona, G. Ferraro, A. Giorgio, A. Merlino and L. Messori, *Inorg. Chem.*, 2019, **58**, 10616–10619.

308 L. Messori, F. Scaletti, L. Massai, M. A. Cinellu, C. Gabbiani, A. Vergara and A. Merlino, *Chem. Commun.*, 2013, **49**, 10100–10102.

309 I. Russo Krauss, L. Messori, M. A. Cinellu, D. Marasco, R. Sirignano and A. Merlino, *Dalton. Trans.*, 2014, **43**, 17483–17488.

310 G. Ferraro, C. Gabbiani and A. Merlino, *Bioconjug. Chem.*, 2016, **27**, 1584–1587.

311 2020 Schrödinger Release 2020-3: Maestro, Schrödinger, LLC, New York, NY, .

312 L. S. Lerman, *J. Mol. Biol.*, 1961, **3**, 18–30.

313 E. C. Long and J. K. Barton, *Acc. Chem. Res.*, 1990, **23**, 271–273.

314 P. E. Pjura, K. Grzeskowiak and R. E. Dickerson, *J. Mol. Biol.*, 1987, **197**, 257–271.

315 D. Suh and J. B. Chaires, *Bioorganic Med. Chem.*, 1995, **3**, 723–728.

316 P. Lincoln, L. M. Wilhemsson and B. Nordén, in *DNA-targeting Molecules as Therapeutic Agents*, ed. M. J. Waring, Royal Society of Chemistry, 2018, pp. 45–73.

317 S. K. Kim and B. Nordén, *FEBS Lett.*, 1993, **315**, 61–64.

318 S. Komeda, T. Moulaei, K. K. Woods, M. Chikuma, N. P. Farrell and L. D. Williams, *J. Am. Chem. Soc.*, 2006, **128**, 16092–16103.

319 T. C. Jenkins, *Methods Mol. Biol.*, 1997, **90**, 195–218.

320 J. B. Chaires, in *DNA-targeting Molecules as Therapeutic Agents*, ed. M. J. Waring, Royal Society of Chemistry, 2018, pp. 74–95.

321 N. C. Garbett, P. A. Ragazzon and J. O. B. Chaires, *Nat. Protoc.*, 2007, **2**, 3166–3172.

322 B. Nordén, *Appl. Spectrosc. Rev.*, 1978, **14**, 157–248.

323 A. Rodger, *Methods Mol. Biol.*, 2010, **613**, 37–54.

324 A. Rodger, *Circular Dichroism and Linear Dichroism*, 2014.

325 M. Eriksson and B. Nordén, *Methods Enzymol.*, 2001, **340**, 68–98.

326 P. H. Johnson and L. I. Grossman, *Biochemistry*, 1977, **16**, 4217–4225.

327 K. D. Cole, *Biotechniques*, 1999, **26**, 748–756.

328 N. C. Stellwagen, *Electrophoresis*, 2009, **30**, 188–195.

329 M. K. Campbell and S. O. Farrell, in *Biochemistry*, Brooks/Cole, 7th edn., 2012, pp. 355–356.

330 S. H. Vosko, L. Wilk and M. Nusair, *Can. J. Phys.*, 1980, **58**, 1200–1211.

331 C. Lee, W. Yang and R. G. Parr, *Phys. Rev. B*, 1988, **37**, 785–789.

332 A. D. Becke, *J. Chem. Phys.*, 1993, **98**, 5648–5652.

333 S. Grimme, J. Antony, S. Ehrlich and H. Krieg, *J. Chem. Phys.*, 2010, **132**, 154104.

334 F. Weigend and R. Ahlrichs, *Phys. Chem. Chem. Phys.*, 2005, **7**, 3297.

335 M. J. Frisch, G. W. Trucks, H. B. Schlegel, G. E. Scuseria, M. A. Robb, J. R. Cheeseman, G. Scalmani, V. Barone, B. Mennucci, G. A. Petersson, H. Nakatsuji, M. Caricato, X. Li, H. P. Hratchian, A. F. Izmaylov, J. Bloino, G. Zheng, J. L. Sonnenberg, M. Hada, M. Ehara, K. Toyota, R. Fukuda, J. Hasegawa, M. Ishida, T. Nakajima, Y. Honda, O. Kitao, H. Nakai, T. Vreven, J. J. A. Montgomery, J. E. Peralta, F. Ogliaro, M. Bearpark, J. J. Heyd, E. Brothers, K. N. Kudin, V. N. Staroverov, T. Keith, R. Kobayashi, J. Normand, K. Raghavachari, A. Rendell, J. C. Burant, S. S. Iyengar, J. Tomasi, M. Cossi, N. Rega, J. M. Millam, M. Klene, J. E. Knox, J. B. Cross, V. Bakken, C. Adamo, J. Jaramillo, R. Gomperts, R. E. Stratmann, O. Yazyev, A. J. Austin, R. Cammi, C. Pomelli, J. W. Ochterski, R. L. Martin, K. Morokuma, V. G. Zakrzewski, G. A. Voth, P. Salvador, J. J. Dannenberg, S. Dapprich, A. D. Daniels, O. Farkas, J. B. Foresman, J. V. Ortiz, J. Cioslowski and D. J. Fox, *Gaussian, Inc., Wallingford CT,*.

336 S. Miertuš, E. Scrocco and J. Tomasi, *Chem. Phys.*, 1981, **55**, 117–129.

337 J. L. Pascual-ahuir, E. Silla and I. Tuñon, *J. Comput. Chem.*, 1994, **15**, 1127–1138.

338 C. Latouche, D. Skouteris, F. Palazzetti and V. Barone, *J. Chem. Theory Comput.*, 2015, **11**, 3281–3289.

339 N. M. O'Boyle, A. L. Tenderholt and K. M. Langner, *J. Comput. Chem.*, 2008, **29**, 839–845.

340 J. Sigmon and L. L. Larcom, *Electrophoresis*, 1996, **17**, 1524–1527.

341 S. Goutelle, M. Maurin, F. Rougier, X. Barbaut, L. Bourguignon, M. Ducher and P. Maire, *Fundam. Clin. Pharmacol.*, 2008, **22**, 633–648.

342 J. B. Lepecq and C. Paoletti, *J. Mol. Biol.*, 1967, **27**, 87–106.

343 X. Zhou, G. Zhang and L. Wang, *Int. J. Biol. Macromol.*, 2014, **67**, 228–237.

344 S. M. V. De Almeida, E. A. Lafayette, L. P. B. G. Da Silva, C. A. Da Cruz Amorim, T. B. De Oliveira, A. L. T. Gois Ruiz, J. E. De Carvalho, R. O. De Moura, E. I. Carneiro Beltrão, M. D. C. De Alves Lima and L. B. De Carvalho, *Int. J. Mol. Sci.*, 2015, **16**, 13023–13042.

345 B. H. Geierstanger and D. E. Wemmer, *Annu. Rev. Biophys. Biomol. Struct.*, 1995, **24**, 463–493.

346 C. J. Cardin and J. P. Hall, in *DNA-targeting Molecules as Therapeutic Agents*, ed. M. J. Waring, Royal Society of Chemistry, 2018, pp. 198–224.

347 J. A. Smith, J. G. Collins and F. R. Keene, in *Metal Complex-DNA Interactions*, eds. N. Hadjiliadis and E. Sletten, Wiley, 2009, pp. 319–340.

348 B. C. Poulsen, S. Estalayo-Adrián, S. Blasco, S. A. Bright, J. M. Kelly, D. C. Williams and T. Gunnlaugsson, *Dalton. Trans.*, 2016, **45**, 18208–18220.

349 J. K. Barton, A. T. Danishefsky and J. M. Goldberg, *J. Am. Chem. Soc.*, 1984, **106**, 2172–2176.

350 I. Haq, P. Lincoln, D. Suh, B. Norden, B. Z. Chowdhry and J. B. Chaires, *J. Am. Chem. Soc.*, 1995, **117**, 4788–4796.

351 F. Höppler, *Chem. Zeitung*, 1933, **57**, 62–63.

352 S. Satyanarayana, J. C. Dabrowiak and J. B. Chaires, *Biochemistry*, 1992, **31**, 9319–9324.

353 Y. Zhang, G. Zhang, X. Zhou and Y. Li, *Anal. Bioanal. Chem.*, 2013, **405**, 8871–8883.

354 E. J. Gabbay, R. E. Scofield and C. S. Baxter, *J. Am. Chem. Soc.*, 1973, **95**, 7850–7857.

355 J. M. Dubois, G. Ouanounou and B. Rouzaire-Dubois, *Prog. Biophys. Mol. Biol.*, 2009, **99**, 87–93.

356 J. M. Kelly, A. B. Tossi, D. J. McConnell and C. OhUigin, *Nucleic Acids Res.*, 1985, **13**, 6017–6034.

357 B. Nordén and T. Kurucsev, *J. Mol. Recognit.*, 1994, **7**, 141–155.

358 B. M. Zeglis, V. C. Pierre, J. T. Kaiser and J. K. Barton, *Biochemistry*, 2009, **48**, 4247–4253.

359 F. Jensen, in *Introduction to Computational Chemistry*, Wiley, third., 2017, pp. 440–441.

360 R. A. Friesner, J. L. Banks, R. B. Murphy, T. A. Halgren, J. J. Klicic, D. T. Mainz, M. P. Repasky, E. H. Knoll, M. Shelley, J. K. Perry, D. E. Shaw, P. Francis and P. S. Shenkin, *J. Med. Chem.*, 2004, **47**, 1739–1749.

361 T. A. Halgren, R. B. Murphy, R. A. Friesner, H. S. Beard, L. L. Frye, W. T. Pollard and J. L. Banks, *J. Med. Chem.*, 2004, **47**, 1750–1759.

362 R. A. Friesner, R. B. Murphy, M. P. Repasky, L. L. Frye, J. R. Greenwood, T. A. Halgren, P. C.

Sanschagrin and D. T. Mainz, *J. Med. Chem.*, 2006, **49**, 6177–6196.

363 K. Roos, C. Wu, W. Damm, M. Reboul, J. M. Stevenson, C. Lu, M. K. Dahlgren, S. Mondal, W. Chen, L. Wang, R. Abel, R. A. Friesner and E. D. Harder, *J. Chem. Theory Comput.*, 2019, **15**, 1863–1874.

364 A. Oleksi, A. G. Blanco, R. Boer, I. Usón, J. Aymamí, A. Rodger, M. J. Hannon and M. Coll, *Angew. Chem. Int. Ed.*, 2006, **45**, 1227–1231.

365 C. Bissantz, B. Kuhn and M. Stahl, *J. Med. Chem.*, 2010, **53**, 5061–5084.

366 N. R. Kallenbach, R. I. Ma and N. C. Seeman, *Nature*, 1983, 305, 829–831.

367 A. L. Ortega, S. Mena and J. M. Estrela, *Cancers (Basel).*, 2011, 3, 1285–1310.

368 J. R. Greenwood, D. Calkins, A. P. Sullivan and J. C. Shelley, *J. Comput. Aided. Mol. Des.*, 2010, **24**, 591–604.

369 J. C. Shelley, A. Cholleti, L. L. Frye, J. R. Greenwood, M. R. Timlin and M. Uchimaya, *J. Comput. Aided. Mol. Des.*, 2007, **21**, 681–691.

370 J. Kralj, A. Bolje, D. S. Polančec, I. Steiner, T. Gržan, A. Tupek, N. Stojanović, S. Hohloch, D. Urankar, M. Osmak, B. Sarkar, A. Brozovic and J. Košmrlj, *Organometallics*, 2019, **38**, 4082–4092.

371 G. R. Fulmer, A. J. M. Miller, N. H. Sherden, H. E. Gottlieb, A. Nudelman, B. M. Stoltz, J. E. Bercaw and K. I. Goldberg, *Organometallics*, 2010, **29**, 2176–2179.

372 O. V. Dolomanov, L. J. Bourhis, R. J. Gildea, J. A. K. Howard and H. Puschmann, *J. Appl. Crystallogr.*, 2009, **42**, 339–341.

373 G. M. Sheldrick, *Acta Crystallogr. Sect. A Found. Adv.*, 2015, **71**, 3–8.

374 G. M. Sheldrick, *Acta Crystallogr. Sect. C Struct. Chem.*, 2015, **71**, 3–8.

375 N. Huang, M. M. Siegel, G. H. Kruppa and F. H. Laukien, *J. Am. Soc. Mass Spectrom.*, 1999, **10**, 1166–1173.